FAIRCHILD HILLER

FABRICATION FEASIBILITY STUDY OF A 30 WATT/POUND ROLL-UP SOLAR ARRAY

SECOND QUARTERLY REPORT

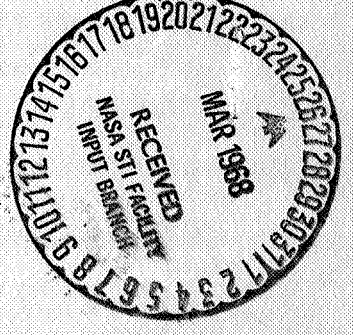
REPORT NO. 652-00102-QR

FEBRUARY 2, 1968

PREPARED FOR THE

JET PROPULSION LABORATORY OF THE CALIFORNIA INSTITUTE OF TECHNOLOGY

UNDER CONTRACT NO. 951969



BY

FAIRCHILD HILLER CORPORATION
SPACE & ELECTRONICS SYSTEMS DIVISION
GERMANTOWN, MARYLAND

PRICE $ _____

TI PRICE(S) $ _____

Hard copy (HC) 3.00

Microfiche (MF) .65

ff July 65

FACILITY FORM 602

N68-19021 (ACCESSION NUMBER) (THRU)

192 (PAGES) 1 (CODE)

CR-93595 (NASA CR OR TMX OR AD NUMBER) 03 (CATEGORY)

FAIRCHILD HILLER

FABRICATION FEASIBILITY STUDY OF A 30 WATT/POUND ROLL-UP SOLAR ARRAY

SECOND QUARTERLY REPORT

REPORT NO. 652-00102-QR

FEBRUARY 2, 1968

PREPARED FOR THE

JET PROPULSION LABORATORY OF THE
CALIFORNIA INSTITUTE OF TECHNOLOGY

UNDER CONTRACT NO. 951969

BY

FAIRCHILD HILLER CORPORATION
SPACE & ELECTRONICS SYSTEMS DIVISION
GERMANTOWN, MARYLAND

FAIRCHILD HILLER CORPORATION

DATE February 2, 1968

SPACE and ELECTRONICS SYSTEMS DIVISION

DOCUMENT NO.

652-00102-QR

TITLE

Second Quarterly Report

Fabrication Feasibility Study of a 30

Pound Roll-up Solar Array

Contract No. 951969

No. Pages

PREPARED _____ ORIGINATOR	**APPROVED** _____ ENGINEERING
APPROVED _____ QA/REL/MAINT	**APPROVED** _____ PROGRAM.
APPROVED _____ MANUFACTURING	**APPROVED** _____
APPROVED _____ SPECS & STDS.	**APPROVED** _____

REVISIONS

"This work was performed for the Jet Propulsion Laboratory, California Institute of Technology, as sponsored by the National Aeronautics and Space Administration under Contract NAS 7-100."

"This report contains information prepared by Fairchild Hiller Corporation under JPL subcontract. Its content is not necessarily endorsed by the Jet Propulsion Laboratory, California Institute of Technology, or the National Aeronautics and Space Administration."

ABSTRACT

Activities and detail design investigations conducted during the second quarter of the program are reported. Included are analysis and descriptions of each major subsystem component associated with the design of a 30 watt/pound roll-up solar array. Each engineering discipline (i.e. Electrical, Thermal, Structural, Mechanical, and Material selection) has been researched in depth to prove the feasibility of attaining a 30 watt/pound roll-up solar array. This report establishes that a 30 watt/pound array is within the 1968 state-of-the art.....

TABLE OF CONTENTS

		PAGE
1.0	INTRODUCTION AND SUMMARY	1-1
1.1	Introduction	1-1
1.2	Summary	1-1
2.0	TECHNICAL DISCUSSION	2-1
2.1	Design Activities	2-1
2.2	Electrical System Design	2-41
2.3	Structural Analysis	2-73
2.4	Materials Engineering	2-114
2.5	Thermal Analysis	2-135
2.6	Reliability	2-165
2.7	Design Selection	2-172
3.0	CONCLUSIONS	3-1
4.0	RECOMMENDATIONS	4-1
5.0	NEW TECHNOLOGY	5-1
6.0	REFERENCES	6-1

LIST OF ILLUSTRATIONS

Fig No.	Title	Page
2.1.1	Roll-Up Array Deployment Arm	2-2
2.1.2	Rolled Array Dia. vs. Array Width	2-4
2.1.3	Foam Backing Rolled Dia. vs. Array Width	2-5
2.1.4a	Single Link Folding Arm (12' wide)	2-6
2.1.4b	Single Link Folding Arm (6' wide)	2-7
2.1.4c	Single Link Folding Arm (6' wide)	2-8
2.1.4d	Single Link Folding Arm (7.6' wide)	2-9
2.1.4e	TEE Collapsible Element Deployment Device	2-10
2.1.4f	TEE Collapsible Element Deployment Device	2-11
2.1.4g	TEE Collapsible Element Deployment Device	2-12
2.1.4h	TEE Collapsible Element Deployment Device	2-13
2.1.5	Hinge Lock Collapsing Tube Deployment Device	2-15
2.1.6	Hingelock Collapsing Tube Mechanism Envelope	2-16
2.1.7	Hingelock Tube Dia. (Inches vs. Weight)	2-17
2.1.8	Hingelock Tube Deployment System	2-18
2.1.9	Solar Cell Stack Weight	2-19
2.1.10	Array Package Volume	2-21
2.1.11	Cell Fracture Load vs. Drum Dia.	2-23
2.1.12	Cell Fracture Load Test	2-24
2.1.13	Storage Drum Configuration	2-25
2.1.14	Solar Array Tensioning Device	2-27
2.1.15	Deployment Arm Joint	2-28
2.1.16	Folding Arm Joint Programming System	2-30
2.1.17	Drive System Concept	2-32
2.1.18	Laced Hinge Tension Test	2-35
2.1.19	Latching Concepts	2-37
2.1.20	Array Folding Arm System	2-38
2.2.1	Voltage Current Characteristics vs. Cell Temperature	2-43
2.2.2	Voltage-Current Characteristics vs. Cell Temperature	2-44
2.2.3	Voltage-Current Characteristics at 55°C	2-45
2.2.4	Voltage-Current Characteristics	2-46
2.2.5	Voltage-Current Characteristics	2-47
2.2.6	Voltage-Current Characteristics	2-49
2.2.7	Effects of Foam Backing on Cell E-I Characteristics	2-50
2.2.8	Solar Cell Module Current Paths	2-51
2.2.9	Expanded Silver Mesh Cell Interconnects	2-54
2.2.10	Power/Weight Ratio vs. Power Loss	2-58
2.2.11	Power/Weight Ratio vs. Aspect Ratio	2-61
2.2.12	Cross Section of Bus Bar Harness	2-62
2.2.13	The Effect of Bus Bar Loading on the Voltage-Current Characteristics	2-64
2.2.14	Bus Bar Connector	2-65
2.2.15	Connector Configuration Showing Test Connection	2-67
2.2.16	Module/Harness Electrical Interface Schematic	2-68

List of Illustrations

Fig. No.	Title	Page
2.2.17	Solar Array Wiring Configuration	2-69
2.3.1	Single Drum Array	2-75
2.3.2	Allowable Bending Stress	2-76
2.3.3	Design Chart For Obtaining Parameters	2-78
2.3.4	Applied Moment vs. Optimum Cylinder Diameter	2-79
2.3.5	Thin Wall Cylinder Drum Length vs Drum Weight	2-80
2.3.6	Thin Wall Cylinder Drum Length vs Drum Weight	2-81
2.3.7	Honeycomb Cylinder Design Data	2-86
2.3.8	Weight Data - .25" sandwich Cylinder	2-87
2.3.9	Weight Data - .25" Honeycomb Cylinder	2-88
2.3.10	Storage Drum Weight vs. Array Weight	2-89
2.3.11	Storage Drum Dia. vs. Storage Drum Weight	2-90
2.3.12	Folding Arm Load Analysis	2-91
2.3.13	Folding Arm Weight vs. Length	2-93
2.3.14	Folding Arm Weight vs. Length	2-94
2.3.15	Folding Arm Weight vs. Length	2-95
2.3.16	Structural System Weight vs. Array Width	2-96
2.3.17	Structural System Weight vs. Array Width	2-97
2.3.18	Structural System Weight vs. Array Width	2-98
2.3.19	30 WAPSA Hingelock Support Boom	2-105
2.3.20	Hingelock Support Boom (Weight vs. Length)	2-106
2.3.21	Hingelock Support Boom (Weight vs. Length)	2-107
2.3.22	Hingelock Support Boom (Weight vs. Length)	2-108
2.3.23	Hingelock Support Boom (Weight vs. Length)	2-109
2.4.1	Laced Joints Between Module Panels	2-121
2.4.2	Creep Data for 3 MIL Kapton H Film	2-122
2.4.3	Effective Emittance Test Set-up	2-129
2.5.1	Temperature and Incident Solar Flux	2-137
2.5.2	Temperature and Incident Solar Flux Transients	2-138
2.5.3	Temperature Decay of Isothermal Solar Cell Array	2-140
2.5.4	Temperature Decay of Array in Planet Shadow	2-142
2.5.5	Temperature Decay of Array in Planet Shadow	2-143
2.5.6	Transient Temperature Behavior of Array	2-144
2.5.7	Steady-State Temperature	2-145
2.5.8	Albedo and Earth Emission Fluxes	2-147
2.5.9	Temperature History of Array	2-148
2.5.10	Array Temperature at Subsolar Point	2-149
2.5.11	Thermal Model of Array and Arm	2-151
2.5.12	Array Temperature Profile	2-153
2.5.13	Array Temperature Profile	2-154
2.5.14	Temperature Distribution	2-155
2.5.15	Array Temperature Profile	2-157
2.5.16	Temperature Distribution	2-158
2.5.17	Circumferential Temperature Distribution	2-160
2.5.18	Array Temperature Profile	2-161

List of Illustrations

Fig. No.	Title	Page
2.5.19	Array Temperature Profile	2-163
2.5.20	Circumferential Temperature Distribution	2-164
2.6.1	Basic Mortality Types	2-168
2.6.2	Folding Arm Mechanism	2-169
2.6.3	TEE Mechanism	2-170
2.6.4	Hingelock Mechanism	2-171
3.1.1	Weight Summary	2-173
3.1.2	Design Selection Summary	2-174
3.1.3	Design Summary	2-176

LIST OF TABLES

Table No.	Title	Page
2.2.1	Module Power Characteristics	2-65
2.2.2	Optimum Bus Power Loss	2-70
2.2.3	Array Power Calculations	2-71
2.3.1	Solar Panel Storage Drum Parametric Study	2-73
2.3.2	Folding Arm Weight Summary	2-85
2.3.3	Control System Weight Summary	2-100
2.4.1a	Design Allowable Properties (Room Temperature)	2-117
2.4.1b	Design Allowable Properties	2-118
2.4.2	Structural Materials Comparative Properties	2-119
2.4.3	Adhesive Properties	2-123
2.4.4	Weight Losses of Adhesives at 140°C	2-125
2.4.5	Loaded Ball Bearing Test	2-127
2.4.6	Emittance of Back Surface of Array	2-131

1.0 INTRODUCTION AND SUMMARY

1.1 Introduction

This document presents the results of the second quarter of a one-year study contract to evaluate the feasibility of fabricating a 30 watt/pound or greater roll-up solar array. The work was conducted by the Fairchild Hiller Corporation, Space and Electronics Systems Division, for the Jet Propulsion Laboratory, California Institute of Technology, under contract Number 951969. This report covers those activities conducted between October 1, 1967 and December 31, 1967.

1.2 Summary

During the second quarter reporting period, efforts were directed toward selection of the basic deployment/retraction mechanism and detail design of the associated array components. The final decision on selection of a deployment mechanism was based on: (1) manufacturing feasibility; (2) reliability; (3) simplicity of design; (4) state-of-the-art (1968) materials, processes and components; and (5) a design that would meet the requirements of the design specification.

A five (5) element folding arm (three full links and two half links) was chosen for the deployment/retraction technique. The arms are three (3) square inch corrugated tubes made of a Boron/Epoxy composite material which was selected for its high strength to weight ratio. One end of the extended arm is fastened to a substrate spreader bar located outboard of the array; the other end interfaces with the spacecraft. A cable and pulley system is used to program the motion of the folding arm joints.

During launch and prior to deployment, the array panel is stored on a light weight Graphite/Epoxy drum which is supported by aluminum end plates that are mounted to the spacecraft. Upon initiation of deployment, an electric motor drives the inboard arm element through 90^{o} of rotation and causes the arms to unfold. As the arms deploy outward, the array is "pulled" from its storage drum. A tension spring is engaged during the final 1/2 turn of the array storage

drum and keeps a tension load on the array while in a deployed condition.

The solar array panel is composed of four (4) sub-panels and each sub-panel consists of 12 identical modules. A modular construction technique is used to simplify fabrication and enhance repairability of the array. Each module consists of two (2) mil Kapton (H film) with 2 cm x 2 cm x 8 mil thick, N on P, silicon solar cells which are protected by 3 mil thick glass cover slips. There are 1290 cells per module arranged in a six (6) cell parallel connected by 215 cell series connected matrix.

Sections 2.1 through 2.6 present the basic design parametric studies. A detail description of the selected system is contained in Section 2.1.6.

2.0 TECHNICAL DISCUSSIONS

2.1 DESIGN ACTIVITIES

Design activities during this period consisted of parametric and detail analyses of mechanical systems and components required for array storage and deployment. Primary attention was directed toward:

- Identifying candidate roll-up solar array systems.
- Conducting parametric studies on each of the roll-up array systems.
- Identifying dominent factors which affect array power/weight ratio.
- Selection of an optimum baseline configuration.
- Fabrication studies.
- System design.

2.1.1 Candidate Systems

Studies of the mechanical deployment devices available for use on a roll-up solar array have shown that there are four basic systems. They are:

- Overlapping foil (TEE-Tubular Extendible Element).
- Collapsible tube (Hingelock-TEE device).
- Folding arm structure.
- Helically wound tube.

Systems 1 thru 3 are shown in Figure 2.1.1. Since most array designs require substrate tension (to prevent the array from billowing and deviating from its intended position in the deployed configuration), the helically wound tubular spring was rejected because its lateral bending stiffness decreases with increase in compressive column loading and is thus inherently inefficient for the proposed application. In addition, there is a general lack of detail design information available on these springs.

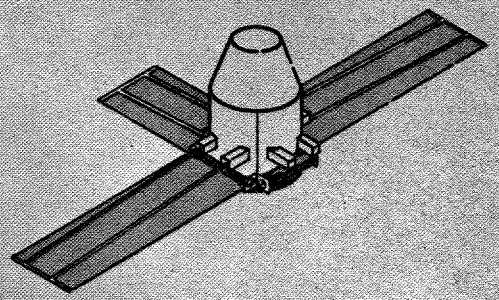
The remaining systems (Hingelock, Tubular Extendible Element and folding arm) were subjected to detail analyses to ascertain which would be the best system.

2.1.2 Parametric Studies

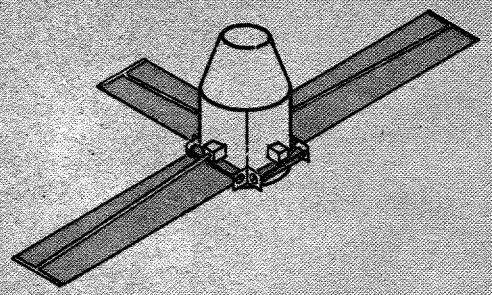
2.1.2.1 Volume Study

A volume study was performed in order to approximate the packaging efficiency of the various systems and to estimate the probably structural complexity.

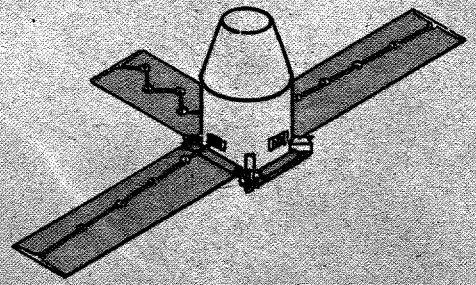
PANEL SUPPORTING SYSTEM CONCEPTS



ROLL-UP ARRAY TUBULAR ELEMENT DESIGN



HINGE-LOCK ROLL-UP ARRAY TUBING ELEMENT DESIGN



ROLL-UP ARRAY DEPLOYMENT ARM DESIGN

Figure 2.1.1

For example, the use of 12-foot arm segments for the deploying arm concept would require an overhang of the 100-inch mounting surface, to permit the structure to support the ends of the arms for launch loads.

Data on roll diameter of the foam and of the substrate, as shown in Figures 2.1.2 and 2.1.3 were generated as aids in sizing the end plates and other structural members. Since manufacturing considerations dictate the minimum gauges practical for fabrication, it was assumed during the study that a larger size structure, even though supporting a lighter load, would be heavier. The folding arm design was studied over a range of array widths combined with the various arm segment lengths required. Results of the volume study for various width arrays are shown in Figure 2.1.4a through 2.1.4h for a configuration using a separate drum to take-up and store the foam damper pad, required for cell stack protection during launch.

2.1.2.2 Weight Summary

The following equation is a summary of the method used in tabulating weights.

$$W_{total} = W_{\substack{array \\ panel}} + W_{long.} + W_{width} + W_{independ.}$$

$$W_{long.} = W_{links} + W_{fittings} + W_{cable,\ chain\ etc.}$$

$$W_{width} = W_{roller} + W_{\substack{spreader \\ bar}} + W_{\substack{top\ \&\ bottom \\ covers}} + W_{\substack{foam\ ret. \\ roller}} + W_{\substack{overhang \\ bkts.}}$$

$$W_{indep.} = W_{damp.} + W_{\substack{drive \\ mech.}} + W_{\substack{rel. \\ mech.}} + W_{\substack{foam\ ret. \\ mech.}} + W_{end\ plates}$$

Array weight is divided into four groups. The first is the weight of the array panel, which is considered constant for all deployment systems. The second group includes those parts dependent on extension length. The third group is dependent on the width of the array and the last contains items which are relatively independent of the array length or width.

Items whose weight are dependent on the length of the array are: the fittings within the folding arm; the folding arm segments themselves; the cable

20 X 20 PER INCH
EUGENE DIETZGEN CO.
MADE IN U. S. A.

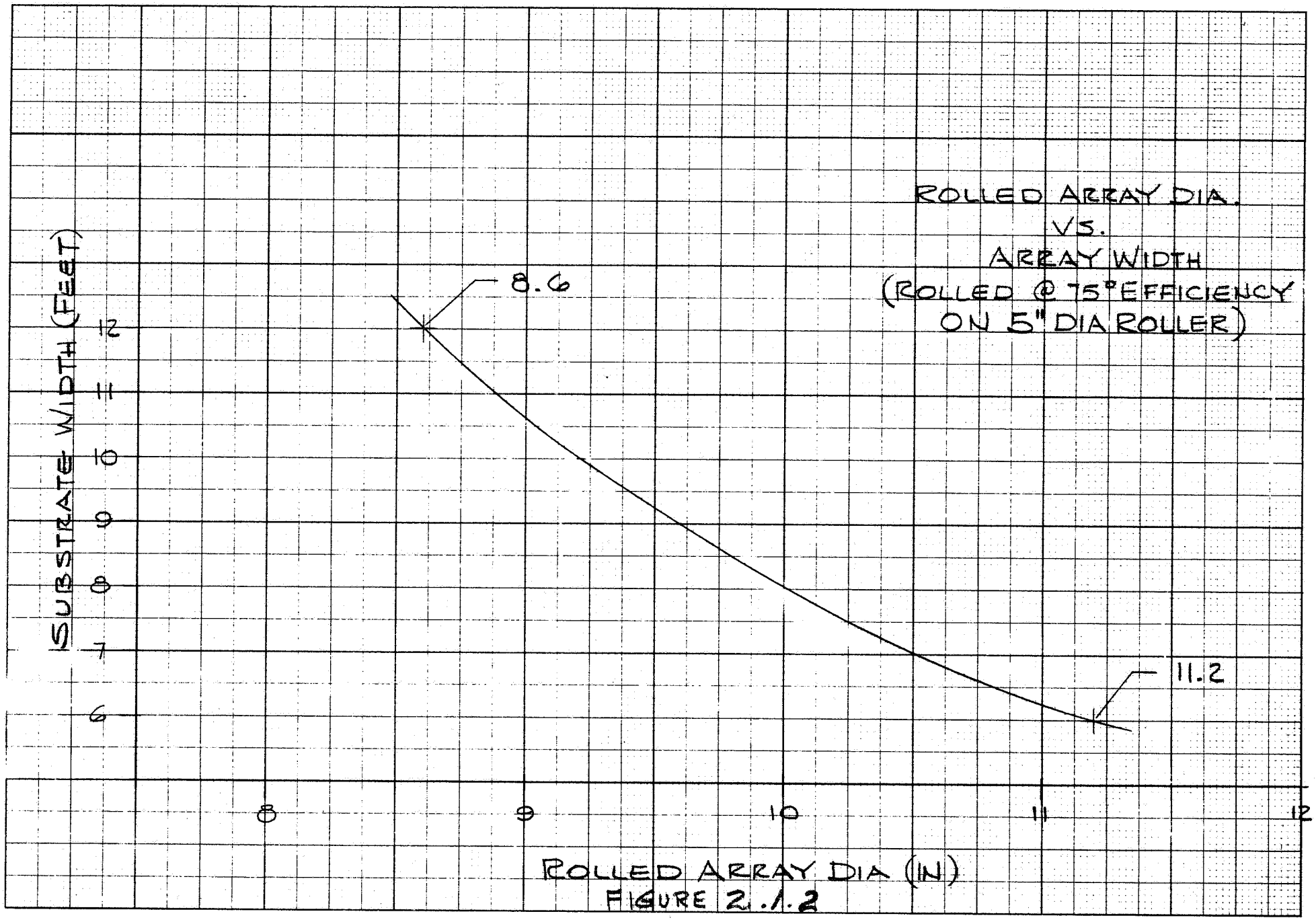


FIGURE 2.1.2

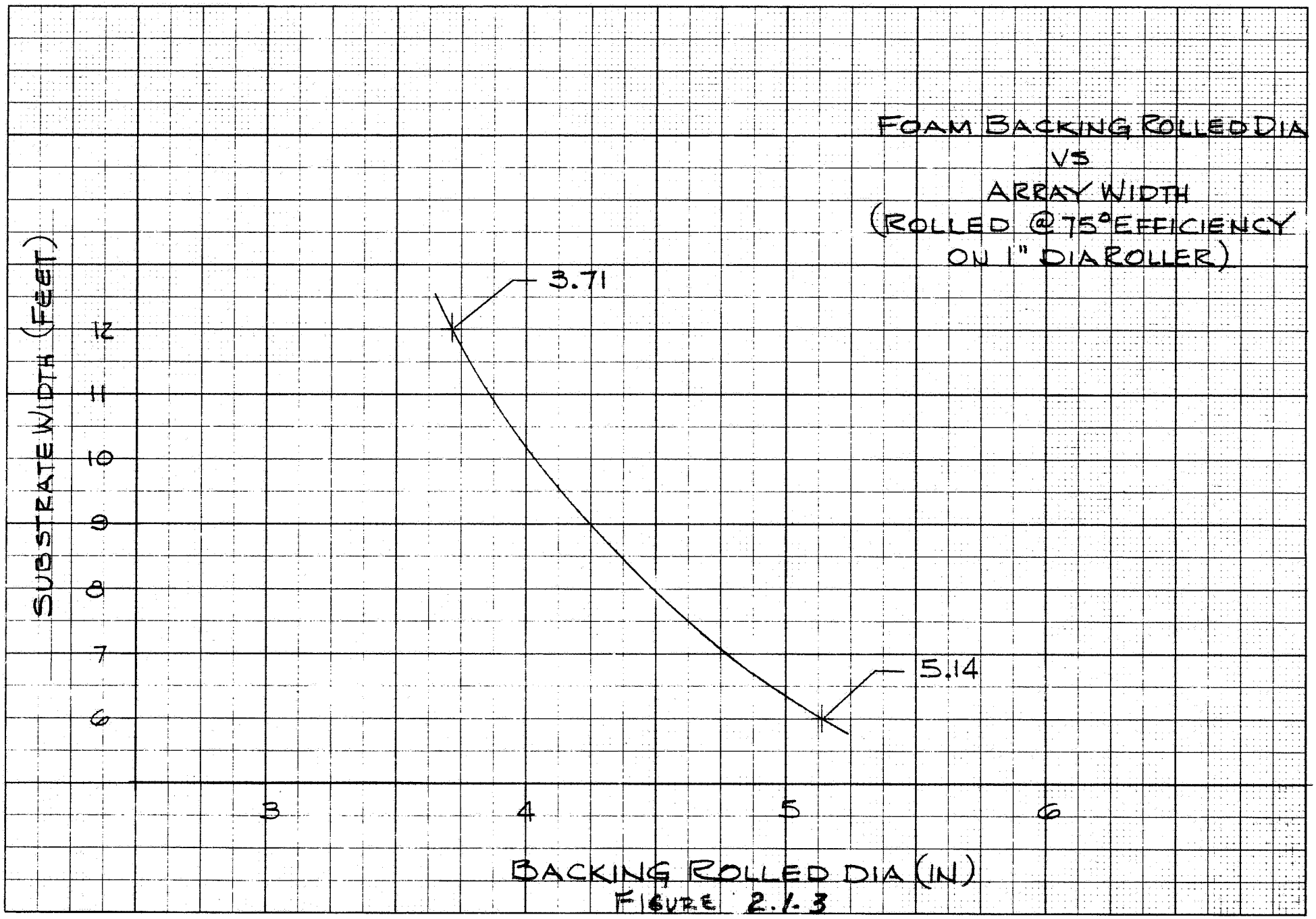
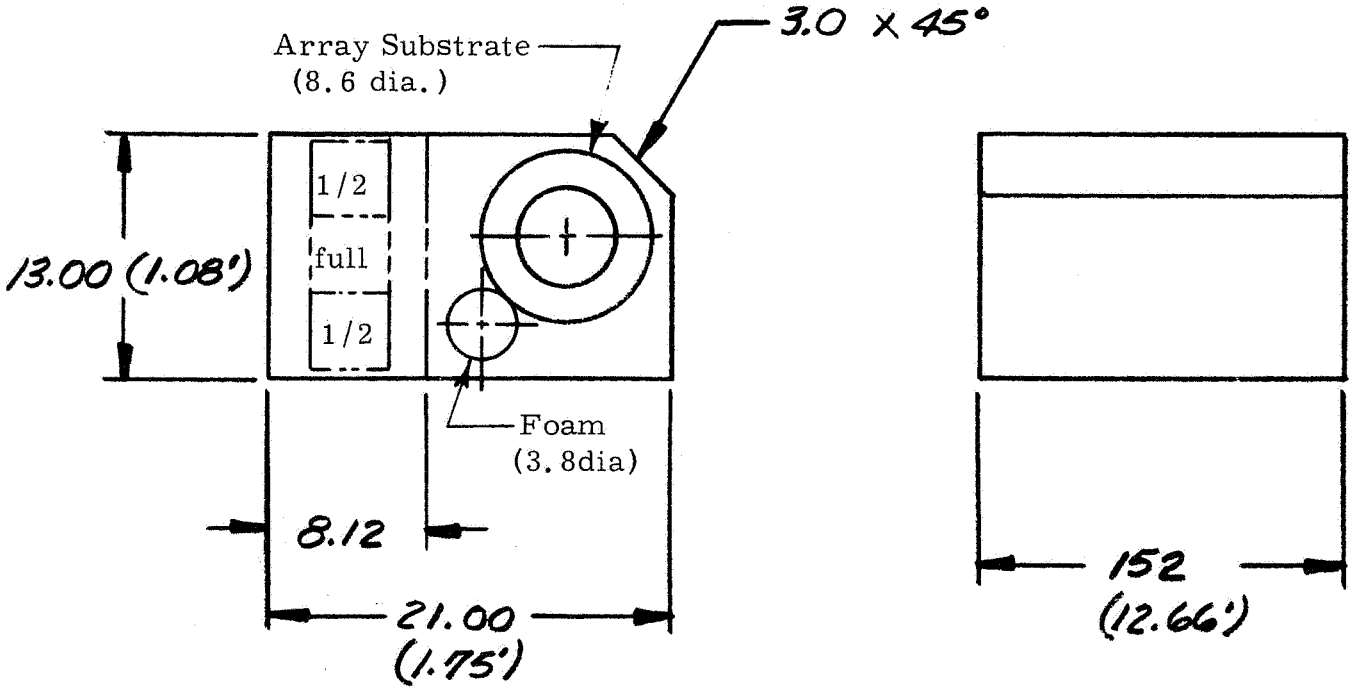

FOAM BACKING ROLLED DIA
VS
ARRAY WIDTH
(ROLLED @ 75° EFFICIENCY
ON 1" DIA ROLLER)
3.71
5.14
SUBSTRATE WIDTH (FEET)
12
11
10
9
8
7
6
3
4
5
6
BACKING ROLLED DIA (IN)

FIGURE 2.1.3

12' WIDE ARRAY

Links = Approximate (longest possible)
2 Half Links = 74.5" (each)
1 Full Link = 149"
2 Hinges
Deployed Length = 24.8' (approx)
Volume = 22.345 cu. ft.

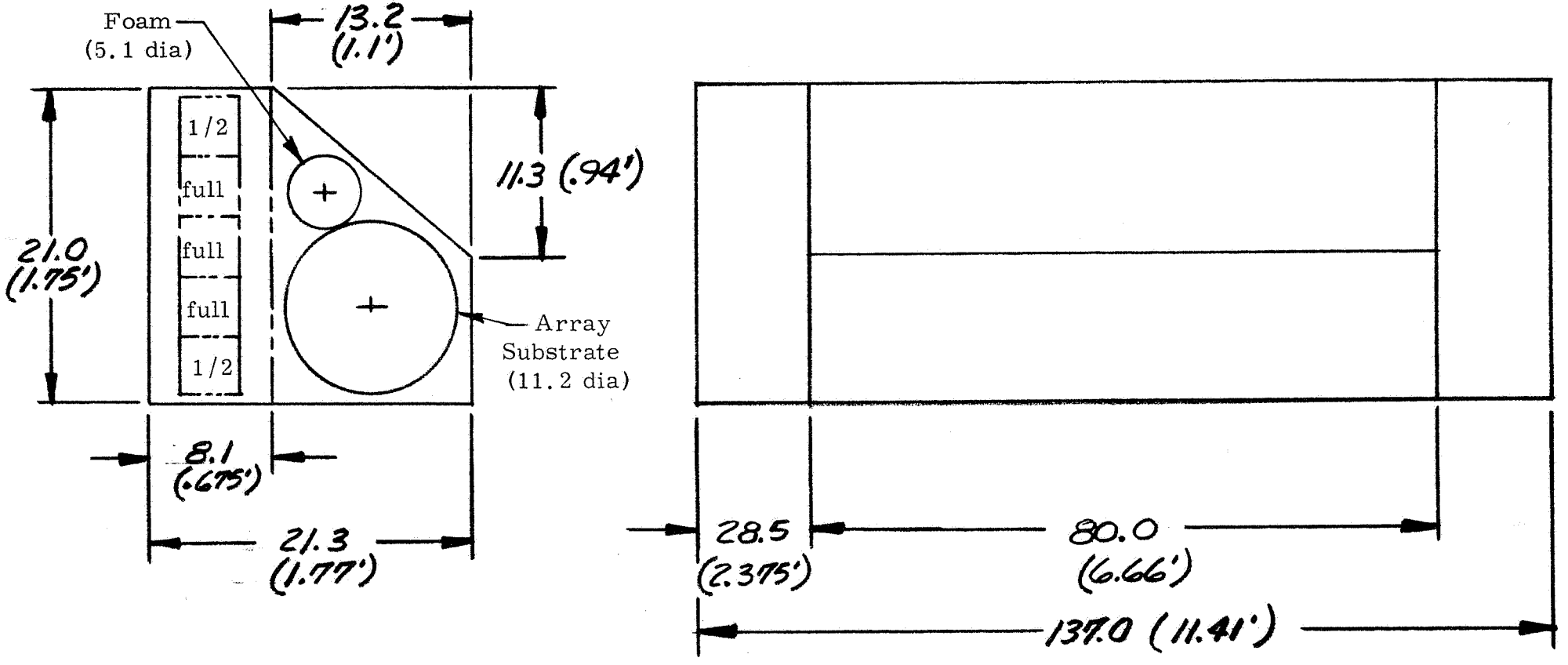


SINGLE LINK FOLDING ARM

FIGURE 2.1.4a

6' WIDE ARRAY (ALTERNATE)

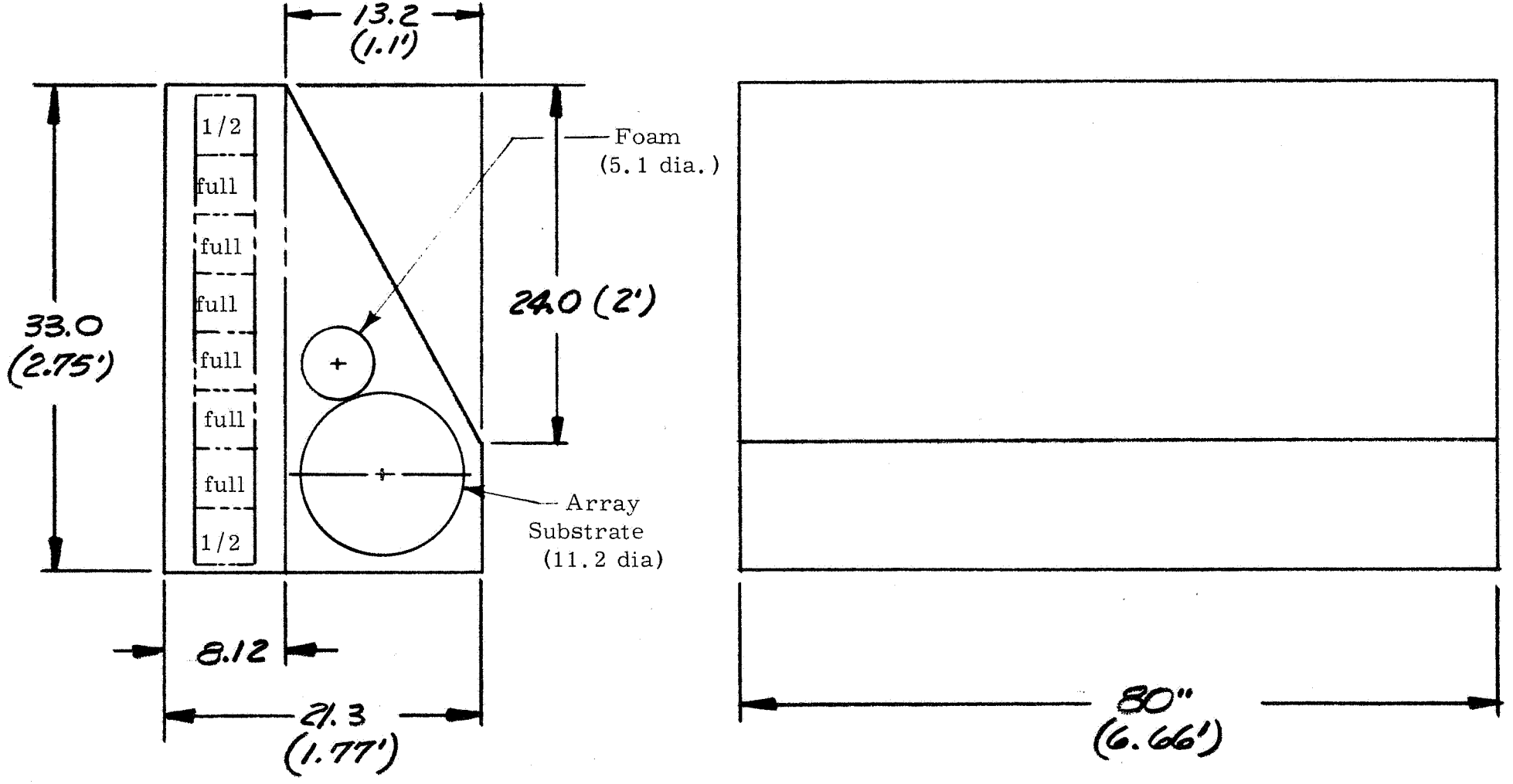
Links = 11.4' approximate
2 Half Links = 68.5" (each)
3 Full Links = 137" (each)
4 Hinges
Deployed Length = 45.6' (approx)
Volume = 20.010 cu. ft.



SINGLE LINK FOLDING ARM
FIGURE 2.1.4b

6' WIDE ARRAY

Links = 6.6' approximate
2 Half Links = 39.5 (each)
6 Full Links = 78.1 (each)
7 Hinges
Deployed Length = 45.6' (approx)
Volume = 25.09 cu. ft.

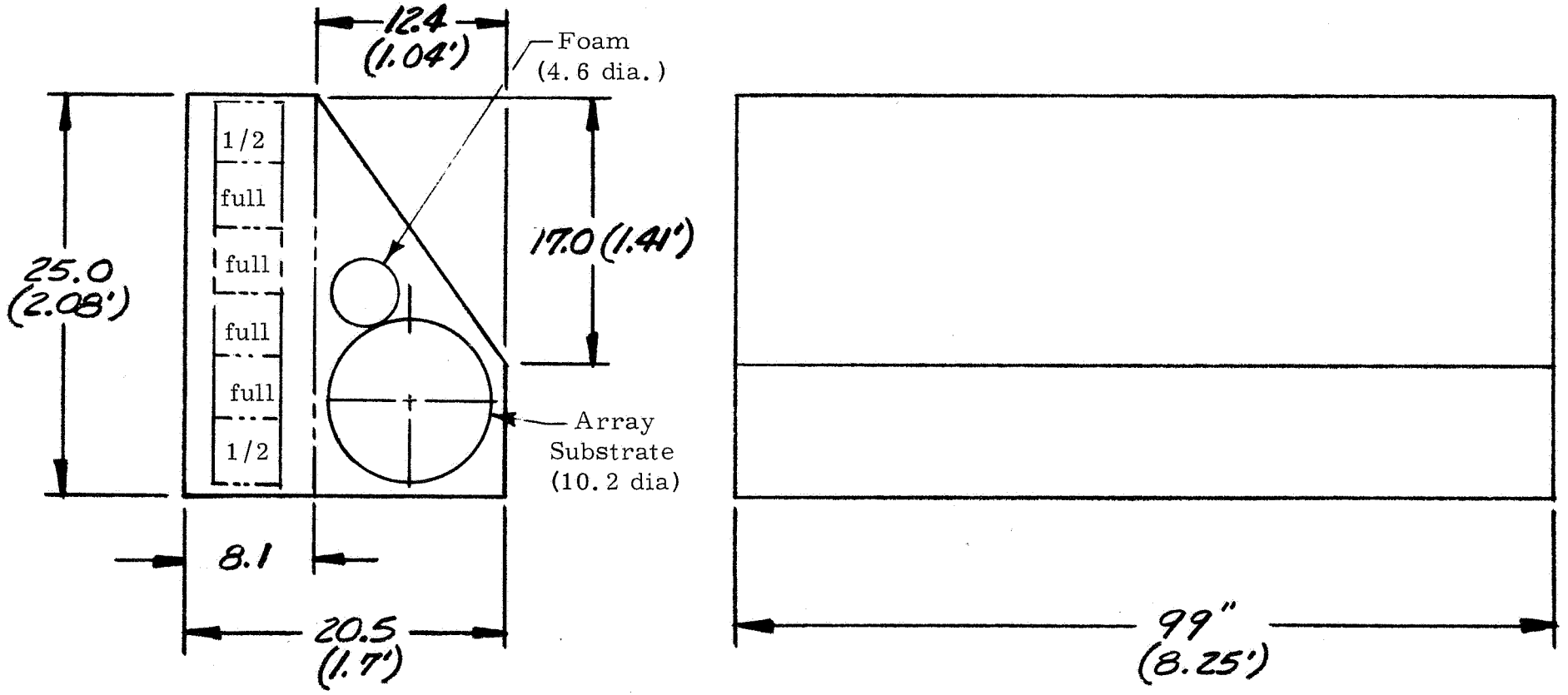


SINGLE LINK FOLDING ARM

FIGURE 2.1.4c

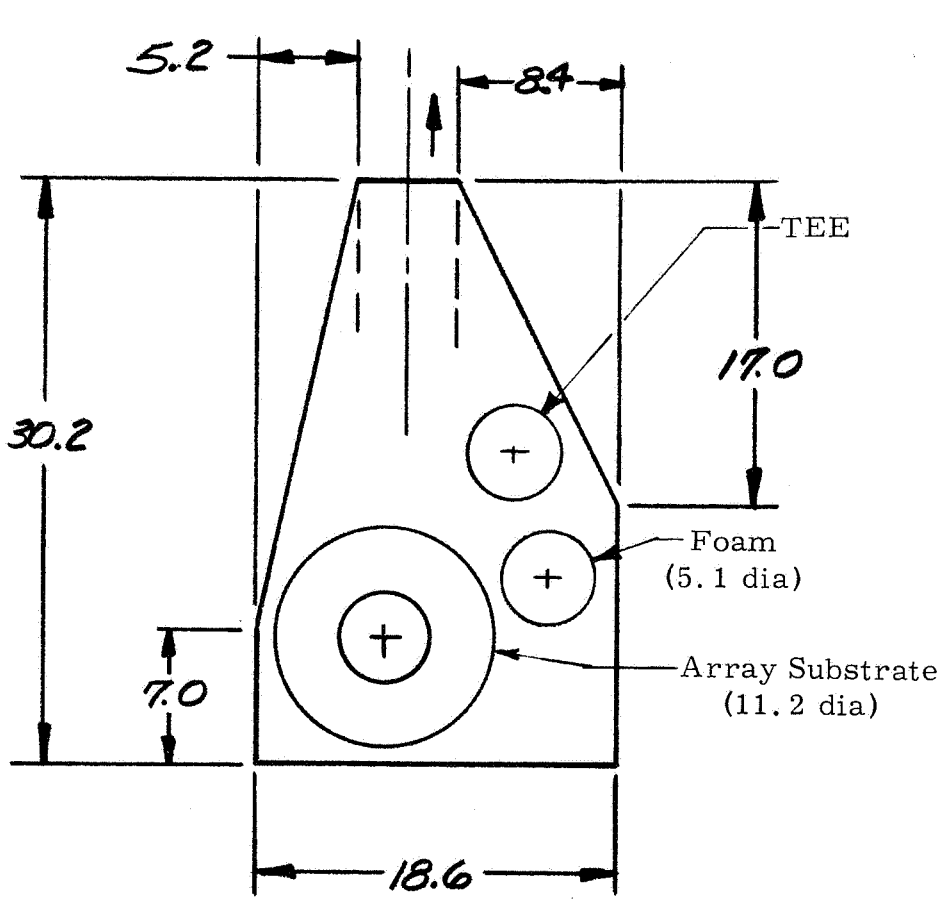
7.6 WIDE ARRAY

Links = 8.2' approximately
2 Half Links = 45.5 (each)
4 Full Links = 91.0 (each)
5 Hinges
Deployed Length = 37.9 approx.
Volume = 23.12 cu. ft.

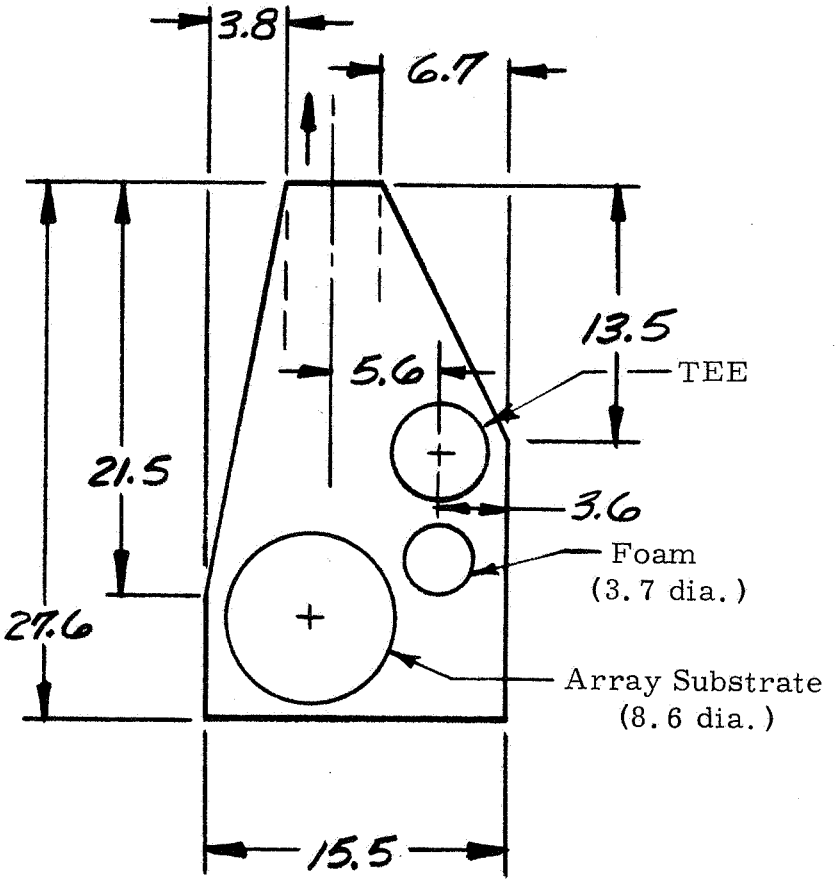


SINGLE LINK FOLDING ARM

FIGURE 2.1.4d



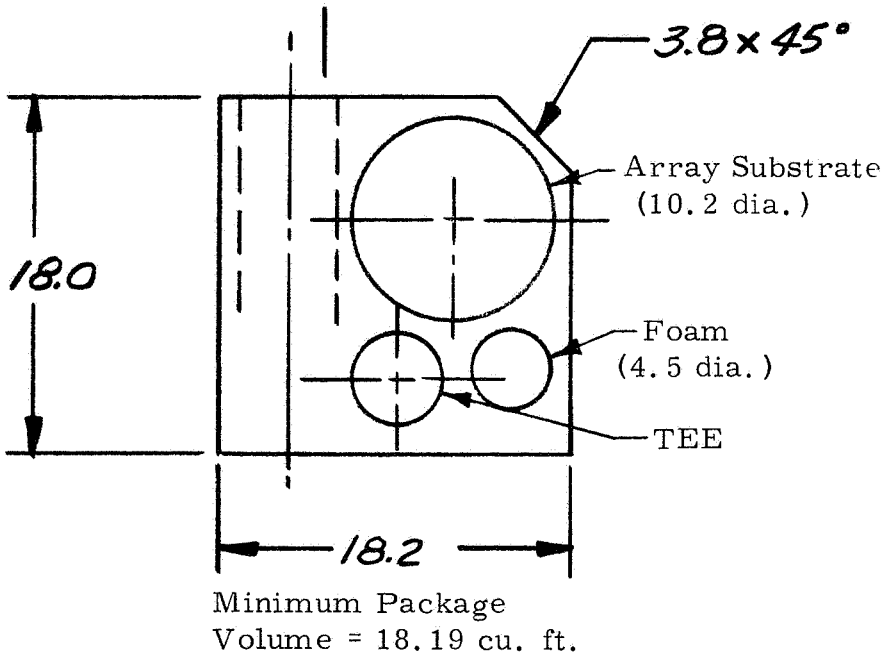
Minimum Eccentricity
Volume = 19.907 cu.ft.



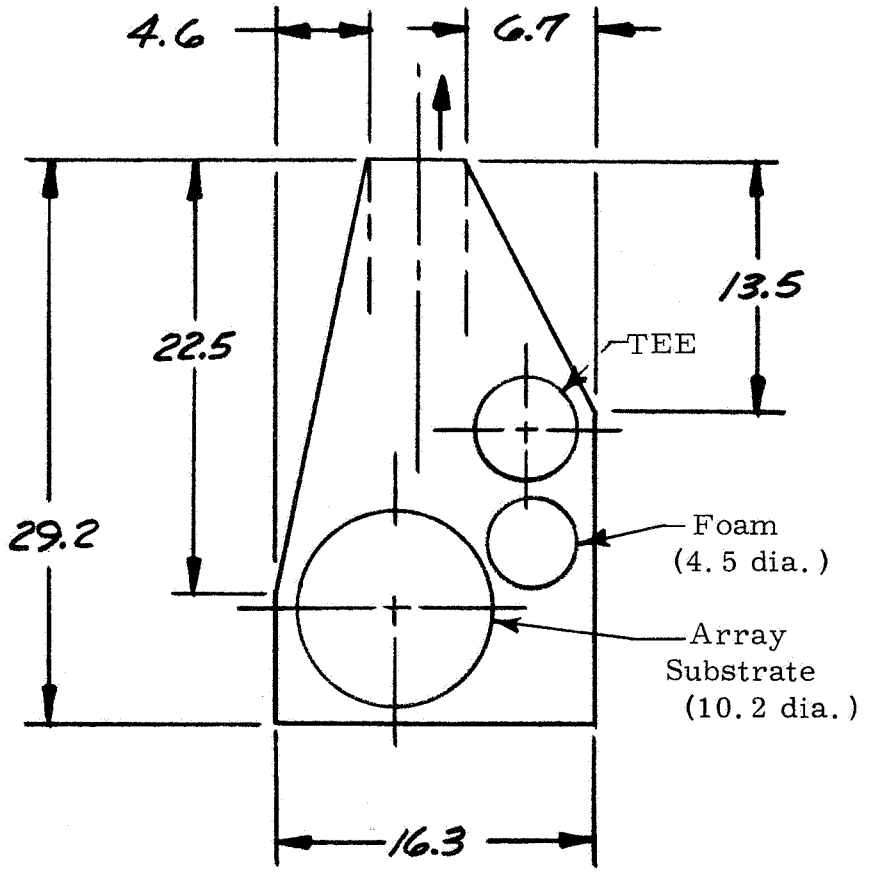
Minimum Eccentricity
Volume = 30.060 cu.ft.

TEE COLLAPSIBLE ELEMENT DEPLOYMENT DEVICE

FIGURE 2.1.4e



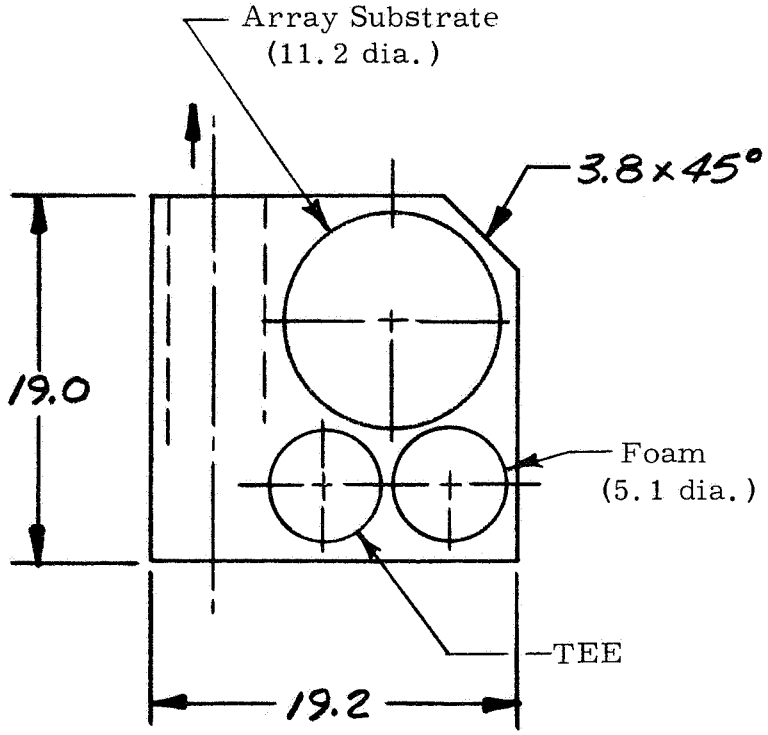
Minimum Package
Volume = 18.19 cu. ft.



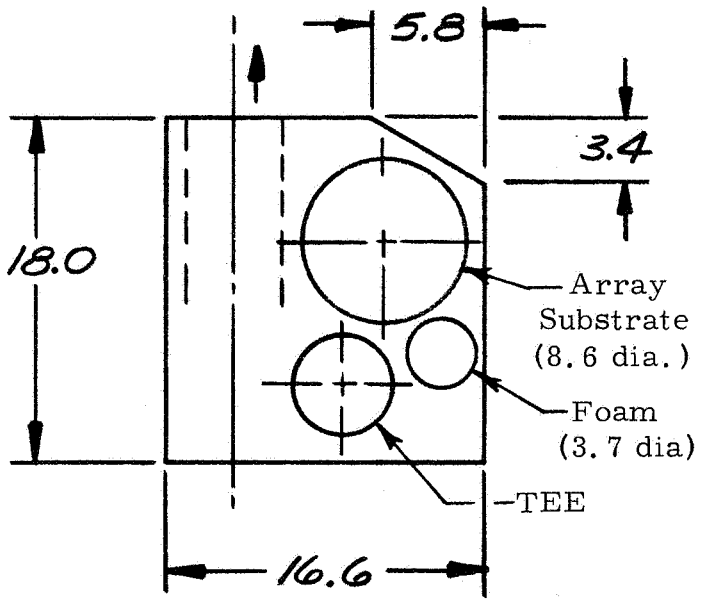
Minimum Eccentricity
Volume = 21.72 cu. ft.

TEE COLLAPSIBLE ELEMENT DEPLOYMENT DEVICE

FIGURE 2.1.4f



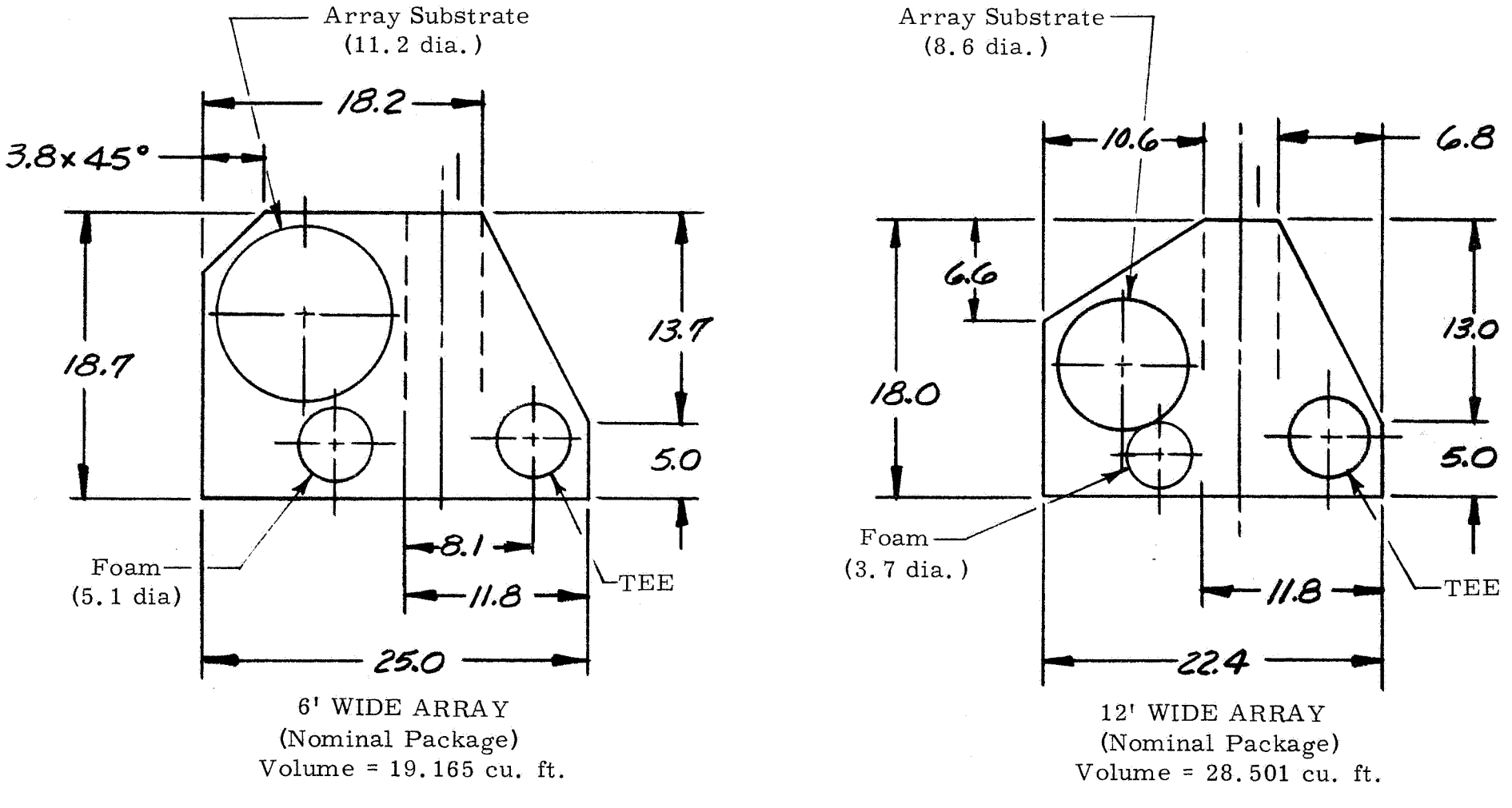
Minimum Package
Volume = 16.565 cu. ft.



Minimum Package
Volume = 25.416 cu. ft.

TEE COLLAPSIBLE ELEMENT DEPLOYMENT DEVICE

FIGURE 2.1.4g



6' WIDE ARRAY
(Nominal Package)
Volume = 19.165 cu. ft.

12' WIDE ARRAY
(Nominal Package)
Volume = 28.501 cu. ft.

TEE COLLAPSIBLE ELEMENT DEPLOYMENT DEVICE

FIGURE 2.1.4h

and pulleys within the arm. The significance of this analysis is that an indication may be obtained whether to use a small number of arms, thus reducing the fitting weights but increasing the arm weights (due to strengthening the arm to take the column loads), or to use more arm elements of shorter length, where in the number of fittings increase but the arm members may be lighter.

For the "Hingelock" system, this phase of the analysis reduces to determining the proper diameter of the support element and scaling up the weight of the drive mechanism. A typical "Hingelock" mechanism is shown in Figure 2.1.5. Figure 2.1.6 is a sketch of a probable dispenser for a 5-inch diameter "Hingelock" tube. The weights used for this study were based on an existing prototype deployment mechanism. Many of the mechanism components remain the same size regardless of the "Hingelock" tube diameters; these weights are held constant. For those mechanism components that do change, the weights were scaled up using the prototype mechanism as a guide.

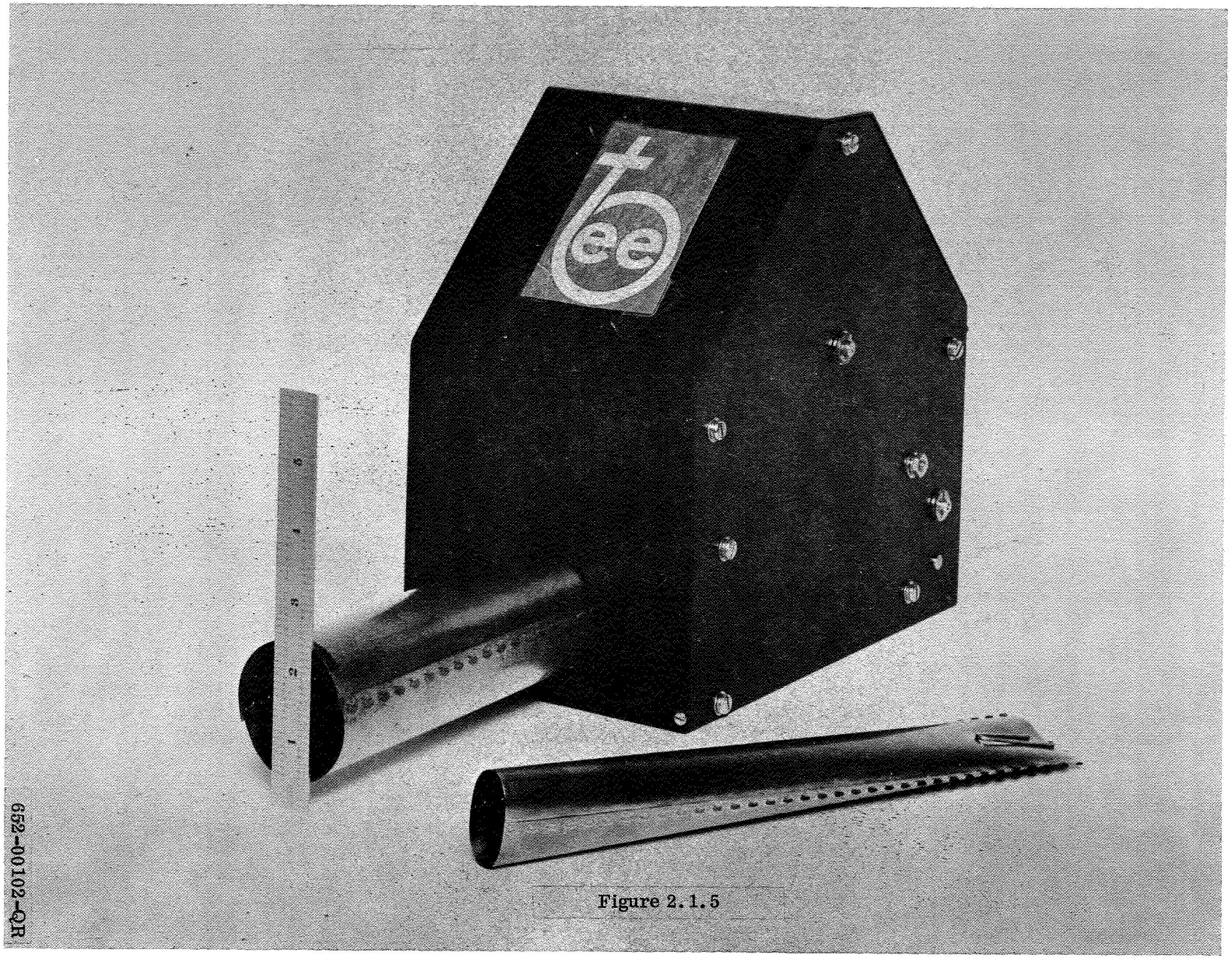
The calculated weight for a 5" inch diameter x 4-1/2 mil BeCu "Hingelock" deployment mechanism is shown in Figure 2.1.7 and 2.1.8.

Parts which are dependent on the width of the array include the array roller, a front plate or spreader bar, enclosing structure for the top and bottom of the assembly, the foam take-up roller (if one is needed), and any over-hanging brackets to support items extending beyond the 100-inch mounting surface.

Those items that are independent of the array length or width include the damper, folding arm drive mechanism, the release mechanisms and the foam take-up mechanisms,if such are to be used.

2.1.3 Power/Weight Ratio

The dominent factors effecting power/weight ratio are the total weight of the solar cell stack, plus the weight of the deployment mechanism. In order to make a reliable estimate of solar cell stack weight, the array was divided into modules and a calculated weight per module and per square foot was generated. The definition of "Module" and the reasons for the selected module size are explained in Section 2.2. Figure 2.1.9 shows the resulting weights generated for the solar cell stack.



652-00102-QR

Figure 2.1.5

HINGELOCK COLLAPSIBLE TUBE MECHANISM ENVELOPE

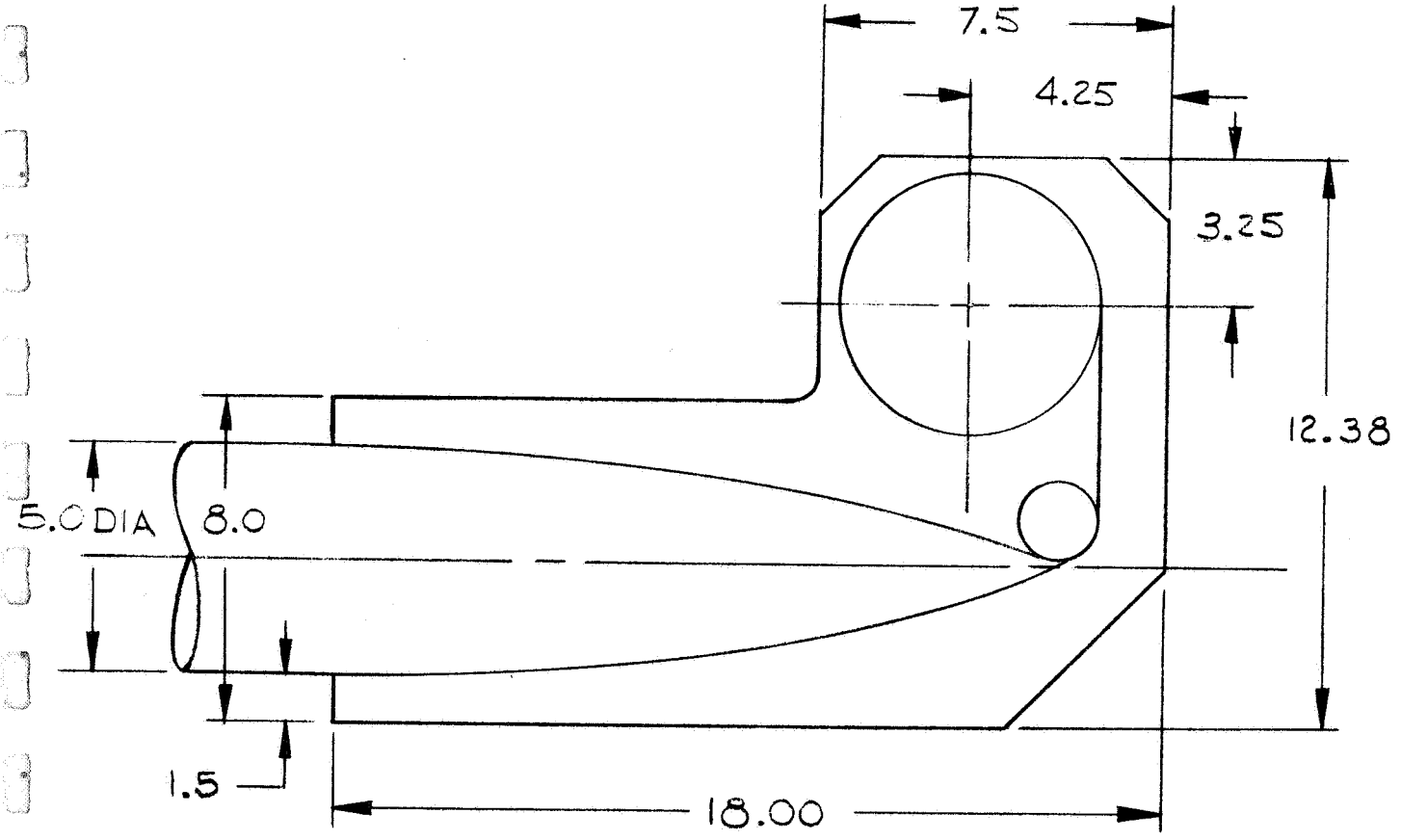


FIGURE 2.1.6

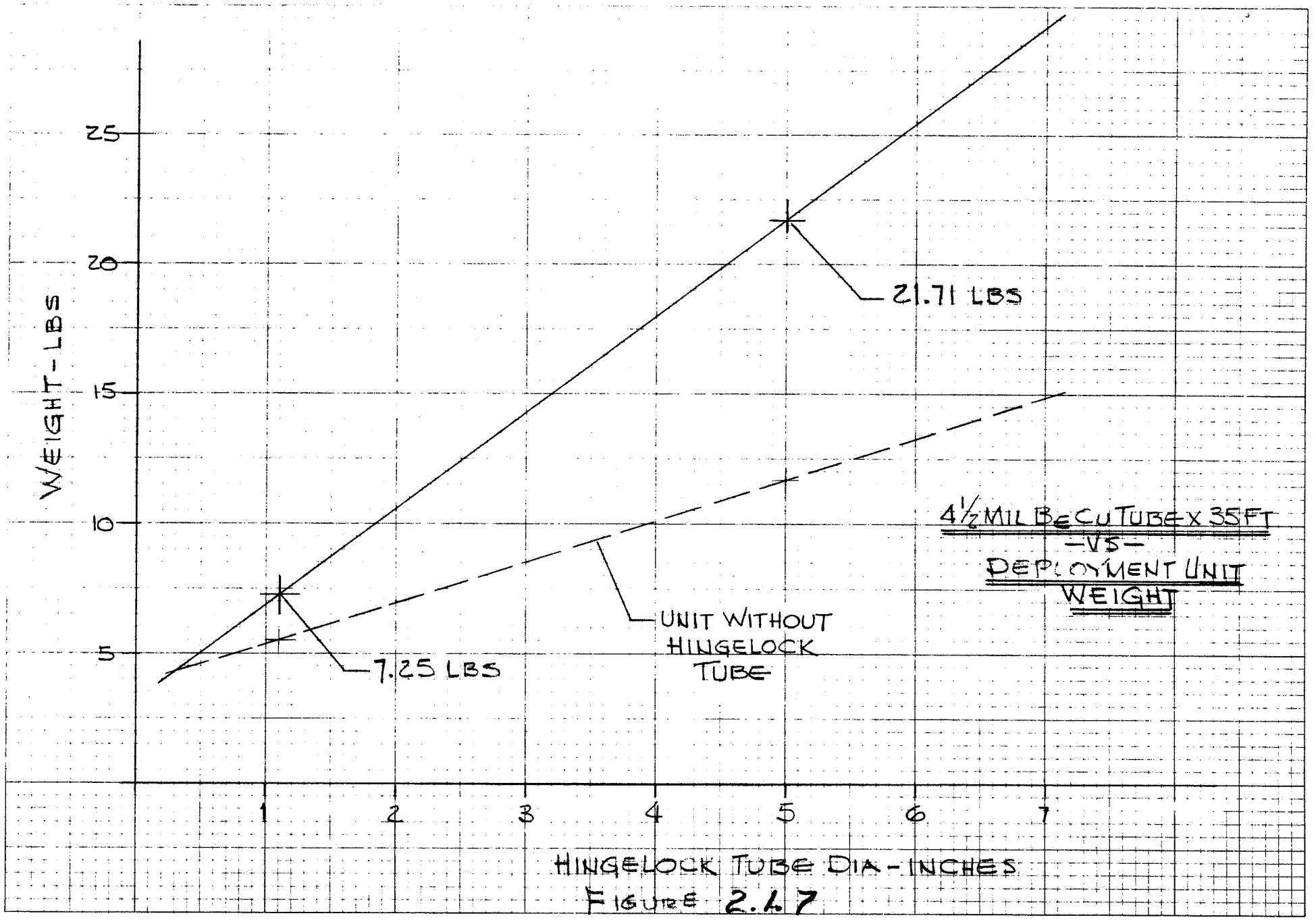

WEIGHT - LBS
25
20
15
10
5
21.71 LBS
7.25 LBS
UNIT WITHOUT HINGELOCK TUBE
4½ MIL BeCu TUBE X 35FT
-VS-
DEPLOYMENT UNIT WEIGHT
1
2
3
4
5
6
7
HINGELOCK TUBE DIA - INCHES

FIGURE 2.1.7

Item	No.	Description	Qty.	Calc. Wt.	Act. Calc Wt. for 4-1/2 Mil Wt. BeCu-5' Diax35'Long Arra
X	050-50023	Assy-Less Cover & H/L			5.275
X	1 ft. 4 mil H/L	Specimen (Ref)			.0493 (x 35' = 1.75-REF)
2	050-50025	Side Pl.	1	.704	1.54
3	050-50026	Side Pl. Acc	1	.554	1.37
4	050-50030	Collar-Reel (SH)	1	.270	.270
5	050-50031	Collar-Reel (LG)	1	.302	.302
6	050-50033	Flange-Reel	2	.134	.134
8	050-40037	Core-Drum	1	.929	3.45
9	050-50045	Roller-Guide	1	.179	1.30
10	050-50046	Dirve Roller	1	.128	1.00
13	050-50050	Block-Ret. Form	1	.105	.608
11	050-50048	Standoff-Side Pl.	3	.075	.516
14	050-50052	Bar. Pivot Sw	1	.005	.005
20	050-50059	Cover	1	.228	.400
		Total	--	3.613	--
1	050-50024	Drive Train Assy Plus Hardware	1	1.890	1.890
					11.607 Total (Less H/L)
		5" dia H/L BeCu x 35 ft	1		Δ 8.93
		1.1 Dia H/L x 35 ft.	1	1.750 Ref	
				*5.503 lbs	21.715 lbs. Total

H/L = Hingelock Boom
* Wt. Less H/L
Δ May be reduced using St'l or Titanium

Figure 2.1.8 Hingelock Tube Deployment System-Weight Calculations

SOLAR CELL STACK WEIGHT

COMPONENT	WT.	
	lb/MODULE	lb/ft^2
COVER GLASS (0.003 in. THICK)	0.183	0 .0318
COVER GLASS ADHESIVE (SYLGARD 182)	0.028	.0049
SOLAR CELL (16gm./100)	0.454	.0788
CELL INTERCONNECTOR & SOLDER	0.051	.0089
CELL ADHESIVE (RTV-108)	0.048	.0083
SUBSTRATE (0.002 KAPTON "H" FILM)	0.092	.0159
FOAM ADHESIVE (DC-281)	0.004	.0007
FOAM (2 lb/ft^3 POLYURETHANE)	0.017	.0029
SUB TOTAL	0.877	.1522
HINGE	0.001	.0002
BUS CABLE	0.005	.0008
ELEC. CABLE TO MODULE ATTACHMENT	0.001	.0002
CONNECTOR (2)	0.001	.0002
LATERAL STIFFENER (5 ea)	0.042	.0072
SUB TOTAL	0.927	.1608
6% GROWTH WT.	.055	.0096
DESIGN TOTAL	.982	.1704

Figure 2.1.9

A detail comparison of various deployment system weights is presented in Section 2.3 of this report.

2.1.4 Base Line Configuration

Figure 2.1.10 presents a comparison of "Array Package Volume" for both the Hingelock and the folding arm concepts. In addition, detail structural and stress analysis of the competing deployment system are presented in Section 2.3.

Based on the parametric studies performed in the first six months of this contract and the experience of Fairchild Hiller in the design and manufacture of other deployment systems, the Folding Arm System was selected as the most reliable, lightest and simplest design for the 30 Watt/Lb Array deployment system. The decision is documented in other sections of this report.

2.1.5 Fabrication Studies

Design investigations were conducted in all areas pertinent to the manufacture of a roll-up array (using the folding arm technique), with emphasis on the design configuration required for space flight hardware. The major mechanical design areas are:

- Spreader bar design.
- Array substrate drum.
- Substrate tension device.
- Folding arm hinge joints.
- Folding arm stowed configuration.
- Folding arm drive system.
- Substrate modular construction techniques.
- Latching and release mechanisms (for the stowed array).

2.1.5.1 Spreader Bar

The spreader bar serves the dual purpose of attaching the array to the deployment mechanism and supporting the linkage during launch. An anodized aluminum, sheet metal channel; designed with stiffeners to resist vibration and incorporating flanged lightening holes, to minimize weight, was chosen for this item. This design represents the best configuration for obtaining maximum strength,

ARRAY PACKAGE VOLUME

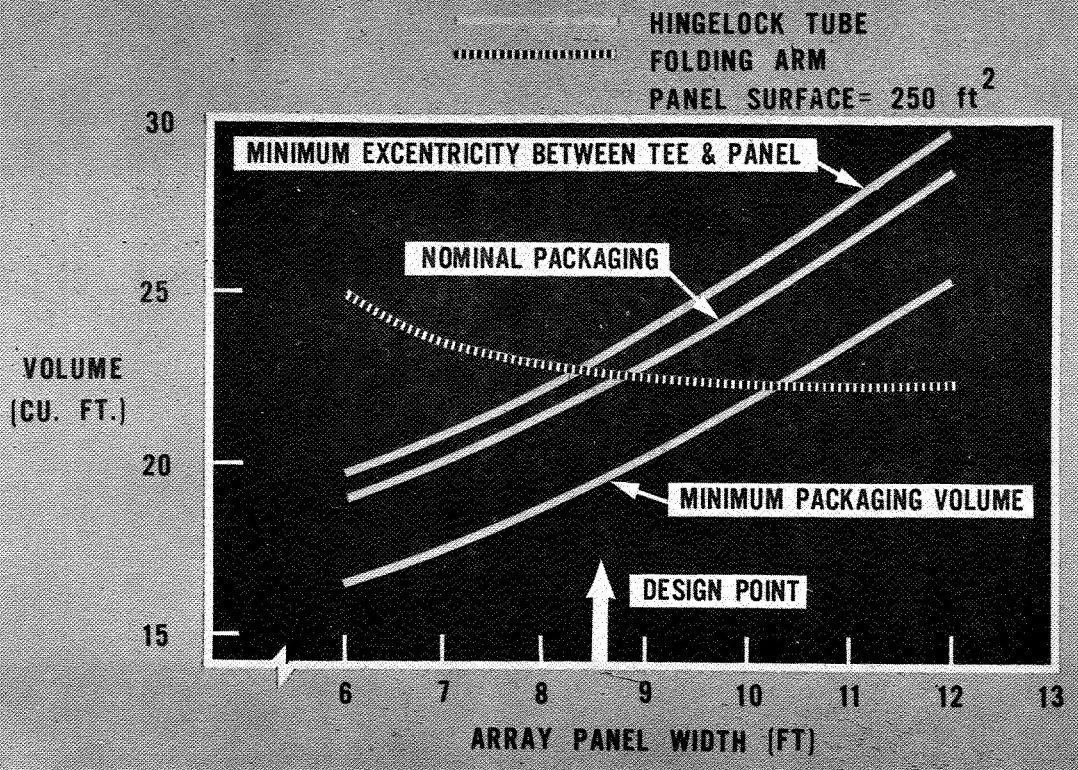


Figure 2.1.10

650-00102-QR

minimum weight and minimum manufacturing complexity and cost.

2.1.5.2 Substrate Drum

The primary consideration in selection of a substrate drum is to obtain a design that will be of minimum weight and withstand launch vibration loads. Parametric investigation disclosed that the primary limiting factor on the drum minimum diameter was: What diameter can an array be successfully rolled onto, without degrading the solar cells either electrically or mechanically? A series of test were performed in order to determine the minimum, allowable drum diameter. Specimen panel sections consisting of solar cells, cover glasses, cell interconnects and 3 mil Kapton substrate were subjected to various substrate tension loads and rolled onto drums of various diameters. Figure 2.1.11 presents the results of these tests and Figure 2.1.12 is a picture of the test set-up. The results of these tests indicate that using a 5" diameter drum (selected by structural requirements) will not cause cell stack degradation. Assuming a tension of 10 lbs. and an approximate substrate width of 96", the maximum load is nominally .1 lbs per inch. It can be seen from Figure 2.1.11 that on a 5" diameter drum, the solar cell stack can withstand approximately 150 times the anticipated loading without failure.

Both a split drum (with center as well as end supports) and a drum with end support only were investigated (Figure 2.1.13). The studies showed the following major disadvantages to the split drum design:

- The split array allowed direct sunlight to fall on the supporting structure, and produced large thermal gradients therein. This in turn, causes large deflections in the array.
- The split drum required additional (center) support structure, bearings, end plates, etc. These weights were considerably greater than the increase in drum weight caused by strength requirements of a drum of equal length but twice as long between support points.

CELL FRACTURE LOAD VS DRUM DIAMETER

2×2 cm. CELL
.008 in. THICK
.003 in. KAPTON H FILM SUBSTRATE

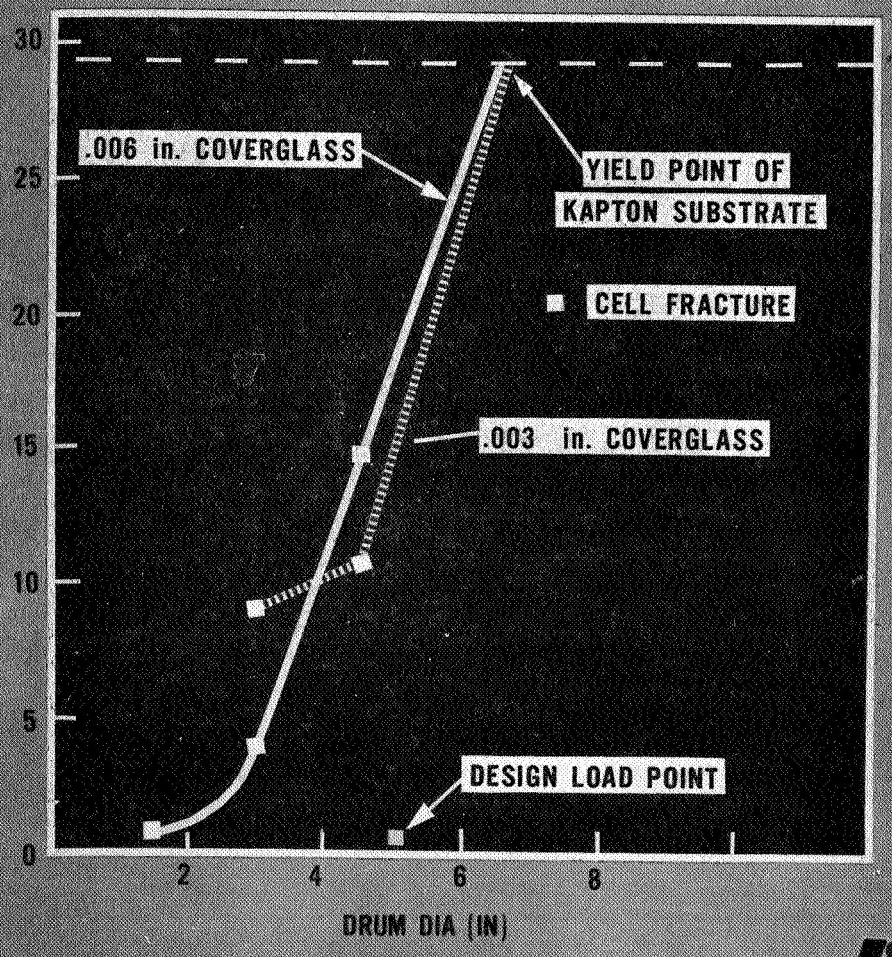


Figure 2.1.11

650-00102-QR

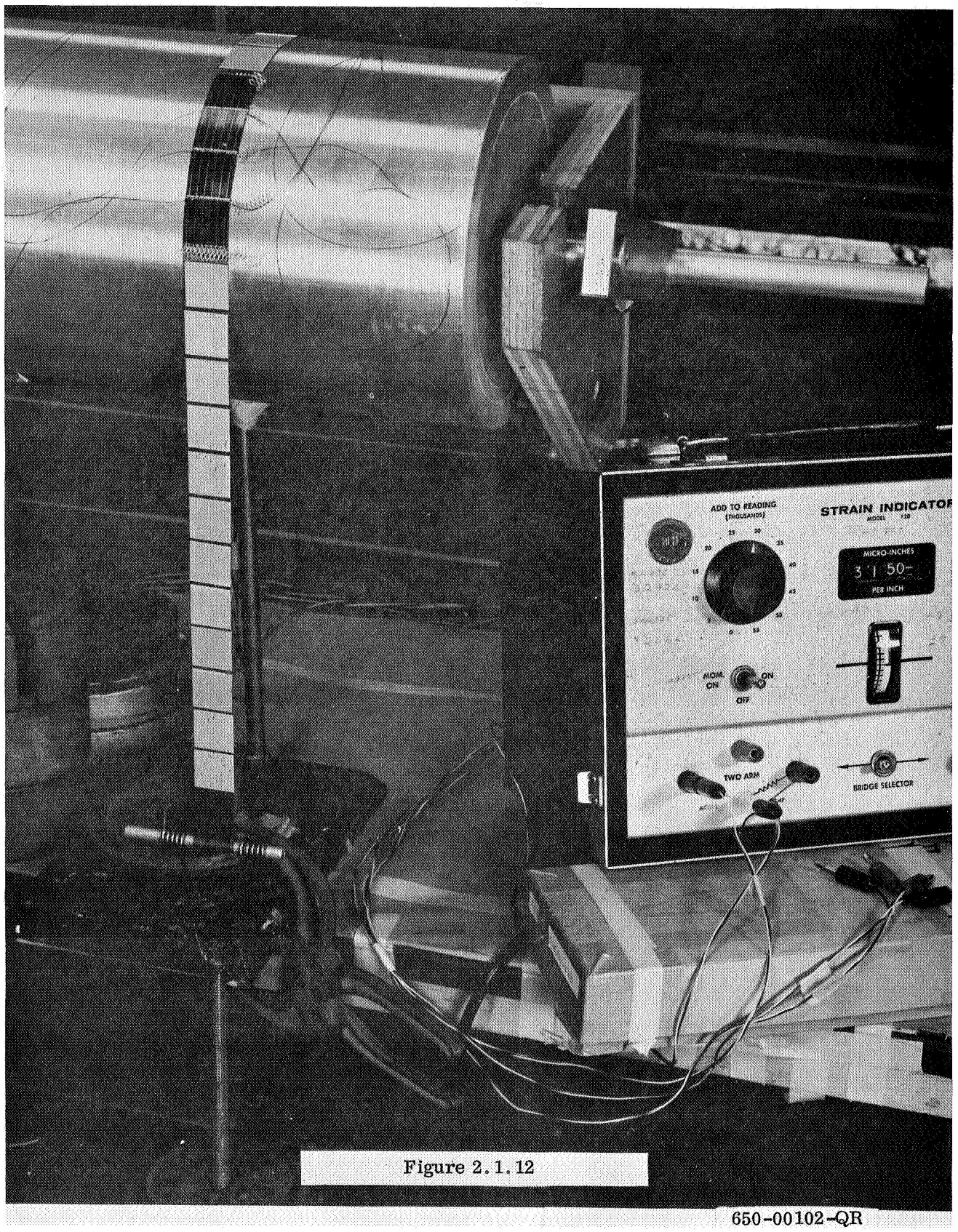


Figure 2.1.12

650-00102-QR

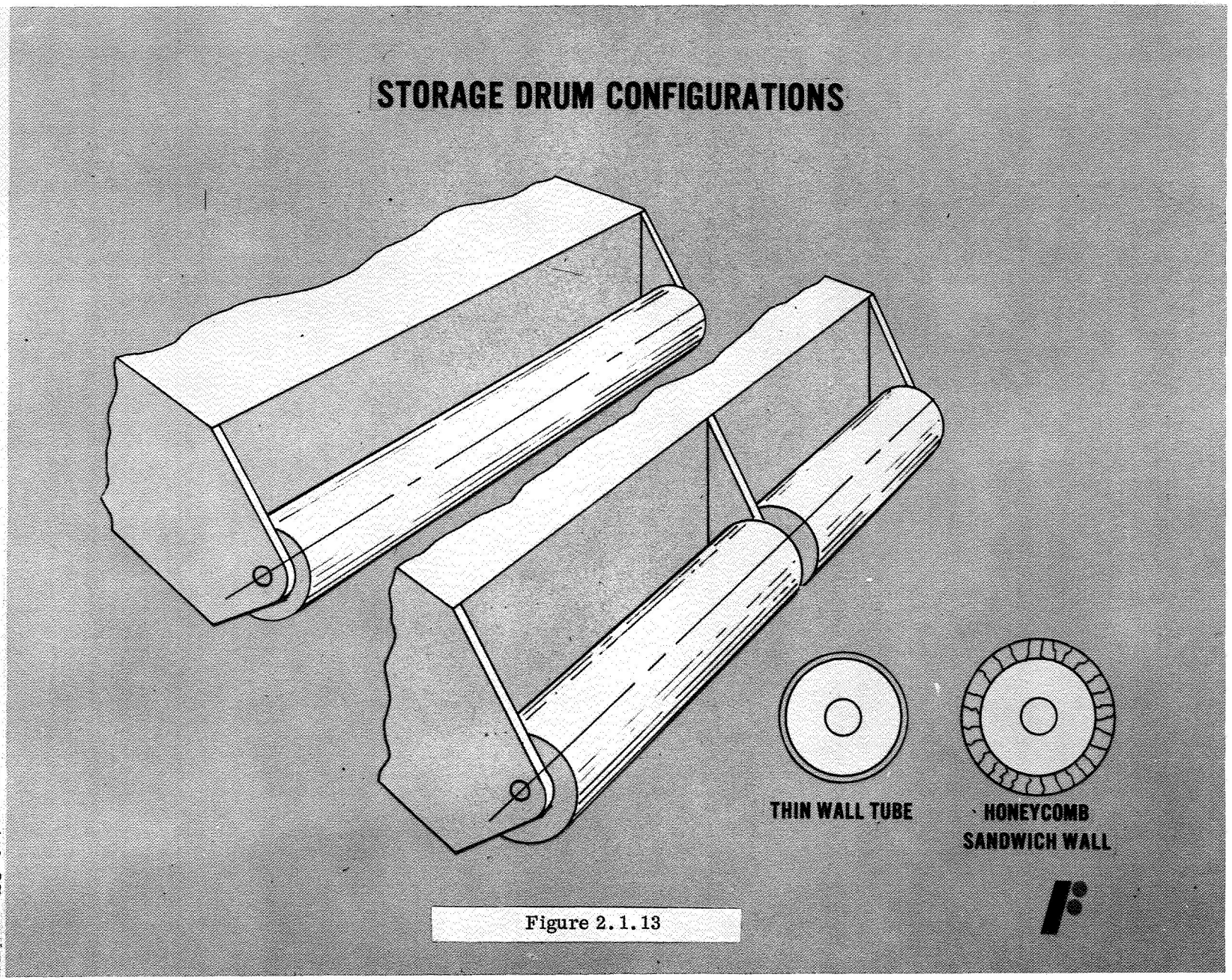


Figure 2.1.13

650-00102-QR

The only disadvantage to the end supported drum was the increased deflection during launch. Through the use of large strength/weight materials, this disadvantage was negated (see section 2.3 for detail drum stress and weight analysis). Detailed analysis proved that drum deflections were of an acceptable magnitude for a drum of sufficient strength to support the induced launch loads.

2.1.5.3 Substrate Tensioning Device

A substrate tensioning device is required to prevent billowing of the array panel and to assure proper tracking during deployment and retraction. Several methods of applying tension were generated and two were selected for detail study.

The "Negator" spring system, using a stainless steel spring and an output drum and take-up drum, can provide 5-10 lbs. of tension in the array for a reasonable cost in terms of fabrication, but at a comparatively high weight.

A torsion spring system with the spring mounted inside the array storage drum or in the drive system offered the lightest tensioning device at the smallest fabrication cost and was selected. Figure 2.1.14 presents the detail design of this system.

2.1.5.4 Folding Arm Joint Design

Three mechanical systems have been considered for programming the hinge joint motion of a folding arm. They were:

- Chain and sprocket drive
- Cable and planetary gear drive
- Cable and pulley drive

The chain and sprocket drive consists of a roller chain driving a sprocket, which is in turn geared through the joint (via 3 shafts and 4 gears) to a second sprocket (see Figure 2.1.15). The estimated weight for a system of this type is 2.32 lbs. and it enjoys an advantage of being inherently reliable.

Initial inspection of the cable and planetary gear drive indicated that the system would be less complex (fewer parts) and lighter in weight. Detail analysis and trade-off studies, however, showed the following disadvantages:

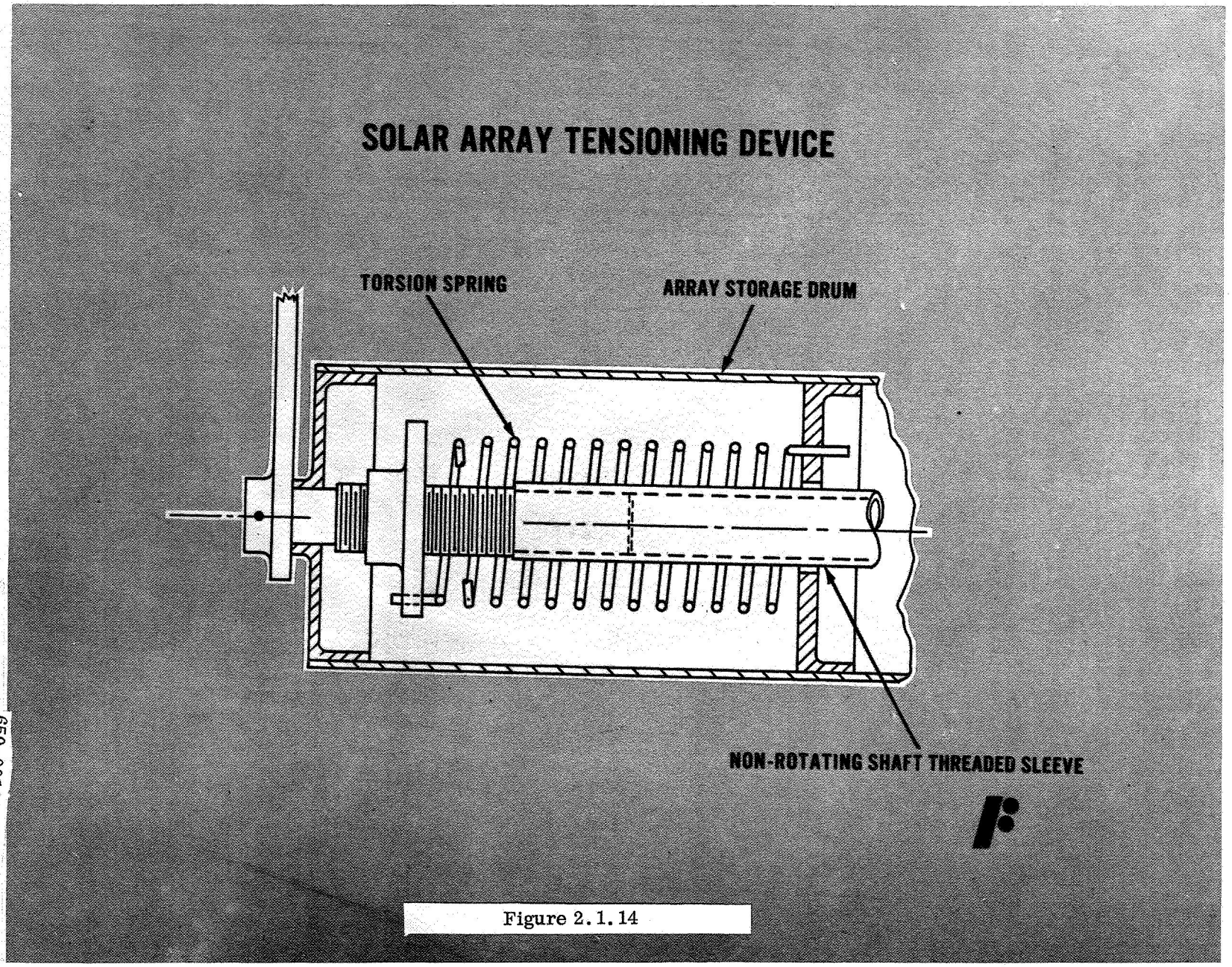

SOLAR ARRAY TENSIONING DEVICE
TORSION SPRING
ARRAY STORAGE DRUM
NON-ROTATING SHAFT THREADED SLEEVE

Figure 2.1.14

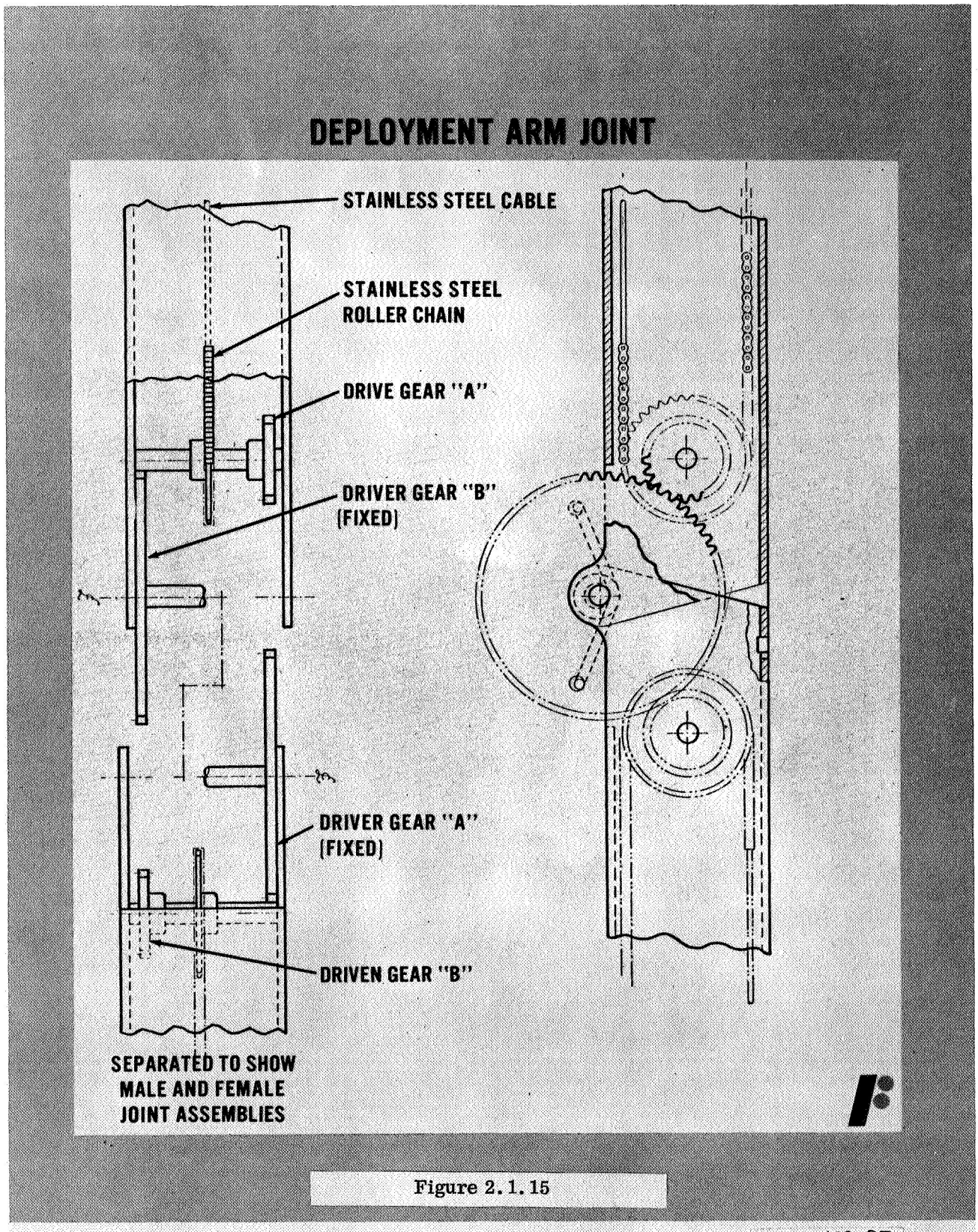

DEPLOYMENT ARM JOINT
STAINLESS STEEL CABLE
STAINLESS STEEL ROLLER CHAIN
DRIVE GEAR "A"
DRIVER GEAR "B" (FIXED)
DRIVER GEAR "A" (FIXED)
DRIVEN GEAR "B"
SEPARATED TO SHOW MALE AND FEMALE JOINT ASSEMBLIES

Figure 2.1.15

- In order to alleviate binding problems, the planetary gear system must be assembled as a unit and kept together as one package. This would require ultra-precision machining of detail parts and make replacement of defective parts extremely difficult.
- To balance the system loads, a second (non-operating) gear must be installed diametrically opposite the functional gear.
- A large diameter ring gear is required and, because of space and location, its supporting structure is minimal. Thus, very light loads can cause extreme deflections and produce binding or even complete failure of the joint.
- Joint fittings become intricate and complex due to the support bosses required for the planetary gear, ring gear and cable drums.
- The planetary gear system has a calculated weight of 2.53 lbs.

Additional time and effort was devoted to investigating the chain and sprocket design because of its simplicity and reliability. This effort evolved the final system; a cable and drum drive (Figure 2.1.16). The cable and drum system consists of two idler arms, a dual pulley drum and associated cabling. This design concept contains the smallest number of parts, is easily repaired, can be manufactured at the smallest cost, and will weigh less than 2 lbs. It combines the mechanical simplicity of the chain and sprocket with a lighter weight design and less expensive manufacturing and assembly costs. Therefore, this concept was chosen for programming the folding arm joint.

2.1.5.5 Folding Arm Stowed Configuration

The solar array deployment arms, when retracted into the stowed position, lay parallel to each other and to the array roller.

The folding arm elements transmit their individual inertia launch loads through the arm pulleys at the link ends into bearing blocks on the end brackets. A small part of the load is reacted by the spacecraft and the spreader bar pivots.

Laterial loads are accomodated by drawing the spreader bar down onto the folding arms and locking the spreader bar in place with pyrotechnic devices.

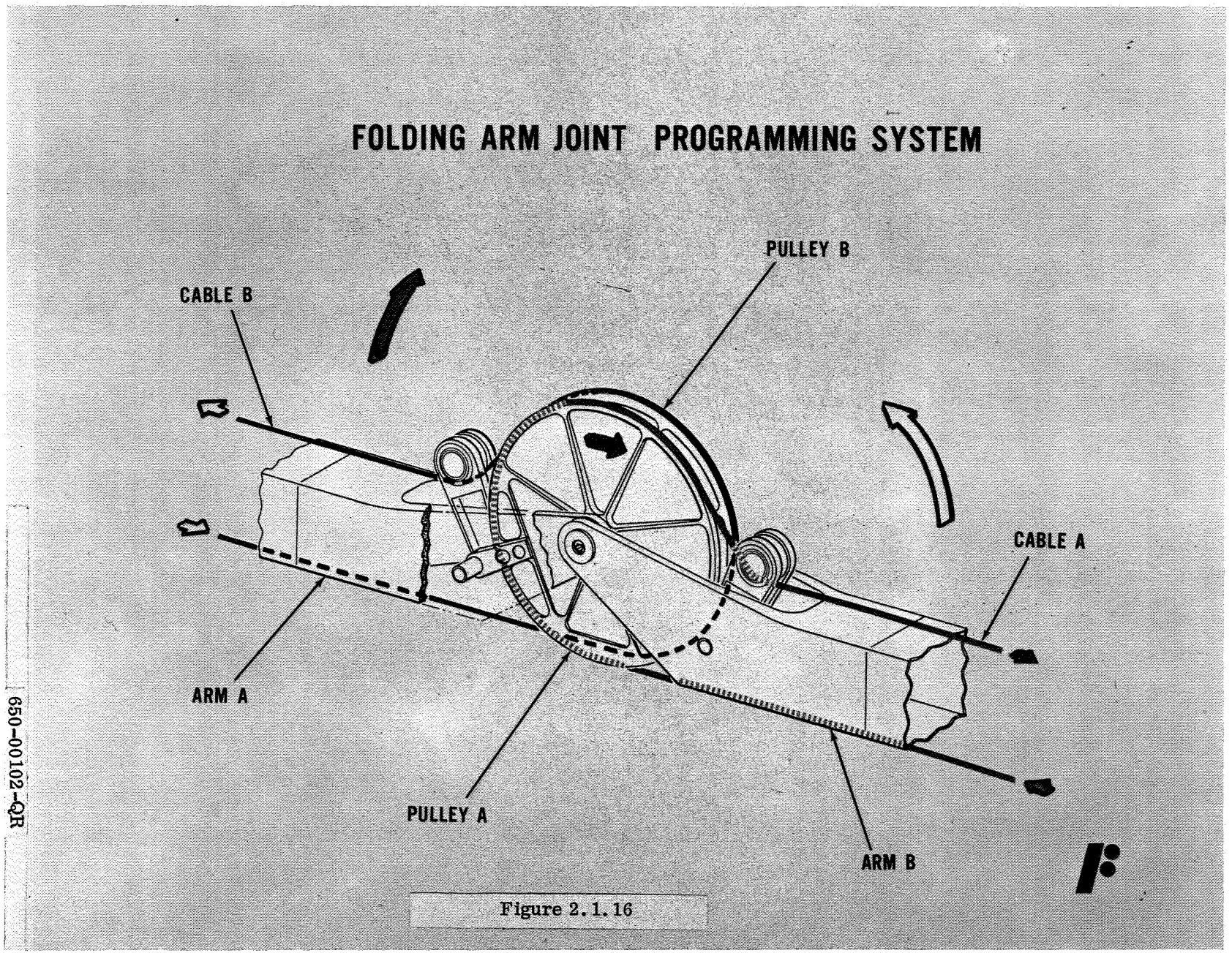

FOLDING ARM JOINT PROGRAMMING SYSTEM
PULLEY B
CABLE B
CABLE A
ARM A
PULLEY A
ARM B

Figure 2.1.16

Lateral loads between the spreader bar, arm links and pulleys are taken out by a compressive bearing member between the spreader bar, arm links and the spacecraft structure. Pads of rubber are placed on the compressive bearing surfaces and the entire assembly is tightly snubbed down by means of cabling or tie down straps.

Four (4) array end brackets are mounted at the corners of the 100 sq. in. spacecraft structure at 45^{o} to any side and are fabricated from a Graphite/Epoxy molded composite material. The end brackets consist of a flat stable web with channels, ZEE boundary members and panel breaker stiffeners of Graphite/Epoxy and bonded together. Bearing supports for the folding arms and pulleys are mounted on the end brackets.

The array roller is supported by two connected, formed channel gussets on the end brackets and through self-aligning bearing housings; to accomodate the roller end shafts. All roller axial loads are taken out through a two way thrust bearing at one end of the roller. The other end "floats" in a bearing, to simplify installation and alignment.

End bracket side loads are carried by three (3) diagonal Graphite/Epoxy tubes attached to the spacecraft structure, 15 inches from the structural corners. Four (4) sets of diagonal braces are also required; one set for each end bracket. Vertical stiffeners at the corner of the spacecraft structure and 15 inches inboard provide the attachment for the diagonals to the spacecraft structure. The design thus makes provisions to transmit all launch and flight loads into the edge members of the 100 inch by 20 inch mounting surface, as specified in the JPL specifications.

2.1.5.6 Folding Arm Drive System

The design of the drive system for the array is presented schematically in Figure 2.1.7. Motive power for the system is supplied by a small direct current motor which drives a differential gear system. The differential system is used to split the motor torque into two drive trains, one of which drives the inboard arm element and activates the folding arm linkage; the second system is used to apply

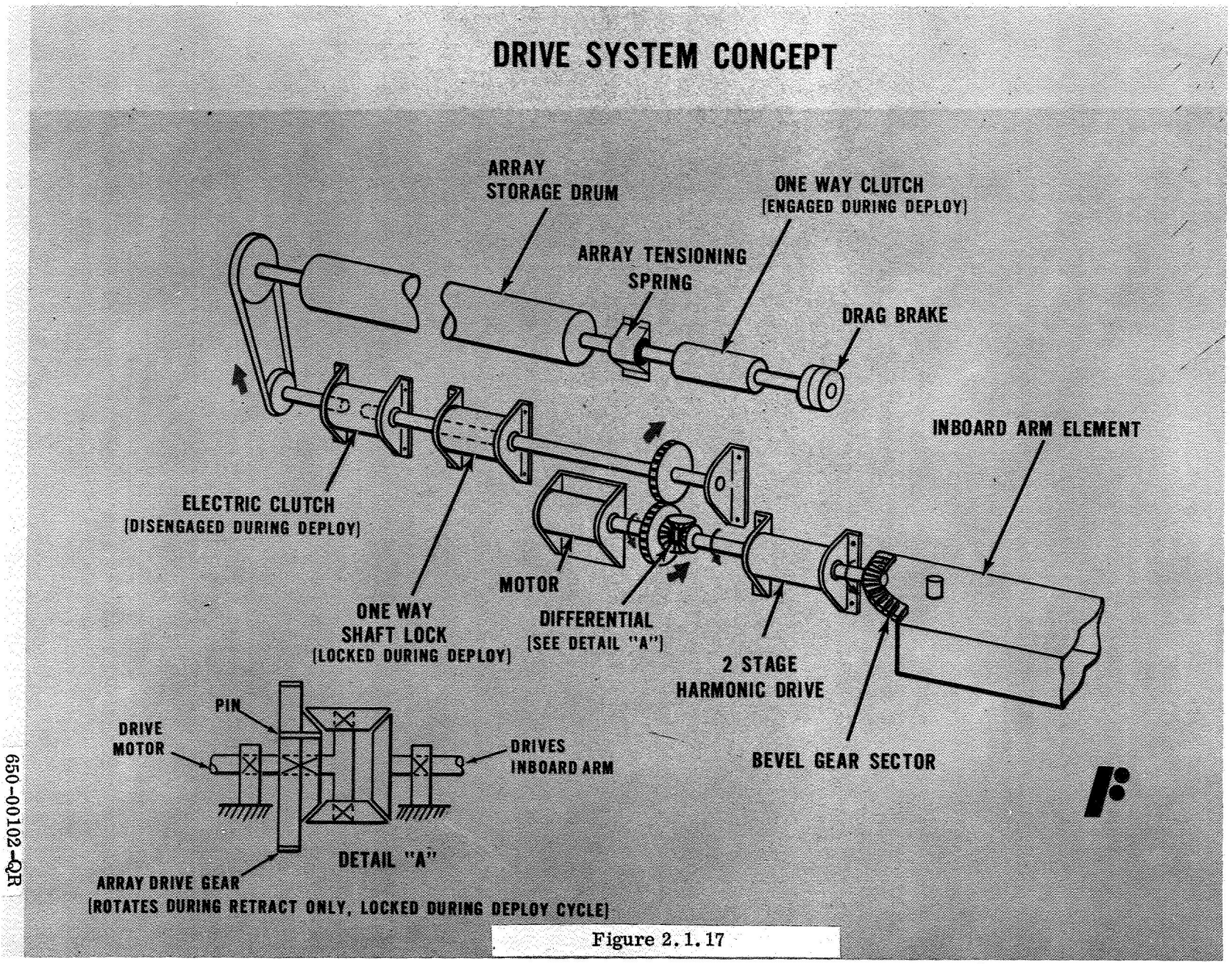

DRIVE SYSTEM CONCEPT
ARRAY STORAGE DRUM
ONE WAY CLUTCH (ENGAGED DURING DEPLOY)
ARRAY TENSIONING SPRING
DRAG BRAKE
INBOARD ARM ELEMENT
ELECTRIC CLUTCH (DISENGAGED DURING DEPLOY)
MOTOR
ONE WAY SHAFT LOCK (LOCKED DURING DEPLOY)
DIFFERENTIAL (SEE DETAIL "A")
2 STAGE HARMONIC DRIVE
BEVEL GEAR SECTOR
PIN
DRIVE MOTOR
DRIVES INBOARD ARM
DETAIL "A"
ARRAY DRIVE GEAR (ROTATES DURING RETRACT ONLY, LOCKED DURING DEPLOY CYCLE)

Figure 2.1.17

torque to the storage drum during the retraction cycle only. A detailed description of the deployment and retractions modes of operation is given in the following sections:

Deployment Mode

The electric clutch in the storage drum drive train is normally not engaged and thus prevents motor power from being applied to the storage drum Upon initiation of the deployment mode, the drive motor is energized to supply torque to the differential in such a manner as to cause the inboard arm element to rotate in the proper direction for deployment. The electric clutch in the array roller drive train remains disengaged. The direction of rotation of the array storage drum drive shaft, between the differential and the electric clutch, is such that action of the one way shaft lock prevents rotation of this shaft. Such action is required to lock one side of the differential gear system and thus enable the system to transmit power to the folding arm drive system. A two stage harmonic drive is used to increase the torque applied by the motor to the folding arm system for both extension and retraction modes.

Extension of the folding arm beam applies tension to the array and unfurls the panel from the storage drum roller. A one way clutch which is actuated by the direction of rotation of the array storage drum shaft during deployment, engages a drag break which provides the desired tension in the array during the deployment mode. This tension is necessary to prevent the array panel from billowing during deployment.

One of the design requirements for the system is that a minimum natural frequency of .04 Hz must be maintained. The natural frequency of the array panel is a direct function of the tension maintained in the panel. Thermal analysis has indicated that, for the projected mission, relatively large excursions of temperatures may be expected both in the array and in the supporting structure. Because of the differences in the coefficients of thermal expansion in the different materials used in the various elements, it would be expected that array tension could vary over a fairly wide range. The method employed to maintain a relatively

constant array tension under these varying conditions is to apply a constant torque to the array storage drum by means of a torsion spring located on the array roller shaft. This spring is engaged only during the last 1/2 revolution of the roller during the deployment mode.

This approach has two advantages: first, the torque applied by the spring, which opposes the array storage roller motion during deployment, is not applied until deployment is essentially complete; second, the geometry of the deployment arms provides a maximum mechanical advantage and hence deployment force to the array panel during the last stage of the deployment cycle. Thus, by restricting the action of the array tensioning spring to this portion of the cycle, a minimum loading is applied to the folding arm system during the deployment mode.

Retraction Mode

Initiation of the retraction mode actuates the electric clutch and couples the differential gear drive system to the array roller. The direction of rotation of the array storage drum drive shaft unlocks the one way shaft lock and permits torque to be applied to the array drum in a direction which tends to roll up the substrate on the drum. The drive motor is energized for rotation in the opposite direction to that of the deployment mode. The differential gear system permits power to be applied simultaneously for array storage drum retract motion and retraction of the folding arm system. The direction of rotation of the array drum shaft also disengages the one way clutch and thus prevents the drag brake from acting during the retraction cycle. The array tensioning spring aids in retraction during the first one/half revolution of the drum and then is disengaged.

2.1.5.7 Modular Construction Techniques

Modular construction techniques are used to facilitate array repairability and simplify manufacturing problems. The initial design concept used a hinge-type construction and fastened the modules together with pins (as in a simple piano hinge). From the original concept the design evolved into a simplier and more efficient method of mechanically joining the modules, in which the hinge is replaced by a "laced" joint (Figure 2.1.18).

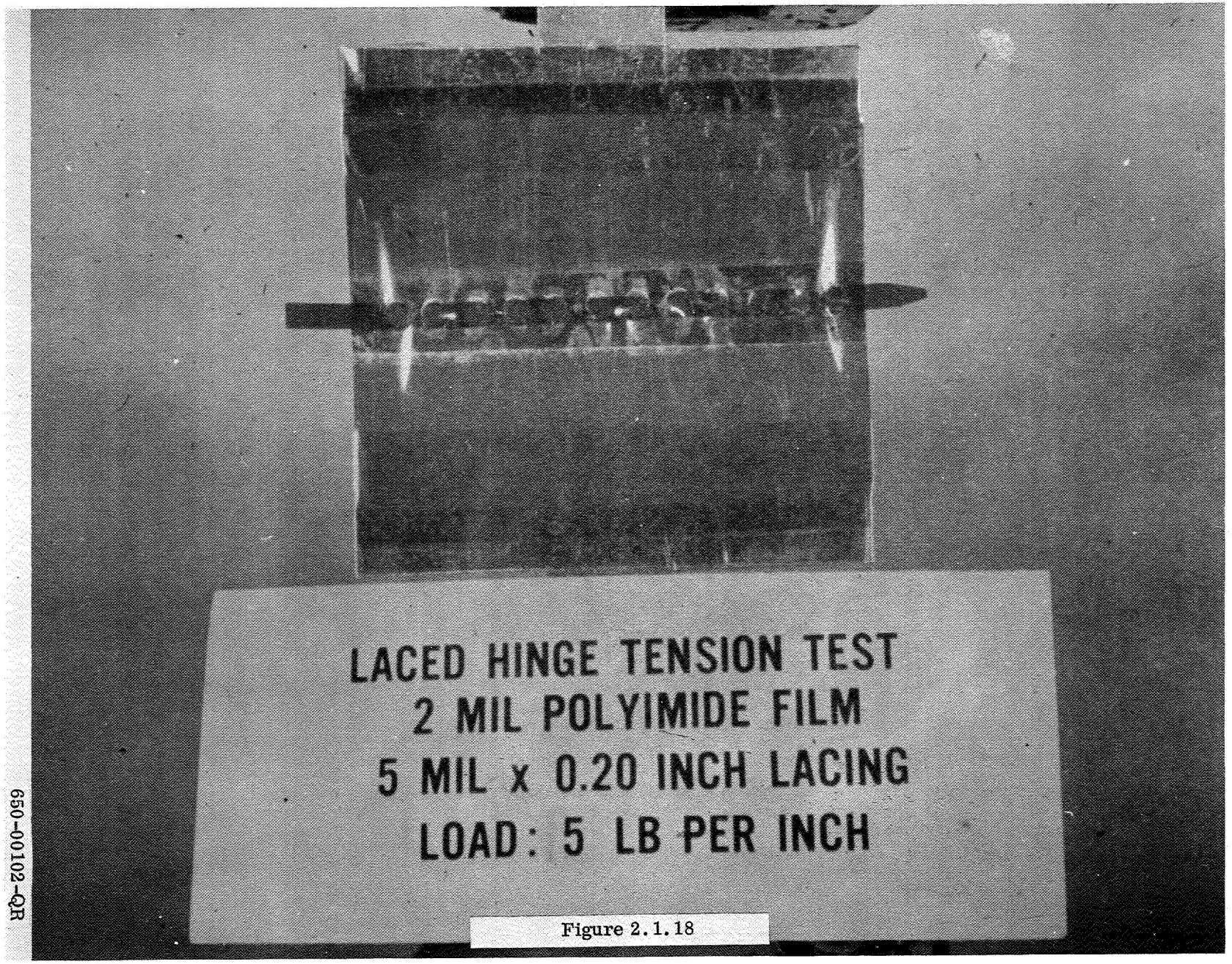

LACED HINGE TENSION TEST
2 MIL POLYIMIDE FILM
5 MIL x 0.20 INCH LACING
LOAD: 5 LB PER INCH

Figure 2.1.18

By using the modular concept, it is possible to produce spare array modules and effectively repair the array through direct substitution of modules at any time prior to flight. In addition, manufacturing costs are held to a minimum by using 48 identical modules. This type of construction also lends itself to semi-automated production procedures and further cost savings are envisioned.

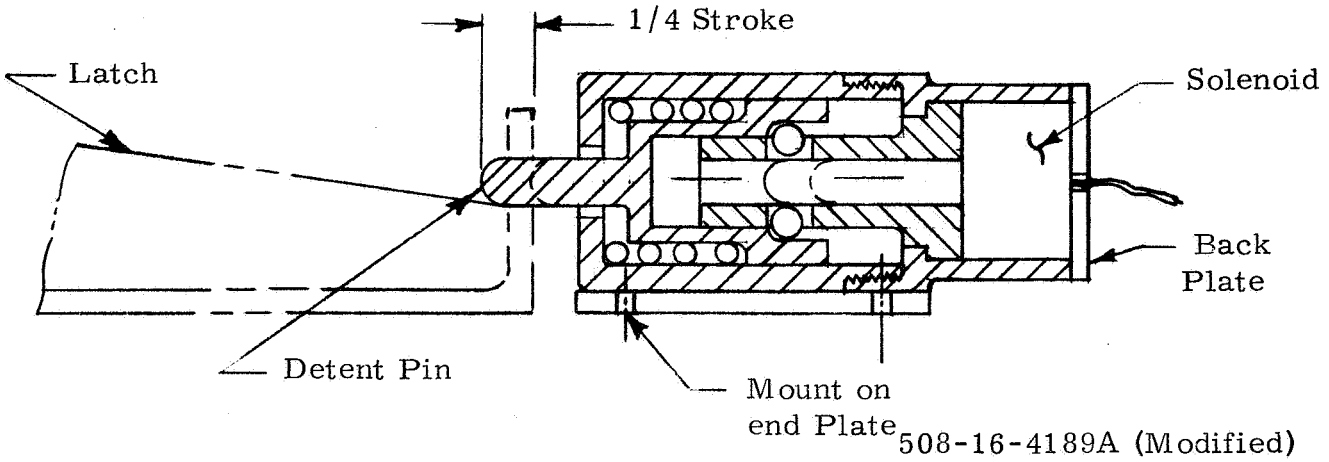
2.1.5.8 Latching and Release Mechanisms

Several latching and releasing mechanisms are presently being investigated. Those of primary interest are shown in Figure 2.1.19. A final design for this system has not, as yet, been selected and study efforts are continuing.

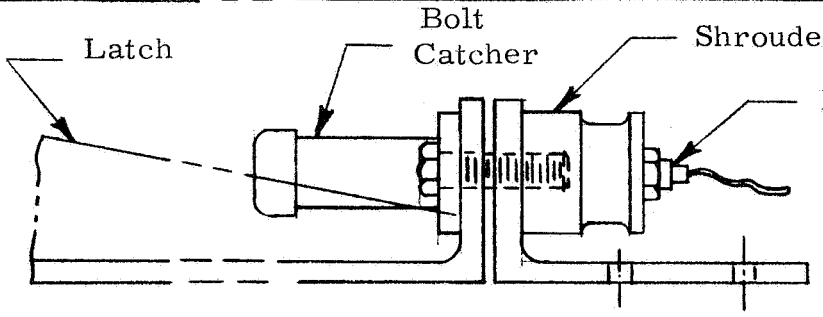
2.1.6 Selected System Design Description

Figure 2.1.20 presents a simplified pictorial of the deployment retraction supporting structure of the selected design. The array panel is composed of four sub-panels which are mechanically fastened together with their power collective harnesses, and stored on a drum during the launch mode. One end of the array panel is attached to the drum and the other end to a spreader bar located at the out board end of a five element folding arm boom. The folding arm joints are programmed during their motion from the retracted to the deployed position by a cable system which interconnects the joints and programs them to insure that the motion of the pivot point, connecting the outboard arm element to the spreader bar, is a straight line function during deployment and retraction. Extension of folding arm supporting structures provides the necessary force to unfurl the array panel from the storage drum. Suitable means are provided to maintain a reasonable tension in the array during deployment to prevent its billowing. Motive power for extension is provided by a DC motor which drives the inboard arm element through a 90^{o} arc. During launch the five arm elements and the spreader bar, at the outboard tip, are retained between two end brackets (which are attached to the spacecraft body) and supported thereby against launch loads. Upon initiation of the first deployment cycle, pyrotechnic activated retaining bolts are released, permitting the deployment system to be extended.

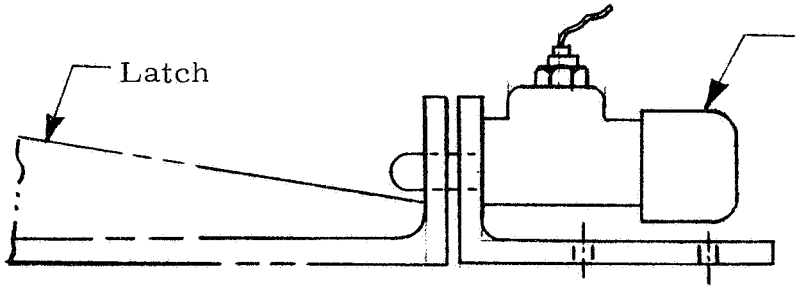
Figure 2.1.19



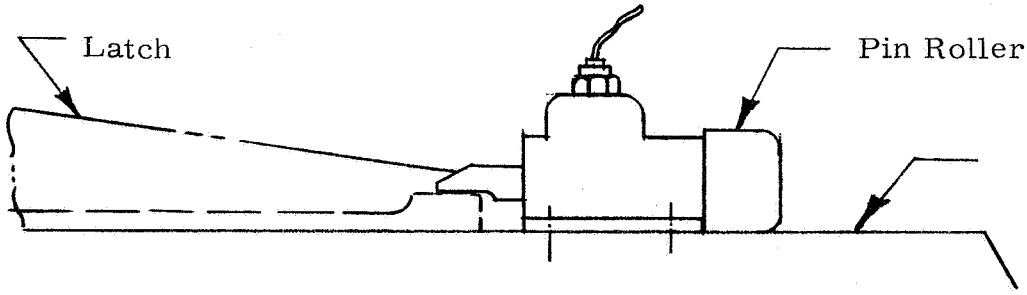
508-16-4189A (Modified)



Shrouded Bolt & Separation Nut
Hi-Shear Corp.



SP 240 Pin Roller
(Modified)
Hi-Shear Corp.



SP 240 Pin Roller
(Modified)
Hi-Shear Corp.

ARRAY FOLDING ARM SYSTEM

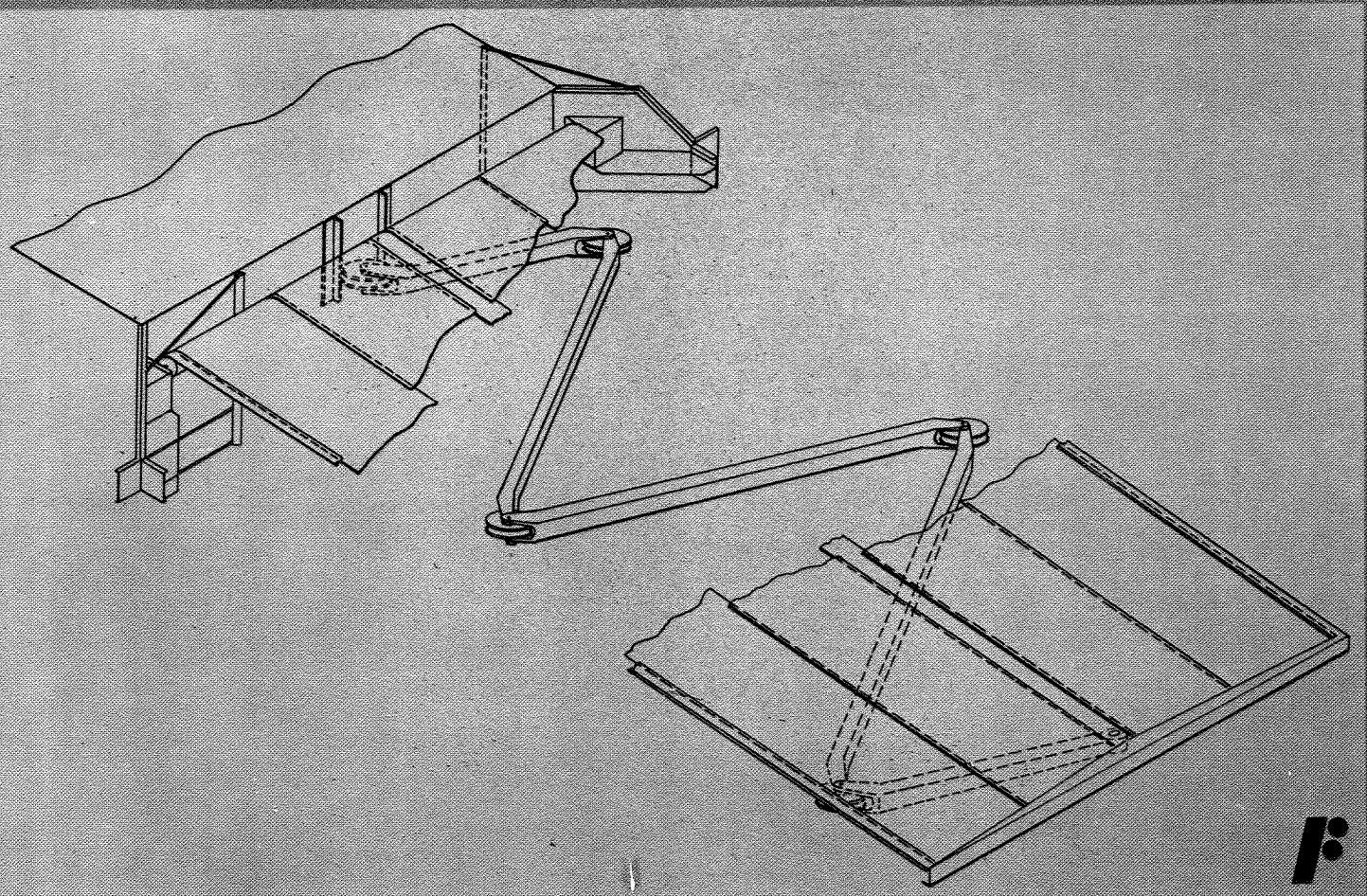


Figure 2.1.20

650-00102-QR

The array panel consists of four sub panels and each sub panel of twelve identical modules. Each sub-panel has its own power collecting harness with the outboard panels having their harnesses located on the outboard edges of these sub-panels and the two inboard sub-panels dump their power into a common harness located between them. Each module incorporates redundant connectors between modules and harness and reduntant wiring in the harness back to the storage drum roller. At the storage drum all 48 module harness conductors are parallel together and carried across the slip ring assembly to a common bus at the array spacecraft interface. The module consists of a two mil Kapton substrate upon which 2 x 2 x 8 mil thick, N on P, silicon solar cells are mounted. There are 1290 cells per module arranged in a 6 cell parallel, connected by 215 cell series matrix. The nominal area covered by solar cells is 277.4 square feet and produces 2762 watts at the spacecraft array interface. The folding arm elements and outboard spreader arm are fabricated from a boron/epoxy composite material and the storage drum roll is a graphite/epoxy composite material. The end brackets which support all of the mechanism are of conventional aluminum sheet metal construction, as are those necessary supporting braces which must span across the mounting surface between the edge or corner attachments. End fittings in the arm tube elements are machined beryllium. Selection of these materials has resulted in the lightest weight structure capable of performing under the specified conditions. Some additional weight may be saved by using either boron or graphite/epoxy composite materials for the end brackets. This saving may be on the order of a pound or two.

Retraction of the array is accomplished by reversing the electric drive motor which, in turn, causes the folding arm beam to accordion back upon itself in a programmed manner. Simultaneously, power from the motor is applied to the storage drum roller to rewind the array panel upon the roller. The details of the various components are contained in the design study section (Reference Section 2.1.5.6).

During the course of the design studies, it was determined that the optimum power/weight ratio configuration for a total array set, consisting of 4 arrays or a total of 1000 square feet, would be obtained by having two adjacent 250 square foot arrays share a common end bracket. This approach has been

selected for the design.

The selected array configuration consists of 48 modules and their power collecting harnesses all laced together to form a continuous sheet. Advantages accuring from this configuration include:

- Protection of the supporting arm structure from the direct rays of the sun, and hence better control of thermal deflection of the supporting system in the extended position.
- Using one interconnected sheet for the array panel it is anticipated that a more uniformed tension may be obtained throughout the panel and this factor, coupled with the pivoted, free floating, spreader bar attachment to the boom, will result in less chance of wrinkles or buckles in the panel occuring during the retraction cycle and roll up of the array panel on the storage drum.
- Tracking of the array panels during retraction also should be enhanced.
- The modular construction of the arms and of the array panel permits rapid and easy replacement of reasonable size parts, if such is necessary.

2.2 ELECTRICAL SYSTEM DESIGN

2.2.1 Cell Characteristics

The JPL detail requirements specification for the array (Reference 2.2.1) states that the power output calculations shall be based on photovoltaic energy conversion devices with a potential of 10 watts/ft^2 output at beginning of life when measured at air mass zero, 55^{o}C, and IAU equivalent solar intensity. This requirement includes losses due to cell mismatch, cover glasses, adhesives, and string interconnections.

2.2.1.1 Solar Cell Efficiency

The cell to be supplied will be a 2 x 2 cm, 10 ohm-cm, N/P solar cell, with silicon thickness of 0.008 inch and active area of 3.9 cm^2. The peak power point of this cell will be a maximum of 49.5 milli-watts under bare cell conditions at 55^{o}C cell temperature.

$$\text{Cell Efficiency (\%)} = \frac{\text{maximum power x 100}}{\text{Photo-voltaic area x solar constant}}$$

$$\text{Cell Efficiency (\%)} = \frac{49.5 \text{ mw x } 100}{3.9 \text{ cm}^2 \text{ x } 140 \text{ mw/cm}^2}$$

$$\text{Cell Efficiency (\%)} = 9.07\% \quad @55^{o}\text{C}$$

This is equivalent to a nominal cell efficiency of 10.78% at 28^{o}C.

2.2.1.2 E-I Characteristics at 55^{o}C

The curves of 2.2.1 (Reference 2.2.2) were used as a base in deriving the E-I characteristics for a cell at 55^{o}C cell temperature. The cells used in generating this empirical data had a nominal cell efficiency of 10.13% at 28^{o}C or 8.42% at 55^{o}C.

In order to interpolate the E-I characteristics for a cell at 55^{o}C from figure 2.2.1, we must assume that there is a linear change in E-I characteristics when the cell temperature is raised from 30^{o}C to 60^{o}C. Then, below the 45^{o} slope point of the knee of the curve (toward V_{oc}), various changes in voltages per degree centigrade were obtained for several constant currents. Above the 45^{o}

slope point of the knee (toward I_{sc}), various changes in current per degree centigrade were obtained for several constant voltages. By use of these coefficients, the E-I characteristics at 55°C cell temperature were obtained (Figure 2.2.2).

The peak power point of this new curve was found to be 46.0 mw and hence the cell efficiency is 8.42% at 55°C (or 10.13% at 28°C). Since the cell to be supplied is 9.07% efficient at 55°C, the E-I curve of Figure 2.2.2 must be adjusted further.

It is Fairchild-Hiller's understanding that different cell efficiencies between two similar cells are caused by two major factors:

1. Varying diffusion lengths, which control the flow of current
2. Varying base resistivities which control the output voltages.

Varying cell efficiencies are caused primarily by two factors and divided thus: 95% of the variation is due to unequal diffusion lengths while only 5% is due to unequal base resistivities. The cell E-I characteristics of Figure 2.2.3 were obtained by assuming the above to be true over the entire E-I curve and the change in cell efficiency to be constant. These new characteristics represent a cell with an efficiency of 9.07% at 55°C and a maximum power point of 49.5 mw (bare cell). At this power, V_{mpp} = 375 mv and I_{mpp} = 132 ma.

Figure 2.2.4 shows the comparison of the E-I characteristics of the original cell at 55°C and of the two different cell efficiencies.

2.2.1.3 E-I Characteristics in Mars Orbit

Figure 2.2.5 represents the bare cell characteristics at the beginning and end of life assuming a Mars mission. One curve represents a cell in an Earth orbit at 55°C, AMO, and IAU. The other curve represents a cell in a Mars orbit at 0°C and an illumination intensity of 65 mw/cm^2. The latter curve was based on the E-I characteristics vs. cell temperature curve at 0°C of Figure 2.2.1 at the reduced illumination of 65 mw/cm^2. The curves do not account for system degradation due to time in the space environment.

VOLTAGE-CURRENT CHARACTERISTICS VS CELL TEMPERATURE

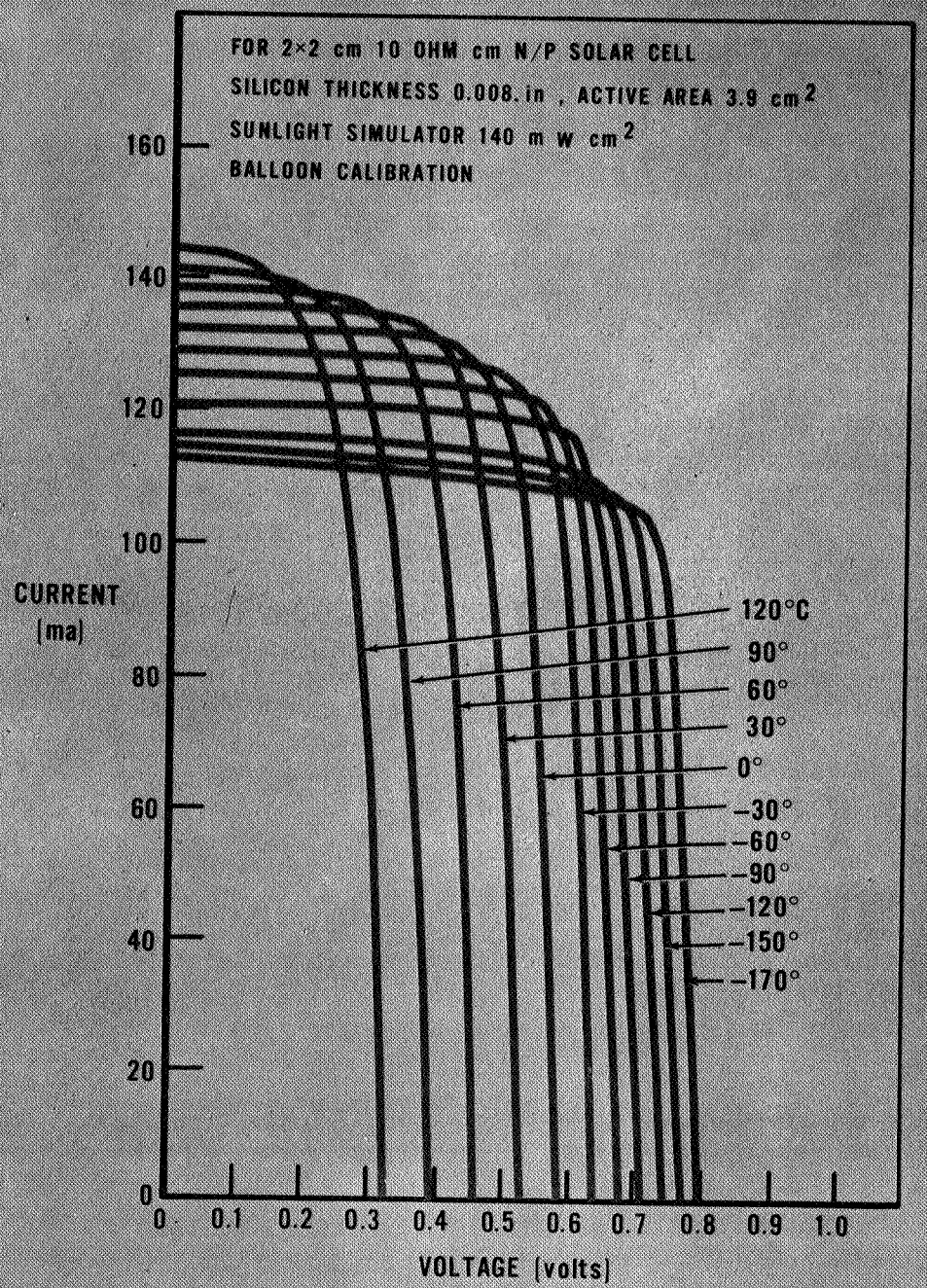


Figure 2.2.1

650-00102-QR

Voltage - Current characteristics vs. Cell Temp.
For 2 x 2 cm 10 Ω cm N/P Solar Cell
Silicon Thickness 0.008 inch,
Active Area 3.9 cm^2
Sunlight Simulator 140 m W/cm^2
Ref. Helioter - Research Paper #118A
"Performance of Very Thin Silicon Solar Cells" by E. L. Ralph

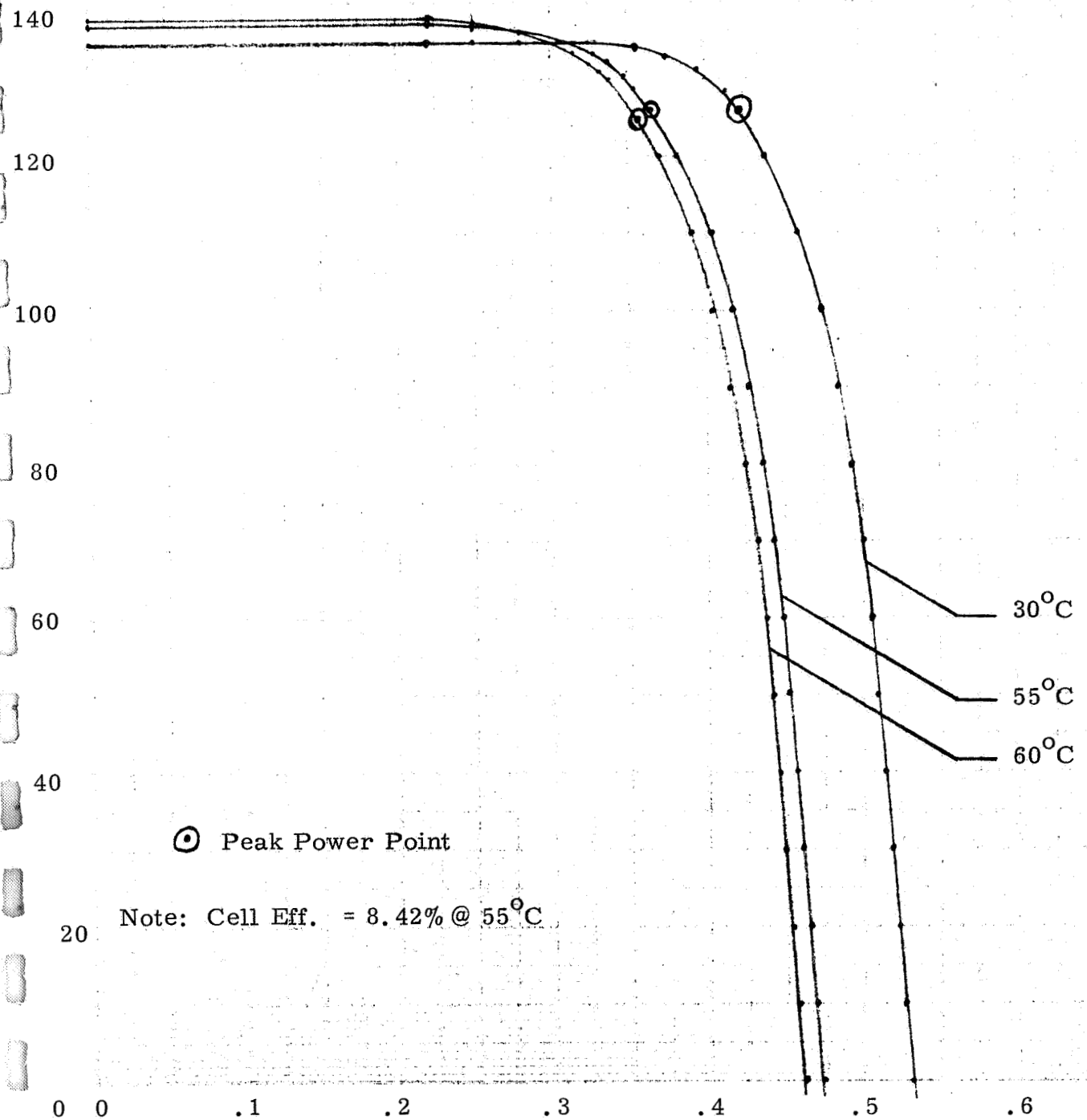
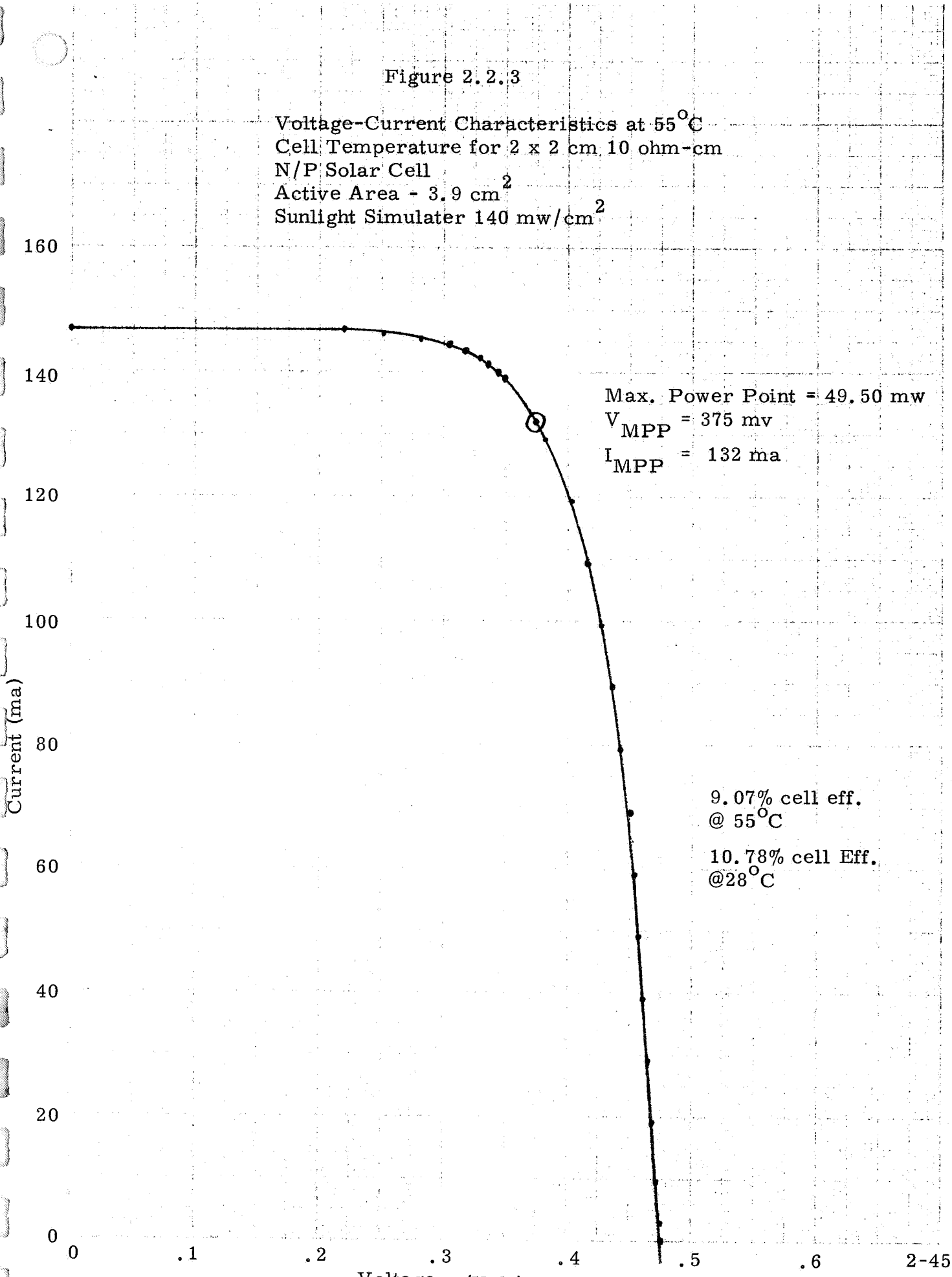


Figure 2.2.2

Figure 2.2.3

Voltage-Current Characteristics at 55°C
Cell Temperature for 2 x 2 cm 10 ohm-cm
N/P Solar Cell
Active Area - 3.9 cm^2
Sunlight Simulater 140 mw/cm^2



652-00102-QR

VOLTAGE-CURRENT CHARACTERISTICS

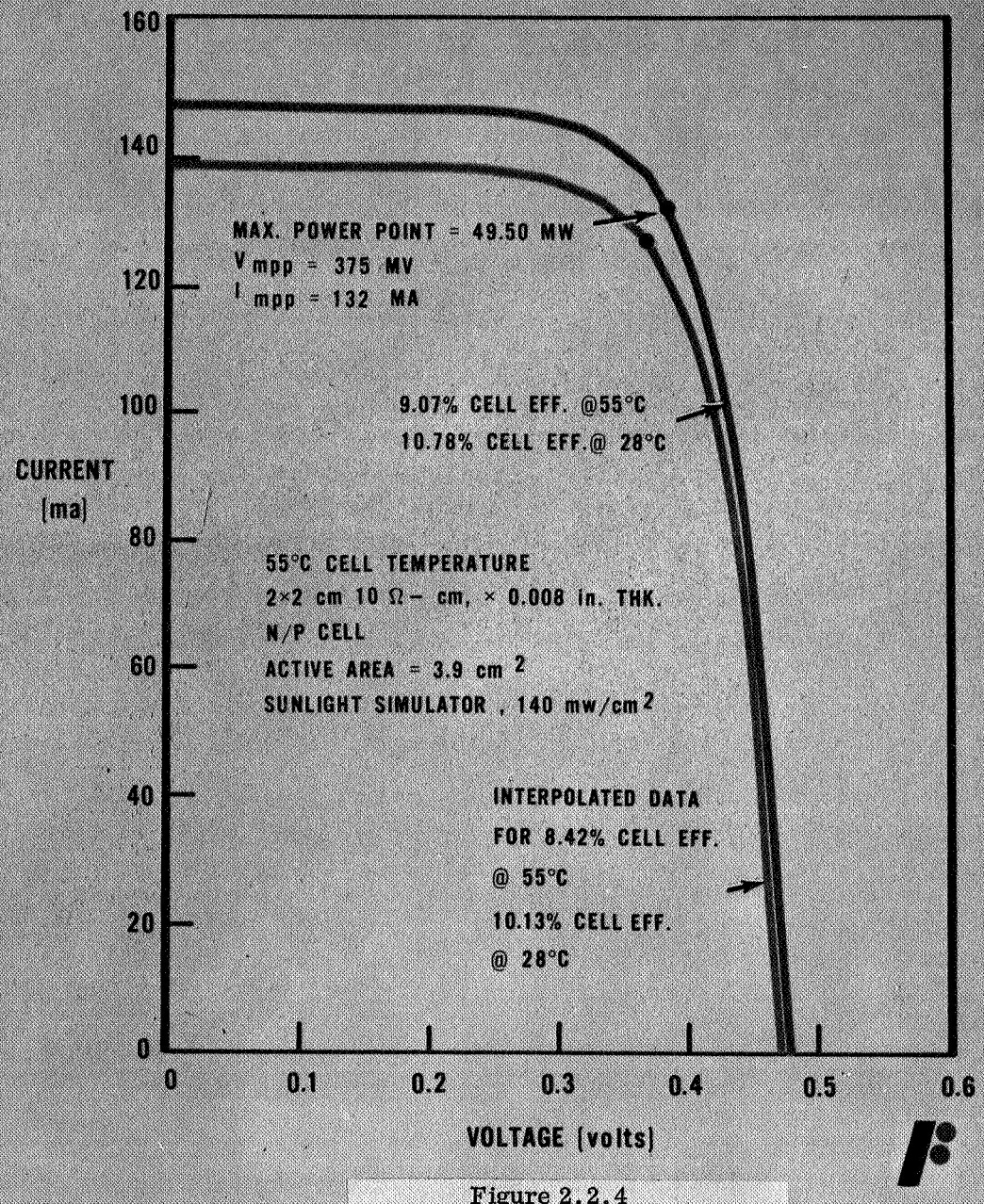


Figure 2.2.4

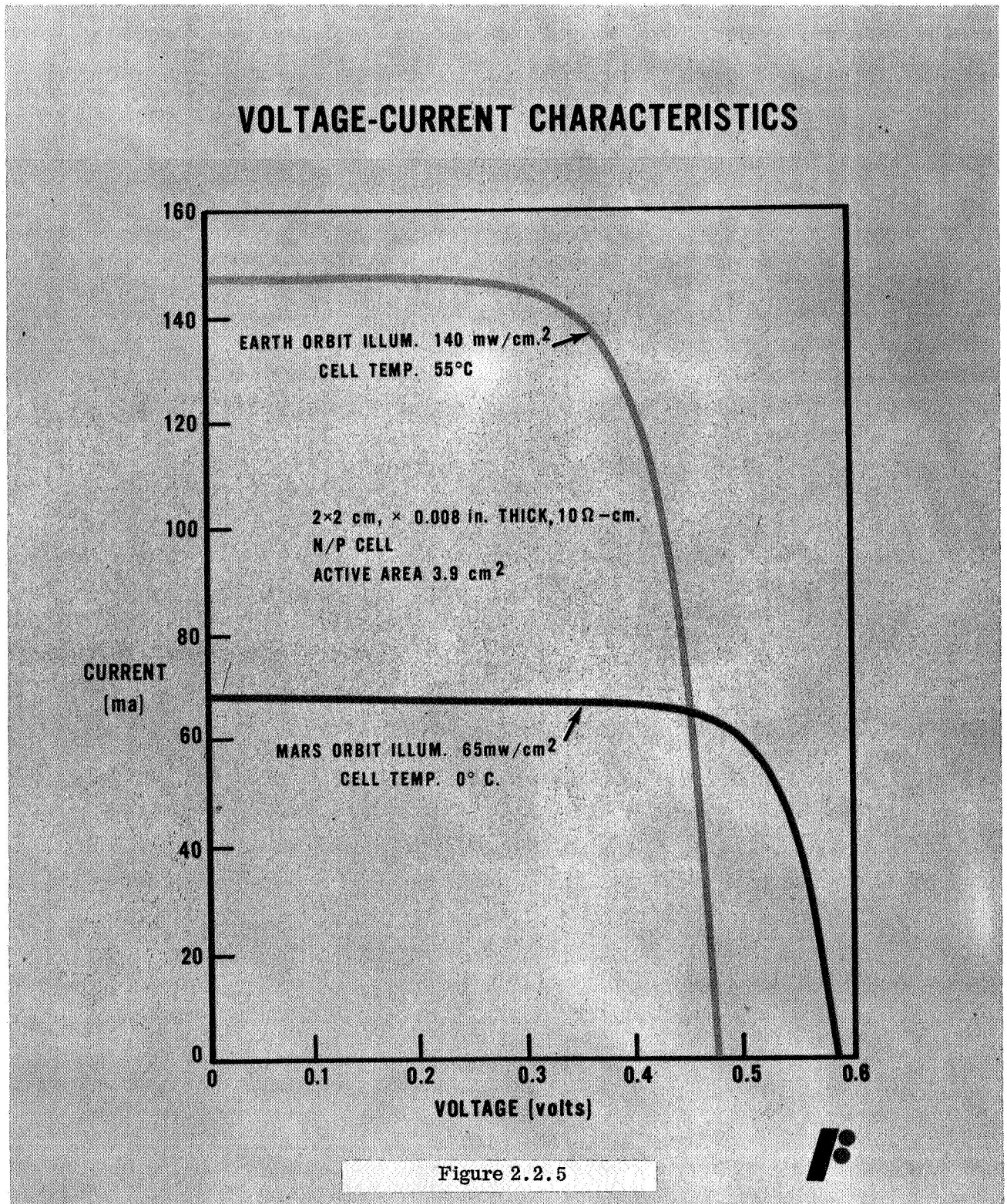

VOLTAGE-CURRENT CHARACTERISTICS
160
140
120
100
80
60
40
20
0
CURRENT
(ma)
EARTH ORBIT ILLUM. 140 mw/cm.2
CELL TEMP. 55°C
2×2 cm, × 0.008 in. THICK, 10Ω-cm.
N/P CELL
ACTIVE AREA 3.9 cm2
MARS ORBIT ILLUM. 65mw/cm2
CELL TEMP. 0° C.
0
0.1
0.2
0.3
0.4
0.5
0.6
VOLTAGE (volts)

Figure 2.2.5

2.2.1.4 Primary Power Loss Consideration

The 10 W/ft^2 requirement is to be based on a bare cell after consideration of the following primary power losses -

1. Cell Mismatching = 1.0%
2. Cover Glass & Adhesive = 4.0%
3. String Interconnections = 1.0%

If we assume a constant-resistive load operating at the maximum power point of 49.5 mw, the cell output will decrease to 46.57 mw when the primary power losses are considered. At this new power, v= 364.1 mw and I = 127.9 ma, as is shown in Figure 2.2.6.

2.2.1.5 Effect of Array Damping Materials on Cell Output

To protect the solar cells with the array in the launch configuration (rolled-up), a layer of low density polyurethane foam is placed between adjacent layers of the array. The foam is attached to the back of the substrate and results in an increase in cell temperature, and consequently a degradation of cell output.

Figure 2.2.1 shows the variation of cell characteristics as a function of cell temperature. By increasing the cell temperature, I_{sc} increases and V_{oc} decreases in such a way as to cause a decrease in output power.

The polyurethane foam will increase the cell temperature by approximately $5^{o}C$ (if the entire back face of the cell is covered) and will, therefore, alter the E-I characteristics as shown in Figure 2.2.7.

Figure 2.2.7 shows the E-I characteristics for 10.13% efficient cells (at $28^{o}C$) with and without the foam backing. By assuming a constant-resistive load, the peak power point of 49.6 mw at $43^{o}C$ will drop to 47.95 mw at $48^{o}C$ when the foam backing is added to the cell. This reflects a degradation in cell output of 3.3%.

2.2.2 Module Design

2.2.2.1 Module Configuration

Figure 2.2.8 shows the current paths of a typical module. To minimize magnetic effects, the module has been divided into 5 strips of 6 cells wide with the

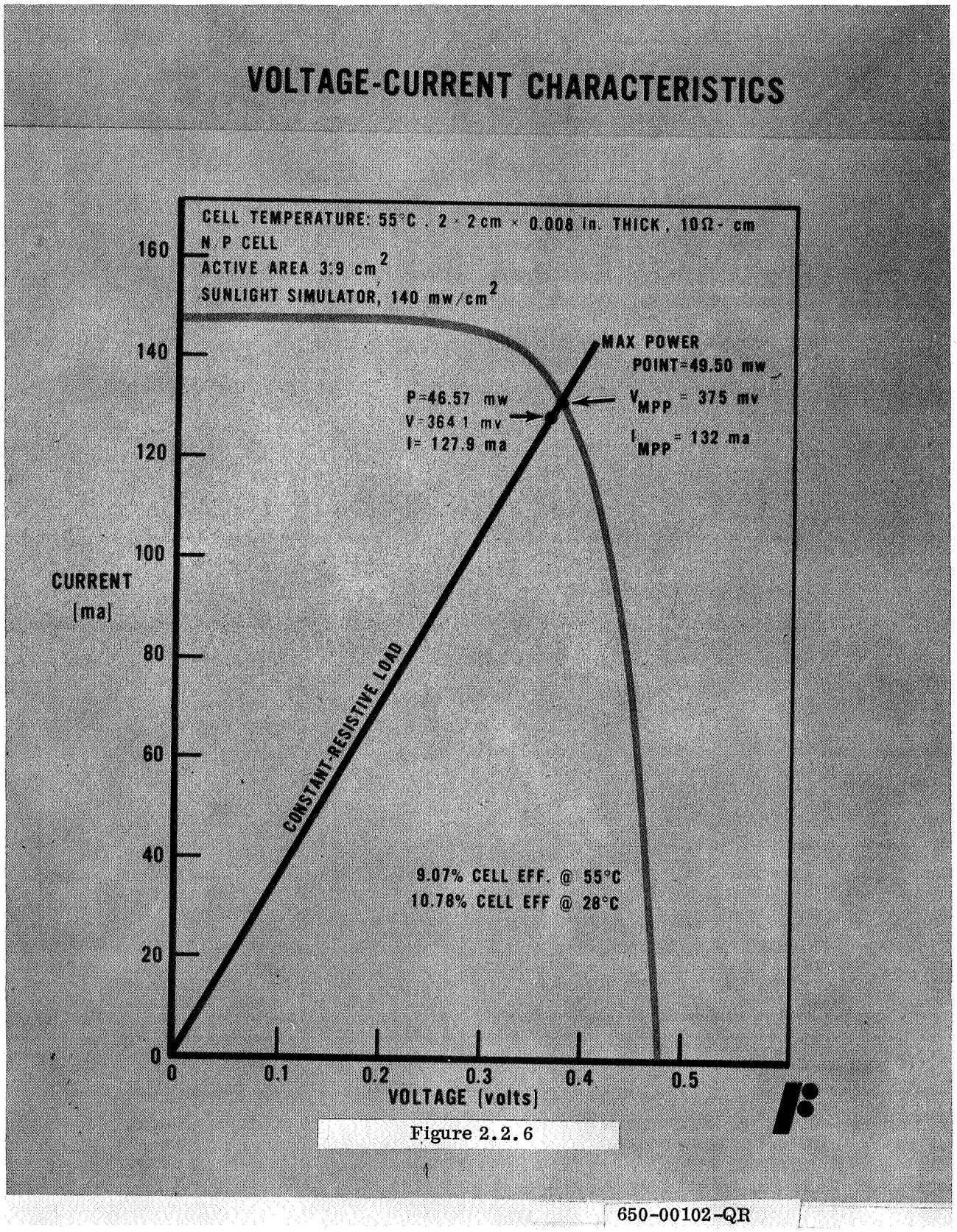

VOLTAGE-CURRENT CHARACTERISTICS
CELL TEMPERATURE: 55°C . 2 · 2 cm × 0.008 in. THICK , 10Ω · cm
N P CELL
ACTIVE AREA 3·9 cm²
SUNLIGHT SIMULATOR, 140 mw/cm²
MAX POWER
POINT=49.50 mw
P=46.57 mw
V=364.1 mv
I= 127.9 ma
V MPP = 375 mv
I MPP = 132 ma
CONSTANT-RESISTIVE LOAD
9.07% CELL EFF. @ 55°C
10.78% CELL EFF @ 28°C
CURRENT (ma)
160
140
120
100
80
60
40
20
0
0
0.1
0.2
0.3
0.4
0.5
VOLTAGE (volts)

Figure 2.2.6

EFFECT OF FOAM BACKING ON CELL E-I CHARACTERISTICS

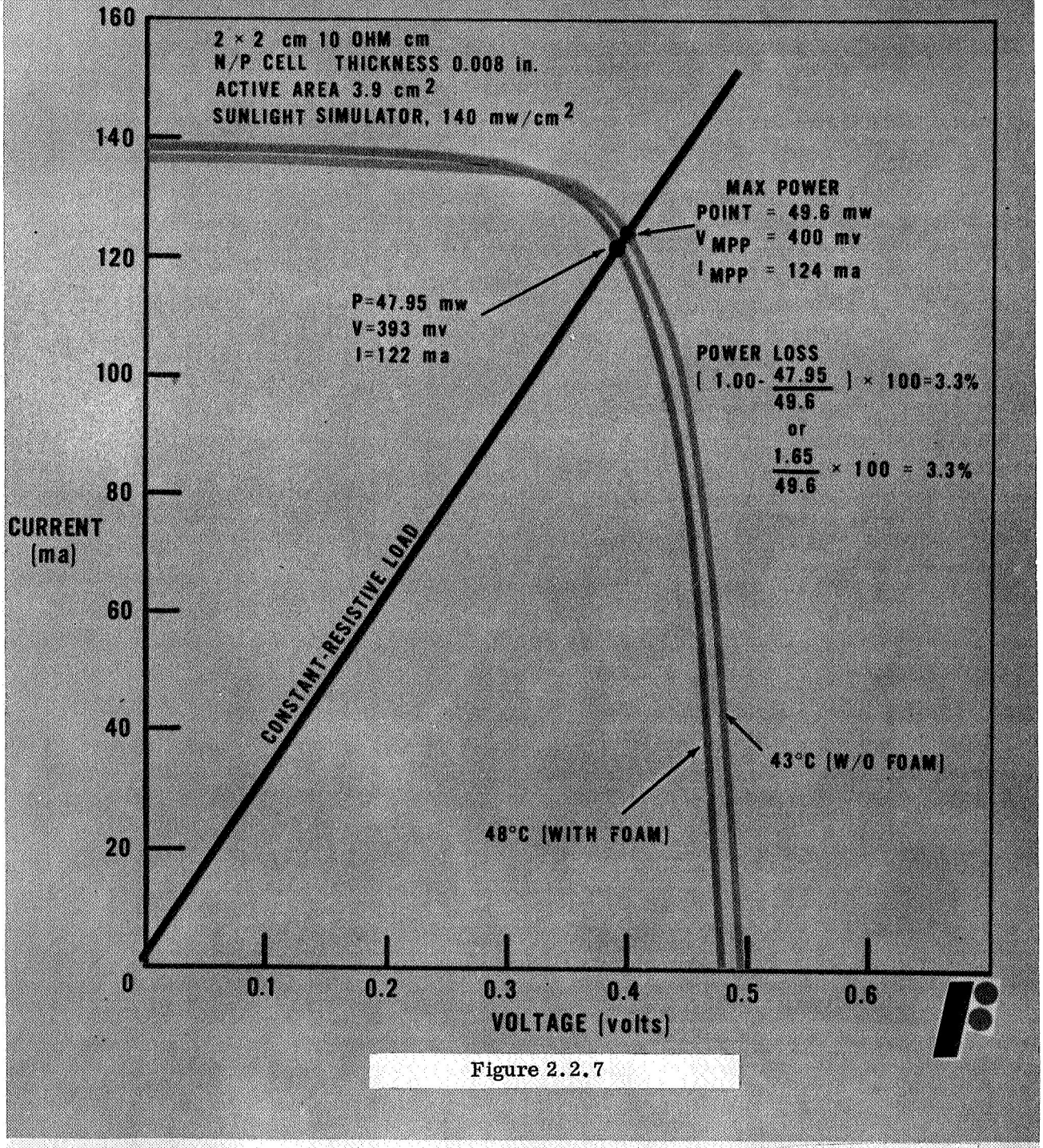


Figure 2.2.7

650-00102-QR

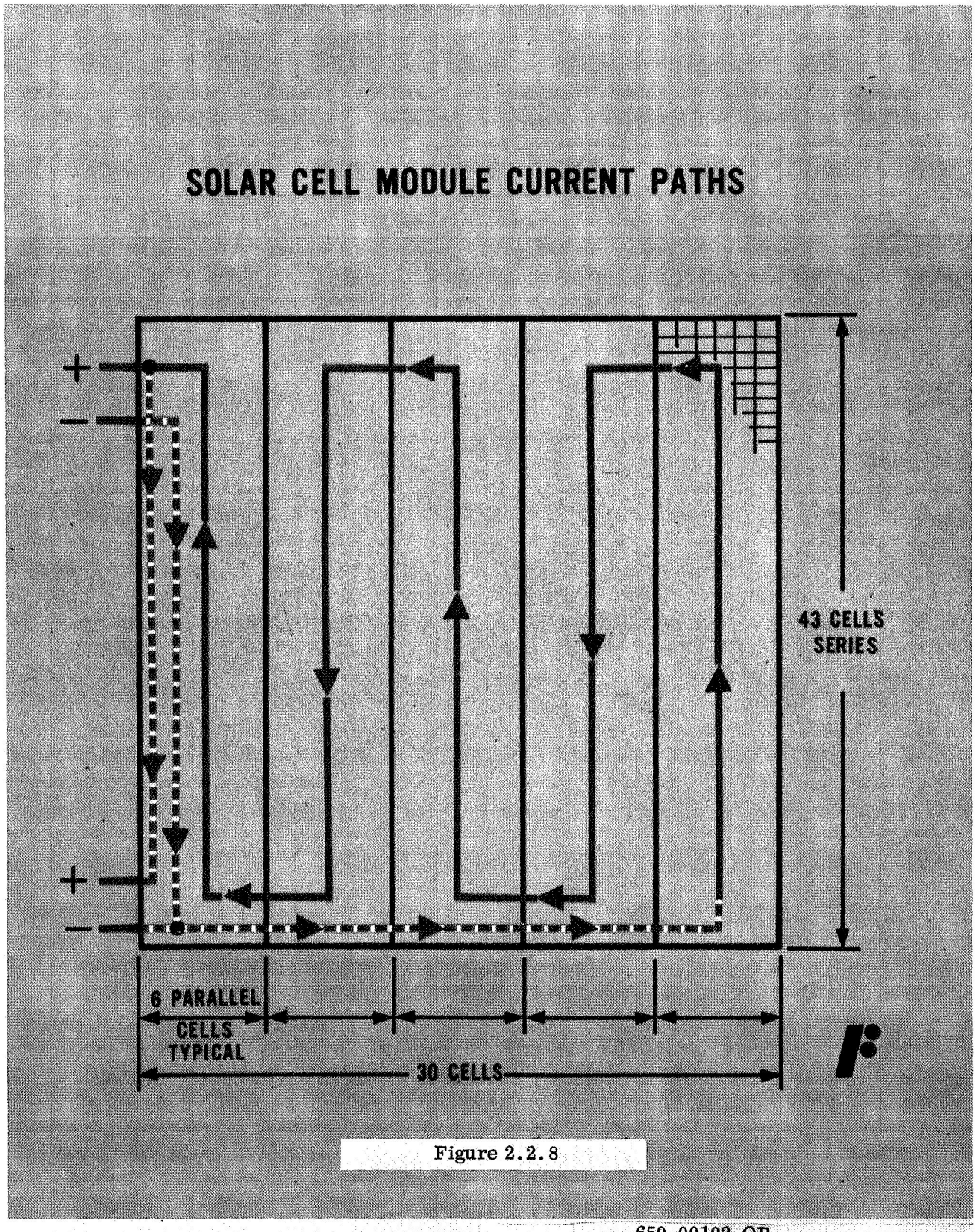

SOLAR CELL MODULE CURRENT PATHS
+
−
+
−
43 CELLS
SERIES
6 PARALLEL
CELLS
TYPICAL
30 CELLS

Figure 2.2.8

direction of current in one strip 180^{o} out of phase with the direction of currents in adjacent strips. There are 6 cells in parallel which yields a current output of 0.7674 amps/module and 215 cells in series which yields a voltage output of 78.28 volts/module. Therefore, the useable power output per module is 60.0732 watts. This output power rating exists at the module electrical connector, after subtracting the primary power losses discussed earlier.

A module contains 1290 cells (43 by 30) with a series spacing of .020 inches and a parallel spacing of .010 inches which is equivalent to a module area of 5.78 square feet. Hence:

$$\text{Power}/_{\text{ft}^2} = \frac{60.0732 \text{ watts}}{5.78 \text{ ft}^2}$$

$$\text{Power}/_{\text{ft}^2} = 10.39 \text{ W}/_{\text{ft}^2}$$

Since each module is an independent power source and all 48 modules are connected in parallel, the array will provide useable power at rated voltage if the array is only partially deployed.

An alternate module was considered with 10 cells in parallel yielding a current output of 1.279 amps module and 129 cells in series, yielding a voltage output of 46.97 volts/module. The power output per module remains the same as before, 60.0732 watts. The disadvantage of this module configuration was the increased current rating. With the larger current per module, a larger bus bar would be necessary for equivalent bus bar I^2R loss. Therefore, to keep the weight down to a minimum, the module with the lower current rating was selected. However, the advantage of this module is its lower bus voltage. Since array shadowing is not a factor to be considered and there is approximately a 23% increase in cell voltage at Mars orbit as compared to Earth orbit, the 78 volts (at 1AU) module will produce a voltage at its peak power point of approximately 96 volts. This voltage can be handled by existing power conditioning equipment designs. Thus, the 78 volt module design is selected as the preferred configuration.

2.2.2.2 Solar Cell Interconnections

Two MIL expanded silver mesh (with the slots in the expanded silver running perpendicular to the flexing direction) are soldered to the solar cells to complete the series and parallel connections. The expanded metal provides multiple current flow paths for redundancy and increased reliability.

The 2 MIL expanded silver with 7 MIL strand widths (Exmet Corp. - Type 2/0E silver mesh) provides approximately 22 connected strands per 2 x 2 cm solar cell as per Figure 2.2.9. Therefore, the current carrying area of the expanded silver per cell is 0.0003 in^2 or 0.0019 cm^2. With a cell separation of 20 mils, the length of one strand is approximately 0.030 in. or 0.076 cm. Using the resistivity of silver (1.81 micro-ohm-cm at 55°C), the resistance of the interconnect conductor was calculated to be 72.4 micro-ohms.

Assume the resistance of a 2 x 2 cm, 8 mil solar cell with 10 ohm-cm base resistivity is nominally 0.25 ohm. Then, the coil interconnect resistance is 0.029% of the total series resistance of the cell; which is well below the limiting value of 2.0%. Figure 2.2.9 shows a typical solar cell interconnection.

2.2.2.3 Module Power Characteristics

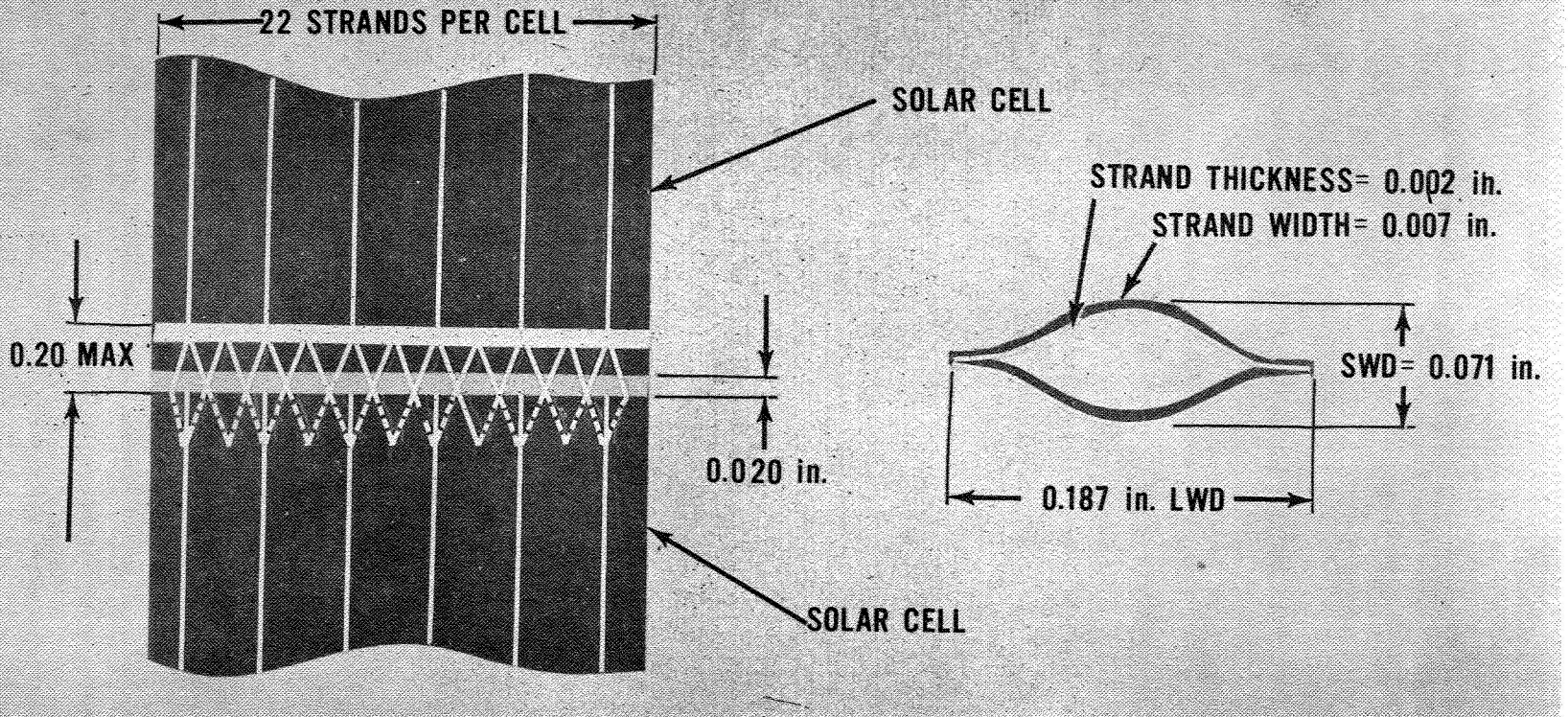
Table 2.2.1 presents the power characteristics of a typical module under three different module conditions.

1. All cells fully operational
2. One cell open circuited
3. One cell short circuited

It is seen from the table that for a module with one open circuit cell, the current decreases and the voltage remains constant causing a 16.7% decrease in power per module. This is equivalent to a 0.35% power loss for a 48 module array. If a cell should short circuit, the current remains constant while the voltage decreases causing a 0.47% decrease in power per module. This is equivalent to a 0.01% power loss for the 48 module array.

2.2.3 Array Wiring Harness

EXPANDED SILVER MESH CELL INTERCONNECTS



EXMET CORP. EXPANDED SILVER MF MESH TYPE 2/0E

Figure 2.2.9

650-00102-QR

TABLE 2.2.1

MODULE POWER CHARACTERISTICS

1290 cells -- (6 parallel x 215 series)

Module * Conditions	Voltage	Current	Power
Fully Operational	78.2815	.7674	60.0732
One Cell Open Circuit	78.2815	.6395	50.061
One Cell Shorted	77.9174	.7674	59.7938

* Data includes module primary power losses.

2.2.3.1 Bus Bar Characteristics

This section presents the derivation of an expression for determining the peak power to weight ratio (or peak efficiency).

Definition of Terms

E	=	Efficiency (Power to weight ratio)
P_T	=	Total Power (Bus bar losses excluded) (watts)
P_L	=	Power loss due to bus bar (watts)
W_S	=	Total system weight (bus bar weight excluded) (lbs)
W_B	=	Bus bar weight (lbs)
l	=	Length of bus bar wire (in.)
r	=	Resistance of bus bar wire/in.
D	=	Density of bus bar material (lbs/in^3)
ρ	=	Resistivity of bus bar material ($\Omega in^2/in$)
A	=	Cross sectional area of bus wire (in^2)
I	=	Current (amps)

The basic equation for computing the efficiency (power to weight ratio) is

$$E = \frac{P_T - P_L}{W_S + W_B} \tag{1}$$

where

$$W_B = l\,DA \tag{2}$$

since

$$A = \frac{\rho}{r} \tag{3}$$

and

$$P_L = I^2 r\, l \tag{4}$$

or

$$r = \frac{P_L}{I^2 l} \tag{5}$$

then equation (3) becomes

$$A = \frac{I^2 \rho l}{P_L} \tag{6}$$

and equation (2) becomes

$$W_B = \frac{DI^2 \rho l^2}{P_L} \tag{7}$$

substituting equation (7) into equation (1) leads to

$$E = \frac{P_T - P_L}{W_S + \frac{DI^2 \rho l^2}{P_L}} \tag{8}$$

or

$$E = \frac{P_T P_L - P_L^2}{W_S P_L + DI^2 \rho l^2} \tag{9}$$

In equation (9) all terms except E and P_L are constants. Therefore the peak "E" is dependent on the value of P_L. To find the value of P_L that will result in a peak E, we must differentiate the E with respect to P_L, Hence,

$$\frac{dE}{dP_L} = \frac{d}{dP_L}\left(\frac{P_T P_L - P_L^2}{W_S P_L + DI^2 \rho l^2}\right) \tag{10}$$

$$\frac{dE}{dP_L} = \frac{\left(W_S P_L + DI^2 \rho l^2\right)\left(P_T - 2P_L\right) - \left(P_T P_L - P_L^2\right)\left(W_S\right)}{\left(W_S P_L + DI^2 \rho l^2\right)^2} \tag{11}$$

Setting equation (11) equal to zero and solving for P_L

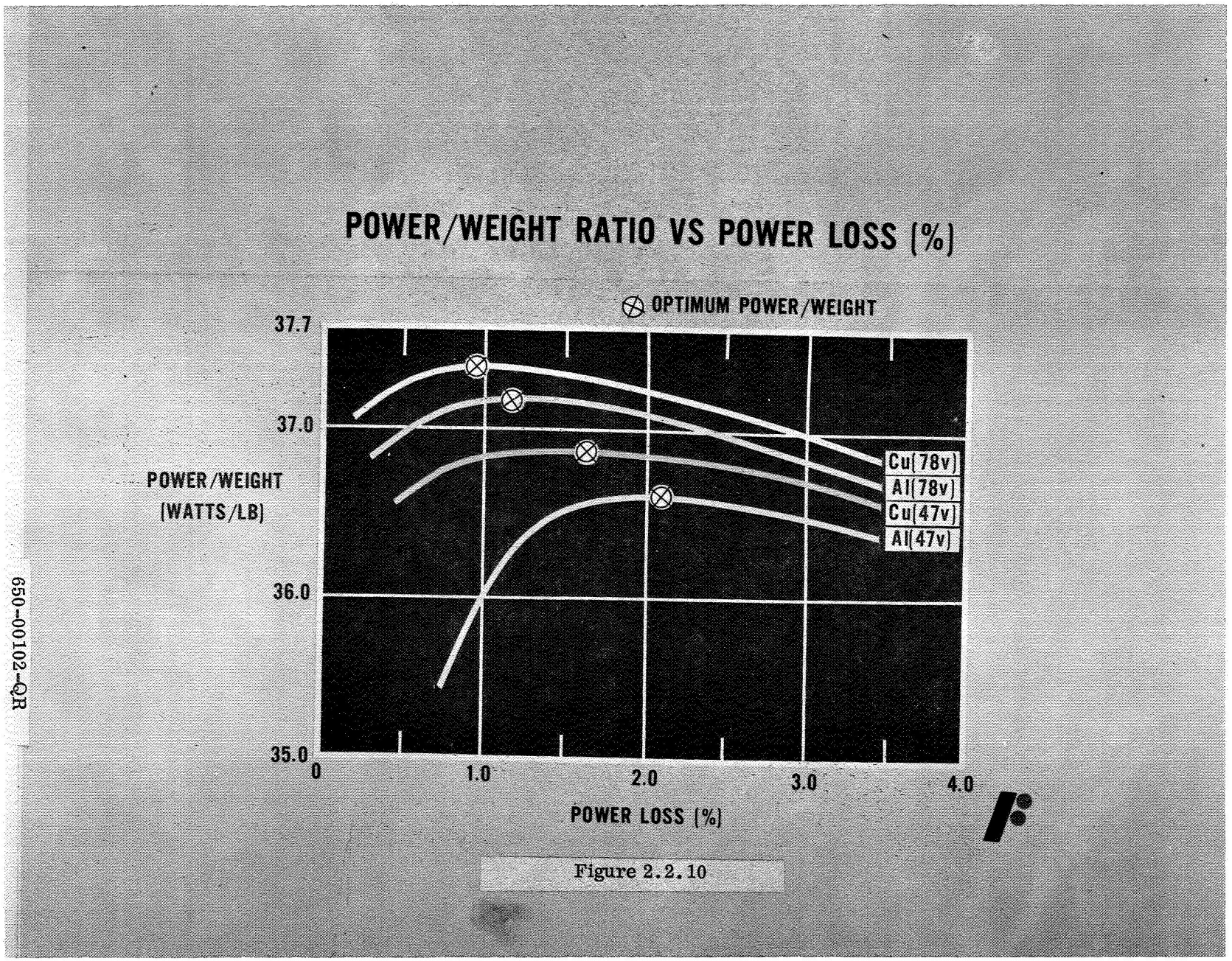
$$\left(W_S P_L + DI^2 \rho l^2\right)\left(P_T - 2P_L\right) - \left(P_T P_L - P_L^2\right)\left(W_S\right) = 0 \tag{12}$$

$$W_S P_L^2 + 2\left(DI^2 \rho l^2\right) P_L - P_T\left(DI^2 \rho l^2\right) = 0 \tag{13}$$

let

$$B = DI^2 \rho l^2 \tag{14}$$

Hence, equation (13) becomes



650-00102-QR

Figure 2.2.10

$$W_S P_L^2 + 2 B P_L - B P_T = 0 \tag{15}$$

solving for P_L

$$P_L = \frac{-2B \pm \sqrt{4B^2 + 4 W_S B P_T}}{2 W_S} \tag{16}$$

It can be shown that the two terms (-2B) and($4B^2$) are insignificant as compared to the ($4 W_S B P_T$) term.

Hence, equation (16) becomes

$$P_L \approx \frac{\pm \sqrt{W_S B P_T}}{W_S} \tag{17}$$

or

$$P_L \approx \pm \sqrt{\frac{B P_T}{W_S}} \tag{18}$$

where $B = DI^2 \rho l^2$

The absolute value of P_L in equation (18) when substituted into equation (9) will yield the peak efficiency or the optimum power to weight ratio.

$$E_{MAX} = \frac{P_T - \left| \sqrt{\frac{B P_T}{W_S}} \right|}{W_S + DI^2 \rho l^2 \left| \sqrt{\frac{B P_T}{W_S}} \right|} \tag{19}$$

2.2.3.2 Peak Power/Weight Ratio As A Function Of The Bus Bar Harness

The curves of Figure 2.2.10 represent the variation of power/weight ratio as a function of bus bar power losses using an average bus length of 17.5 feet. Two bus materials (copper and aluminum) and two bus voltages (78V and 47V) were considered. The peak power/weight points on these curves were computed from equation (19) and are listed in Table 2.2.2.

TABLE 2.2.2

Optimum Bus Power Losses

Material	Voltage (volts)	Power Loss (%)	Peak Power/Weight (W/lb)
Copper	78	0.98	37.37
Aluminum	78	1.24	37.18
Copper	47	1.64	36.88
Aluminum	47	2.07	36.57

It can be seen from the curves of Figure 2.2.10 and Table 2.2.2 that a copper bus operating at a bus voltage of 78V would give the maximum power/weight ratio of 37.37 w/lb. at a power loss of 0.98%. These figures were arrived at by not only considering the density of the bus bar material but also heeding the density of the insulation associated with the bus bar harness. By using the bus bar density alone and not the insulation density, aluminum at 78 volts showed a maximum power/weight ratio. The weight of the insulation contributes substaintially to the overall harness weight and thus, was included in the selection of the optimum conductor size and material.

2.2.3.3 Power/Weight vs. Array Aspect Ratio

Figure 2.2.11 respresents the variation of the power/weight ratio as a function of aspect ratio. The aspect ratio was defined as the length of the array divided by the width of the array. The average bus bar length will vary as a function of the aspect ratio. The aspect ratio that yields the maximum power/weight ratio will determine the optimum average bus bar length and also the length and width of the array. Equation (19) was used to calculate the curve of Figure 2.2.11. It can be seen from the figure that an aspect ratio of approximately 4 will give the maximum power/weight ratio.

2.2.3.4 Bus Harness Configuration

By use of the optimum power loss of 0.98% obtained from Figure 2.2.10, the size of the copper bus bars was calculated. Figure 2.2.12 depicts the cross

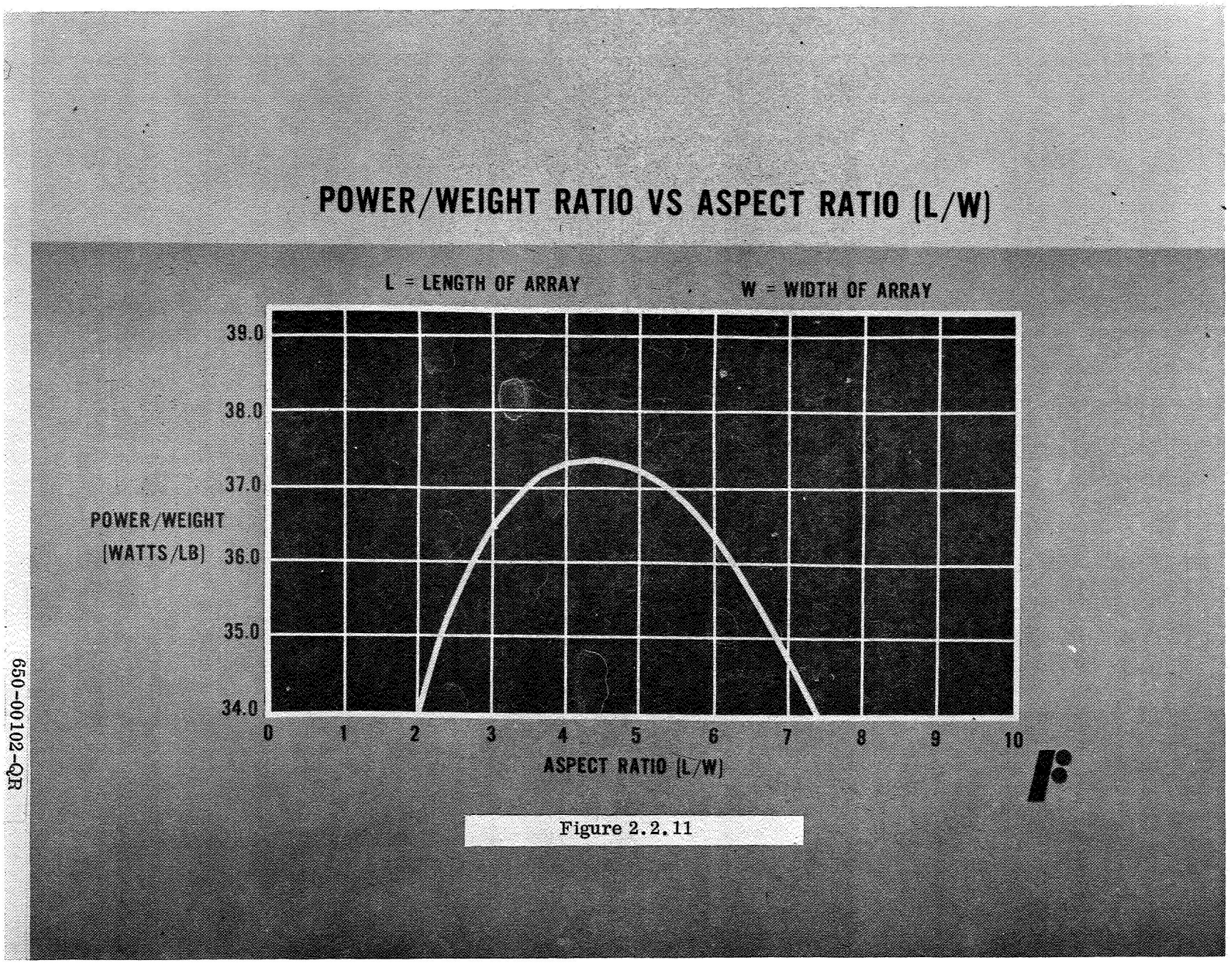

POWER/WEIGHT RATIO VS ASPECT RATIO (L/W)
L = LENGTH OF ARRAY
W = WIDTH OF ARRAY
39.0
38.0
37.0
36.0
35.0
34.0
POWER/WEIGHT
(WATTS/LB)
0
1
2
3
4
5
6
7
8
9
10
ASPECT RATIO (L/W)

Figure 2.2.11

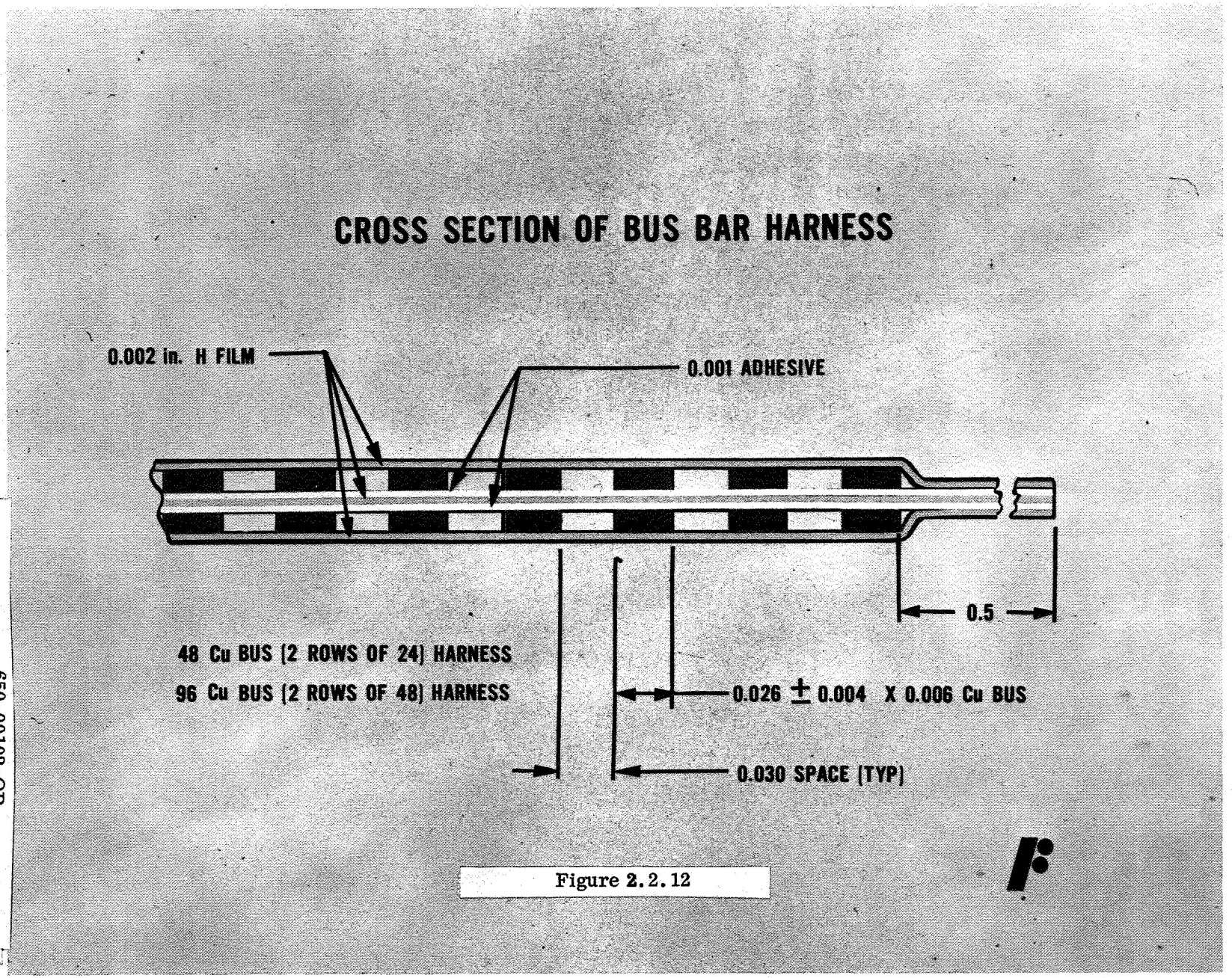

CROSS SECTION OF BUS BAR HARNESS
0.002 in. H FILM
0.001 ADHESIVE
0.5
48 Cu BUS (2 ROWS OF 24) HARNESS
96 Cu BUS (2 ROWS OF 48) HARNESS
0.026 ± 0.004 X 0.006 Cu BUS
0.030 SPACE (TYP)

Figure 2.2.12

section of a typical bus bar harness. The width of each copper bar is 0.26 inches ± .004 inches and the thickness is 0.006 inches. There is redundancy in the conductors of each circuit. If one of the conductors should fail, the remaining conductor will carry the load, however at twice the power loss (1.96%). There is .030 inch spacing between buses and 0.5 inch of insulation on the sides of the harness, so that it may be laced to the modules. There are two layers of bus bars in order to save space.

2.2.3.5 Effect of Harness Length on Cell Operating Point & Array Power Output

Figure 2.2.13 shows the band of operating points of cells along the array. The cells near the outboard end of the array have longer bus lengths and therefore see a greater load than cells near the storage drum. Hence, different cell operating points are anticipated due to the varying power losses in the buses.

Cells located at the outboard end of the array will have to operate at a higher voltage, than cells near the storage drum in order to maintain a constant voltage at the space craft interface. By selecting the peak power vs the operating point for the cells near the center of the array, the band of cell operating points over the entire array were obtained and are plotted in Figure 2.2.13.

Cells at the outboard end of the array will be operating at a higher voltage lower current, and lower power while cells near the storage drum will be operating at a lower voltage, higher current, and lower power;as compared to cells near the middle of the array operating at the peak power point. Due to this condition, the average cell output will decrease from 49.5 mw to 49.39 mw. This is equivalent to a 0.22% loss in array power output.

2.2.3.6 Module Bus Harness Electrical Connectors

Figure 2.2.14 gives the physical dimensions and electrical characteristics for the connector used in connecting the module to the bus bars. The selected connector is an ITT Cannon Electric, type MTB (Diallyl Phthalate Insulator) with an average contact resistance of 4 milliohms and an average voltage drop of 12 milli volts at 3 amps. The anticipated power loss is 0.002% per module. Each module has two redundant 4 pin connectors.

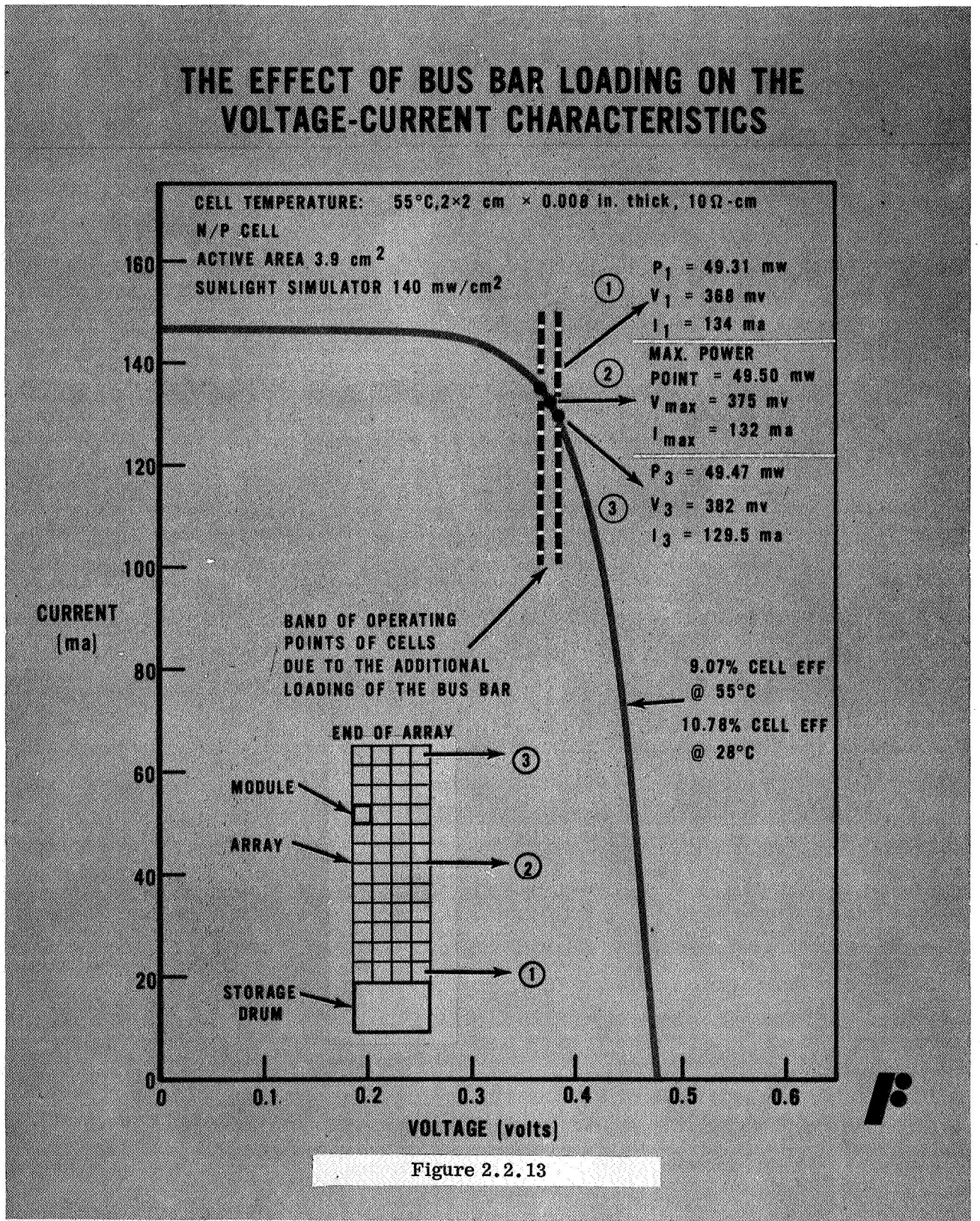
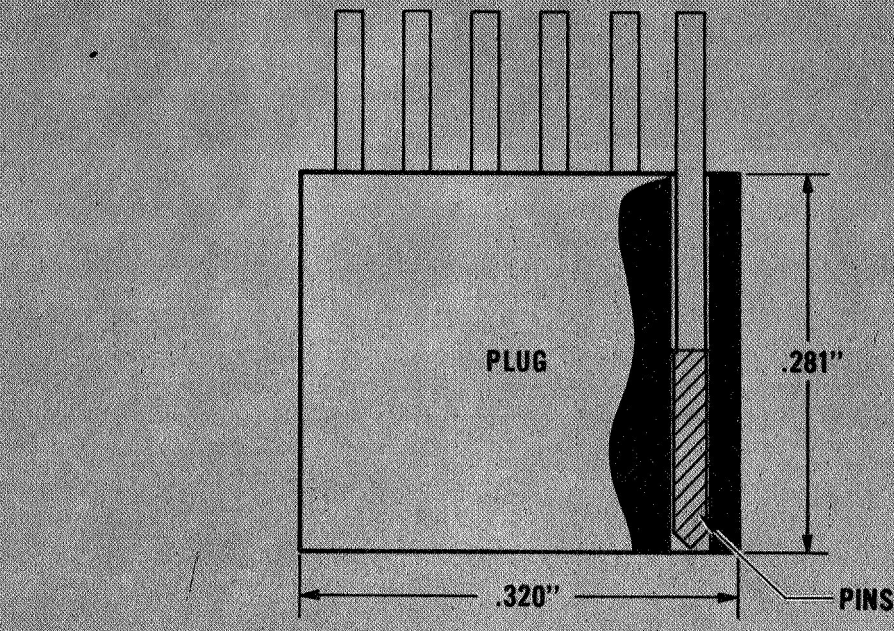
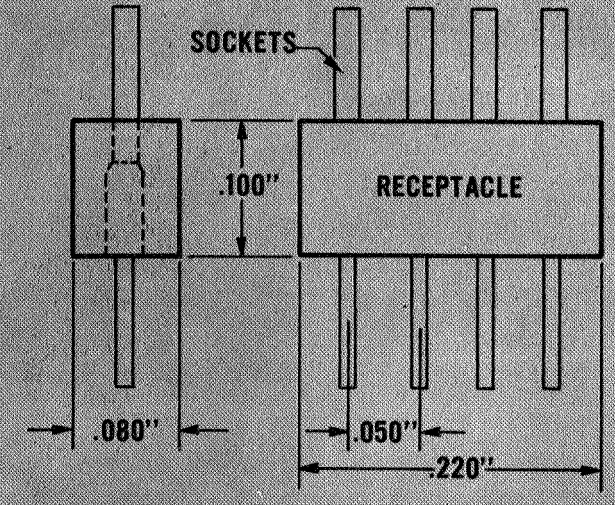

THE EFFECT OF BUS BAR LOADING ON THE VOLTAGE-CURRENT CHARACTERISTICS
CELL TEMPERATURE: 55°C, 2×2 cm × 0.008 in. thick, 10 Ω-cm
N/P CELL
ACTIVE AREA 3.9 cm²
SUNLIGHT SIMULATOR 140 mw/cm²
P1 = 49.31 mw
V1 = 368 mv
I1 = 134 ma
MAX. POWER POINT = 49.50 mw
V max = 375 mv
I max = 132 ma
P3 = 49.47 mw
V3 = 382 mv
I3 = 129.5 ma
9.07% CELL EFF @ 55°C
10.78% CELL EFF @ 28°C
BAND OF OPERATING POINTS OF CELLS DUE TO THE ADDITIONAL LOADING OF THE BUS BAR
END OF ARRAY
MODULE
ARRAY
STORAGE DRUM
CURRENT (ma)
VOLTAGE (volts)
0
20
40
60
80
100
120
140
160
0.1
0.2
0.3
0.4
0.5
0.6

Figure 2.2.13

BUS BAR CONNECTOR





MANUFACTURER-
ITT CANNON ELECTRIC

TYPE-
MTB-DIALLYL PHTHALATE
INSULATOR

AVERAGE CONTACT RESISTANCE-
4 MILLI OHMS

AVERAGE VOLTAGE DROP-
12 MILLI VOLTS AT 3 AMPS

Figure 2.2.14

Each connector has 2 additional pins which provide a test point for the module, as shown in Figure 2.2.15.

Figure 2.2.16 shows the overall method of connecting the module to the bus harness. The connectors are keyed to insure proper mating. The connector pins, the connectors, and the harness conductors are all dual and thus, redundant.

2.2.4 Panel Wiring Configuration

Figure 2.2.17 shows the wiring configuration for a 48 module array, since the bus bar harness has an upper and lower layers, the upper layer is designated by a solid line and the lower layer by a dashed line. The right and left bus bar harness assemblies each have 48 conductors arranged in two layers of 24. The center bus bar harness has 96 conductors arranged in two layers of 48. All circuits are paralleled together at the storage drum.

Electric current is transfered across the drum by means of a slip ring assembly which consists of 10 rings and 20 brushes (half for the positive line and half for the negative line). There are two brushes per ring for redundancy. The current per ring with all contacts operational is 7.367 amps and the current per brush is 3.6835 amps.

2.2.5 Summary of Array Electrical Characteristics

Table 2.2.3 is a summary of the array output power calculation. It presents (1) bare cell outputs, (2) module outputs with the primary power losses considered, and (3) the array output with other system and configuration power losses considered. The other system and configuration power losses are defined as:

Foam Backing	0.8%
Beam Reflection	1.0%
Module Connectors (2 per module)	0.002%
Slip Rings	0.118%
Bus Harness	0.98%
Bus Loading Effect	0.22%
Blocking Diodes (two diodes per module type Unitroden UT-262)	1.03%

CONNECTOR CONFIGURATION SHOWING TEST CONNECTIONS

CONNECTORS ARE KEYED FOR CORRECT MATING

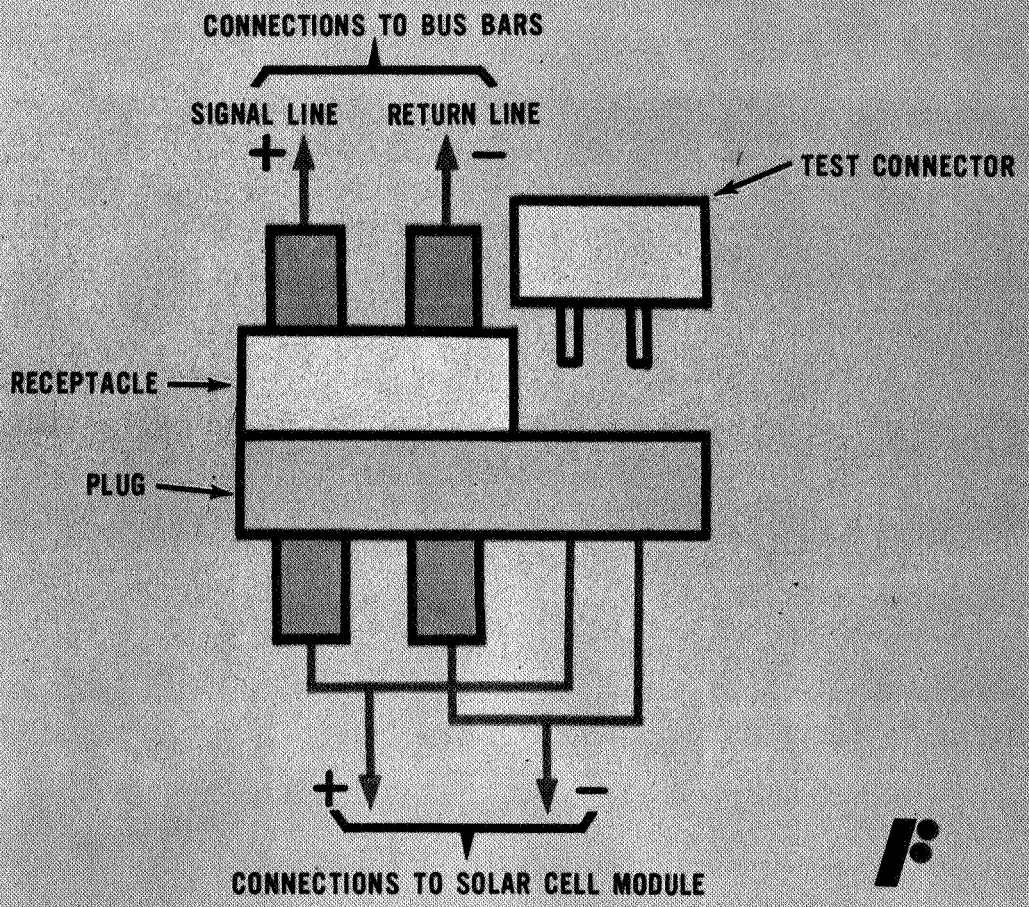


Figure 2.2.15

MODULE/HARNESS ELECTRICAL INTERFACE SCHEMATIC

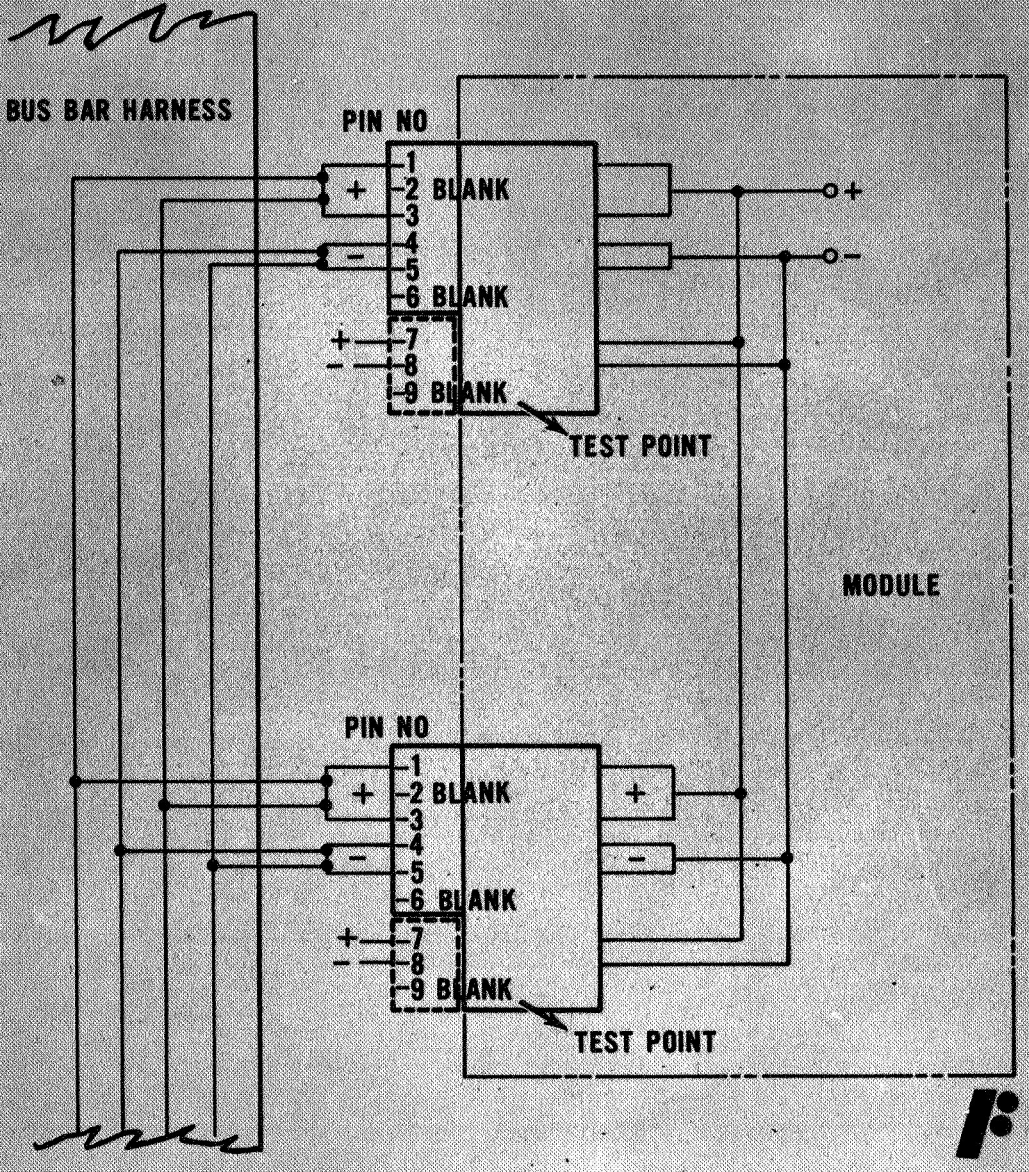


Figure 2.2.16

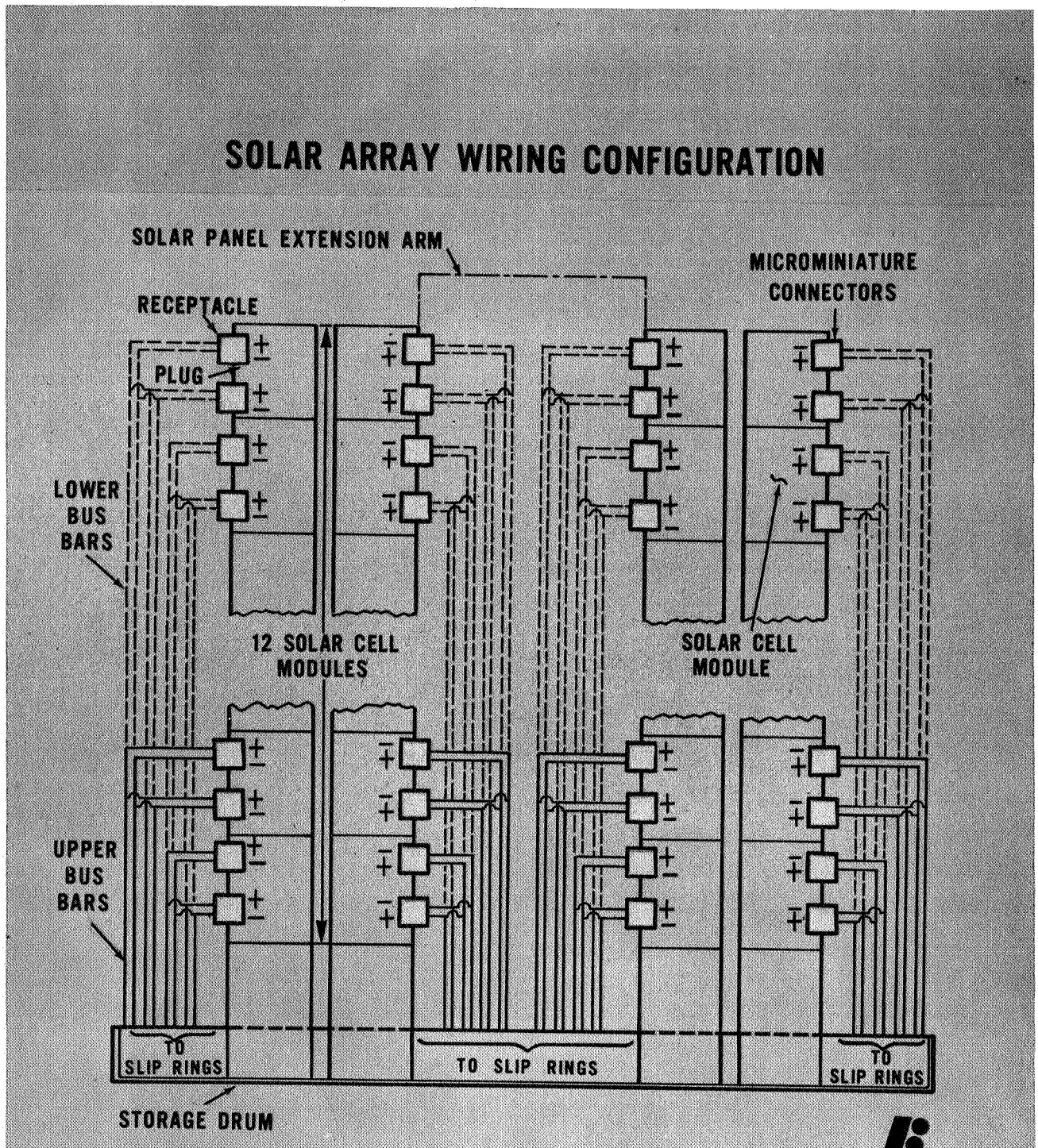

SOLAR ARRAY WIRING CONFIGURATION
SOLAR PANEL EXTENSION ARM
MICROMINIATURE CONNECTORS
RECEPTACLE
PLUG
LOWER BUS BARS
12 SOLAR CELL MODULES
SOLAR CELL MODULE
UPPER BUS BARS
TO SLIP RINGS
TO SLIP RINGS
TO SLIP RINGS
STORAGE DRUM

Figure 2.2.17

The array output with the above losses considered has been calculated to be 2762 watts at a bus voltage of 74.9834 volts and a current of 36.835 amps.

Beam reflections - The folding arm assembly will cause a slight heating of cells nearest to it. The power resulting from this condition has been calculated to be less than 1.0%.

Blocking Diodes - Will not be used in the final design, however they were used in the calculation of the preliminary array output power.

FAIRCHILD HILLER
SPACE AND ELECTRONICS SYSTEMS DIVISION

TABLE 2.2.3
Array Power Calculation Summary

Cell
2 x 2 cm x .008 in. thk.
N/P cell at 55°C
Active arm = 3.9 cm^2
Illum. - 140 mw/cm^2

Primary Power Losses
Cell Mismatch - 1.0%
Cover glass & Adhesive - 4.0%
String interconnections - 1.0%

Other system & Configuration Power Losses
Foam Backing - 0.3%
Beam Reflection - 1.0%
Modular Conn. - 0.002%
Slip Files - 0.113%
Harness - 0.98%
Blocking Diodes - 1.03%
Bus Loading - 0.22%

Configuration	Bare Cell C			Cell With Primary Losses			Array Output Characteristics		
	Voltage (volts)	Current (amps)	Power (watts)	Voltage (volts)	Current (amps)	Amp (watts)	Voltage (volts)	Current (amps)	Power (watts)
Cell @ 55°C, IAU	.375	.132	.0495						
Module 1290 cells, in parallel, 215 in series	80.625	.792	63.855	78.28 97.1%	0.7674 96.9%	60.0732 94.0%			
Array 4.8 parallel Modules	80.625	38.016	3065.0				74.9834 93.0%	36.835 96.8%	2762.0 90.0%

2.3 STRUCTURAL ANALYSIS

All parametric analysis were completed. Weight studies of Folding Arm and Hingelock deployment system components for a range of solar panel aspect ratios and tensions are presented in this report. Hingelock tube weights and total structural weights (not including drive motor and gear train) of the Folding Arm concepts were determined. An analysis for the array storage drum (applicable to all deployment systems) is also submitted. Natural frequency analyses of the solar cell panel and a limited weight analysis for the TEE system were concluded in the First Quarterly Report, 652-00101-QR. No further effort was exerted for the TEE concept as it proved to be appreciably heavier than the other systems.

2.3.1 Solar Array Storage Drum

2.3.1.1 Thin-Wall Cylinders

A parametric study was conducted for thin-walled cylinders. Drum lengths were varied from 6 ft. to 12 ft. Solar panel unit weights between 0.09 lb/ft.^{2} and 0.30 lb/ft.^{2} were considered.

Aluminum, titanium, stainless steel, beryllium, boron-epoxy composites, and graphite-epoxy composites were the materials investigated. Magnesium and fiberglass laminates were regarded as non-competitive because of their low structural index, $\frac{EF_{cy}}{W}$, where E is Young's modulus of elasticity, lbs/in^2; F_{cy} is the allowable compression yield stress, lbs/in^2; and W is the density, lbs/in^3. Titanium and stainless steel cylinders were eliminated from the study after preliminary analysis showed them to be too heavy.

The parameters and ultimate loading criteria are presented in Table 2.3.1. The 5.0 g input is equal to the launch sinusoidal vibrational peak g of 4.0 multiplied by the 1.25 safety factor. A peak amplification factor of 20 at resonance for the drum was assumed at center (5% structural damping). The ultimate maximum load factor for the drum is therefore 4.0 x 1.25 x 20 or 100 g's. A peak amplification factor of 10 for the solar panel was assumed (10% structural damping). The ultimate peak load factor for the solar panel is therefore 4.0 x 1.25 x 10 or 50 g's. Ten percent (10%) damping was assumed for the solar panel.

SUBJECT SOLAR PANEL STORAGE DRUM PARAMETRIC STUDY

TABLE - 2.3.1

VARIABLES

DRUM WIDTH 72" to 144"

SOLAR PANEL WEIGHT .09 lb/ft² to .30 lb/ft²

DRUM DIAMETER 3" MINIMUM

DRUM MATERIAL AL, BE, BORON/EPOXY COMPOSITE, GRAPHITE/EPOXY COMPOSITE

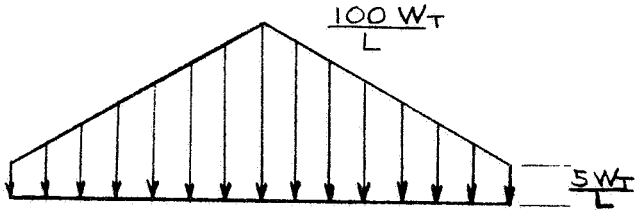
SOLAR PANEL AREA (A_S) 266 SQ-FT

ULTIMATE LOADING CONDITIONS

DRUM { 100 g AT CENTER; 5 g AT ENDS

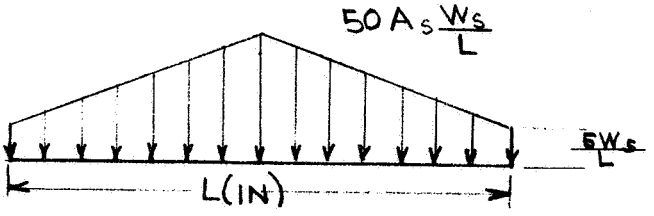
SOLAR PANEL { 50 g AT CENTER; 5 g AT ENDS

LOADING FROM DRUM MASS



(#/IN)

LOADING FROM SOLAR PANEL



(#/IN.)

W_S = SOLAR PANEL WEIGHT (#/FT²)
W_T = STORAGE DRUM WEIGHT (LBS.)
L = STORAGE DRUM LENGTH (INCHES)

Figure 2.3.1 presents maximum bending moments in the drum as a function of array unit weight and drum length (array width) and for a unit drum weight for the inertial loadings described. The moment for the unit drum weight must be multiplied by the actual drum weight to obtain the incremental design moment. The following analysis, optimizing aluminum thin-walled cylinders, typifies the studies conducted for all materials considered.

Allowable bending stresses, for thin-wall cylinders as a function of D/t, are typified by the curve for aluminum cylinders in Figure 2.3.2. They were derived using the procedure presented in NASA TN 3783, pages 32, 33, 34 and Figure 7. The characteristic equation is:

$$\sigma_{cr} = C_b \, Et/r = 1.3 \, CEt/r$$

Where:

C varies with r/t and U
E = modulus of elasticity (lb/in^2)
t = thickness (in.)
r = radius (in.)
U = unevenness factor (.00035)

The analysis to determine minimum weight cylinders for a given applied moment follows procedures presented by F. R. Shanley in "Weight-Strength Analysis of Aircraft Structures" 1st Edition, McGraw Hill, 1952, pages 40-45. Applied bending stresses in a cylinder can be expressed as:

$$f_b = \frac{4M}{\pi D_m^{\,2} t}$$

Where:

M = moment (in-lb)
D_m = mean diameter (in.)
t = thickness (in.)

or:

$$\frac{M}{D_m^{\,3}} = \left(\frac{\pi}{4}\right) \frac{f_b}{D_m/t}$$

SINGLE DRUM ARRAY

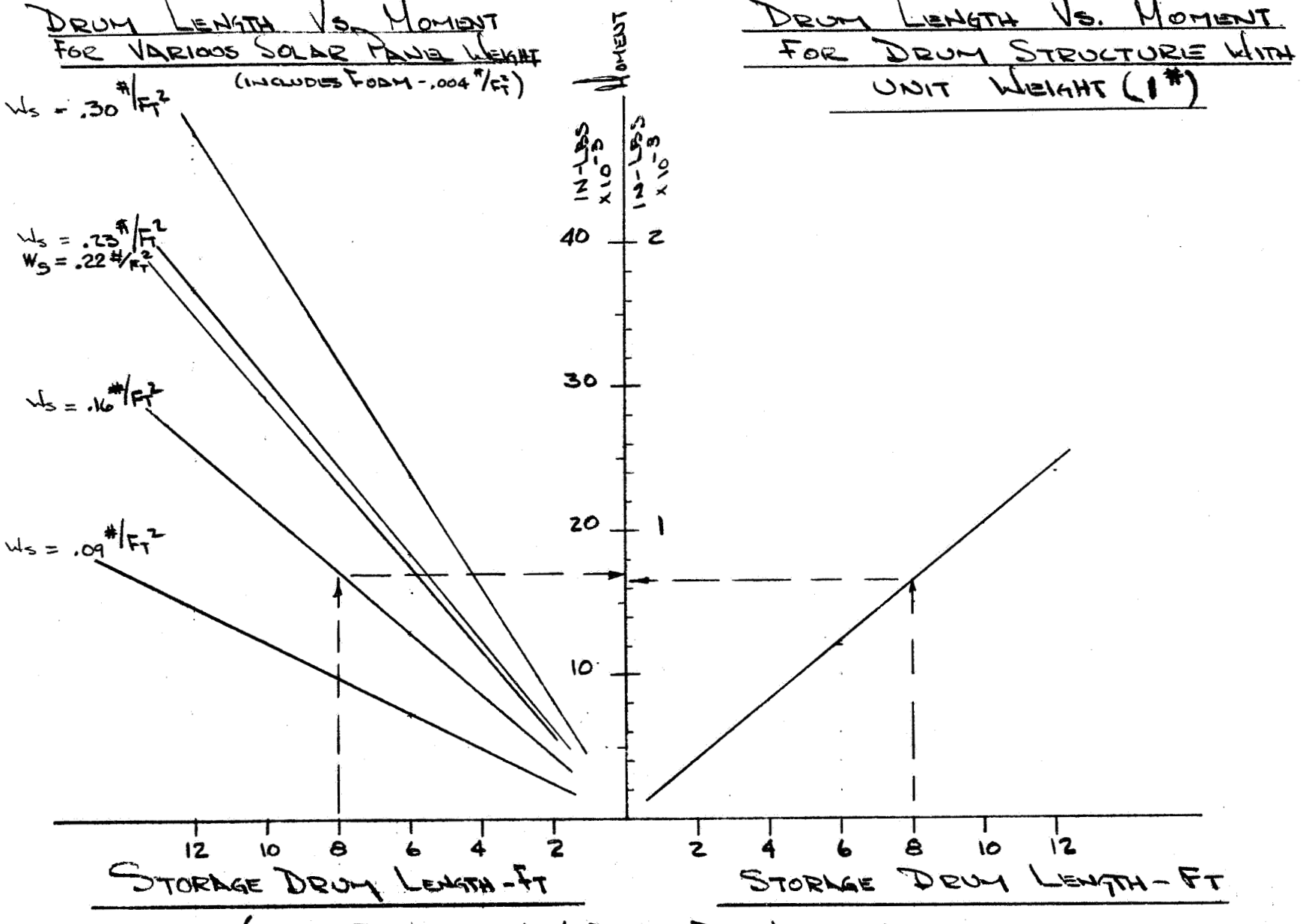


FIGURE 2.3.1

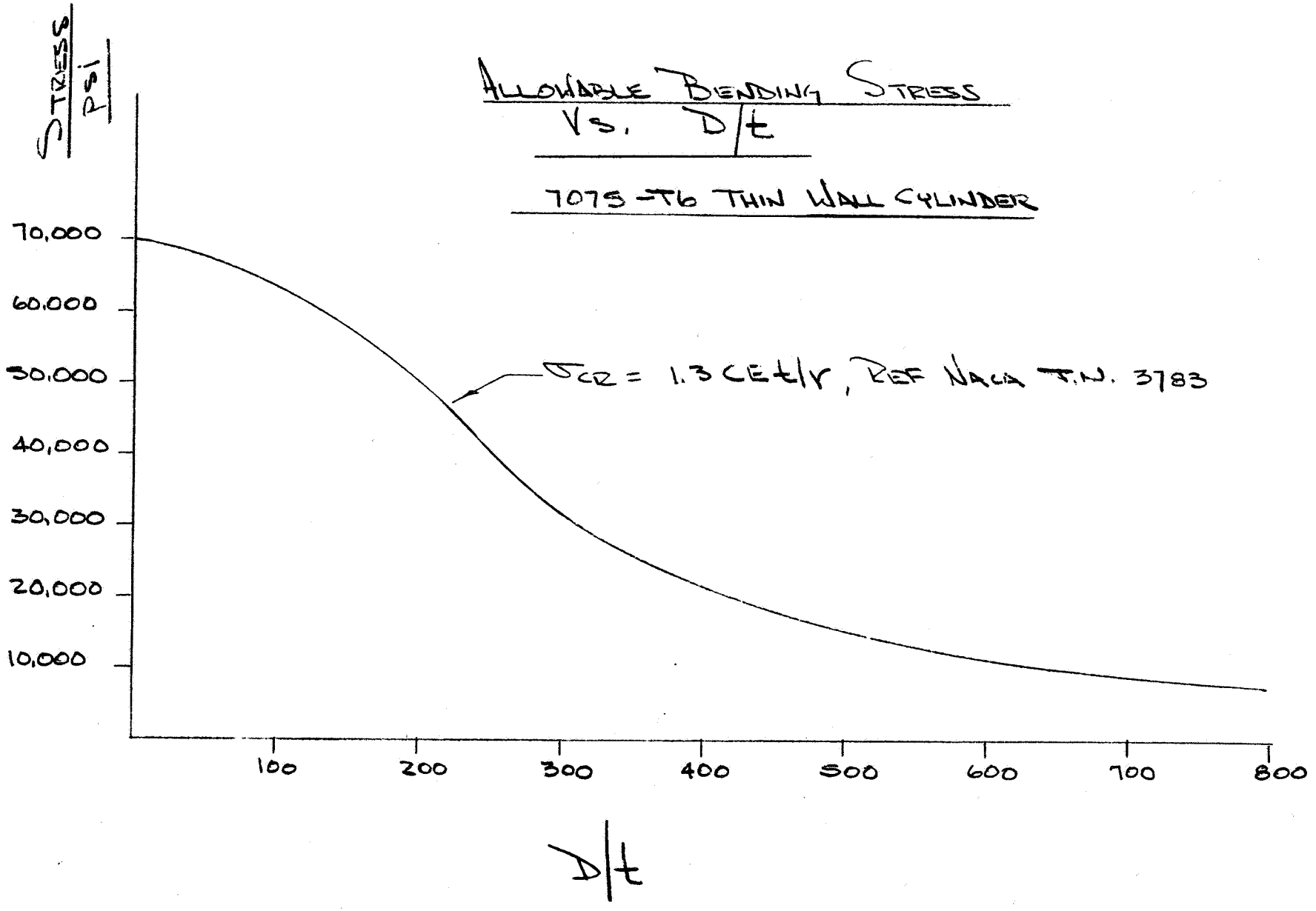

STRESS PSI
ALLOWABLE BENDING STRESS
VS. D/t
7075-T6 THIN WALL CYLINDER
70,000
60,000
50,000
40,000
30,000
20,000
10,000
$\sigma_{CR} = 1.3 C E t/r$, REF NACA T.N. 3783
100
200
300
400
500
600
700
800
D/t

FIGURE 2.3.2

Knowing the relations between f_b and D_m/t (Figure 2.3.1), the quantity M/D_m^3 was obtained. The cube root of M/D_m^3 was then plotted versus stress (Figure 2.3.3). A tangent to the above mentioned curve from the origin defines an optimum $M^{1/3}/D_m$.

$$D_{opt} = \frac{M^{1/3}}{K}$$

Where:

K is the abcissa at the tangent point.

Thus for any moment, an optimum diameter is obtained. Similarly, the optimum area can be obtained from the relation

$$A_{opt} = \frac{4M}{D_{opt} f_{opt}}$$

Where:

f_{opt} is the ordinate at the tangent point.

Figure 2.3.4 is a plot of optimum diameter versus applied moment as well as optimum area. Knowing the area, the resulting drum weight is read from the same figure for various drum lengths.

An example of the design procedure for obtaining a thin-walled storage drum follows: Assume 7075-T6 aluminum, an array width of 8 ft. (i.e. drum length of 8 ft.), and an array unit weight of .16 lb/ft.^{2}. Enter Figure 2.3.1 as shown and read M = 17,000 in-lb (solar panel weight only).

Enter Figure 2.3.4 with M = 17000 and read D_{opt} = 4.2 in. area = .305 in.^{2} and weight = 3.0 lb.

Return to Figure 2.3.1 for the unit weight of 1.0 lb., M_{drum} = 820 in-lb and for the 3 lb. drum, M = 2460 in-lb.

M_{total} = 17000 + 2460 = 19460 in-lb. Re-enter Figure 2.3.4 as before to obtain a new diameter, area, and weight. Continue the iteration until significant differences disappear.

The results of this study are shown in Figures 2.3.5 and 2.3.6. A minimum drum diameter of three inches was assumed.

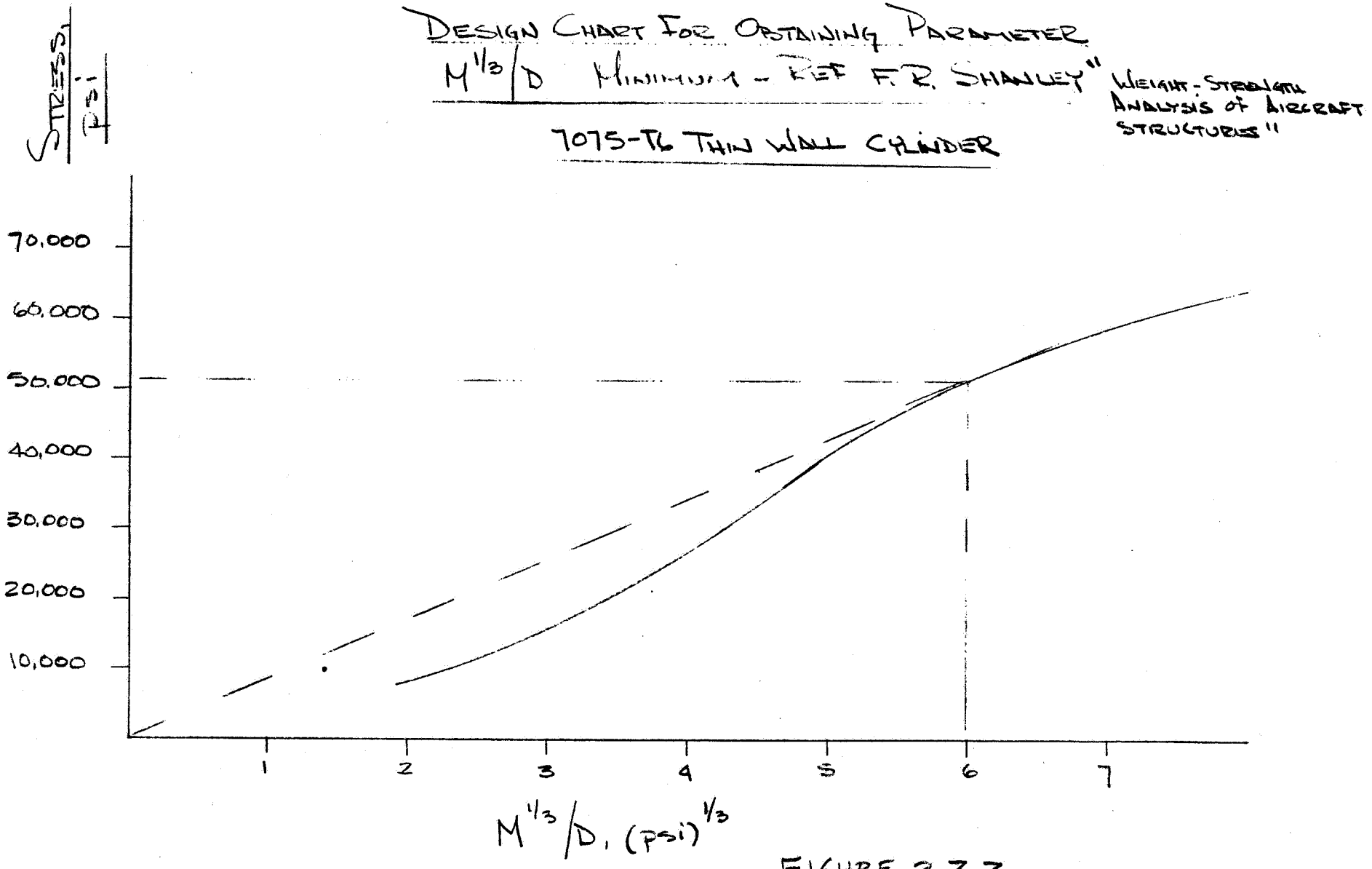

DESIGN CHART FOR OBTAINING PARAMETER
$M^{1/3}/D$ MINIMUM - REF F.R. SHANLEY "WEIGHT-STRENGTH ANALYSIS OF AIRCRAFT STRUCTURES"
7075-T6 THIN WALL CYLINDER
STRESS, PSI
70,000
60,000
50,000
40,000
30,000
20,000
10,000
1
2
3
4
5
6
7
$M^{1/3}/D$, $(psi)^{1/3}$

FIGURE 2.3.3

APPLIED MOMENT VS. OPTIMUM CYLINDER DIAMETER

7075-T6

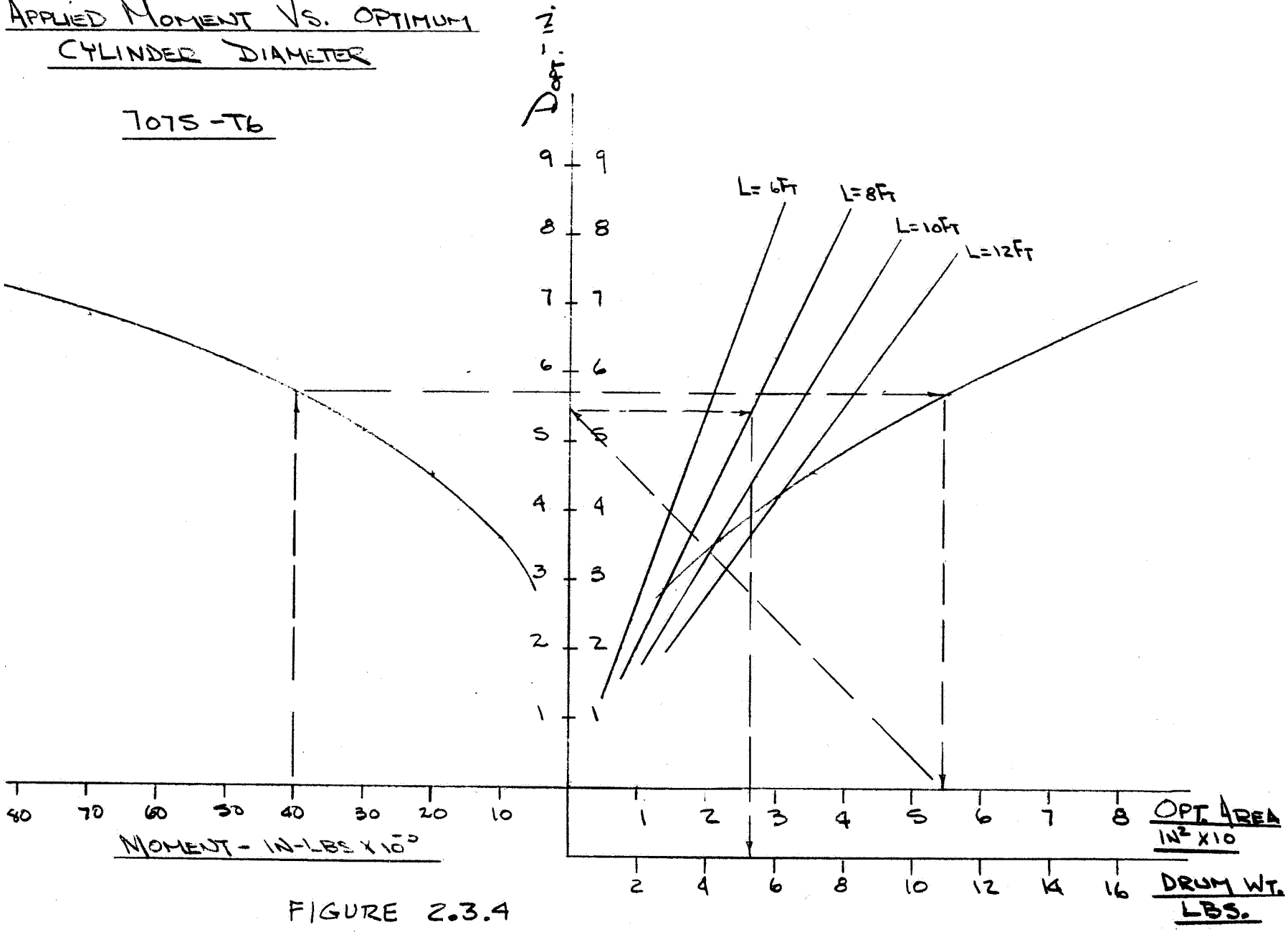


FIGURE 2.3.4

FIGURE 2.3.5

THIN WALL CYLINDER DRUM LENGTH VS DRUM WEIGHT

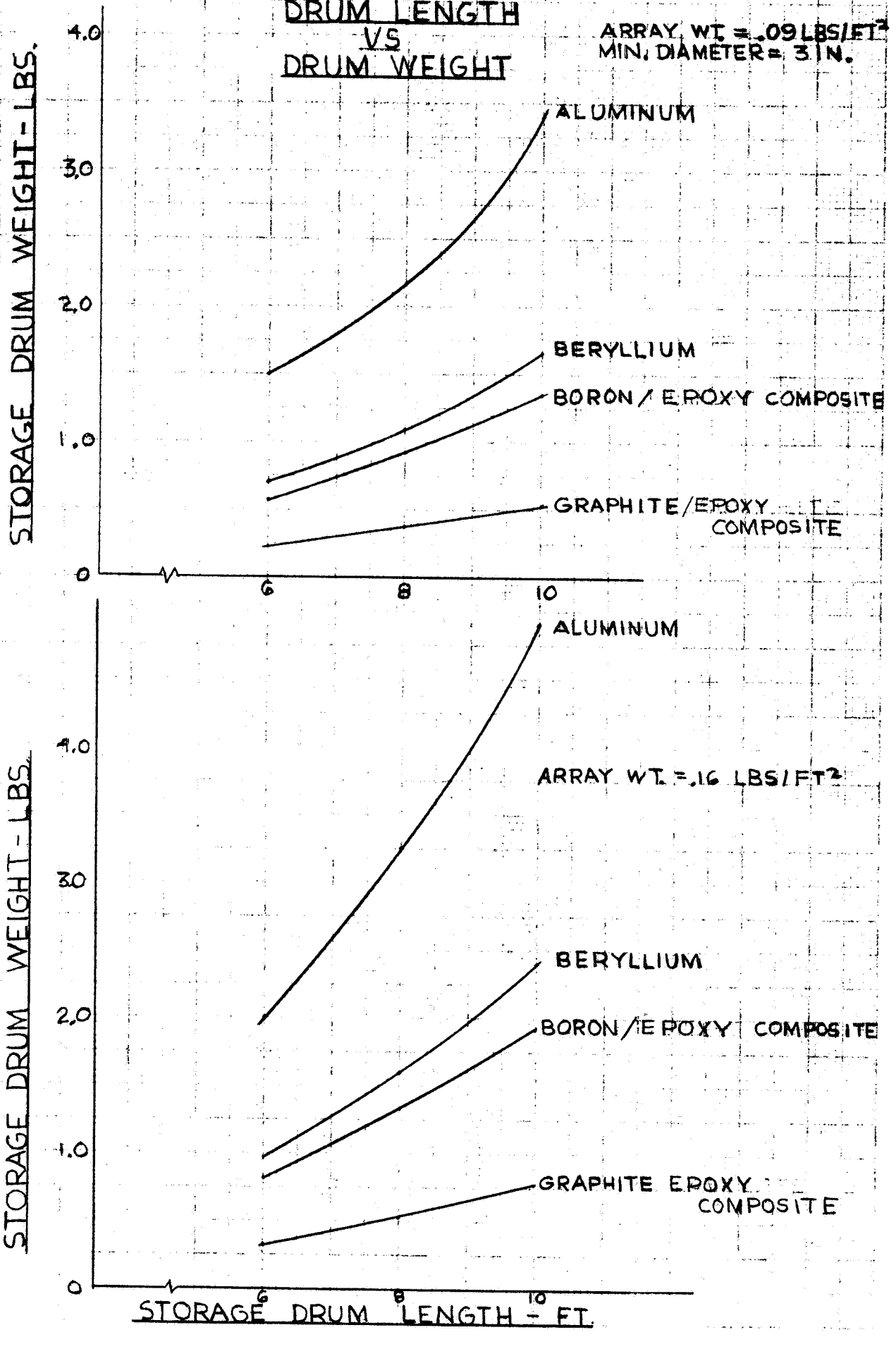
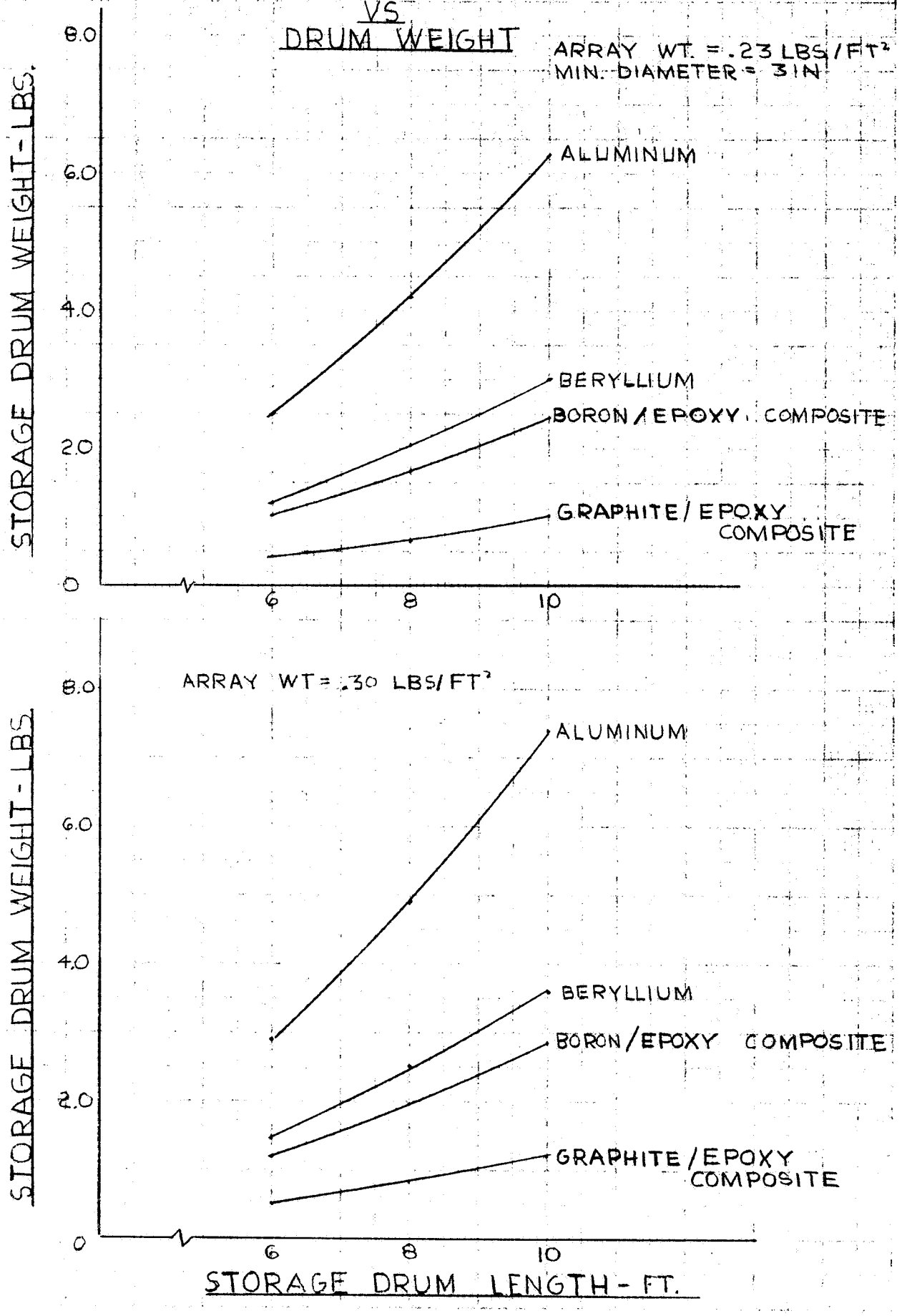


FIGURE 2.3.6

THIN WALL CYLINDER
DRUM LENGTH
VS
DRUM WEIGHT



2.3.1.2 Sandwich Cylinders

A study of the required thicknesses for 8 foot long, thin-walled cylinders; made from beryllium, or the composites, indicates sandwich construction to be inadvisable.

Beryllium must be chemically milled to obtain thicknesses below 0.020 in. The milling thickness tolerance is 0.003 in. and drawing dimensions must reflect these tolerances to guarantee required minimum thicknesses.

The maximum allowable bending stress for the thin wall cylinder is 48,000 psi. Sandwich construction would permit a maximum stress of 60,000 psi. The theoretical required thickness of each face would be $.5\ (.011)\ \frac{48,000}{60,000}$ or .0045 in. With tolerance, the thickness could be .0075 in. per face or a total of .015 in. This exceeds the thickness, and therefore the weight, of the thin-wall cylinder.

The graphite-epoxy composite and boron-epoxy composite thin-walled cylinders for the range of array weights studied, do not require more than a four ply layup. The minimum thickness for a sandwich face is two plies, due to the orthotropic characteristics of a filament layup. The two faces are obviously heavier than the monocoque cylinder.

The foregoing arguments are not applicable to an aluminum drum, as required cylinder wall thicknesses for the heavier solar arrays range up to 0.032 in. and sandwich faces can be as thin as 0.005 in.

The two major failure modes for sandwich cylinders are: (1) elastic instability of the cylinder; and (2) intracellular buckling of the faces. Analyses for instability of 0.25 in. thick sandwich cylinders as large as 5 inches in diameter, performed in accordance with the method outlined in MIL-Hdbk-23, indicate this failure mode as not critical. The governing criteria are F_{cy} of the material and a honeycomb cell size small enough to preclude dimpling.

General design curves were developed for 0.007 in. 7075-T6 faced sandwich cylinders. The faces can be stressed to F_{cy} using 0.125 inch cell honeycomb core. Solving for the minimum drum diameter, to work the faces to this

limit, results in a minimum weight drum. Figures 2.3.7 through 2.3.9 were used, in conjunction with Figure 2.3.1, to develop curves for the weight and size of an 8 foot long sandwich drum vs. array weight density. These curves are presented in Figures 2.3.10 and 2.3.11, with a thin-walled cylinder plotted for comparison. It shows that, except for very lightweight arrays, thin-walled construction is heavier.

2.3.2 Folding Arm Design - Parametric Studies

Parametric weight studies for the system introduced in the First Quarterly Report were concluded and the results are shown in Figures 2.3.16, 17 and 18. Table 2.3.2 is a typical compilation for the various arm materials evaluated. This is for the gear-drum deployment system concept (originally gear-sprocket). The components of the system evaluated to obtain a total structural system weight are:

- Arms, including end fittings
- Control system
- Spreader bar
- Array storage roller
- Support structure

It should be noted that drive motor and gear train are not included.

2.3.2.1 Arm Study (arms only)

The arm weight is a function of arm material, array width and preload tension. Since the array area is a fixed quantity, its length, and therefore the total arm length, decreases with an increase in width. The lengths of the long arm segments were established as approximately 100", or the width of the spacecraft mounting surface. The First Quarterly Report indicated arm segment length as a parameter, but later analysis of structures required to support arm much longer than the spacecraft envelope showed them to be excesively heavy.

Parameters

Materials - aluminum, steel, titanium, beryllium , boron epoxy and graphite/epoxy composites mechanical parameters are:

Material	F_{cy} (KSI)	E (PSI x 10^{-6})	Wgt. Density (lb./in^3)	ǂ Thickness (in)
Aluminum	66	10.3	0.10	0.012
St. Steel	230	29	0.28	0.008
Titanium	152	16	0.16	0.008
Beryllium	50	40	0.067	0.020
Boron/epoxy lam.	115*	35 **	† 0.075	0.010
Graphite/epoxy lam.	100*	30 **	† 0.045	0.015

* F_{tu} There is no F_{cy} since the stress-strain diagram is essentially a straight line to ultimate.

** For a 15^{o} half-angle layup.

† Densities used in the study were 0.095 and 0.055 for the boron graphite composites respectively. The later, and more correct densities shown in the chart became known after the study was completed.

ǂ Considered as practical minimums. Two plies were assumed for the composites. The faces of the square tube are corrugated to preclude local buckling below the allowable column stress.

Load Analysis

Maximum bending and column loads occur in the arm segments at initial deployment and reduce to very small column loads, equal to the array tension when the arm is fully deployed. The general load analysis for this initial deployment attitude is shown in Figure 2.3.12.

The preliminary strength analysis presented in the First Quarterly Report was predicated upon the arm segments loaded as cantilever beam-columns subjected to a column load and an end transverse shear load. A more exact load analysis of the multi-segment arm indicates that the loads induced in the outboard arm elements are less than computed in the original analysis, but increase from element to element; reaching a maximum in the element attached to the spacecraft. This refined load analysis, shown in Figure 2.3.12, indicates that the arm segments are loaded as cantilever beam-columns subjected to a column load, an end transverse shear

REPORT NO. | FAIRCHILD HILLER SPACE SYSTEMS DIVISION | PAGES | PAGE

MODEL | PREPARED BY BONTYA | CHECKED BY | APPROVED BY

DATE 20 DEC 1967

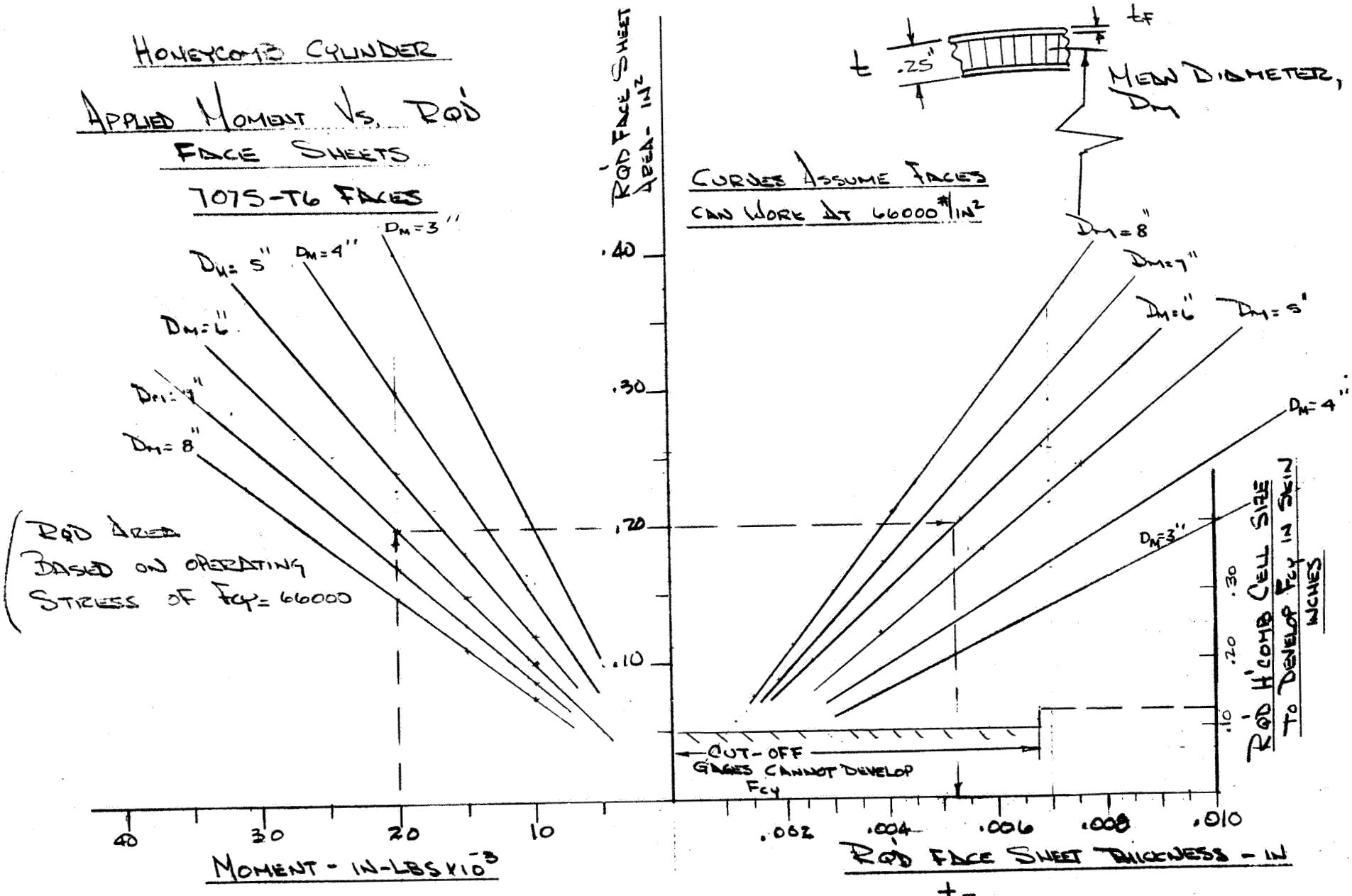
SUBJECT FOLDING ARM WEIGHT SUMMARY

REVISED

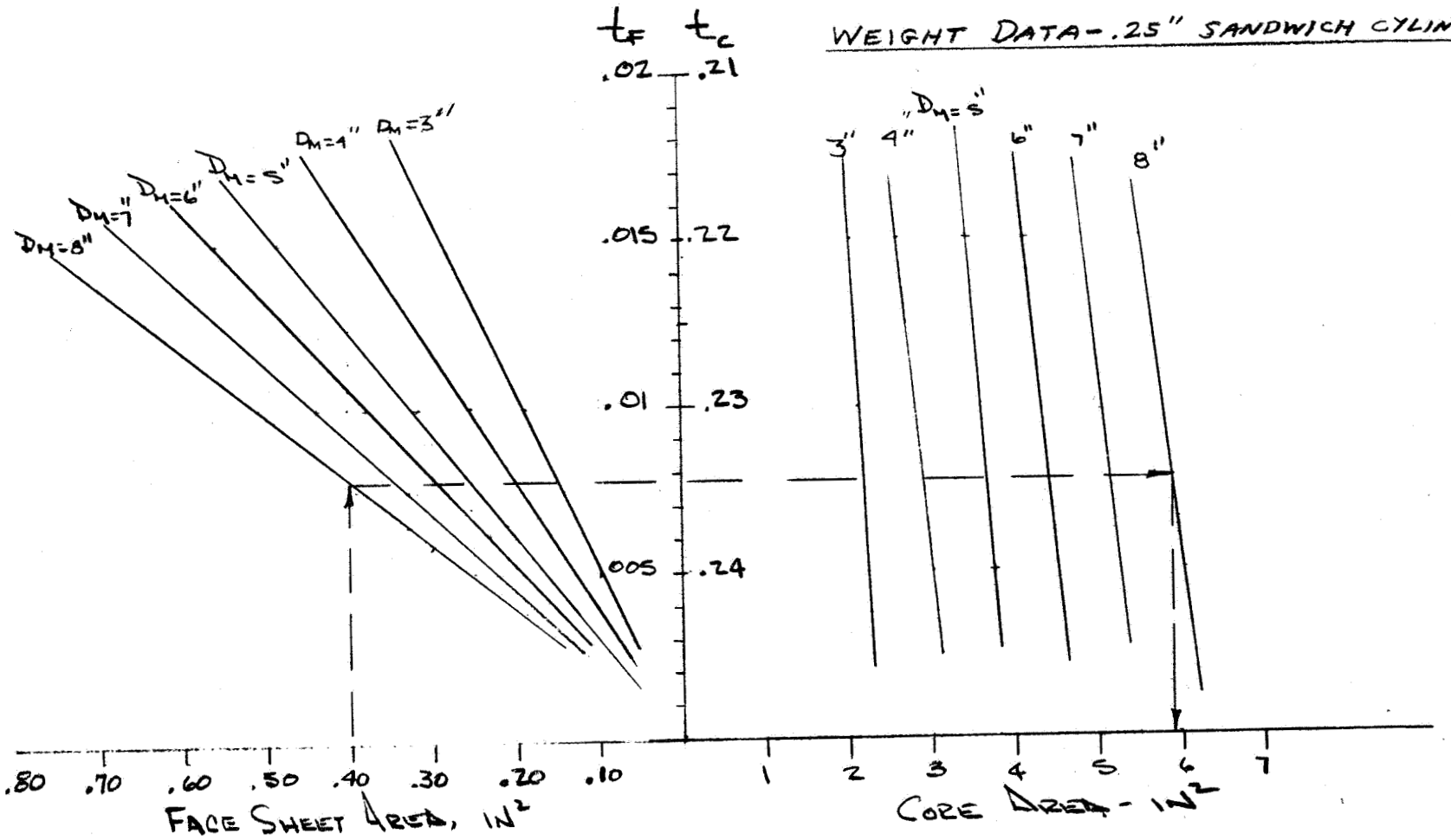
BORON COMPOSITE ARM - STRUCTURAL SYSTEM WGT

	ARRAY T-5#			10#			15#			20#		
	ARRAY WIDTH			6	8	10	6	8	10	6	8	10
	6 FT	8	10									
ARMS	5.16	3.91	3.26	5.34	4.00	3.26	5.94	4.40	3.26	6.18	4.72	3.36
END FITTINGS	1.58	1.13	1.13	1.71	1.27	1.13	2.12	1.41	1.13	2.45	1.63	1.22
CONTROL SYS.	7.61	4.17	3.23	12.63	7.04	5.69	17.94	9.41	7.83	23.34	12.30	10.19
SPREADER BAR	.77	1.00	1.24	.80	1.02	1.24	.88	1.11	1.24	.93	1.17	1.28
STORAGE ROLLER	.69	.96	1.30	.69	.96	1.30	.69	.96	1.30	.69	.96	1.30
SUPPORT STRUCT.	6.00	6.00	12.50	6.00	6.00	12.50	6.00	6.00	12.50	6.00	6.00	12.50
Σ	21.81	17.17	22.66	27.17	20.29	25.12	33.57	23.49	27.26	39.59	26.78	29.85

TABLE 2.3.2



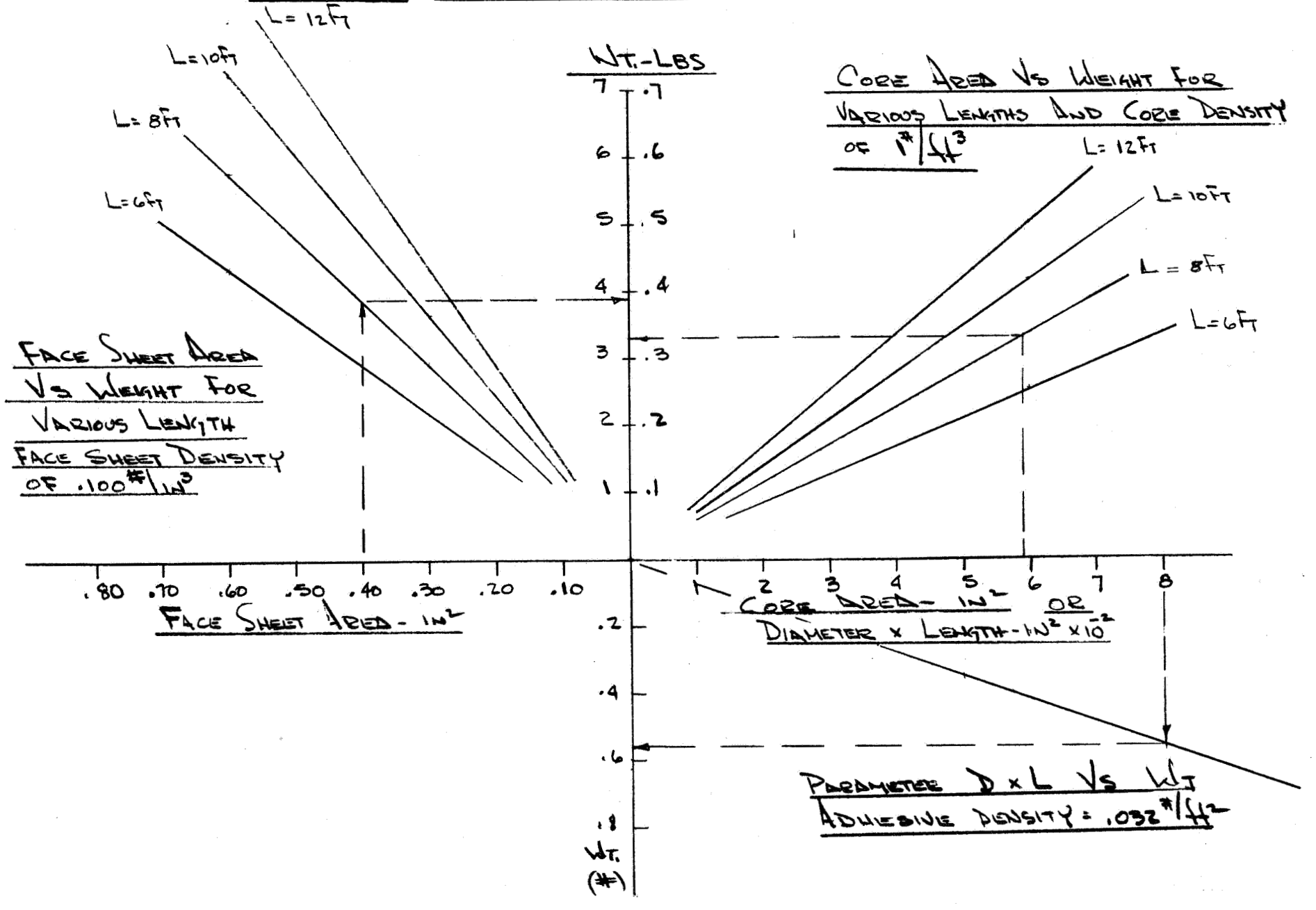
HONEYCOMB CYLINDER DESIGN DATA
FIGURE 2.3.7



FACE SHEET AREA VS FACE SHEET THICKNESS FOR VARIOUS DIAMETERS — COMPATIBLE CORE THICKNESS AND CORE AREA - .25" SANDWICH.

FIGURE 2.3.8

FIGURE 23.9 WEIGHT DATA – .25 IN HONEYCOMB CYLINDER



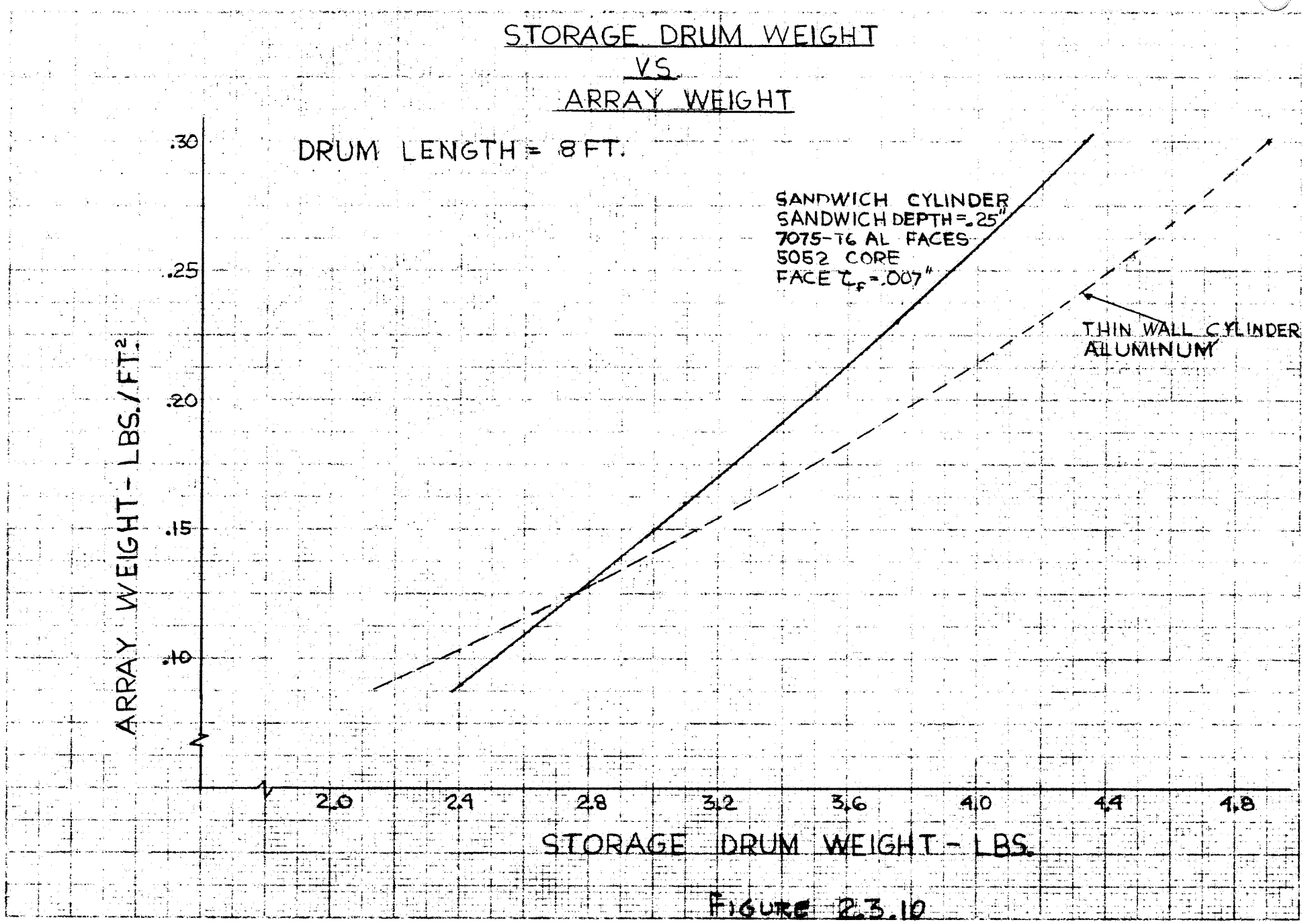

STORAGE DRUM WEIGHT
VS.
ARRAY WEIGHT
DRUM LENGTH = 8 FT.
SANDWICH CYLINDER
SANDWICH DEPTH = .25"
7075-T6 AL FACES
5052 CORE
FACE t_f = .007"
THIN WALL CYLINDER
ALUMINUM
ARRAY WEIGHT - LBS./FT.²
.30
.25
.20
.15
.10
2.0
2.4
2.8
3.2
3.6
4.0
4.4
4.8
STORAGE DRUM WEIGHT - LBS.

FIGURE 2.3.10

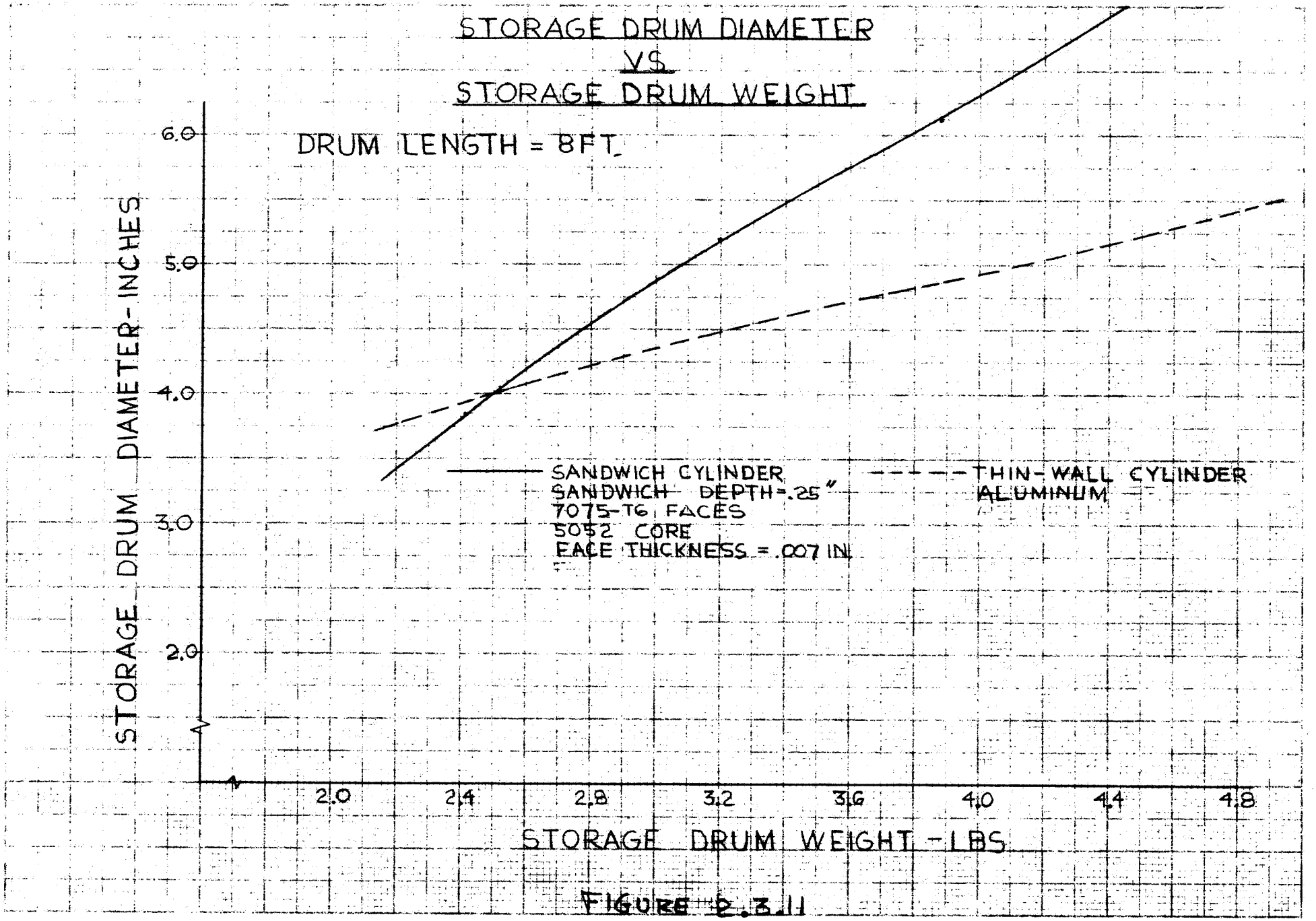
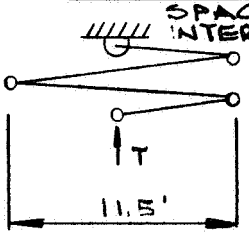
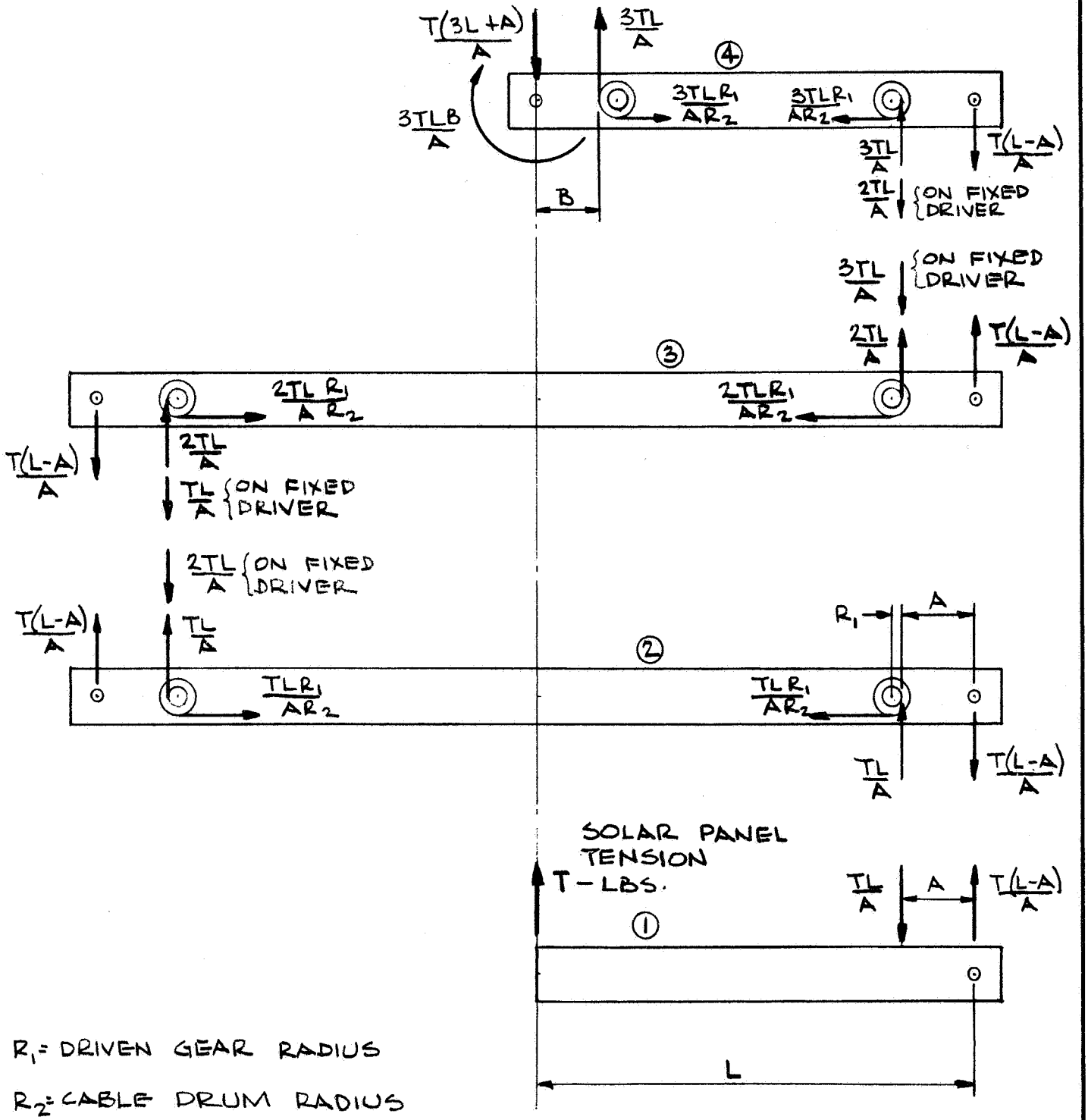

STORAGE DRUM DIAMETER
VS
STORAGE DRUM WEIGHT
DRUM LENGTH = 8FT.
STORAGE DRUM DIAMETER - INCHES
6.0
5.0
4.0
3.0
2.0
SANDWICH CYLINDER
SANDWICH DEPTH=.25"
7075-T6 FACES
5052 CORE
FACE THICKNESS = .007 IN.
THIN-WALL CYLINDER
ALUMINUM
2.0
2.4
2.8
3.2
3.6
4.0
4.4
4.8
STORAGE DRUM WEIGHT - LBS

FIGURE 2.3.11



FOLDING ARM – LOAD ANALYSIS

FIGURE 2.3.12



R_1 = DRIVEN GEAR RADIUS

R_2 = CABLE DRUM RADIUS

load and an end moment.

Figure 2.3.13 through 2.3.15 present the result of the parametric study for arm weights. The following analysis is typical of those studies conducted to derive these figures:

Material - Beryllium

Array width = 8 ft.

T = Array tension = 10 lbs limit = 12.5 lb. ult.

Number of segments = 5

L = Short arm length = 4.3 ft. = 51.6 in.

t = Wall thickness = 0.020 in.

From the system load analysis, Figure 2.3.12

Column load (cable load), $P = \frac{3\,TL\;R_1}{AR_2}$

(Maximum load in long arm of 5 segment system)

Gearing geometric ratios are assumed constant for all systems and are referenced to the original baseline design for a 4.0" square tube.

Baseline reference dimensions:

H = 4.0 in (tube size)

A = 2.4 in = sun gear radius = $2.4 \times \frac{H}{4}$ = .6H

R_1 = 1.1 in. = planetary gear radius

R_2 = 1.6 in. = drum pitch radius

Geometric constant, $C = \frac{R_1}{AR_2} = \frac{1.1}{.6H\,(1.6)} = 1.145/H$

P = 3 TL (1.145/H)

By iteration, H was obtained as 2.05 in.

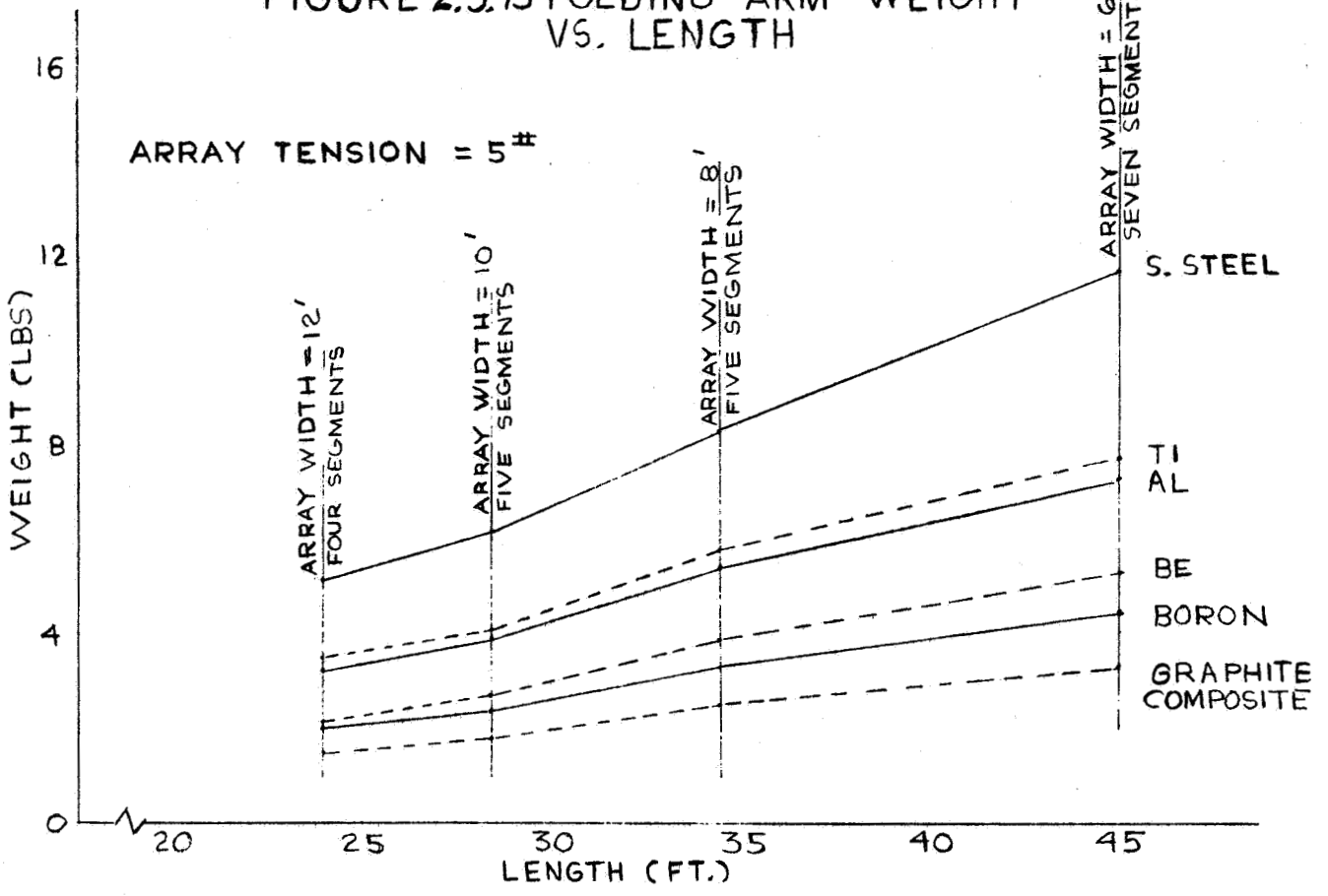
P = 3 (12.5) (51.6) (1.145) / 2.05 = 1082#

Tube area = 4 H t = 4 (2.05) (.020) = .164 in.^{2}

f_c = 1082/.164 = 6600 psi

From Euler's column equation,

FIGURE 2.3.13 FOLDING ARM WEIGHT VS. LENGTH



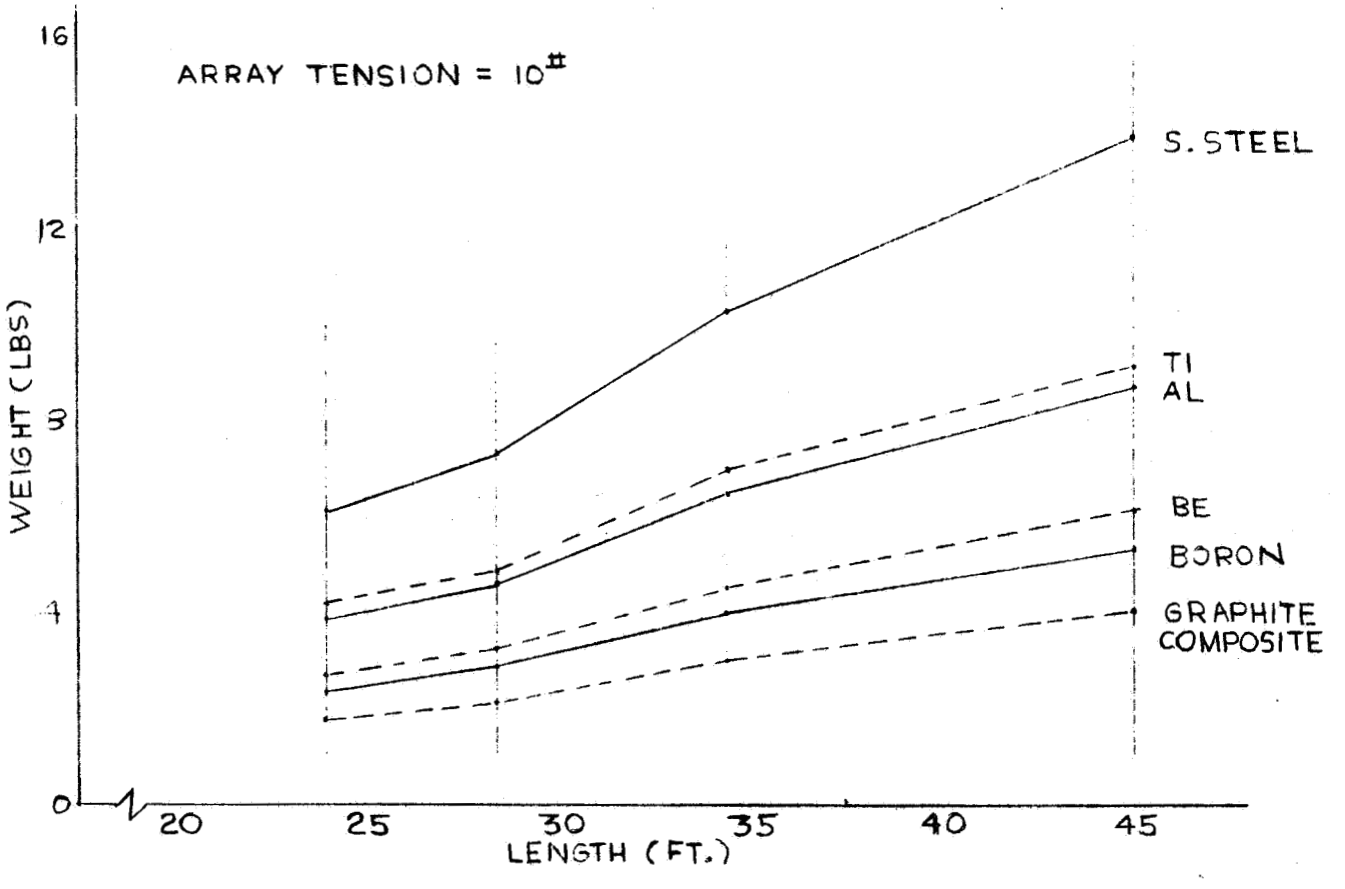
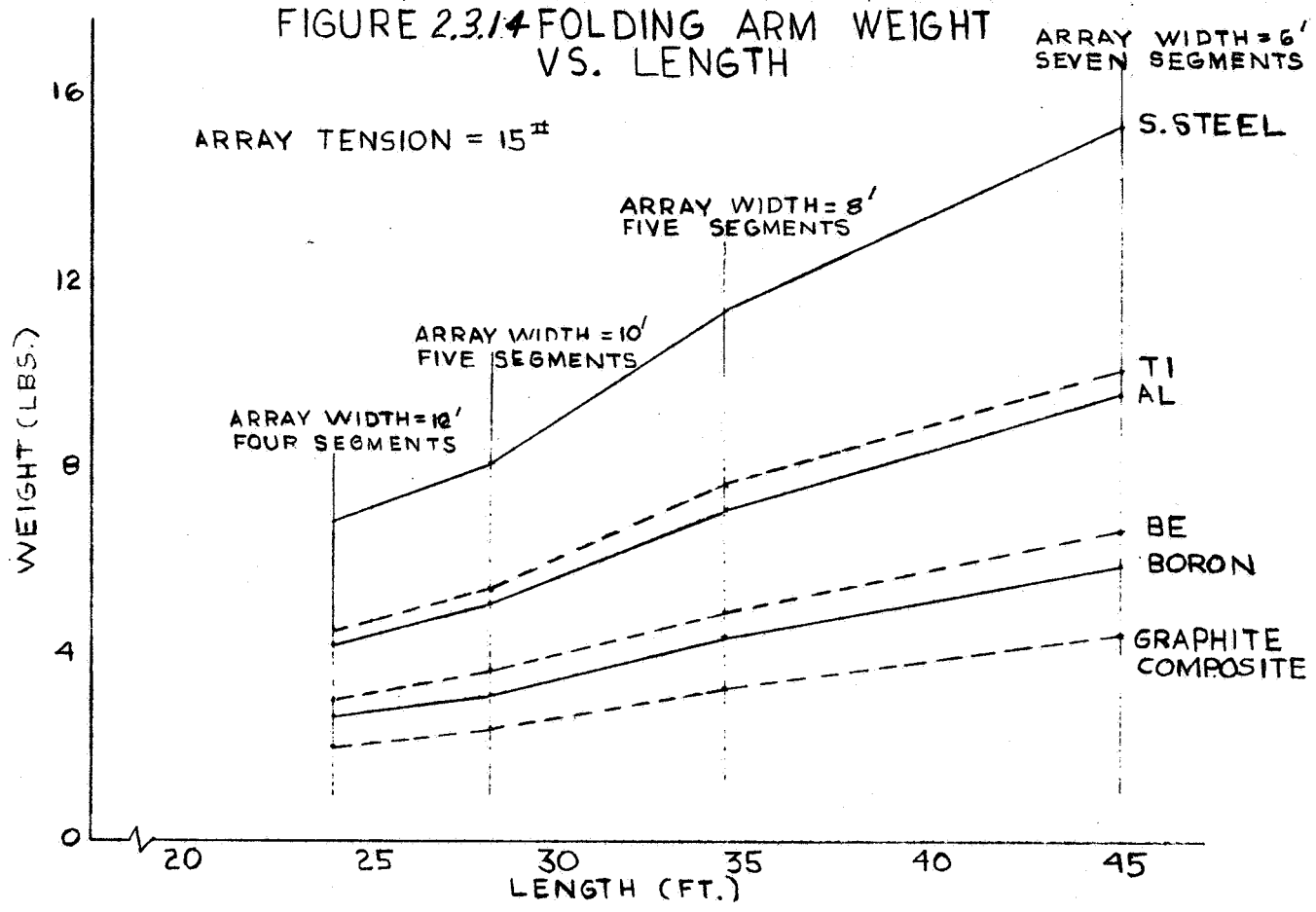


FIGURE 2.3.1-4 FOLDING ARM WEIGHT VS. LENGTH



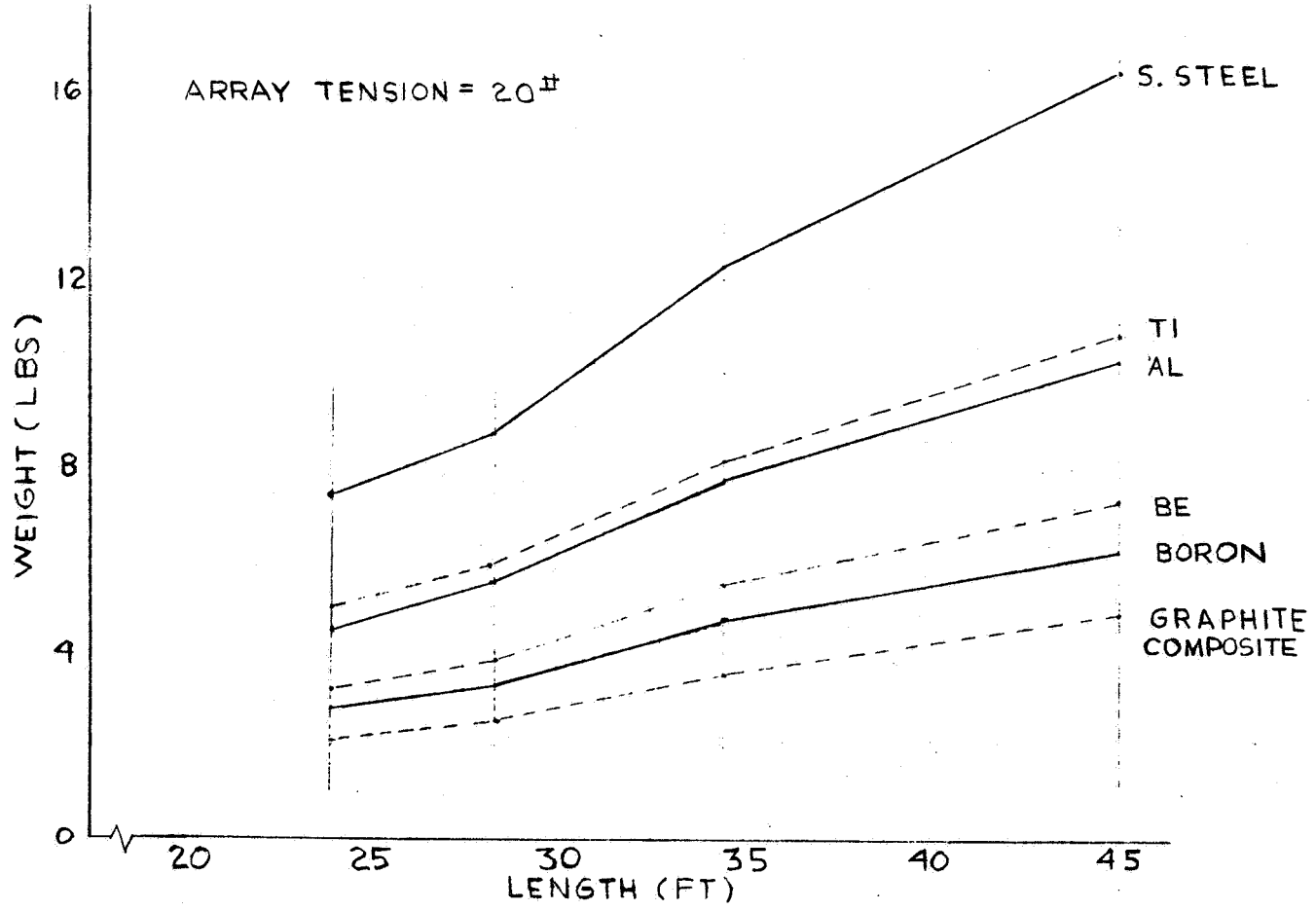
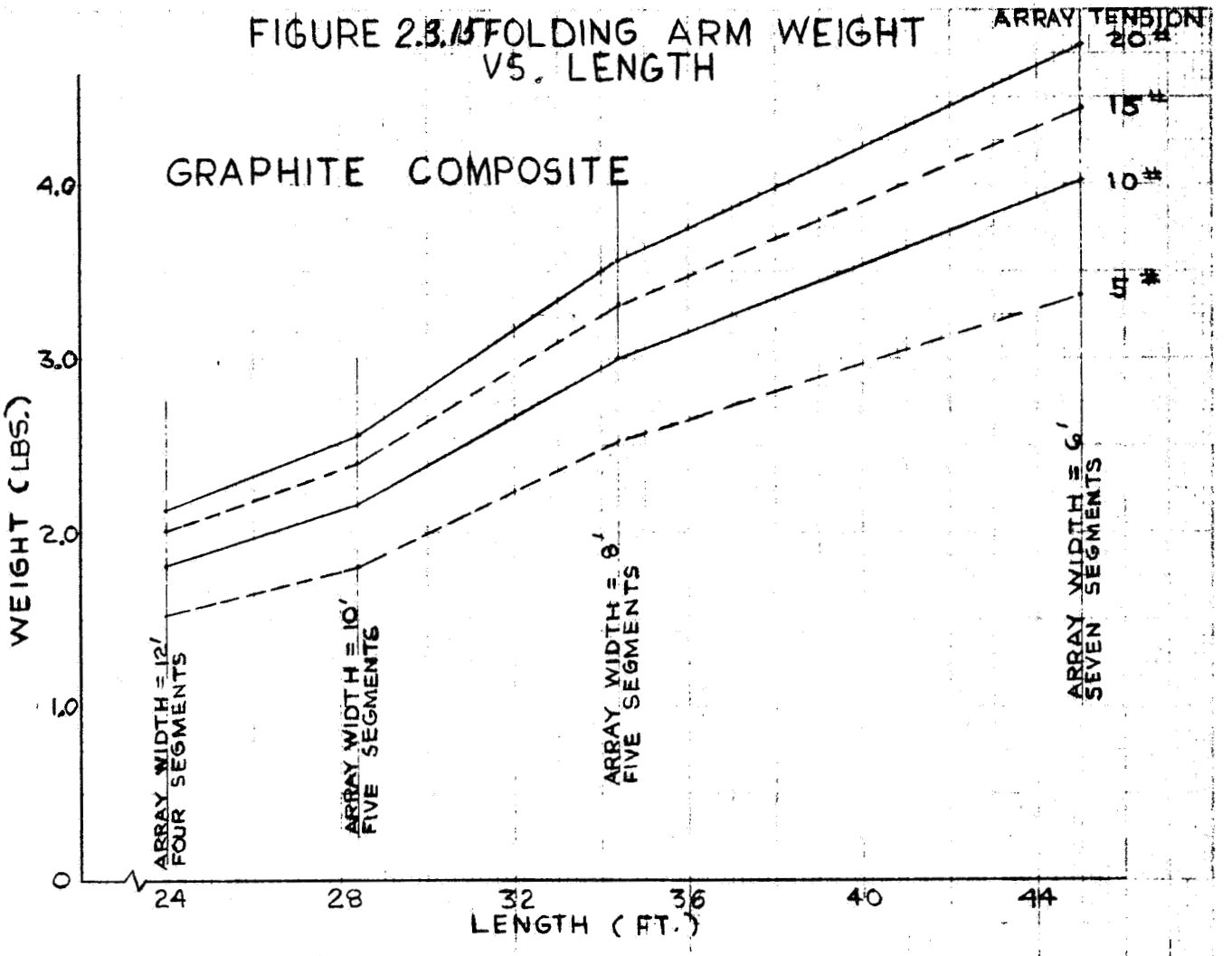


FIGURE 2.3.15 FOLDING ARM WEIGHT VS. LENGTH



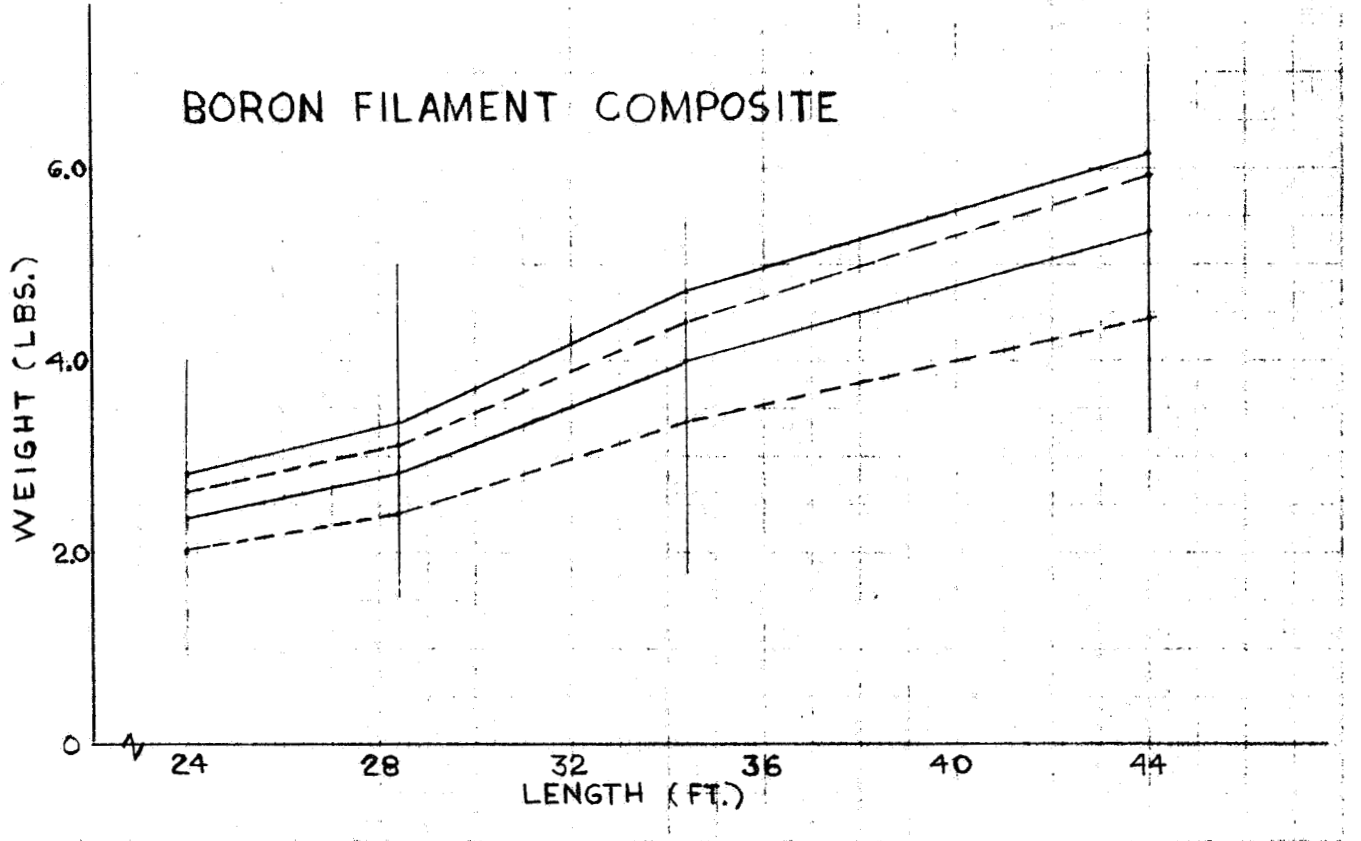
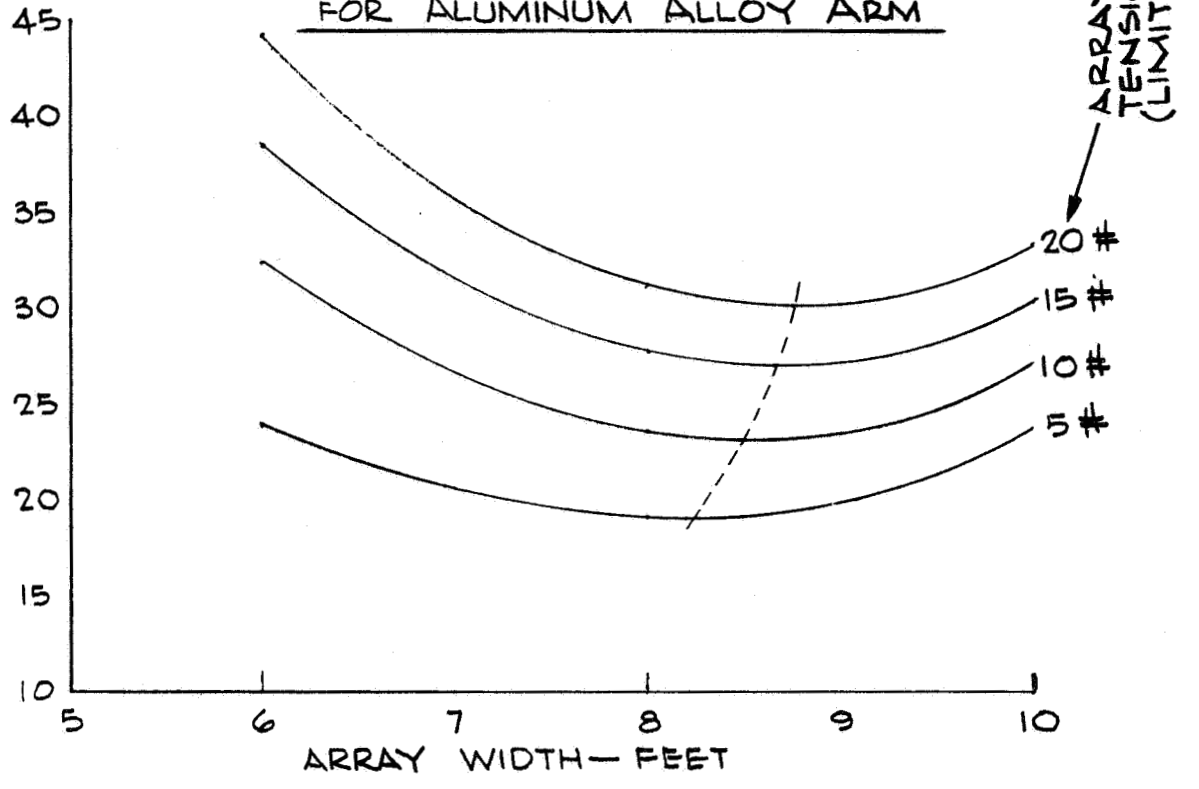


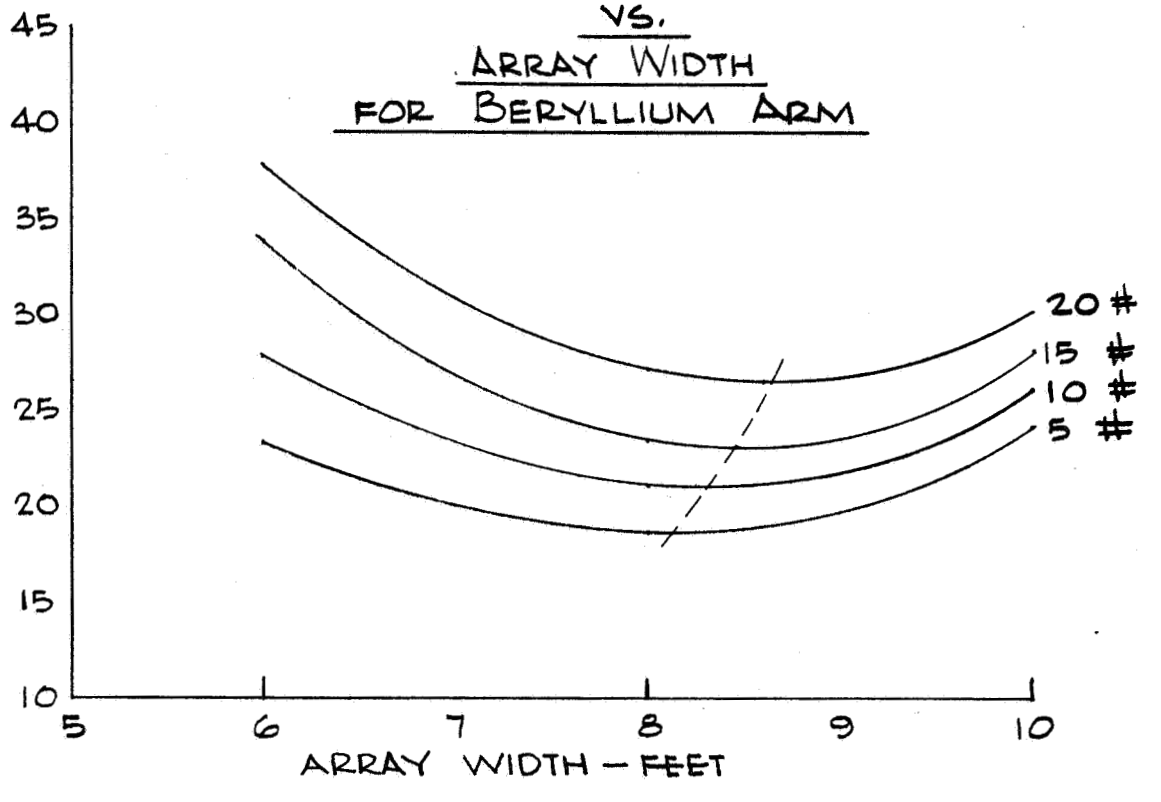
FIGURE 2.3.16

STRUCTURAL SYSTEM WEIGHT* VS. ARRAY WIDTH FOR ALUMINUM ALLOY ARM



ARRAY UNIT WEIGHT = 0.23 LBS./FT.^{2}

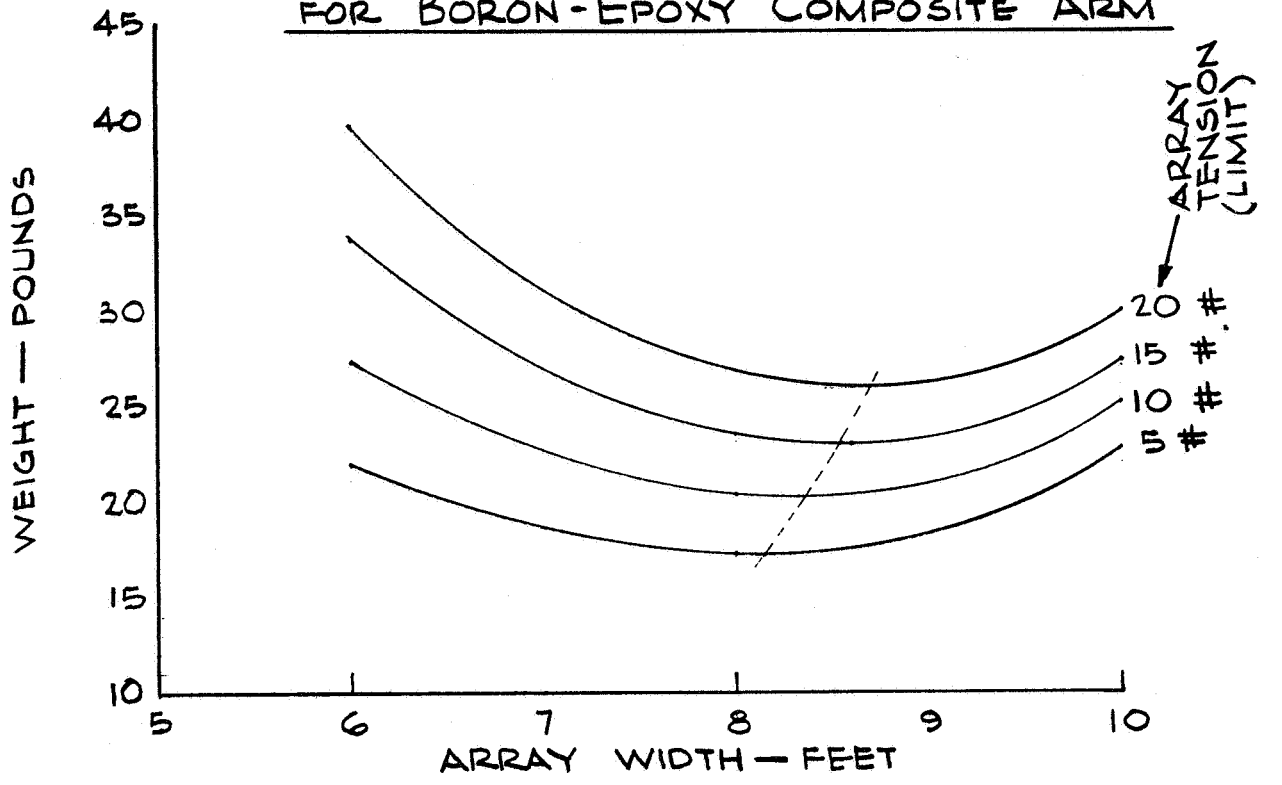
STRUCTURAL SYSTEM WEIGHT VS. ARRAY WIDTH FOR BERYLLIUM ARM



* TOTAL SYSTEM WEIGHT LESS DRIVE MOTOR, GEAR TRAIN & SOLAR ARRAY WEIGHTS.

FIGURE 2.3.17

STRUCTURAL SYSTEM WEIGHT VS. ARRAY WIDTH FOR BORON-EPOXY COMPOSITE ARM



ARRAY UNIT WEIGHT = 0.23 LBS./FT.^{2}

STRUCTURAL SYSTEM WEIGHT VS. ARRAY WIDTH FOR GRAPHITE-EPOXY COMPOSITE ARM

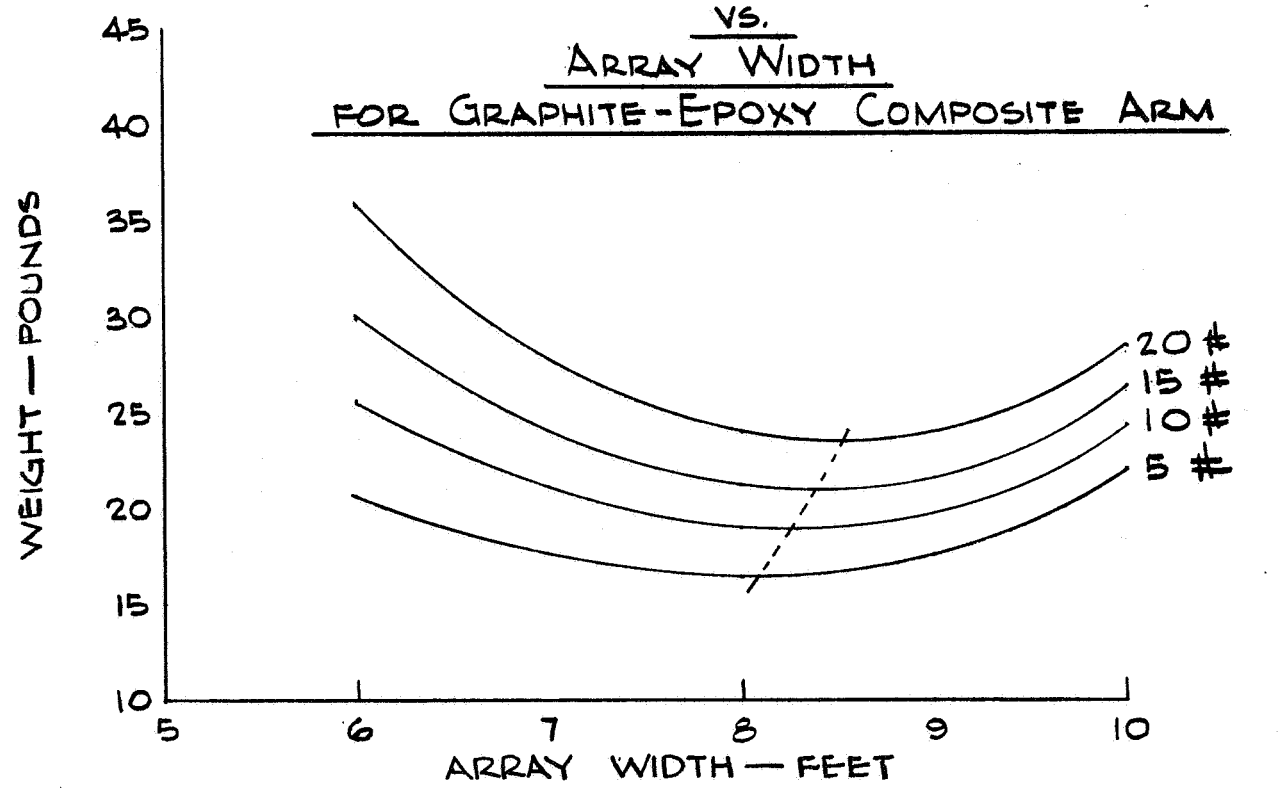
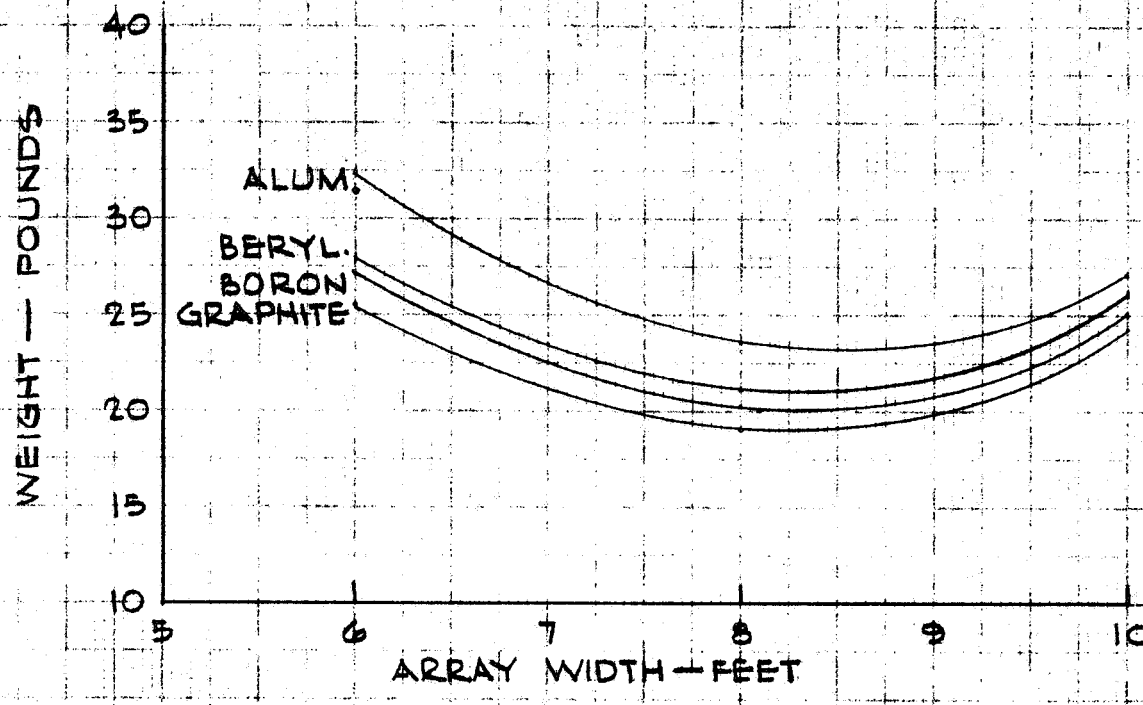


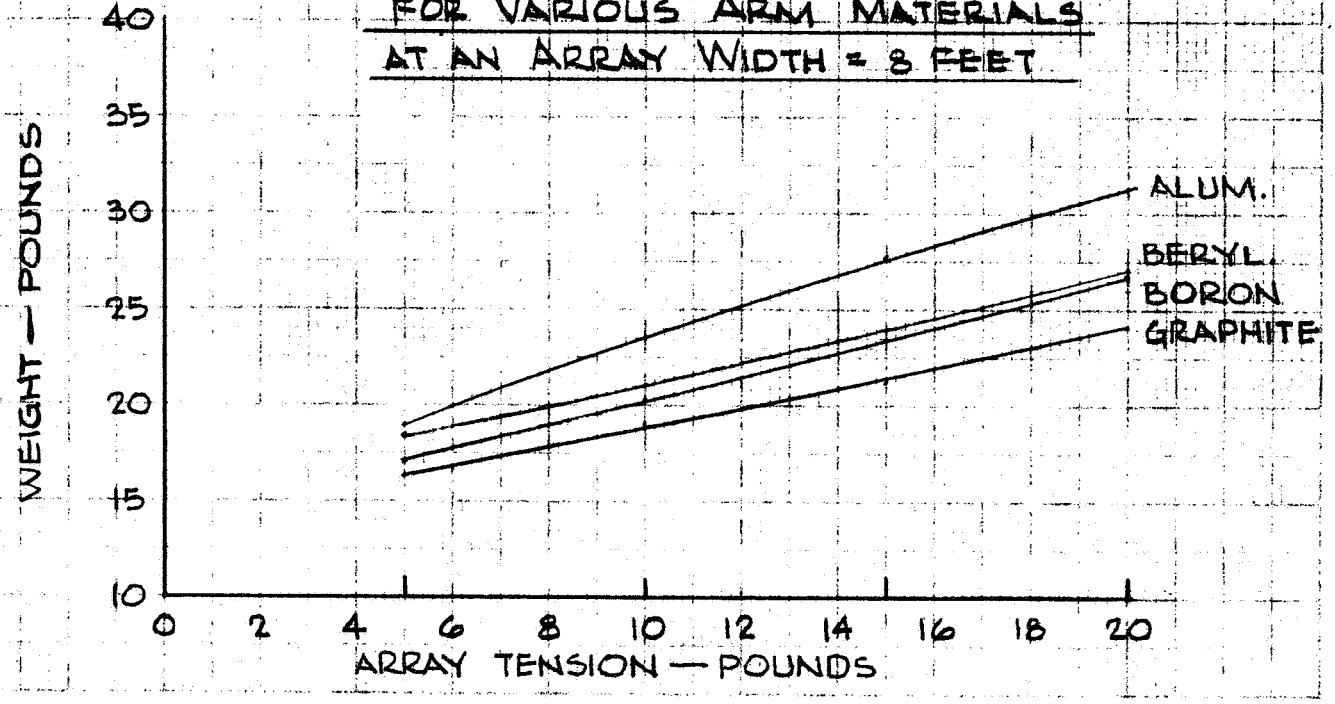
FIGURE 2.3.18

STRUCTURAL SYSTEM WEIGHT VS. ARRAY WIDTH FOR VARIOUS ARM MATERIALS AT AN ARRAY TENSION = 10



ARRAY UNIT WEIGHT = 0.23 LBS./FT.^{2}

STRUCTURAL SYSTEM WEIGHT VS. ARRAY TENSION FOR VARIOUS ARM MATERIALS AT AN ARRAY WIDTH = 8 FEET



$F_{col} = \pi^2 E/4 (L/\rho)^2 = 6800$ psi

M. S. = (6800/6600) -1 = + 0.03

Total arm length = 4 (12) (8.6) = 413 in.

Material volume = .164 (413) = 67.8 $in.^3$

Tube weight = .067 (67.8) = 4.55 lb.

2.3.2.2 Control System Weight Analysis

A typical folding arm control system weight summary is presented in Table 2.3.3.

The weights of individual control system elements are a function of array tension; array width; arm segment materials; the material of the control system element; and control system geometry.

Dimensions of parts for tube sizes determined in Section 2.3.2.1, (e.g., gear diameters) were defined as a function of the original baseline design for a 4.0 square tube.

With these relationships, general weight equations were derived for the primary components of the control system and are presented herein.

Pertinent baseline reference dimensions, Figure 2.3.12:

H = 4.0 in (tube size)

A = 2.4 in = 0.6H (labeled "A" in Figure 2.3.12)

R_1 = 1.1 in.

R_2 = 1.6 in.

Geometric constant, $C = \frac{R_1}{AR_2} = \frac{1.1}{.6H\,(1.6)} = 1.145/H$

These data will be referred to in the various detail analyses presented in this section.

Shaft Hinge

The equation used to determine the weight of the shaft hinges was derived by considering the folding arm segment as essentially being loaded in double shear.

FAIRCHILD HILLER

REPORT NO. | PAGES | PAGE

MODEL | PREPARED BY | CHECKED BY | APPROVED BY

DATE

SUBJECT FOLDING ARM — CONTROL SYSTEM WEIGHT SUMMARY

REVISED

BORON COMPOSITE ARM TABLE 2.3.3

	5#			10#			15#			20#		
	6 FT	8	10	6	8	10	6	8	10	6	8	10
SHAFT HINGE	.08	.06	.05	.09	.06	.06	.10	.07	.06	.10	.07	.06
CABLE	1.11	.61	.45	1.86	1.11	.82	2.28	1.42	1.13	3.08	1.69	1.35
DRUM	.84	.35	.26	1.17	.75	.55	2.45	.85	.68	2.83	1.76	1.39
DRUM SHAFT	.69	.38	.30	1.29	.71	.55	1.86	1.00	.77	2.35	1.28	1.00
GEAR - PLANET.	.91	.53	.43	1.54	.87	.68	2.16	1.16	.96	2.71	1.47	1.20
GEAR - FIXED	2.47	1.23	1.07	4.81	2.53	2.02	7.22	3.67	2.99	9.45	4.79	3.95
CABLE FTGS. - TI	1.51	1.01	.67	1.87	1.01	1.01	1.87	1.24	1.24	2.82	1.24	1.24
Σ	7.61	4.17	3.23	12.63	7.04	5.69	17.94	9.41	7.83	23.34	12.30	10.19

$$F_{SU} = \frac{P}{2A} \qquad A = \frac{P}{2F_{SU}}$$

$$W = \text{WEIGHT} = AH\rho\,(N-1) = \frac{PH\rho(N-1)}{2F_{SU}}$$

Where $P = \frac{T(L-a)}{a} \approx \frac{TL}{a} = \frac{TL}{.6H}$

H = Square tube size, in. (shaft length)

T = Array tension, lb.

N = Number of arm segments

ρ = Material density, lb./in.^{3}

F_{SU} = Material allowable shear stress

$$W = \frac{TLH\,\rho\,(N-1)}{.6H\,(2)\,(F_{SU})} = \frac{TL\,\rho\,(N-1)}{1.2\,F_{SU}}$$

For: L = 50 in. - Approx. constant for all arm systems

ρ = .16 #/in^3 for titanium

F_{SU} = 98,500 PSI

$$W = \frac{T\,(50)\,(.16)\,(N-1)}{1.2\,(98500)} = \frac{T\,(N-1)}{14,800}$$

Cable

Music wire was selected for minimum weight and minimum cable stretch. To insure adequate safety of personnel, an ultimate factor of safety of 1.5 (in lieu of 1.25) is used. The equation for total cable weight was derived to be:

$$P_{\text{cable (max)}} = \frac{(N-1)\,TLR_1}{AR_2} \qquad \text{(Ref. Figure 2.3.12)}$$

Where

N = Number of arm segments

Then

$$P = CTL\,(N-1) = \frac{1.145\,TL\,(N-1)}{H}$$

$$\text{Cable Area, } A = \frac{P}{F_{TU}} = \frac{1.145\ TL\ (N-1)}{H\ F_{TU}}$$

$$\text{Cable Weight, } W = (\ell)\ (N-1.5)\ (2)\ \rho$$

$$= \frac{1.145\ TL\ (N-1)}{H\ F_{TU}} \qquad \left[\ell\ (N-1.5)\ (2)\ \rho\right]$$

As $\ell = 2\ L$ and $\rho = .3$ lb./in^3,

$$\text{Weight, } W = \frac{1.38\ (N-1)\ (N-1.5)\ TL^2}{H\ F_T}$$

Where

T = Array tension, lb.

H = Segment arm cross-section dimension, in.

F_T = Cable material allowable tension stress, psi

N = Number of Segments

Cable Drum

Cable drum material is aluminum. Sizing is dictated by geometry (drum pitch diameter required for system motion) and space requirements to store the cables during array deployment and retraction. The original drum was sized for the baseline configuration defined earlier. Weight was then varied with drum diameter.

Drum Shaft

The drum shaft is loaded in bending and torque. Sizing was based on the stress ratio relationship of $R_b + R_s^2 = 1.0$ where R_b is the stress ratio in bending and R_s is the stress ratio in shear. Early analyses indicated R_b and R_s^2 to be approximately equal to 0.50. Analysis was then simplified using $R_b = 0.50$ and neglecting R_s^2.

The equation derived for drum shaft weight was:

$$P_{\text{max. cable LD.}} = CTL\ (N-1) = \frac{1.145\ TL\ (N-1)}{H}$$

$$M = \frac{P\ell}{4} = \frac{PH}{4} = \frac{1.145\ TL\ (N-1)\ (H)}{4H} = .286\ TL\ (N-1)$$

$$\frac{f_b}{F_b} = .50 = \frac{M_c}{IF_{tu}} = \frac{32M}{\pi D^3 F_{tu}}$$

$$D = \left(\frac{64M}{\pi\ F_{tu}}\right)^{1/3} = \left[\frac{64\ (.286)\ TL\ (N-1)}{\pi\ F_{tu}}\right]^{1/3}$$

$$= 1.8 \left[\frac{TL\ (N-1)}{F_{tu}}\right]^{1/3}$$

$$W = \text{Weight} = \frac{\pi D^2}{4}\ .H\rho\ (N-1)\ (2)$$

$$= 5.1H\ \rho (N-1) \left(\frac{TL\ (N-1)}{F_{tu}}\right)^{2/3}$$

T = Array tension, lbs.

H = Arm segment cross-section dimension, in.

ρ = Material density

N = Total number of arm segments

F_{tu} = Drum shaft materials allowable tension stress, PSI

Planetary and Fixed Gears

Sets of steel planetary and fixed spur gears are located at the ends of the arm segments. Rim size was based on the Lewis formula for spur gears and the web designed as a non-buckled shear web.

Cable Fittings

The cable turnbuckles are standard aircraft turnbuckle dimensionally, but are made of titanium.

2.3.2.3 Arm End Fittings

The loads acting on this member are small and minimum, practical, gages for fabricating were used. The fittings were assumed to be aluminum. The size and weight therefore, is a function of the arm size and number of arm segments.

2.3.2.4 Spreader Bar

Since the loads acting on this member are small, minimum gages were used. Material selected was beryllium. Spreader bar weight is then a function of the arm segment cross-section and length.

2.3.2.5 Support Structure

Preliminary analyses of the arm and array storage drum support structure, subjected to dynamic launch environment, indicated a minimum sheet metal design to be adequate. The heavier support structure for the 10 foot wide array (indicated in Table 2.3.3) was necessitated to support an array considerably wider than the 100 inch wide spacecraft mounting surface. An ell-shaped structure capable of sustaining torsion, in addition to shear and bending, was required.

2.3.3 Hingelock Support Beam - Parametric Studies

The hingelock concept was analyzed as a beam column subjected to solar array tension. Three materials, beryllium copper, titanium and steel, were evaluated. Boom weight for these materials, determined for boom lengths up to 45 feet and array tensions to 20 pounds, are shown in Figures 2.3.20 through 2.3.22, for the individual materials. Figure 2.3.23 compares the three materials for a nominal 10 pound array tension load.

Method of Analysis

The hingelock support boom was analyzed as a cantiliever beam-column subjected to an axial end load, a shear load and an end moment resulting from solar panel tension. This is graphically illustrated in Figure 2.3.19. The principle of superposition was used in deriving the equations for the shear load and end moment.

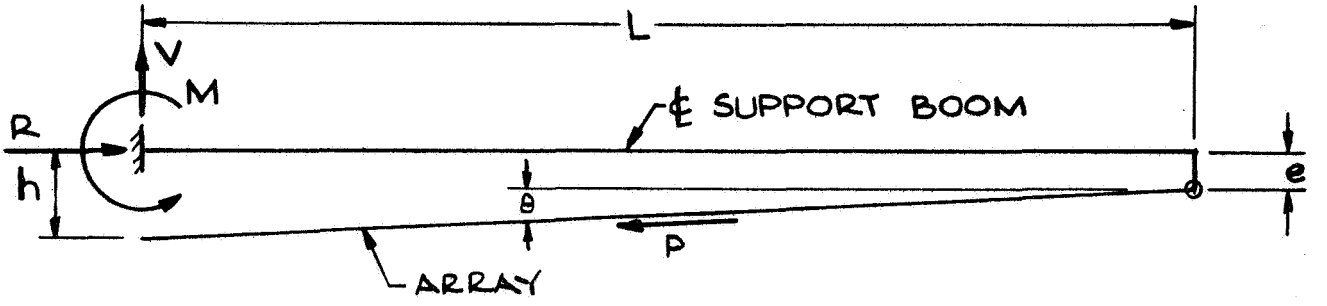
REPORT NO.	FAIRCHILD HILLER	PAGES	PAGE
MODEL	PREPARED BY BONTYA / CHECKED BY	APPROVED BY	

DATE 26 OCT 1967

SUBJECT 30 WAPSA HINGELOCK SUPPORT BOOM

REVISED

GEOMETRY FIGURE 2.3.19



L = SUPPORT BOOM EXTENDED LENGTH

e = ECCENTRICITY = $\frac{D}{2} + 1$

D = DIAMETER OF SUPPORT BOOM

h = OFFSET = 5.5 + e

$\theta = \tan^{-1} \frac{5.5}{L}$

P = ARRAY PRE-LOAD

R = P(COS θ) = P

V = P(SIN θ)

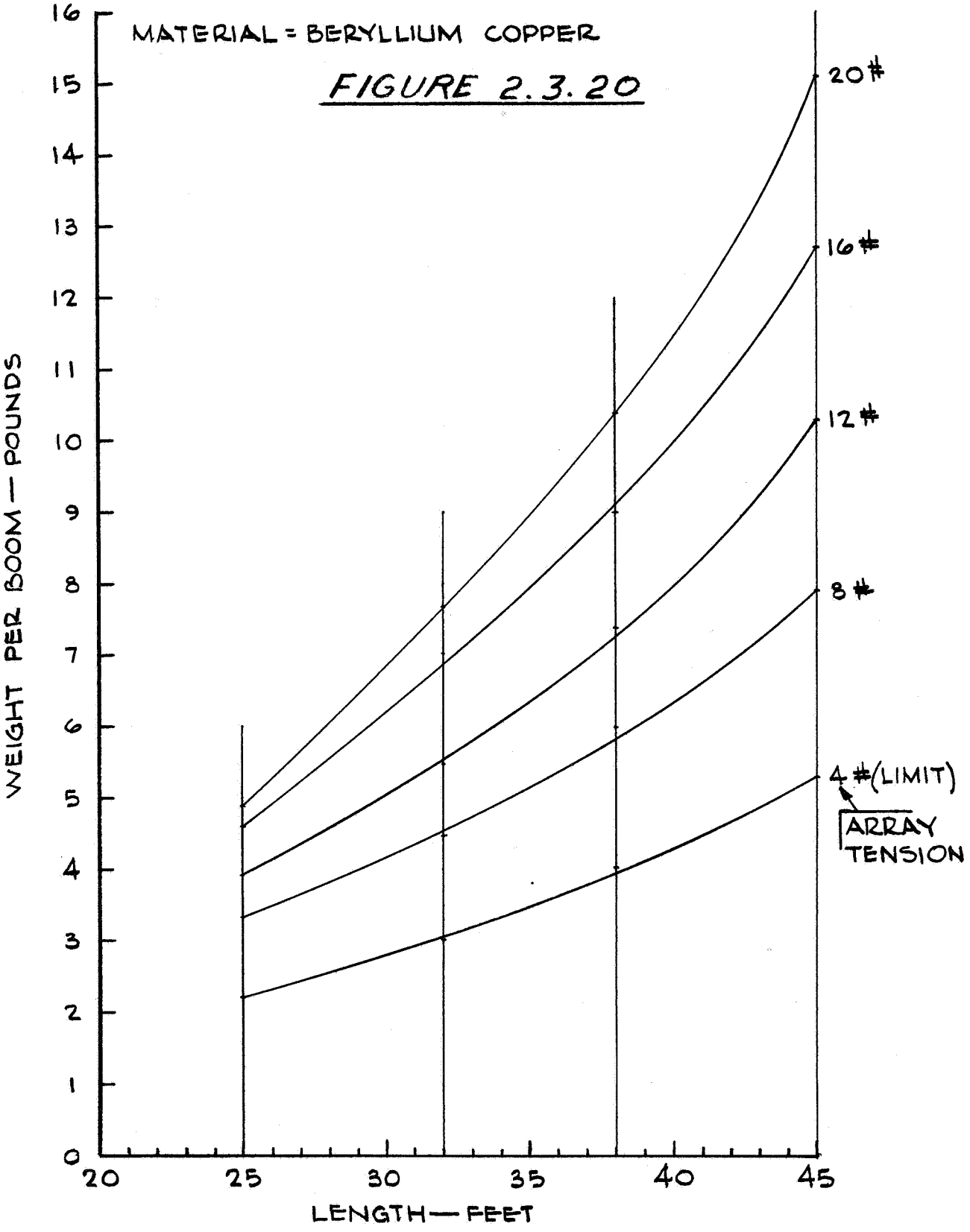
M = SUPPORT BOOM BASE MOMENT, INCLUDING BEAM-COLUMN EFFECT.

HINGELOCK SUPPORT BOOM

WEIGHT VS. LENGTH AT VARIOUS PRE-LOADS

MATERIAL = BERYLLIUM COPPER

FIGURE 2.3.20

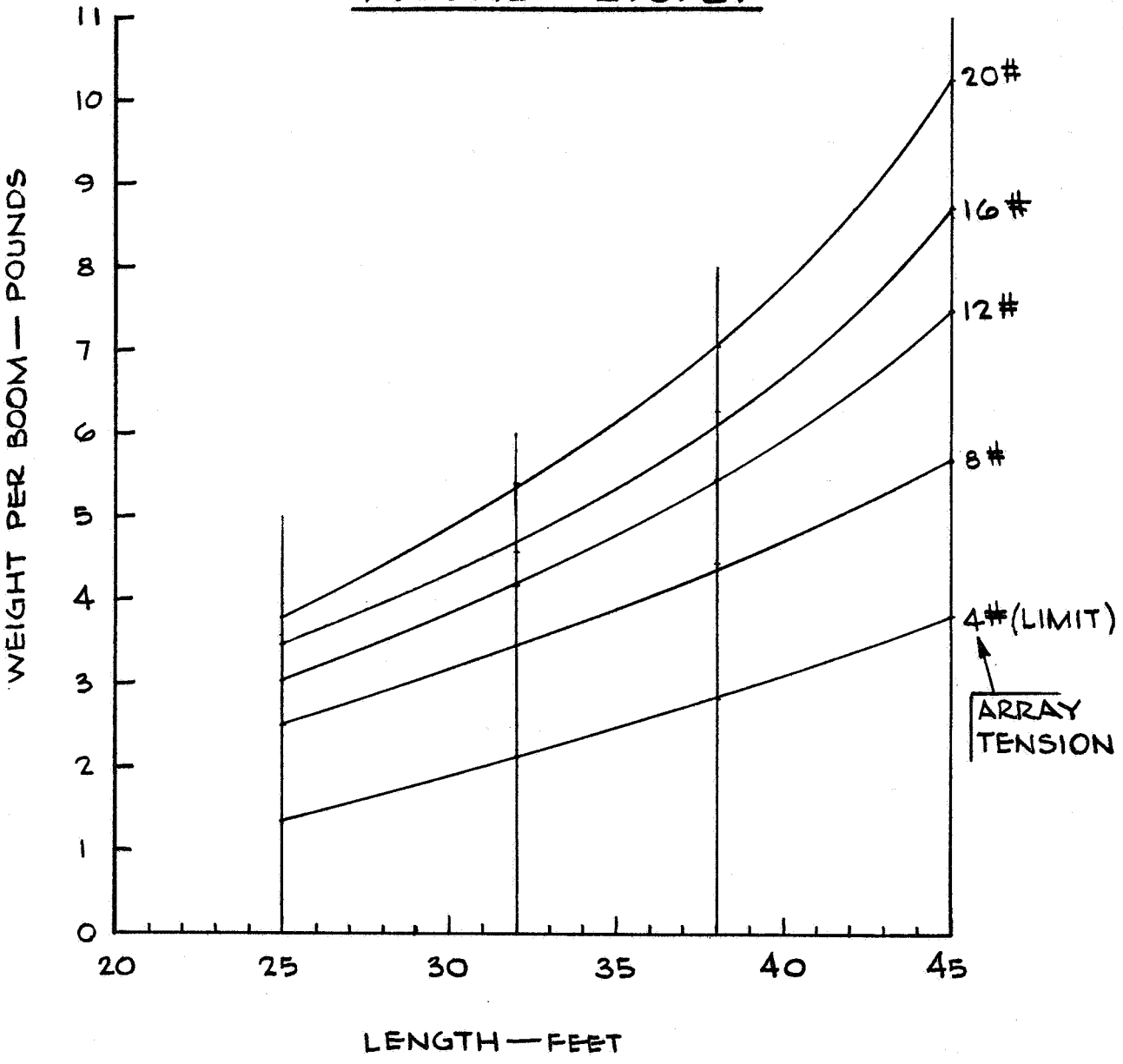


HINGELOCK SUPPORT BOOM

WEIGHT VS. LENGTH AT VARIOUS PRE-LOADS

MATERIAL = STEEL

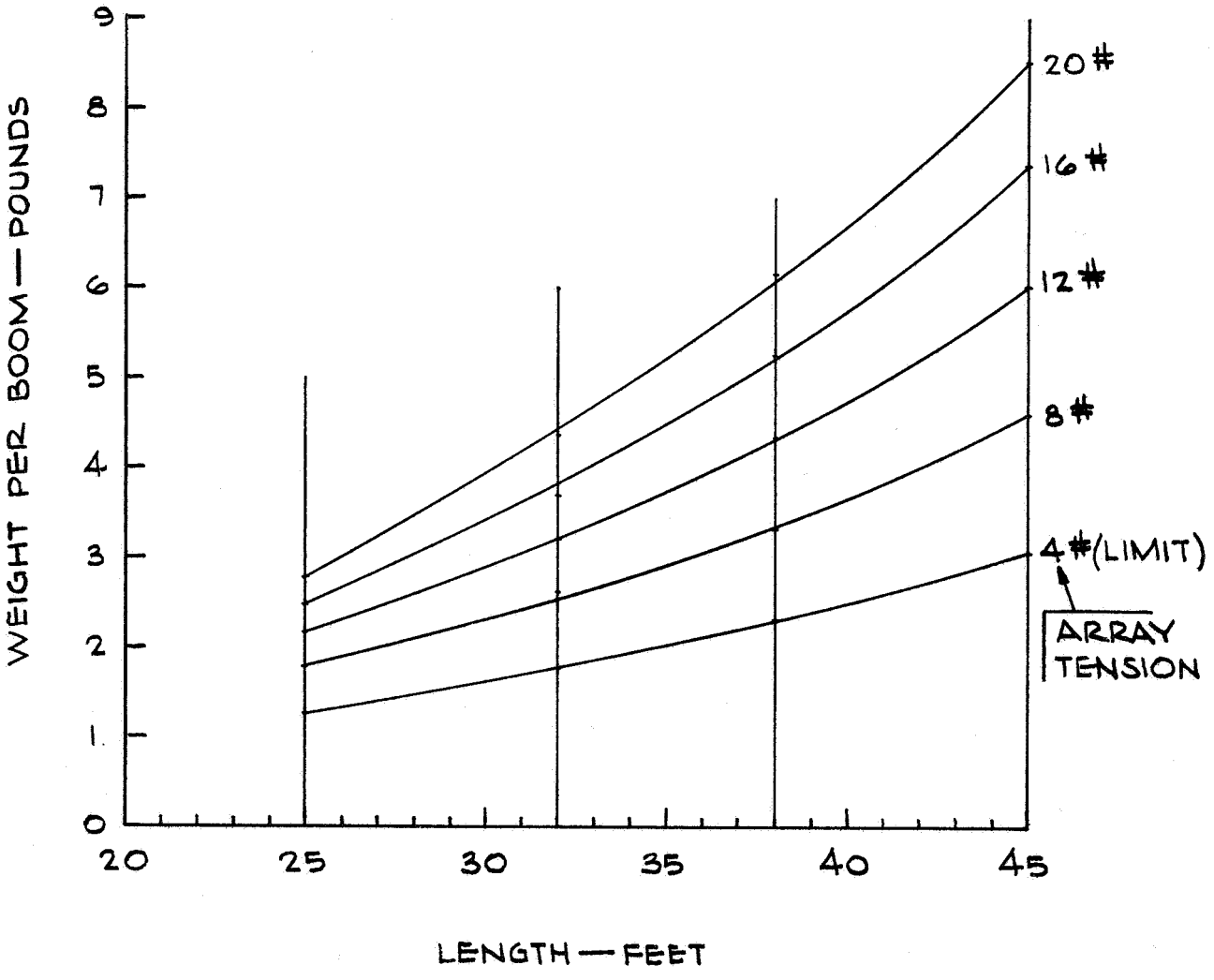
FIGURE 2.3.21



HINGELOCK
SUPPORT BOOM
WEIGHT VS. LENGTH
AT VARIOUS PRE-LOADS

MATERIAL = TITANIUM

FIGURE 2.3.22



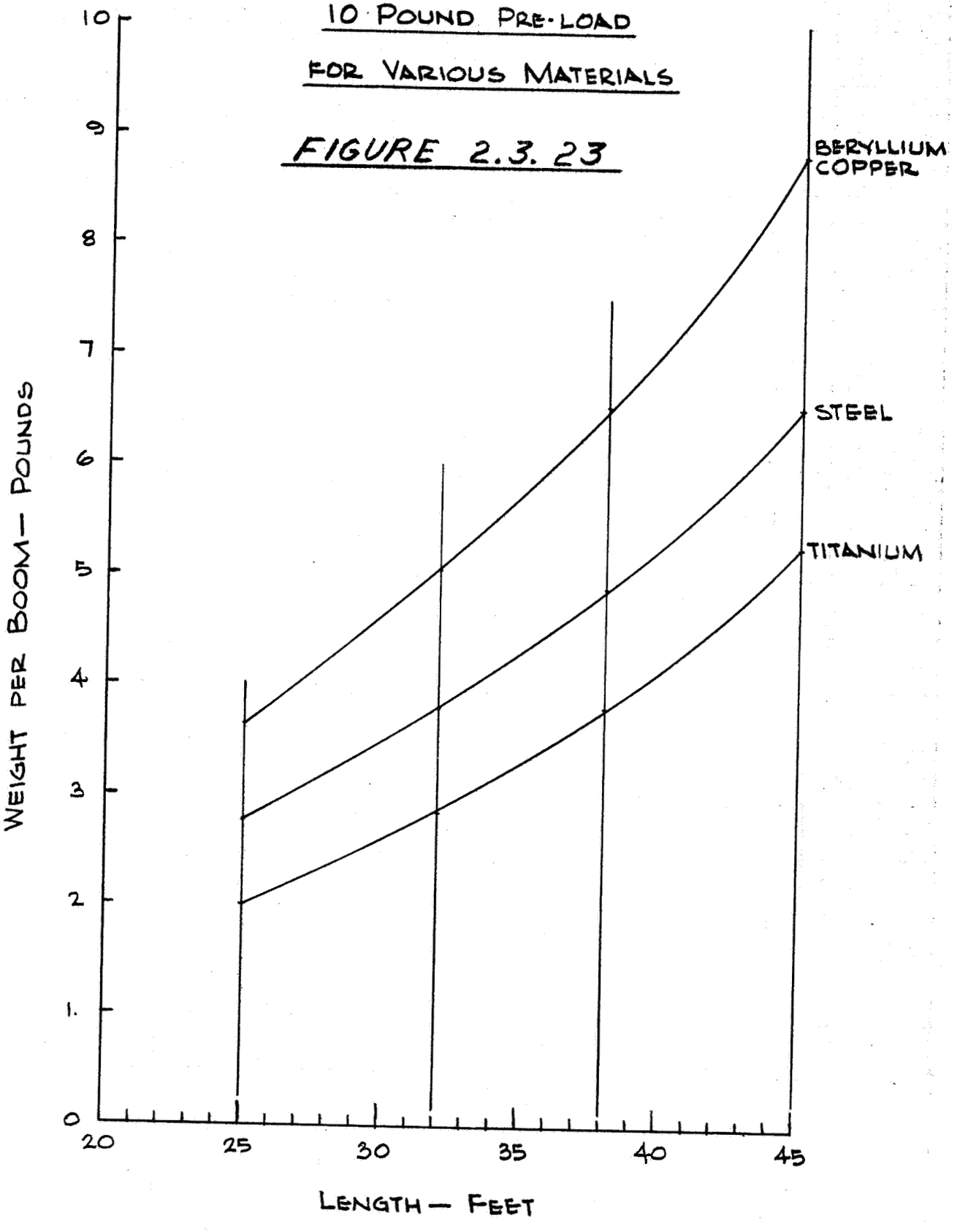
HINGELOCK SUPPORT BOOM

WEIGHT VS. LENGTH

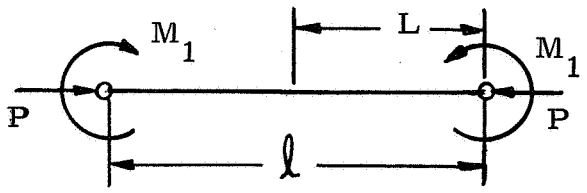
10 POUND PRE-LOAD

FOR VARIOUS MATERIALS

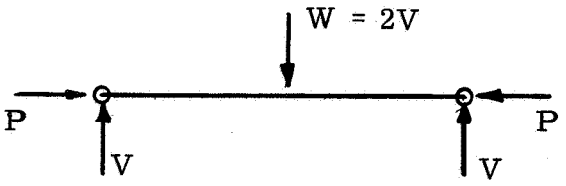
FIGURE 2.3.23



From Table VI, "Formulas for Stress and Strain" by R. J. Roark.



Case 7



Case 3

L = Cantilever Length of Hingelock = 1/2

U = ℓ/j

$$M_{Max} = M_1 \sec \frac{U}{2} = M_1 \Big/ \cos \frac{U}{2} = M_1 \Big/ \cos \frac{L}{j}$$

$$y = \frac{M_1}{P} \left(\frac{1 - \cos \frac{U}{2}}{\cos \frac{U}{2}} \right) = \frac{M_1}{P} \left(\frac{1 - \cos \frac{L}{j}}{\cos \frac{L}{j}} \right)$$

$$M_{Max} = 1/2\ W\ j \tan \frac{U}{2} = V\ j \tan \frac{U}{2} = V\ j \tan \frac{L}{j}$$

$$y = \frac{Wj}{2P} \left(\tan \frac{U}{2} - \frac{U}{2} \right) = \frac{Vj}{P} \left(\tan \frac{L}{j} - \frac{L}{j} \right)$$

Combining eqautions:

$$M_{max} = \frac{M_1}{\cos \frac{L}{j}} + V\ j \tan \frac{L}{j} \quad \text{(in. lbs)} \quad (2.3.3.1)$$

$$y_{max} = \frac{M_1}{P} \left(\frac{1 - \cos \frac{L}{j}}{\cos \frac{L}{j}} \right) + \frac{Vj}{P} \left(\tan \frac{L}{j} - \frac{L}{j} \right) \text{(in)} \quad (2.3.3.2)$$

where:

M_1 = end moment = P e

$$j = \sqrt{\frac{EI}{P}}$$

The deflection calculated by Equation 2.3.3.2 is a maximum and will be reduced due to thermal bending when the array is subjected to a solar flux.

Actual stress are then determined using the following equations:

$$F_c = \frac{P}{A} \quad \text{(psi)}$$

$$F_b = \frac{Mc}{I} = \frac{M_{max}}{\pi R^2 t} \quad \text{(psi)}$$

The allowable stresses are determined as:

$$F_c = \frac{\pi^2 E}{\left(L/\rho\right)^2} \quad \text{(Euler column equation)}$$

$$F_b = \frac{1.3\, c\, E}{R/t} \quad \text{(NASA TN D-163)}$$

Interaction Margin of Safety

$$M.S. = \frac{1}{\frac{f_b}{F_b} + \frac{f_c}{F_c}} - 1$$

Typical computations demonstrating the application of the above equations follow. The small deflection calculated for the beam in the sample problem indicated that no further deflection studies were necessary.

Sample Problem

L = 384 in. (32 ft.)

D = 5.0 in.

e = 2.5 + 1.0 = 3.5 in.

h = 5.5 + e = 5.5 + 3.5 = 9.0 in.

$\theta = \text{TAN}^{-1} \frac{5.5}{L} = \text{TAN}^{-1} \frac{5.5}{384} = \text{TAN}^{-1} .01432 = 0^{o}49'$

P = 20 x 1.25 = 25 # (ult.)

R = P (cos θ) = P = 25 # (ult.)

V = P (sin θ) = (25) (.01432) = 0.356 # (ult.)

Material = Titanium

Density = 0.160 #/in.^{3}

E = 16,000,000 psi

t = .0044 in. (obtained by iteration)

$D/_t = \frac{5}{.0044} = 1,137.$ $R/_t = 568.5$

$\rho = .707R = 1.768$ in.

$L/_\rho = (2)\ \frac{384}{1.768} = 434$

$A = \pi Dt = \pi (5) (.0044) = 0.0691$ in^2

$I = \pi R^3 t = \pi (2.5)^3 (.0044) = 0.216$ in^4

$$M_{max} = \frac{M_1}{\cos \frac{L}{j}} + Vj \left(\text{TAN } \frac{L}{j}\right)$$

$M_1 = Pe = 25 \times 3.5 = 87.5$ in-# (ult.)

$$j = \sqrt{\frac{EI}{p}} = \sqrt{\frac{(16)(10)^6(.216)}{25}} = 372. \text{ in.}$$

$$\cos \frac{L}{j} = \cos \frac{384}{372} = \cos 1.033 = .514$$

$$\text{TAN } \frac{L}{j} = 1.671$$

$$M_{max} = \frac{87.5}{.514} + (.356)(372)(1.671) = 170.2 + 222.5 = \underline{392.7} \text{ in-lb (ult.)}$$

$$f_c = \frac{P}{A} = \frac{25}{.0691} = \underline{362} \text{ psi (ult.)}$$

$$f_b = \frac{(M_{max})(c)}{I} = \frac{(392.7)(2.5)}{.216} = \underline{4,540} \text{ psi (ult.)}$$

Allowable Stresses

$$F_c = \frac{\pi^2 E}{(L/\rho)^2} = \frac{\pi^2 (16)(10)^6}{(434)^2} = \underline{836} \text{ psi}$$

$$\sigma_{cr_b} = \frac{1.3\, c\, E}{R/t} = \frac{(1.3)(.19)(16)(10)^6}{568.5} = 6,960 \text{ psi}$$

For values of c, see Figure 7 of NASA TN 3783 (U = 0.00035)

$$R_c = \frac{f_c}{F_c} = \frac{362}{836} = .433$$

$$R_b = \frac{f_b}{\sigma_{cr_b}} = \frac{4,540}{6,960} = .652$$

$$\text{Margin of Safety} = \frac{1}{R_c + R_b} = \frac{1}{.433 + .652} = \underline{-0.077}$$

$$y_{max} = \frac{M_1}{\rho}\left(\frac{1-\cos\frac{L}{j}}{\cos\frac{L}{j}}\right) + \frac{Vj}{p}\left(\text{TAN}\ \frac{L}{j} - \frac{L}{j}\right)$$

$$= \left(\frac{87.5}{25}\right)\left(\frac{1 - .514}{.514}\right) + \frac{(.356)(372)(1.671 - 1.033)}{25}$$

$$= 3.31 + 3.38$$

$$y_{max} = 6.69 \text{ in. (ult.)}$$

Weight = π DtLρ = AL ρ = (.0691) (384) (.160) = $\underline{4.24}$ lbs.

2.4 MATERIALS ENGINEERING

The following studies, relative to the feasibility of fabricating a 30 watt per pound roll-up solar array, were conducted:

- Boron - composite
- Graphite - composite
- Beryllium
- Design Data
- Polyimide Film
- Adhesives
- Solar Flare Radiation Effects
- Lubrication
- Emittance of the Back Surface of the Array
- Slip Rings and Brushes

In order to select the best material for each application it is important that good engineering judgement be exercised. There are many incentives to utilize new and sophisticated materials as they become available, but, where performance and reliability are of predominant importance, novelty and sophistication must be subordinated to firm design data and established confidence levels.

2.4.1 Boron-Composite

Continuous monofilaments of boron are manufactured by deposition from boron trichloride-hydrogen mixture vapor, onto 1/2 mil diameter tungsten wires (Reference 2.4.1). Typical (filament) properties are:

Density	0.085 lb in^{-3}
E	64×10^6 psi
k	1.86 BTU $hr^{-1} ft^{-1} {}^oF^{-1}$
α	$2.8 \times 10^{-6} {}^oF^{-1}$
C	0.309 BTU $lb^{-1} {}^oF^{-1}$
F_{tu}	300,000 psi
ν	0.06
Dia.	0.004 mils ± 0.0005

Composite impregnated unidirectional tapes are prepared by conventional filament winding processes and fabricated into sheet, tubes etc. with the required cross-ply angles. These materials are manufactured by: Hercules Powder Co.; Brunswick Corp.; Narmco; and Texaco Experiment. Their average physical properties (Reference 2.4.2) are:

Density	0.075 lb in^{-3} (49% BP907 Resin-Unidirectional)
E_t	33.6×10^6 psi
F_{tu}	235,000 psi
Laminar Shear	8.5 - 16,000 psi

Typical properties of Boron/epoxy composites (2-ply x .010 inch thick with a 15^o cross ply angle) are shown as part of Figure 2.4.1 (a).

2.4.2 Graphite Composite

Graphite composites are manufactured by graphitizing continuous yarns (e.g. Viscose Rayon). Since Thornel 25 (Union Carbide materials with $E = 25 \times 10^6$) was introduced in 1966, development has been rapid and is continuing. Yarns with modulus greater than 40×10^6 psi are commercially available from Union Carbide, HITCO, and Royal Aircraft Establishment (England). Currently yarns with 50-60 $\times 10^6$ psi modulus are in the developmental stage. Typical properties of these materials (Example: Union Carbide "Thornel 40" Reference 2.4.3 and 2.4.4) are:

Density	0.056 lb in^{-3}
E	40×10^6 psi
k	60 BTU $hr^{-1} ft^{-1} {}^oF^{-1}$
α	$-0.6 \times 10^{-6} {}^oF^{-1}$
C	0.17 BTU $lb^{-1} {}^oF^{-1}$
F_{tu}	250,000 psi
ν	0.007
Dia.	10-12 mils (effective ply thickness)

Properties of a "Thornel 40-Epoxy" composite (Reference 2.4.3) are:

Density	0.052 lb in^{-3} (35% ERL 2256/MPDA)
E_t	22×10^6 psi

F_{tu}	112, 000 psi
Laminar Shear	3, 400 psi

Recently the General Technologies Corp. has commenced commercial production of graphite yarn with a silicone carbide whisker treatment which (according to Naval Ordnance Laboratory Tests) provides substantial improvement in laminar shear strength (Reference 2.4.4 and 2.4.5). HITCO, Brunswick Corp., Narmoc, Cordo, and Hercules are potential fabricators of composite graphite parts.

2.4.3 Beryllium

End fittings of beryllium can be machined to about 0.125 inch thickness; chemical milling can further reduce the thickness to perhaps 0.06 inches. Hot formed sheet, with corrugation, can be produced and brazed to fabricate long thin wall elements. Complex highly specialized operations are required, however, including grinding, press flattening, regrinding, chemical milling (to reduce the 0.020 commercial thickness), hot pressing, and special machining. Brazing is preferred for joints, where possible, because it is lighter and has better thermal properties than adhesive bonding. Among the possible fabricators are Fairchild Hiller Corp. (Republic Aviation Div.) and International Harvester Co. (Solar Div.). Excessively high fabrication cost, long lead times and high tooling investments, however, discourage use of this material.

2.4.4 Design Data

The mechanical and physical properties used for parametric studies are summarized in Tables 2.4.1 (a) and 2.4.1 (b).

For application where maximum stiffness or strength with least weight is required, the comparative properties in Table 2.4.2 show that beryllium, or a high modulus composite, provides significant and attractive weight advantages over other potential materials.

2.4.5 Polyimide Film

Selection of Kapton H film was based upon its superior thermal and radiation resistant performance (Reference 2.4.6). Although ductile, thin films can tear easily due to stress concentrations at edge defects

TABLE 2.4.1 (a)

DESIGN ALLOWABLE PROPERTIES (Room Temperature)

Material	Aluminum 7075 T6	Aluminum 7075 T6	Beryllium 2% BeO	Beryllium-Copper Alloy 25	Boron/ Epoxy	Graphite Epoxy
Specification	QQ-A-200/11 Extruded	QQ-A-225/9 Bar	S-200C Sheet Cross Rolled	QQ-C-533 Strip	Borofil/ BP 907 15^{o} cross ply	Thornel 50/ ERL 2256 15^{o} cross ply
Properties						
Mech. Prop.						
Ftu, ksi	76	77	70	160	115	100
Fty, ksi	65	66	50	120	--	--
Fcy, ksi	67	64	--	120	--	--
Fsu, ksi	46	46	--	87	16	3
E, 10^6 psi	10.3	10.3	42.5	18.5	35	30
Ec, 10^6 psi	10.5	10.5	42.5	--	--	--
G, 10^6 psi	3.9	3.9	20	6.9	12	10
ν	0.33	0.33	0.03	0.3	0.25	0.25
ϵ, %	7	4	5	10	0.3	0.3
Phys. Prop.						
W, lb in^{-3}	0.101	0.101	0.067	0.297	0.075	0.052
C, btu, $lb.^{-1}$ $^{o}F^{-1}$	0.23	0.23	0.445	0.1	0.20	0.20
K, btu, hr^{-1} ft $^{o}F^{-1}$	75.1	75.1	104	61	0.56	0.56
α, 10^{-6} $^{o}F^{-1}$	13.1	13.1	6.4	9.2	2.7, 16	0.4, 16

TABLE 2.4.1 (b)

DESIGN ALLOWABLE PROPERTIES (Room Temperature)

Material	Kapton H	Copper OFHC Hard	Silver	Stainless Steel 17-7 PH Cond CH900	Titanium 6Al4V Aged
Specification		--	--	MIL-S-25043 (Strip)	MIL-T-9046 Type III Comp. C
Properties					
Mech. Prop.					
Ftu, ksi	25	64	18.2	235	157
Fty, ksi	10	30	7.9	230	143
Fcy, ksi	--	--	--	--	152
Fsu, ksi	--	--	--	152	16.4
E, 10^6 psi	0.43	17	10	29.0	16
Ec, 10^6 psi	--	--	--	--	--
G, 10^6 psi	0.14	6.4	3.6	11.6	6.1
ν	0.5	0.33	0.37	0.25	0.33
ϵ, %	70	1.5	48	2	4
Phys. Prop.					
W, lb in^{-3}	0.051	0.321	0.376	0.277	0.160
C, btu lb^{-1} $^oF^{-1}$	0.26	0.092	0.056	0.11	0.128
K, btu hr^{-1} ft^{-1} $^oF^{-1}$	0.094	226	242	9.5	4.0
α, 10^{-6} $^oF^{-1}$	11	9.3	9.4	6.1	4.8

TABLE 2.4.2

STRUCTURAL MATERIALS

COMPARATIVE PROPERTIES

	Specific Stiffness Tension Modulus / Density	Specific Strength Tensile Strength / Density
Boron Filament/Epoxy Composite (2 ply - 15° Half Angle Lay-up)	466	154
Graphite Fiber/Epoxy Composite (2 ply - 15° Half Angle Lay-up)	666	222
Beryllium (2% BeO)	635	104
Titanium (6A14V)	102	98
Stainless Steel (17-7 PH)	104	85
Aluminum (7075-T6)	102	75
Magnesium (AZ31B)	102	61

which may not be easily detectable visually. One method for preventing tearing is to use adhesive bonded edge doublers which increase reliability by reducing the probability of coincident edge defects.

Module panels are joined by a laced mechanical joint (Figure 2.4.1). Two mil thick Kapton material, joined by lacing, has been tested to a load of 9 pounds per inch where it unlaced instead of tearing. With a 5 pounds per inch load, only a small ripple at the laced joint was observed. At 2 pounds per inch the joint remained straight. This construction technique is more than adequate since substrate tension design load is approximately 0.1 lbs per inch.

Fragmentary data on the effects of solar ultraviolet radiation indicates that it may cause deterioration of Kapton H film. If this is true, a thin film of silicone resin may be used as an effective protective coating.

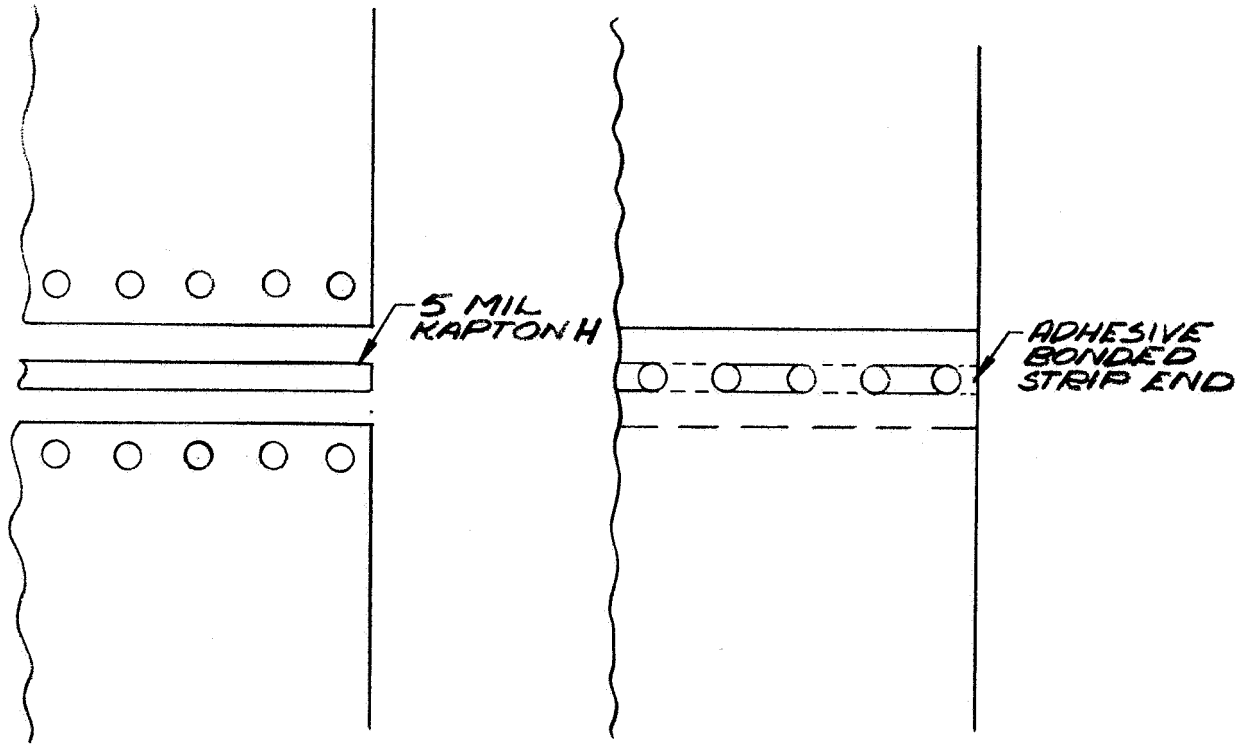
Negligible progressive extension is assured at 50 psi (0.1 lb per inch) by the data measured for Figure 2.4.2. The creep rate at 135°C is less than twice that at 25°C (Reference 2.4.1).

2.4.6 Adhesives

The properties of several adhesives are shown in Table 2.4.3 and those which were selected for use are identified.

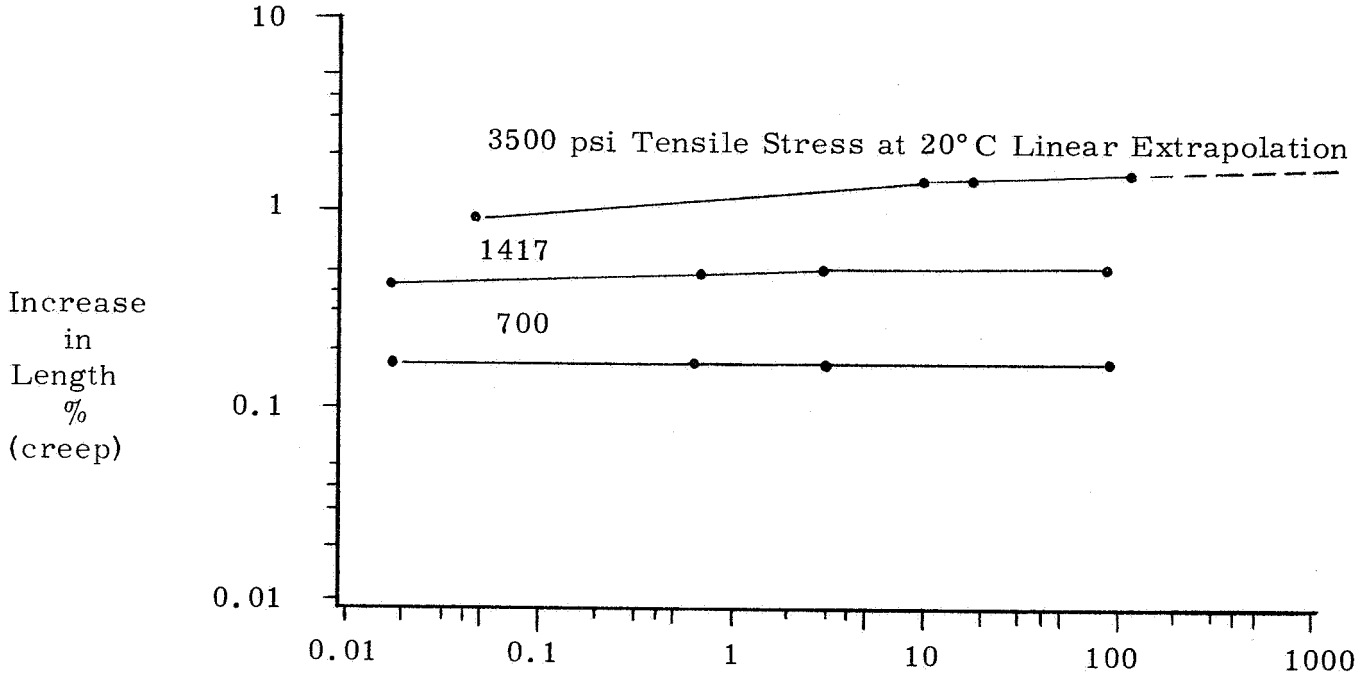
Cover glasses are bonded to the solar cell with Sylgard 182 (silicone resin) and the interconnecting conductors are soldered in place. This assembly is then bonded to the module substrate with RTV 108 (silicon adhesive). The RTV 108 is optically transparent and permits visual inspection of the cells and interconnections after assembly. When the substrate is rolled-up under tension on the drum, the strength of RTV is adequate to assure a reliable bond between the solar cell and the substrate. However, it's moderate peel strength allows cells to be removed for repair with little or no difficulty.

For bonding substrate doublers, stiffeners, etc. an epoxy-phenolic film adhesive, HT 432 (Bloomingdale Rubber Co.), was chosen. The primary advantage of this material is its exceptional thermal and radiation resistance.



LACED JOINTS BETWEEN MODULE PANELS

FIGURE 2.4.1



Creep Data for 3 mil Kapton H Film

Figure 2.4.2

TABLE 2.4.3

ADHESIVE PROPERTIES

Adhesive	Density (5 mils) psf	Adhesion Strength Shear psi	Adhesion Strength Peel ppi	Temperature ^{o}F	Radiation Tolerance RADS	Remarks
DC 281 (Silicone, pressure sensitive, Dow Corning)	0.08	--	50	-80 to 500	10^7	Selected for bonding foam backing
Silastic 140 (Silicone-Thixotropic, Dow Corning)	0.08	--	20	-100 to 500	10^7	
RTV 108 (Silicone - Thixotropic, General Electric)	0.08	200	20	-75 to 300	10^7	Selected for bonding cells to substrate
Sylgard 182 (Silicone, Transparent, Dow Corning)	0.07	--	--	-65 to 400	10^7	Selected for bonding cover glasses
RTV 602 (Silicone, Transparent, General Electric)	0.07	--	--	-65 to 300	10^7	
HT 432 (Epoxy, Bloomingdale)	0.05	1850	10	-425 to 500	10^9	Selected for bonding substrate doublers, connectors etc.
Permacel 18 (Phenolic-butyral Permacel)	0.02	2000	8	250 max.	--	

To verify its integrity, a sample of Kapton H film was bonded with HT 432 and tested for 5 minutes at -195°C (in a LN_2 atmosphere) and at 60°C for 168 hours. No degradation of the bonded joint was noted.

A 0.031 in. thick polyurethane foam (Scott Standard 2 lb/ft^{-3}) is bonded to the back of the array with a .5 mil thickness of Dow Corning DC 281 (silicone adhesive). Under vacuum conditions, outgassing of this bonding agent can cause a high weight-loss (approximately 20%, see Table 2.4.4). A foam to substrate bonded joint was tested for 5 hours at 150°C and for 5 minutes at -195°C (LN_2 atmosphere) and no degradation of the bond was detectable. Therefore, DC 281 is functionally acceptable for its intended use. If outgassing is objectionable, bonded surfaces can be preconditioned to eliminate their volatile constituents.

2.4.7 Solar Flare Radiation Effects

Based on the energy distribution curves given in Reference 2.4.8, an average solar flare proton flux of 2×10^9 p cm^{-2} yr^{-1} is assumed. However below 1 MEV a Maxwell energy distribution is adopted to approximate closely the Apollo standard in the range $0.5 < E < 1$ MEV.

The rate of energy absorption (Reference 2.4.9) was assumed to be:

(1) $S = 242\ E^{-0.78}$ MEV $cm^{-2} g^{-1}$ for Kapton H, Carbon

(2) $S = 228\ E^{-0.78}$ for Adhesives, Polyethylene

Numerical analysis gives estimated annual doses as follows:

Adhesives with 2 mil Kapton shielding	2.9×10^5 RADS yr^{-1}
Kapton H, surface dose	8.7×10^6

Based upon tolerances of 10^7 and 3×10^9 RADS, respectively, a useful life of approximately 30 years is predicted.

2.4.8 Lubrication

Special problems created by space vacuum include fast evaporation rates for ordinary oils and greases and fast migration of low surface energy oils to high surface energy metal surfaces (surface tension driving force). If the lubricating oil film is lost, diffusion welding of bearing metallic parts may result unless they are separated by a solid film lubricant or suitable non-metallic insert.

TABLE 2.4.4

Weight Losses of Adhesives at 140°C

Adhesive	Hours Exposure 1	24	70	168
	Ave. Weight Loss (%) *			
A-12 Rigid (Epoxy)(1)	0.20	0.40	0.44	0.73
A-12 Flex (Epoxy)(1)	0.20	0.43	0.64	0.84
18 (Phenolic-Butyrote)(2) (Permacel Co.)	0.20	0.20	0.20	0.22
269 (Silicone)(3)	3.40	5.7	6.2	6.6
281 (Silicone)(3)	16.2	19.2	19.2	20.4
HT - 424 (Epoxy-Phenolic)(4)	0.0	0.0	0.0	0.0
HT-432 (Epoxy - Phenolic) (4)	0.0	0.0	0.0	0.0
4000 (Silicone)(3)	1.8	6.4	7.6	8.7

* Average for duplicate test in 2 in diameter cups.

Manufacturers

(1) Armstrong Products Co.
(2) Permacel
(3) Dow Corning
(4) Bloomingdale

In addition to the generally required running-in period for detection of hidden defects, elimination of roughness, and distribution of lubricant, test operation of each bearing for a period above and below the design temperature range is recommended. This will assure against ill effects of thermal expansion-contraction or freeze up due to incorrect lubricant or excessive lubricant loading.

Experience with very highly loaded slow speed bearings exposed to hard space vacuum is limited. The solar panel drive shaft pinion for Nimbus 2 is AISI 4340 alloy steel mating with a hard anodized 2014 T4 aluminum alloy gear. Nitrided 135M nitralloy external ring glass and ball bearings with 440 C stainless steel balls and races lubricated with 25% pack of G-300 grease was also used, the retainer being paper base phenolic. The OGO solar array drive used gold plated 440C balls and races, gold plated 416 stainless retainer, and was lubricated with dry unbonded molybdenum sulfide. Pegasus 1 and 2 used gold plated 52100 steel races, Rulon C ball retainers, and 440 stainless steel. Torrington needle bearings with 440C needles in 1012 steel cups (nickel plated) were used with dry unbonded molybdenum sulfide lubrication. Mariners and Rangers used molybdenum sulfide lubrication for external actuator gears and latches (Reference 2.4.10).

The requirement for low break away (static) friction might best be met by oil or grease lubrication. However, the probability of oil evaporation and migration from bearings or greases is recognized. The dynamic coefficient of friction of molybdenum sulfide burnished onto steel is typically 0.06 to 0.10 during sliding (vacuum) but the static coefficient rises to about 0.35 after several hours of non-operation in vacuum. (Reference 2.4.11)

Molecularily distilled hydrocarbons and oils with low vapor pressures have been investigated for space lubrication (Reference 2.4.10). Apiezon C oil (10^{-9} mm vapor pressure at 20^{o}C) was used to impregnate the graphite brushes for electric motors and Apiezon L grease (10^{-11} mm vapor pressure at 20^{o}C) was used to lubricate hinges of OSO-2. Shaft bearings of OGO used retainers impregnated with Apiezon K oil (10^{-9} mm vapor pressure at 20^{o}C). Apiezon T (M.P. 257^{o}F, 10^{-8} mm vapor pressure at 20^{o}C) survived longer than any other grease in a loaded high temperature ball bearing test in vacuum (See Table 2.4.5).

TABLE 2.4.5 (Reference 2.4.12)

Loaded Ball Bearing Test at 325^{o}F (Motor Case) and 10^{-6} Torr

Grease	Type	Life
Anderol L-795	Diester	70 hours
Versilube G-300	Silicone	170-286
Apiezon T	Hydrocarbon	424

Apiezon H (Reference 2.4.13) appears to be a good homogeneous choice for an oily film to provide low static friction. It has 10^{-9} mm vapor pressure at room temperature which is sufficiently high to assure vapor transfer to dry surfaces in a bearing, but not so high that evaporation losses will be intolerable. It has no dry non-lubricating solids to cause thickening and freeze up or high static friction after partial evaporation, like solid thickened G-300 silicone grease for example. It softens but does not melt at 488°F.

Therefore, hard and strong steels should be used for bearings and gears, they should be burnished with molybdenum sulfide which functions as an antiseize coating and dynamic lubricant, and after run-in, a homogenous film forming lubricant such as Apiezon H should be applied as a thin film for low static friction. Retainer rings of Vespel polyimide have inherently low friction coefficients, do not generate fibers like reinforced phenolic laminates for example, and are soft enough to withstand imbedment of hard particles without failing (Reference 2.4.14).

2.4.9 Experimental Determination of the Emittance of the Back Surface of the Array

Presently, the back surface consists of a 2 mil layer of Kapton with strips of 0.031 in. thick polyurethane foam covering approximately 25% of the surface area. Since the 2 mil thickness of Kapton is roughly 30% transparent to infrared radiation (from a 300°K blackbody), any material beneath the Kapton film is thermally significant. This substance, RTV 108 cell adhesive, is nearly opaque to infrared, so the emittance of the solar cell rear surfaces contributes negligibly to the overall emittance.

A thermal test, as opposed to optical measurement, is the most reliable means of obtaining a substrate back surface effective emittance referenced to cell temperature. Thermal measurement would include conduction effects through the adhesive, film and foam layers as well as the ill-defined radiation paths through and from the foam layer.

Figure 2.4.3 illustrates the set-up for the thermal test. The surface of the aluminum plate, to which the Kapton film was adhered, was cleaned and lightly polished to simulate the emittance of the "solder" rear cell surface, although for

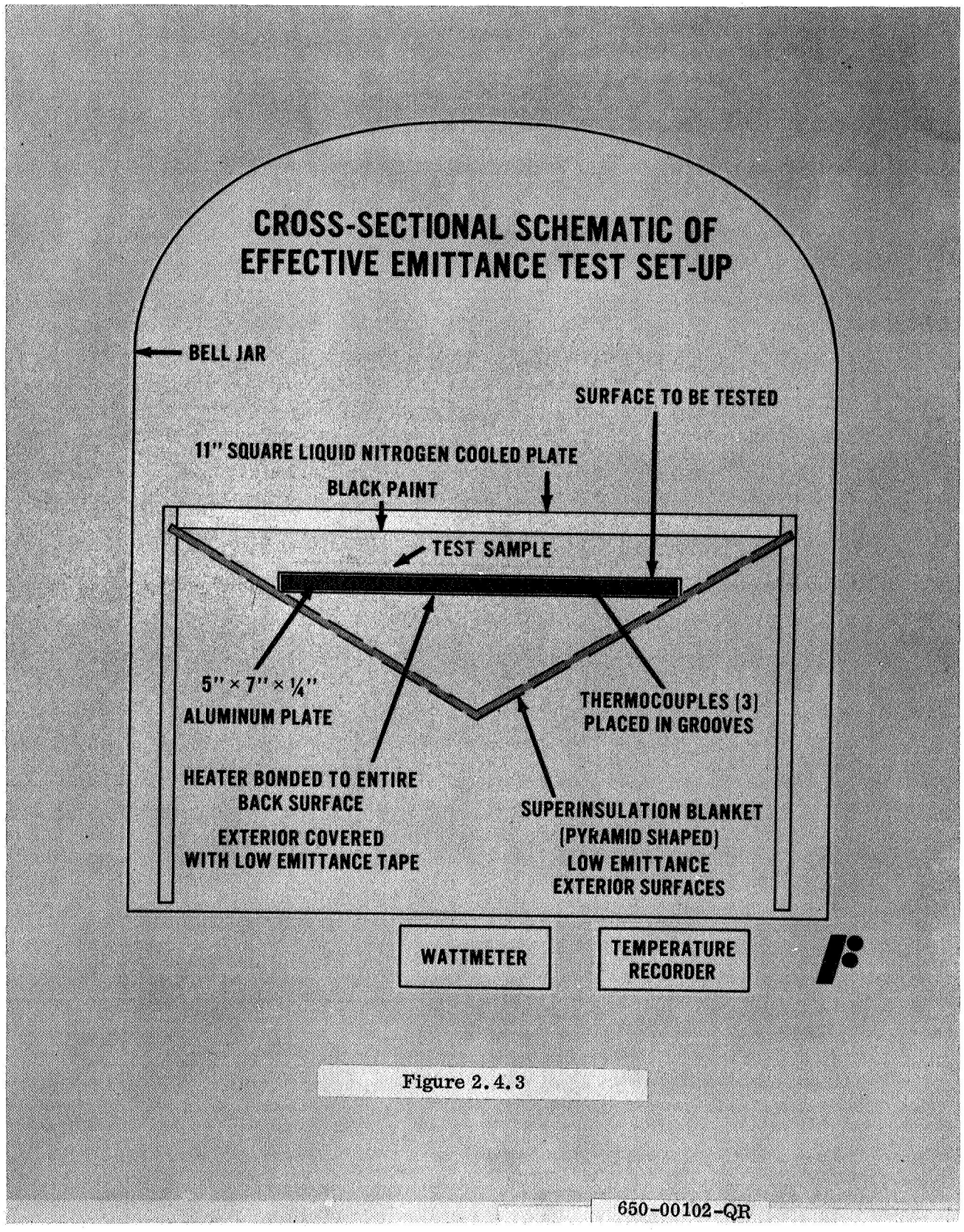

CROSS-SECTIONAL SCHEMATIC OF
EFFECTIVE EMITTANCE TEST SET-UP
BELL JAR
SURFACE TO BE TESTED
11" SQUARE LIQUID NITROGEN COOLED PLATE
BLACK PAINT
TEST SAMPLE
5" × 7" × ¼"
ALUMINUM PLATE
THERMOCOUPLES (3)
PLACED IN GROOVES
HEATER BONDED TO ENTIRE
BACK SURFACE
EXTERIOR COVERED
WITH LOW EMITTANCE TAPE
SUPERINSULATION BLANKET
(PYRAMID SHAPED)
LOW EMITTANCE
EXTERIOR SURFACES
WATTMETER
TEMPERATURE
RECORDER

Figure 2.4.3

reasons previously mentioned, this surface is believed a negligible contributor to overall effective emittance. The first series of tests (three different power dissipations and steady-state temperatures) was run with the 2 mil Kapton. To this same Kapton sheet the foam layer was applied with Dow-Corning 281 adhesive and another series of dissipations and steady-state temperatures were obtained. A third test was made (with the Kapton removed) to determine the emittance of the "bare" RTV 108 adhesive on the aluminum plate. The test results and calculated values are given in Table 2.4.6.

The emittance factor (F_ϵ) is obtained from the relation:

$$q = \sigma A F_\epsilon (T^4_{plate} - T^4_{LN_2})$$

where q is the heat dissipation in the plate

$\sigma = .171 \times 10^{-8}$ BTU/hr ft^2 $^oF^4$, and

A is the total frontal area of the plate, 35 in^2.

The effective emittances of the sample surface ϵ_{eff} and black LN_2 plate ϵ_b, are related to F_ϵ by

$$F_\epsilon = \frac{0.60}{\frac{1}{\epsilon_{eff}} + \frac{1}{\epsilon_b} - 1} + 0.40\,\epsilon_{eff}$$

This expression was derived on the basis of configuration factor calculations, showing that 60% of the radiant energy from the sample plate is reflected back to the plate from the black plate. Thus 60% of the radiated energy can be approximately described by the expression for an "infinite parallel plate" exchange (assuming most of the energy is absorbed after one reflection); 40% of the radiated flux leaving the sample surface essentially never returns via reflections but is absorbed directly or after reflections by the LN_2 plate. Losses from the sample plate edges, rear surface and power - thermocouple leads are estimated to be 2% of the total heat dissipation, and thus a correction factor of .98 has been applied to the "average F_ϵ" to obtain a "corrected F_ϵ".

TABLE 2.4.6

Emittance of Back Surface of Array

Exposed Surface	Dissipation (watts)	Steady State Temperature (^{o}F)	Computed F_{ϵ}	Average F_{ϵ}	Corrected F_{ϵ}	Computed ϵ_{eff} (ϵ_b = .90)
	10	93	.88			
Kapton	12	126	.837	.855	.84	.89
	14	147	.848			
	10	114	.758			
Foam	12	143	.746	.754	.74	.78
	14	164	.757			
	10	86	.927			
Adhesive	12	112	.922	.923	.905	.96
	14	135	.919			

The contribution of the high emittance adhesive (ϵ = .96) to the relatively high emittance (ϵ = .89) of the substrate rear surface (in light of the 30% transparancy and no more than 60% absorption of the 2 mil Kapton to IR radiation) is a significant 1/3 (approximately). The remaining 2/3 emittance contribution can be attributed to the film itself.

If 3/16" wide foam strips are applied to cover approximately 25% of the rear surface (one strip per cell row), then the average effective emittance of the rear surface would be (.75 x .89 + .25 x .78), or 0.86. Throughout previous thermal analyses, rear array surface emittance has been taken to be 0.85. The thermal analysis requires no correction since the experimentally derived emittance is substantically identical.

2.4.10 Slip Rings and Brushes

Silver slip rings and composite brushes consisting of silver - 15% niobium diselenide have functioned well in Nimbus II. They were first reported in Reference 2.4.15, covering the development of the electrical sliding contacts for application in space environment. Stackpole Carbon (St. Maries Pa.) is a supplier of the composite brush material.

2.4.11 References

2.4.1 Schwartz and Schwartz (Wright Patterson AFB), Characteristics of Boron Fibers and Boron Fibers - Reinforced Plastic Composite, AIAA J., 5 No. 2, Feb. 1967, pp 289-93.

2.4.2 Prepreg Monofilament Boron Wide Goods Data Sheet, Hercules Inc. Dec. 1967.

2.4.3 "Thornel" 40 Graphite Yarn, Bulletin No. 465-202-GG, Union Carbide Corp.

2.4.4 Blakslee, Pallozzi, Doig, Spence, and Hanley, Fabrication, Testing, and Design Studies with "Thornel" Graphite-Fiber, Epoxy-Resin Composites, 12th National SAMPE Symposium, Oct. 1967.

2.4.5 Prosen and Simon (U. S. Naval Ordnance Laboratory), Carbon Fiber Composites for Hydro and Aerospace, Filament Winding Conference, The Plastics Institute (London), Oct. 1967.

2.4.6 Kapton Polyimide Film, DuPont Bulletin H-2, Wilmington, Del.

2.4.7 J. T. Milek, Polyimide Plastics, State of Art, EPIC 5-8, Oct. 1965, p. 182.

2.4.8 Natural Environment and Physical Standards for the Apollo Program, NASA M-DE 8020.008B, April 1965, p. 39.

2.4.9 Martin O. Burrell, Calculation of Proton Penetration and Dose Rates, 2nd. Symp. Protection Against Radiation in Space, NASA SP-71, Oct. 1964, pp 493-506.

2.4.10 Goetzel, Space Materials Handbook Supplement 1, Space Materials Experience, NASA SP-3025, 1966, pp 36-8.

2.4.11 Johnson and Vaughn, MoS_2 Lubrication in Vacuum, J. Appl. Physics, Vol. 27, Oct. 1956, pp 1173-9.

2.4.12 Goetzel, Space Materials Handbook, AFML ML-TDR64-40, (Second Edition) Jan. 1965, pp 221-2.

2.4.13 Apiezon Oils, Greases Etc., James Biddle Co.

2.4.14 Vespel Precision Parts, DuPont.

2.4.15 Moberly and Johnson, Electrical Sliding Contacts for Applications in Space Environment, IEEE Trans. Aerospace AS3, 1965, p 252-257.

PRECEDING PAGE BLANK NOT FILMED

2.5 THERMAL ANALYSIS

2.5.1 Array Temperature Transients Associated With Planet Shadow

Of serious concern to the power systems engineer is the surge of voltage and power from the cold solar array as it emerges from planet shadow into the full solar flux. If the simple and conservative assumption of a discontinuous step-change in incident solar energy (from zero to full sun in zero time) is considered, then at the instant of sun emergence there is a maximum power condition which is not alleviated by any warm-up of the solar cells, since in zero time the temperature rise of a finite thermal mass is zero. The more realistic condition of a gradual, continuous, increase in incident solar flux as the array passes through the planet's penumbra has been studied; the primary result of this study has been array temperature and incident solar flux, both as functions of time.

Solar flux as a function of time has been derived with the assumptions of: (1) a planet with no atmospheric distortion effects, (2) a solar disk emerging from behind a straight planet horizon, and (3) the solar disk velocity relative to the horizon is constant.

It is believed that any atmospheric affects which would distort the solar flux path would tend to make the increase in incident solar energy even more gradual than has been assumed with no atmosphere, and therefore a slight degree of conservatism is implied in the atmosphere-free assumption.

The straight horizon assumption appears reasonable when considering that the relative view diameters of Earth and Sun at a synchronous orbit altitude, for example, are in the ratio of approximately 30 to 1; in lower orbits, this ratio is higher still.

For circular or near-circular orbits, with the spacecraft trajectory within the penumbra closely approximating constant velocity in a relatively straight path, the assumption of a constant "apparant Sun velocity" is justified.

The transient temperature of the (isothermal) array is described, on a per unit area basis, by the relation

$$mc \frac{dT}{dt} = S(t)\alpha + I\epsilon - 2\epsilon\sigma T^4 \qquad (2.5.1)$$

where mc is the thermal mass of the array,

T is array temperature,

t is time,

α, ϵ are the average thermal properties of the array surfaces; the front and rear surface ϵ's are taken as equal,

S(t) is the solar flux as a function of time incident on the front surface,

σ is the Stefan-Boltzman constant, and

I is the constant infrared flux from the dark side of the planet.

From circle (the Solar disc) geometry,

$$S(t) = \frac{SC}{\pi}\left[\text{Arcsin}\left(\frac{2t}{P} - 1\right) + \left(\frac{2t}{P} - 1\right)\sqrt{1 - \left(\frac{2t}{P} - 1\right)^2} + \frac{\pi}{2}\right] \qquad (2.5.2)$$

where SC is the "unshadowed" solar intensity

and P is the total time the spacecraft spends in penumbra.

It is assumed that the array has reached an equilibrium temperature on the dark side of the planet which is the initial array temperature, Ti, upon entering penumbra (t = 0). Thus,

$$Ti^4 = \frac{I}{2\sigma}, \qquad (2.5.3)$$

assuming the flux I is normal incident on half the total array surface.

Equation (2.5.1) has been treated numerically with computer aid (program described in Reference 2.5.1), and several representative examples have been solved for illustrative purposes. Figures 2.5.1 and 2.5.2 show incident solar flux and array temperature as a function of time for two extreme "P's": A "minimum altitude" circular orbit with a 100 minute period would have a 9 second duration in each of

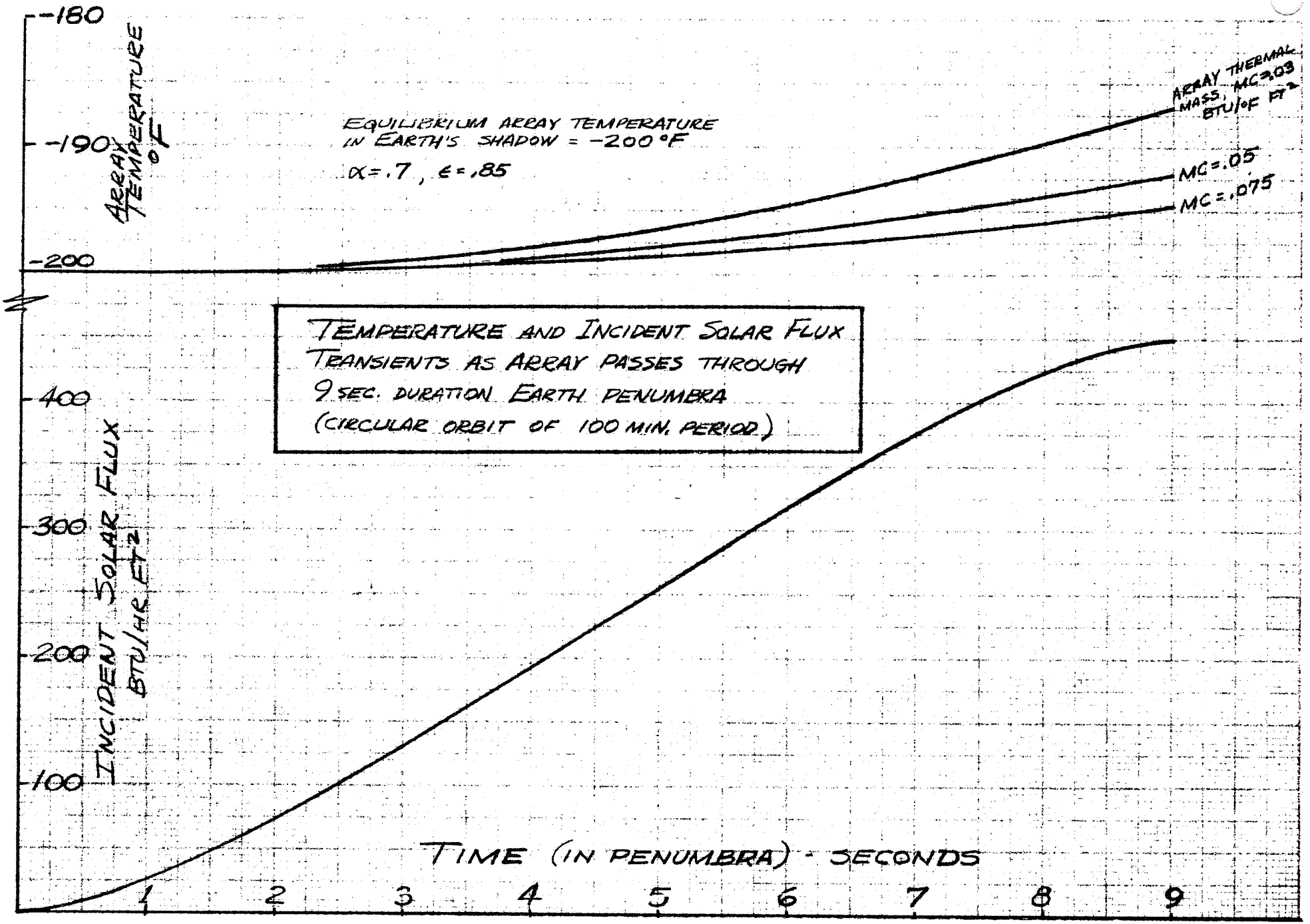

-180
-190
-200
ARRAY TEMPERATURE °F
EQUILIBRIUM ARRAY TEMPERATURE IN EARTH'S SHADOW = -200°F
α = .7 , ε = .85
ARRAY THERMAL MASS, MC=.03 BTU/°F FT²
MC=.05
MC=.075
TEMPERATURE AND INCIDENT SOLAR FLUX TRANSIENTS AS ARRAY PASSES THROUGH 9 SEC. DURATION EARTH PENUMBRA (CIRCULAR ORBIT OF 100 MIN. PERIOD)
400
300
200
100
INCIDENT SOLAR FLUX BTU/HR FT²
TIME (IN PENUMBRA) - SECONDS
1
2
3
4
5
6
7
8
9

FIGURE 2.5.1

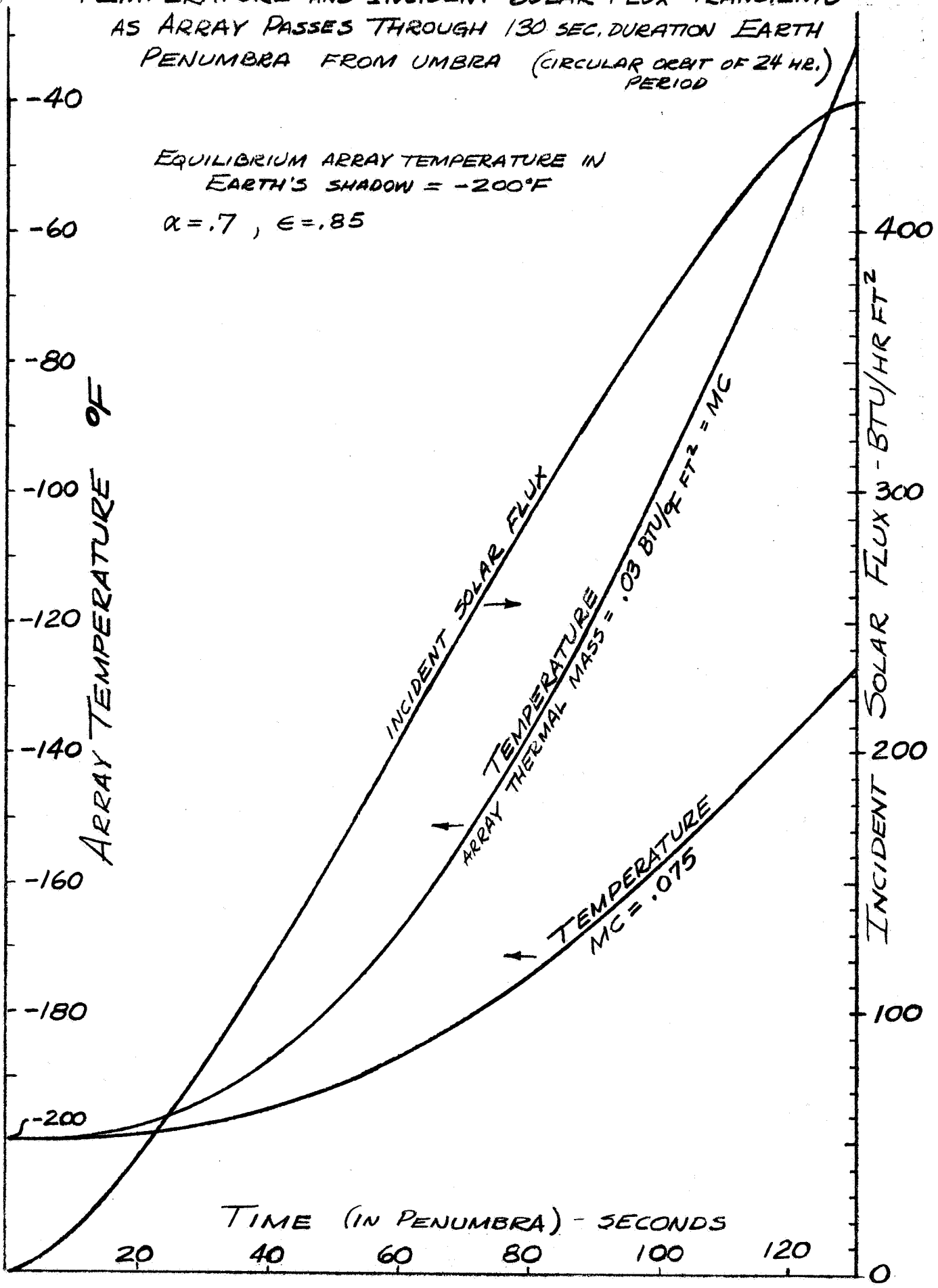

TEMPERATURE AND INCIDENT SOLAR FLUX TRANSIENTS AS ARRAY PASSES THROUGH 130 SEC. DURATION EARTH PENUMBRA FROM UMBRA (CIRCULAR ORBIT OF 24 HR. PERIOD)
EQUILIBRIUM ARRAY TEMPERATURE IN EARTH'S SHADOW = -200°F
α = .7 , ∈ = .85
ARRAY TEMPERATURE °F
-40
-60
-80
-100
-120
-140
-160
-180
-200
INCIDENT SOLAR FLUX - BTU/HR FT²
400
300
200
100
0
INCIDENT SOLAR FLUX
TEMPERATURE ARRAY THERMAL MASS = .03 BTU/°F FT² = MC
TEMPERATURE MC = .075
TIME (IN PENUMBRA) - SECONDS
20
40
60
80
100
120

FIGURE 2.5.2

the two penumbra regions (P = 9 sec); at synchronous altitude, with a 24 hour orbit period, the time increases to 130 seconds (P = 130 sec). It is interesting to note that, for circular orbits, the fraction of the orbit period spent in penumbra is a constant, regardless of orbit altitude. For Earth, this fraction is approximately .0015; for Mars, approximately .0009 . The range of thermal mass from .03 to .075 BTU/^{o}F ft^{2} should include all array configurations to be considered. An initial temperature (Ti) of -200^{o}F has been used in these examples; any other initial temperature below, say, -100^{o}F, can be applied with negligible loss of accuracy simply by applying the same temperature difference as a function of time.

2.5.1.1 Negligible Penumbra Effects

In low altitude orbits, for which penumbra effects may be conveniently ignored, transient temperature analyses for both heat-up and cool-down have been performed, based upon the heat balance relation of Equation (2.5.1). Now, however, the solar flux S is considered either a constant finite magnitude after emerging from planet shadow, or zero, after passing into planet shadow. Again the constant planet emitted flux I is assumed incident on half the total array surface. This equation is readily solved for the case of S = 0, I = 0, corresponding to a temperature decay with no radiative heat input:

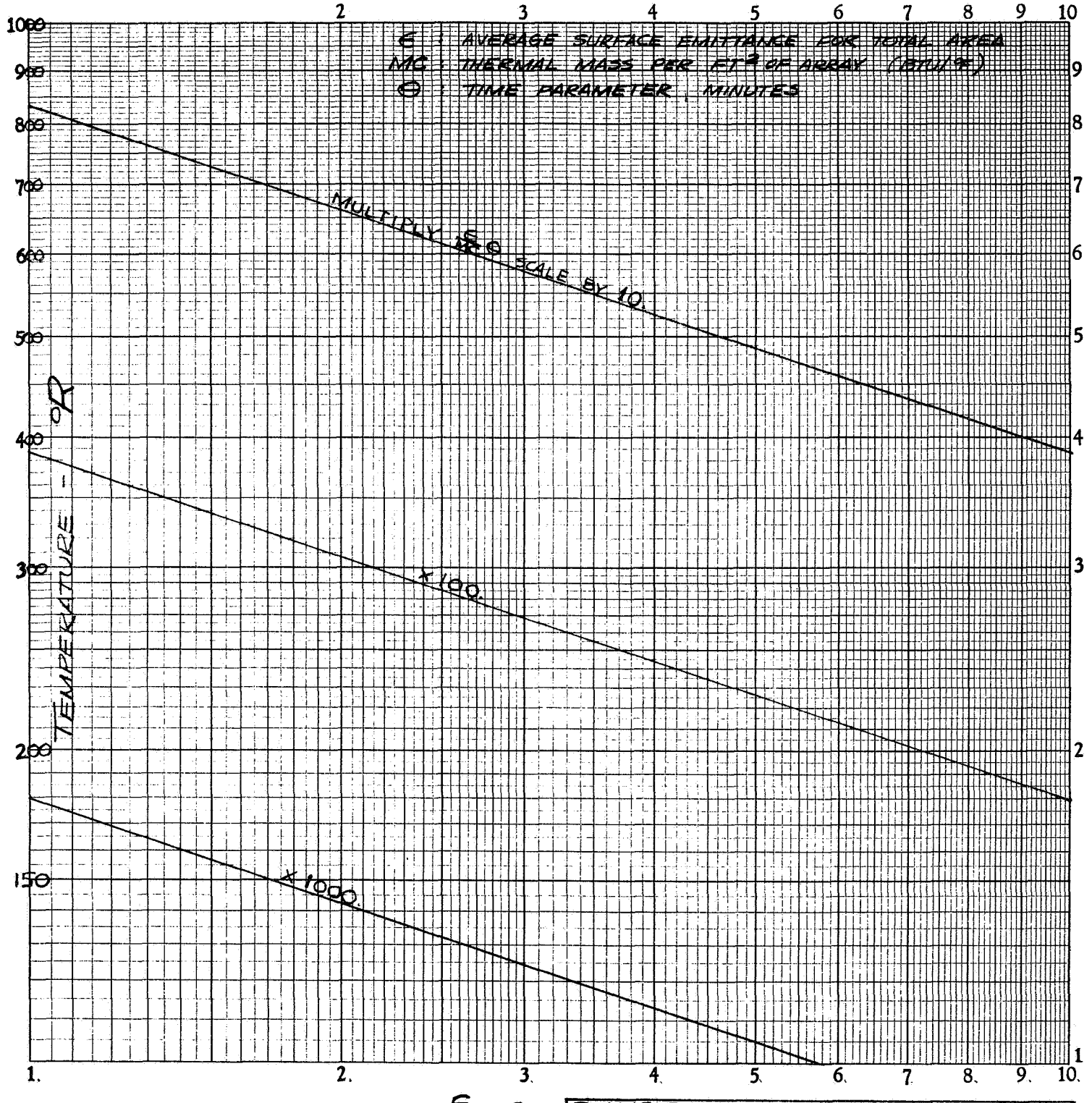
$$\left.\frac{1}{T^3}\right]_{T_1}^{T_2} = \left.\frac{6\,\sigma\,\epsilon}{MC}\,t\right]_{t_1}^{t_2}$$

This relation is presented in Figure 2.5.3, enabling temperature-time solutions to be obtained between any limits.

The case of a non-zero I has been treated numerically with computer aid and solutions for $\frac{\epsilon}{MC}$ = 10, 20, 30, and 40^{o} F/BTU per ft^{2} and for I = 0, 20, 40, and 60 BTU/hr. ft. are presented in Figures 2.5.4 and 2.5.5.

For the condition of an array emerging from planet shadow where S = 450 BTU/hr. ft.^{2} at time zero, the absorptance α of the front array surface becomes an

TEMPERATURE DECAY OF ISOTHERMAL SOLAR CELL ARRAY WITH NO RADIATIVE HEAT INPUT



EXAMPLE: TIME REQUIRED FOR ARRAY OF $\frac{\epsilon}{MC} = 20$ °F/BTU FT² TO COOL FROM 140° TO -100°F

$\left(\frac{\epsilon}{MC}\Theta\right)_{600°R} = 26.8$; $\Theta_{600} = \frac{26.8}{20} = 1.34$

$\left(\frac{\epsilon}{MC}\Theta\right)_{360°R} = 124.$; $\Theta_{360} = \frac{124}{20} = 6.2$

$\Theta_{360} - \Theta_{600} = 6.2 - 1.34 = 4.86$ MIN.

FIGURE 2.5.3

additional parameter. A representative set of computer obtained solutions is illustrated in Figure 2.5.6 for $\frac{\alpha}{2\epsilon}$ = .4 and .45 and for $\frac{\epsilon}{MC}$ = 10, 20, 30, and 40.

2.5.1.2 Steady-State Array Temperature in Earth Shadow

It is seen from Figures 2.5.4 and 2.5.5 that an "equilibrium" array temperature is approached in Earth shadow depending upon the magnitude of the incident Earth emitted radiative flux. For the condition of high $\frac{\epsilon}{MC}$ and high Earth flux, this steady-state temperature is closely approached within 20 minutes after entry into Earth shadow. It is quite reasonable to assume, therefore, that for Earth orbits with the orbital plane approximately parallel to the solar vector, when shadow duration times can run from 40 minutes for a close-Earth orbit to several hours for an elliptical orbit with apogee far from Earth, minimum array temperature in shadow (or array temperature just before emergence into sunlight) can be calculated based upon the magnitude of incident Earth radiation. However, Earth radiation input is a function of both array altitude and attitude. As an array proceeds in its shadowed orbit, it is likely that, even with constant altitude, the spacecraft attitude control system will not keep a constant Earth-array orientation. Thus, a constant array temperature in shadow, after the initial cool-down, can not be expected. Due to the relatively high $\frac{A\epsilon}{MC}$ ratio and (possible) low rate of attitude change with time, temperature can be considered in a quasi steady-state and array temperature immediately before emerging into sunlight can be assumed to be a function of array attitude and altitude at this pre-emergence time. Figure 2.5.7 gives this quasi steady-state temperature as a function of array attitude and altitude; the radiation configuration factors between array and Earth were obtained from Reference 2.5.2. It is assumed that direct and reflected radiative input from the spacecraft is negligible, as is shadowing of Earth input by the spacecraft.

2.5.1.3 Array Temperatures With Albedo and Earth I. R. Input

As shown in Figure 2.5.6, array temperature will, within some five minutes of emerging from shadow, assume a temperature close to a steady-state corresponding to the particular array surface thermal properties and Earth input. Constant direct solar flux and constant Earth emission were assumed for this example although there will actually be a time-varying albedo and Earth I. R. input

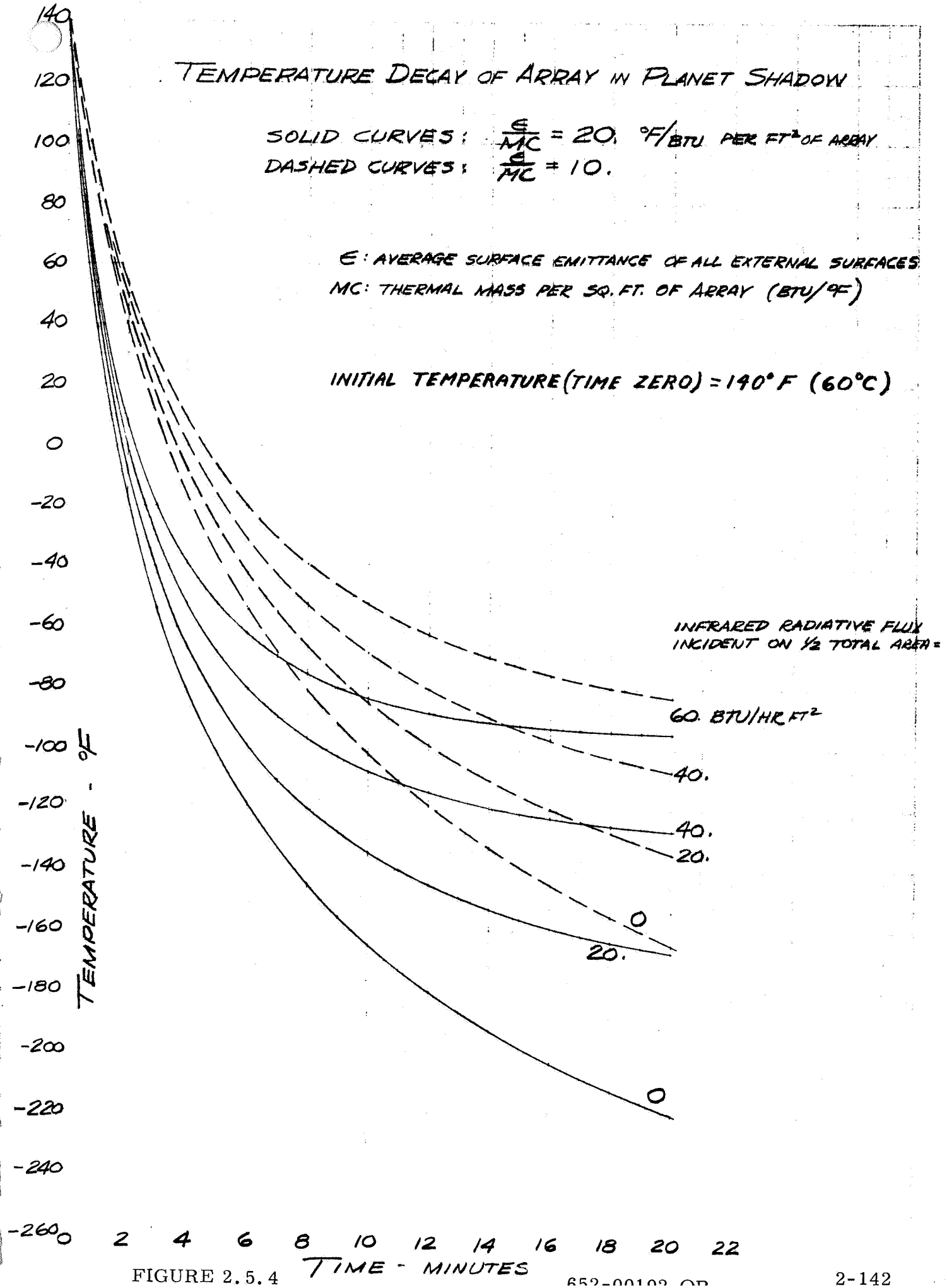

TEMPERATURE DECAY OF ARRAY IN PLANET SHADOW
SOLID CURVES: $\frac{\epsilon}{MC}$ = 20. °F/BTU PER FT² OF ARRAY
DASHED CURVES: $\frac{\epsilon}{MC}$ = 10.
ε: AVERAGE SURFACE EMITTANCE OF ALL EXTERNAL SURFACES
MC: THERMAL MASS PER SQ. FT. OF ARRAY (BTU/°F)
INITIAL TEMPERATURE (TIME ZERO) = 140° F (60°C)
INFRARED RADIATIVE FLUX INCIDENT ON ½ TOTAL AREA =
60. BTU/HR FT²
40.
40.
20.
0
20.
0
TEMPERATURE - °F
140
120
100
80
60
40
20
0
-20
-40
-60
-80
-100
-120
-140
-160
-180
-200
-220
-240
-260
0 2 4 6 8 10 12 14 16 18 20 22
TIME - MINUTES

FIGURE 2.5.4

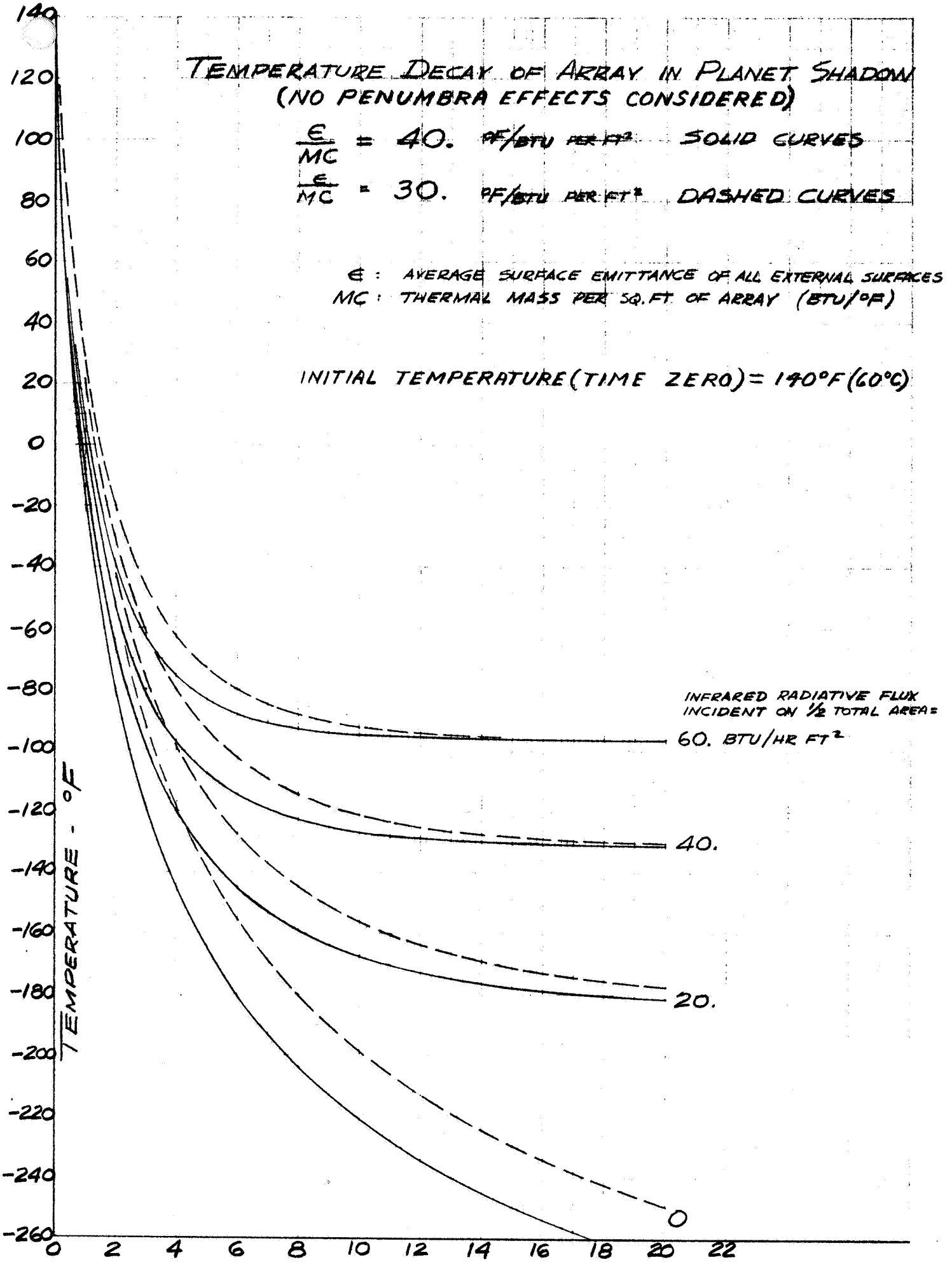

TEMPERATURE DECAY OF ARRAY IN PLANET SHADOW
(NO PENUMBRA EFFECTS CONSIDERED)
ε/MC = 40. °F/BTU PER FT² SOLID CURVES
ε/MC = 30. °F/BTU PER FT² DASHED CURVES
ε : AVERAGE SURFACE EMITTANCE OF ALL EXTERNAL SURFACES
MC : THERMAL MASS PER SQ. FT OF ARRAY (BTU/°F)
INITIAL TEMPERATURE (TIME ZERO) = 140°F (60°C)
INFRARED RADIATIVE FLUX INCIDENT ON ½ TOTAL AREA =
60. BTU/HR FT²
40.
20.
0
TEMPERATURE - °F
140
120
100
80
60
40
20
0
-20
-40
-60
-80
-100
-120
-140
-160
-180
-200
-220
-240
-260
0
2
4
6
8
10
12
14
16
18
20
22
TIME - MINUTES

FIGURE 2.5.5

FIGURE ~~2.5.~~6

TRANSIENT TEMPERATURE BEHAVIOR OF ARRAY UPON EMERGING FROM EARTH SHADOW - PENUMBRA IGNORED

CONSTANT INFRARED FLUX OF 20. BTU/HR FT² ON HALF OF TOTAL ARRAY SURFACE AREA

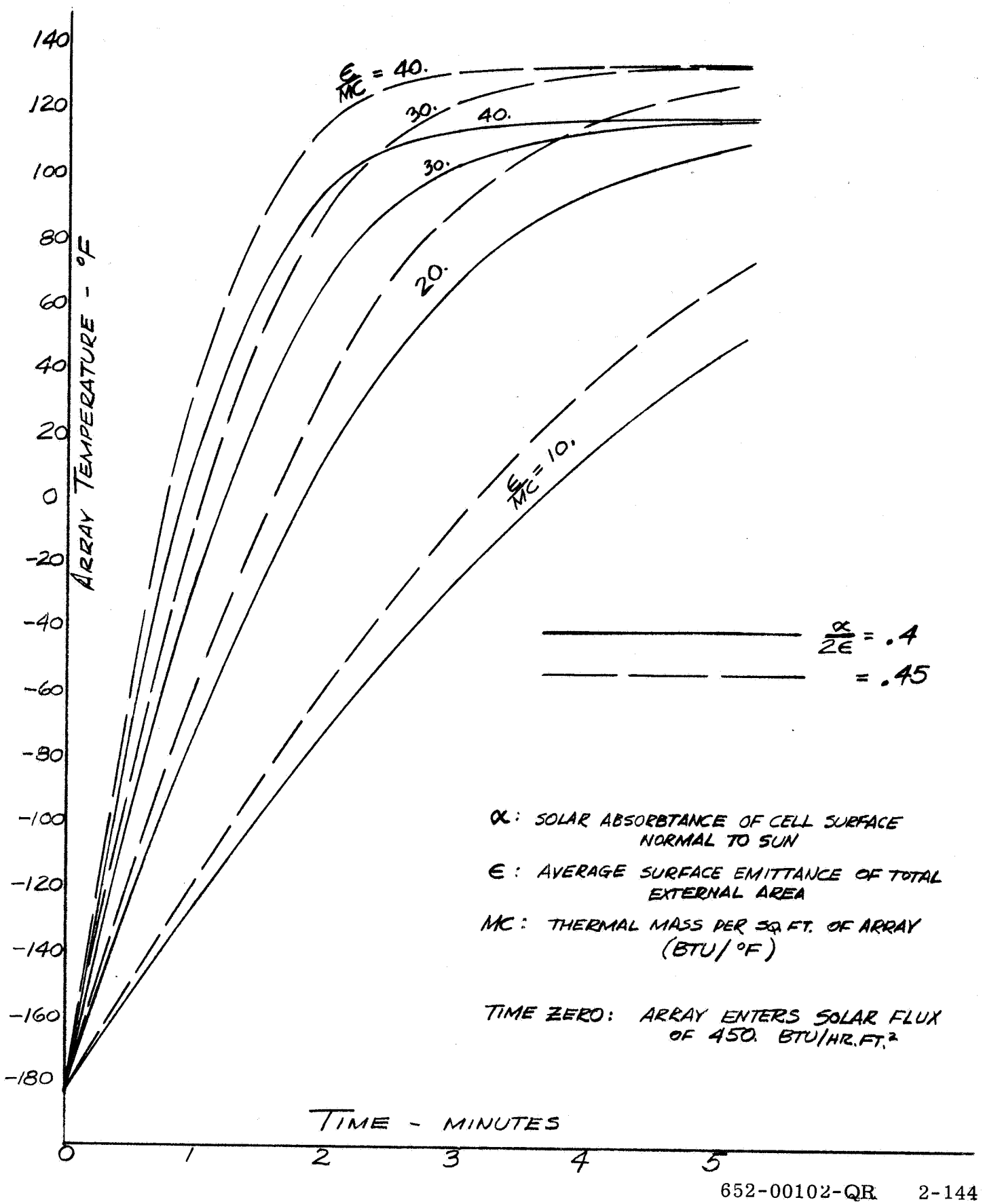
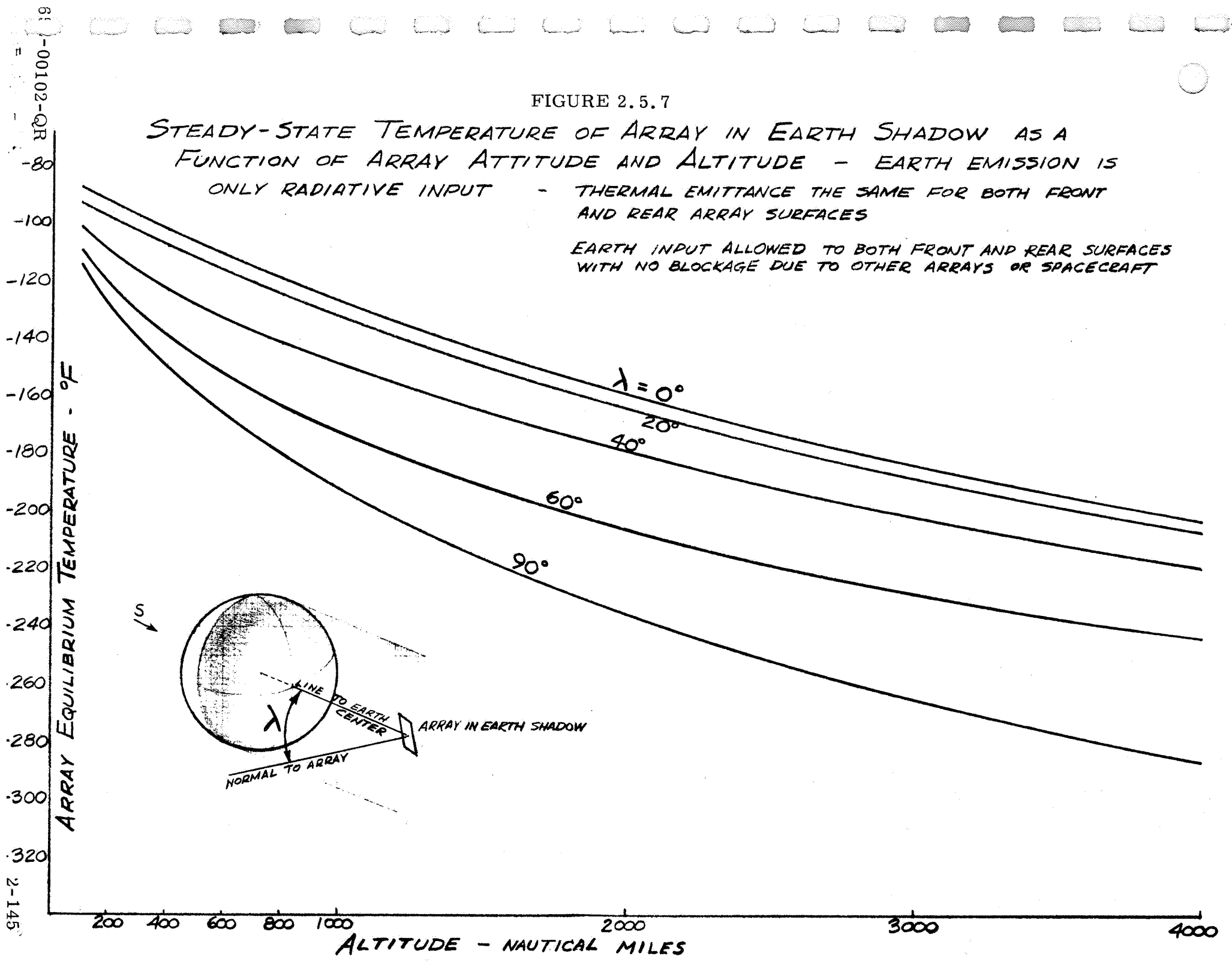


FIGURE 2.5.7

STEADY-STATE TEMPERATURE OF ARRAY IN EARTH SHADOW AS A FUNCTION OF ARRAY ATTITUDE AND ALTITUDE - EARTH EMISSION IS ONLY RADIATIVE INPUT - THERMAL EMITTANCE THE SAME FOR BOTH FRONT AND REAR ARRAY SURFACES

EARTH INPUT ALLOWED TO BOTH FRONT AND REAR SURFACES WITH NO BLOCKAGE DUE TO OTHER ARRAYS OR SPACECRAFT



to the sun-oriented array as it proceeds through the sunlit portion of its orbit. These variable incident fluxes were computed for a 100 nautical mile circular orbit, orbital plane containing the solar vector, utilizing Reference 2.5.2, and are illustrated for a quarter of an orbit in Figure 2.5.8.

To aid in a parametric evaluation of rear surface thermal properties, the resultant array temperatures were computed for the conditions of rear surface emittances of .75 and .85 and absorbtances of .4, .7, and 1., as shown in Figure 2.5.9. The effects upon array temperature of the thermal properties of the rear surface are thus made graphic. For close-Earth orbits, such as the one examined, these thermal properties do have significance. The orbit considered is admittedly extreme (the altitude is minimum and the solar vector lying in the orbital plane maximizes albedo). To obtain a feeling for the variation of array temperature with altitude, the maximum array temperature (that at the subsolar point) is presented as a function of altitude in Figure 2.5.10. It is seen that there is no significant relief of these maximum temperatures until orbit altitudes are in the order of several thousand nautical miles or more.

As the orbit plane is tilted out of the Earth-sun line, Earth input will diminish. The maximum array temperature for such a tilted orbit will occur at the point where the solar vector is perpendicular to the orbit path. Because of the attitude similitude created by array sun orientation, this temperature can be extracted from Figure 2.5.9 (for the 100 nautical mile orbit) by converting the abscissa to "the angle between the Earth-sun line and the orbital plane", using the same angle scale. The ordinate would then become "maximum array temperature".

2.5.2 Optimum Extension Arm Thermal Coating

The folding arm of corrugated square cross section was examined under two radically different thermal environments: First, with a longitudinal gap in the array substrate sheet directly above the entire arm length, and second, with a continuous substrate (no gap).

2.5.2.1 Array Gap Directly Above Arm

Arm external coating selection (with the array gap) is dictated primarily by the requirement that the solar flux which impinges directly on the top arm surface

FIGURE 2.5.8

ALBEDO AND EARTH EMISSION FLUXES INCIDENT ON SUN ORIENTED ARRAY IN SUNLIT PORTION OF NEAR-EARTH ORBIT - 100 NAUMILE CIRCULAR ORBIT, ORBITAL PLANE CONTAINING THE EARTH-SUN LINE

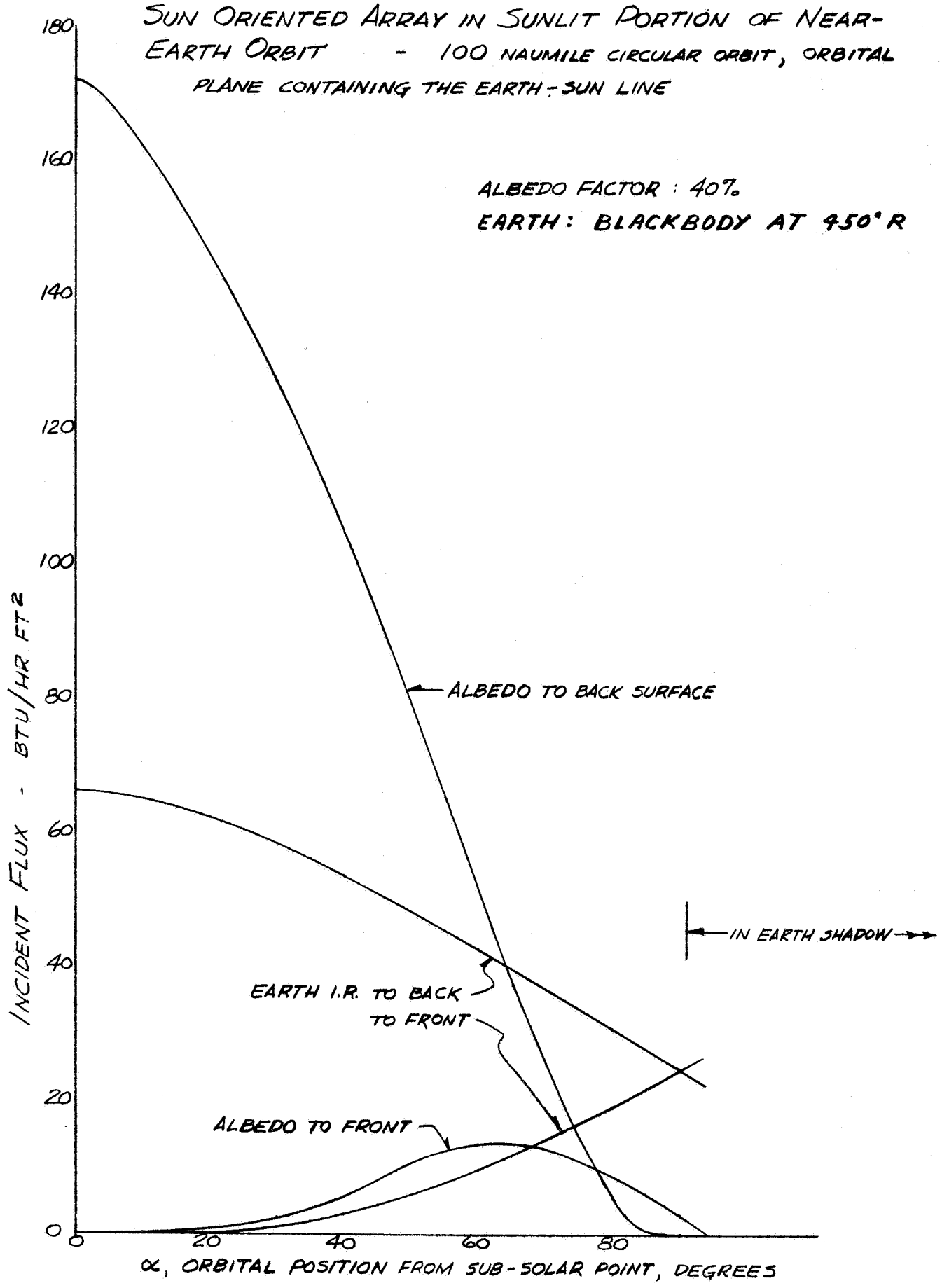


FIGURE 2.5.9

TEMPERATURE HISTORY OF ARRAY IN SUNLIT PORTION OF LOW ALTITUDE EARTH ORBIT, WITH ALBEDO AND EARTH I.R. INPUTS

100 NAUMILE CIRCULAR ORBIT, ORBITAL PLANE CONTAINING THE EARTH-SUN LINE
SUN ORIENTED ARRAY
INCIDENT FLUXES : REFERENCE PREVIOUS FIGURE

THERMAL PROPERTIES OF SUNLIT ARRAY SURFACE : $\alpha = .7$, $\epsilon = .85$
BACK SURFACE EMITTANCE $\epsilon = .85$ ——————
$\epsilon = .75$ — — — —

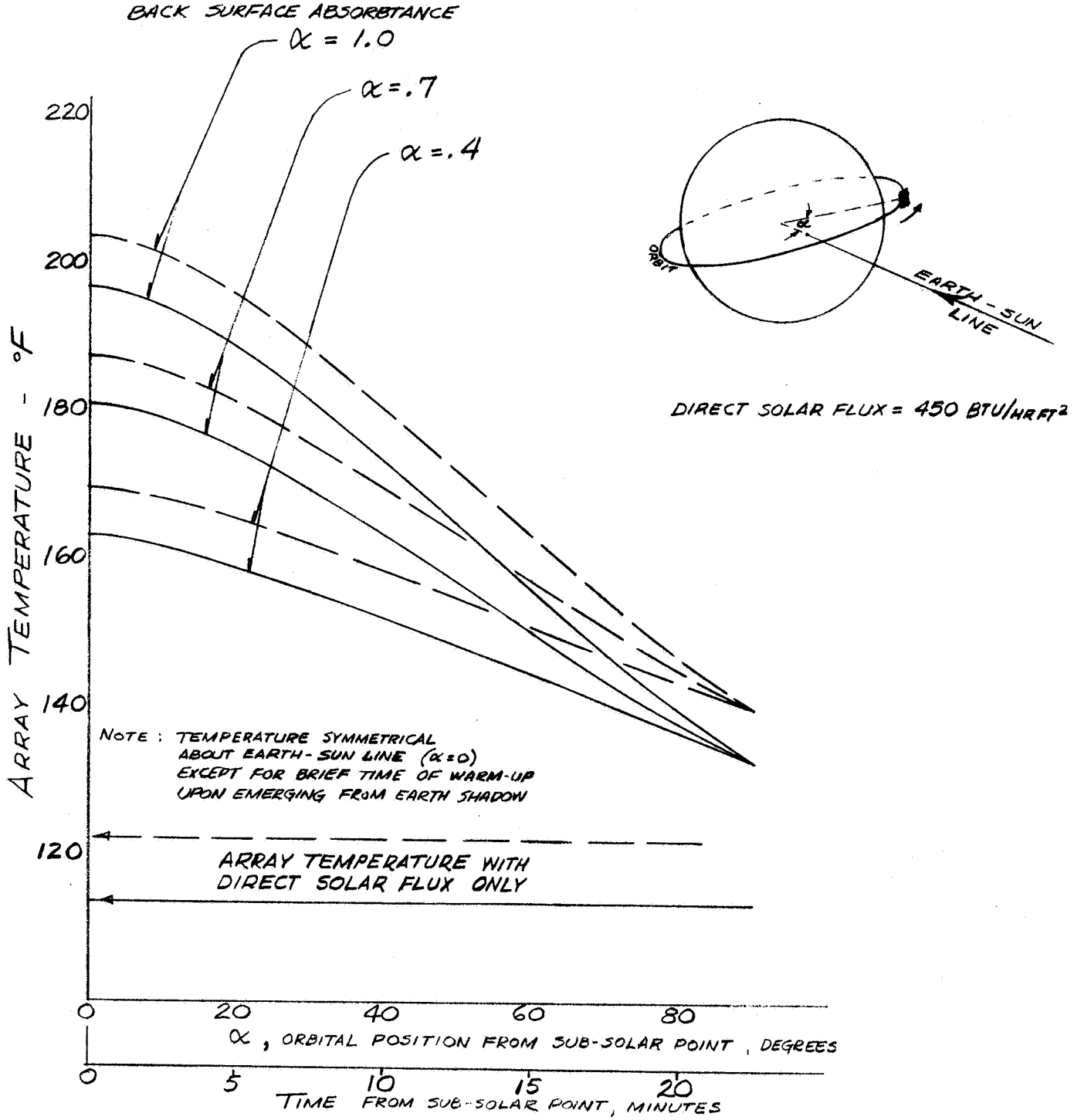
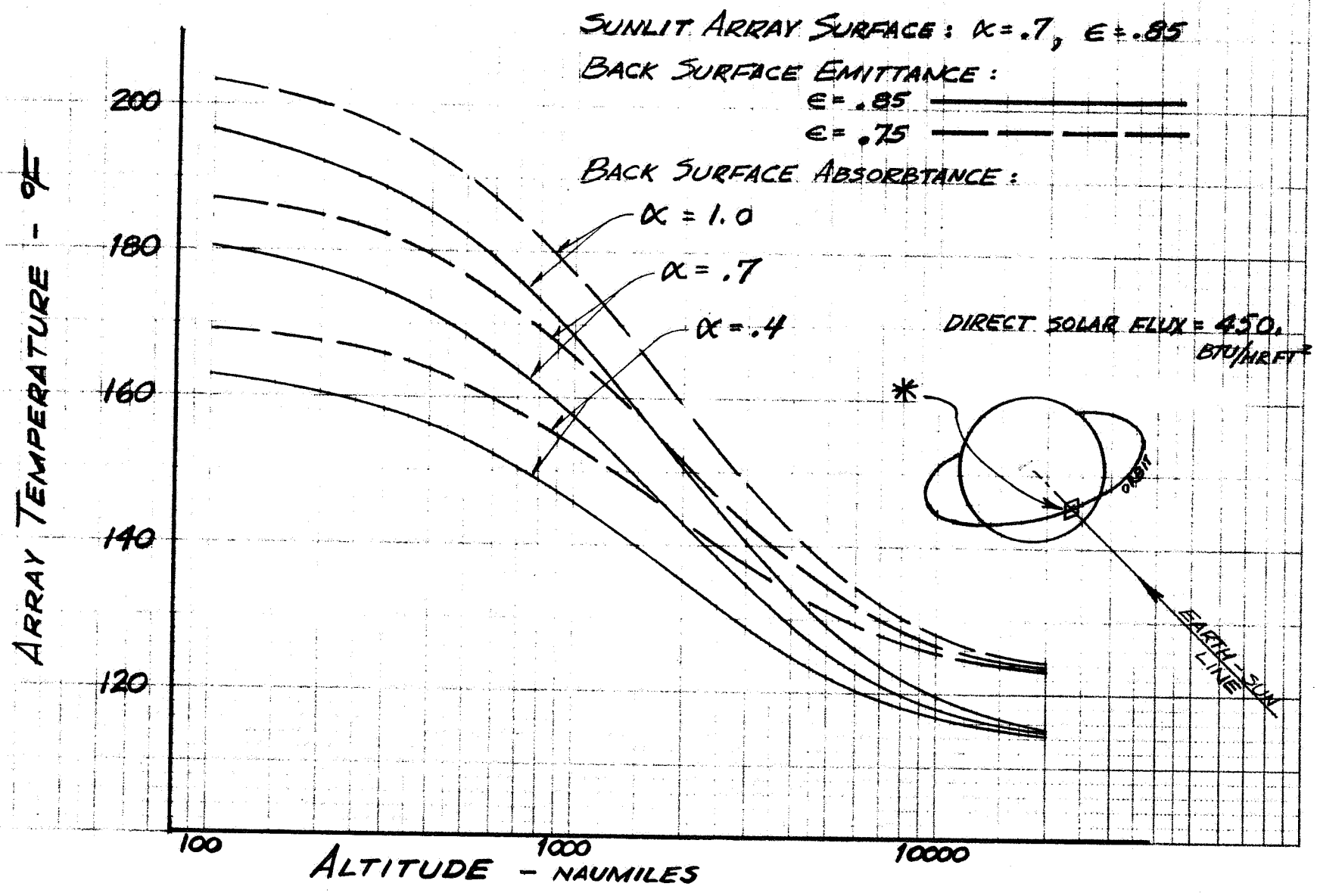


FIGURE 2.5.10

ARRAY TEMPERATURE AT SUBSOLAR POINT* (MAXIMUM ORBITAL TEMPERATURE) WITH ALBEDO AND EARTH I.R. INPUT VS. ALTITUDE



be prevented from reflecting back onto the array rear surface.

While a minimum absorptance surface would minimize both arm temperatures and infrared radiative input from arm to array, it would also result in a maximum solar reflected input to the array. This is an intolerable condition when considering the almost catastrophic rise in local array temperature when solar input is almost doubled (e.g. from, say, 115°F to 220°F). In an attempt to direct all reflected solar flux back through the gap, away from the array, the corrugated surface (which would approximate a diffuse reflector) should be covered with a perfectly flat surface, which must be maintained normal to the sun at all times. Considering the very likely possibilities of an array assembly which is not aligned normal to the sun or an arm with a torsional twist due to slight thermal or mechanical stress or imperfect fabrication, this concept must be abandoned. It is therefore imperative that the arm top surface be given a high solar absorptance; ie., a low solar reflection.

A thermal model of the arm and array was developed, as illustrated in Figure 2.5.11. The arm-array separation was taken as 2" with a 2-1/4" square arm cross section. Two extreme arm materials were considered, corresponding to a graphite composite and beryllium: One of low conductivity, 0.5 BTU/hr.ft.°F, and .015" thick, and a high conductivity .87 BTU/hr. ft.°F with a .02" thickness. Both a 2-1/4" and 1-1/2" gap width were studied; it is seen that for a 2-1/4" width, node 10 "disappears". Since much of the I. R. flux to the array emanates from the top arm surface, a reduction in the emittance of this surface, while raising overall arm temperatures, may lower the radiative input to the back array surface. Therefore, an emittance of 0.1 (applied to a smooth flat surface) was considered in addition to the more readily obtained 0.85. The corrugated "texture" of the arm surface can be conveniently thermally ignored for the high α and ϵ surfaces; such a surface irregularity essentially increases through multiple reflections the α and ϵ of the corresponding "optically flat" surface.

The temperature results of the analyses employing this thermal model are shown in Figures 2.5.12, 2.5.13, 2.5.14. It can be seen from Figure 2.5.12 that lowering the emittance on the top arm surface from .85 to .1, while lowering maximum array temperatures for the low conductivity arm, causes an increase in

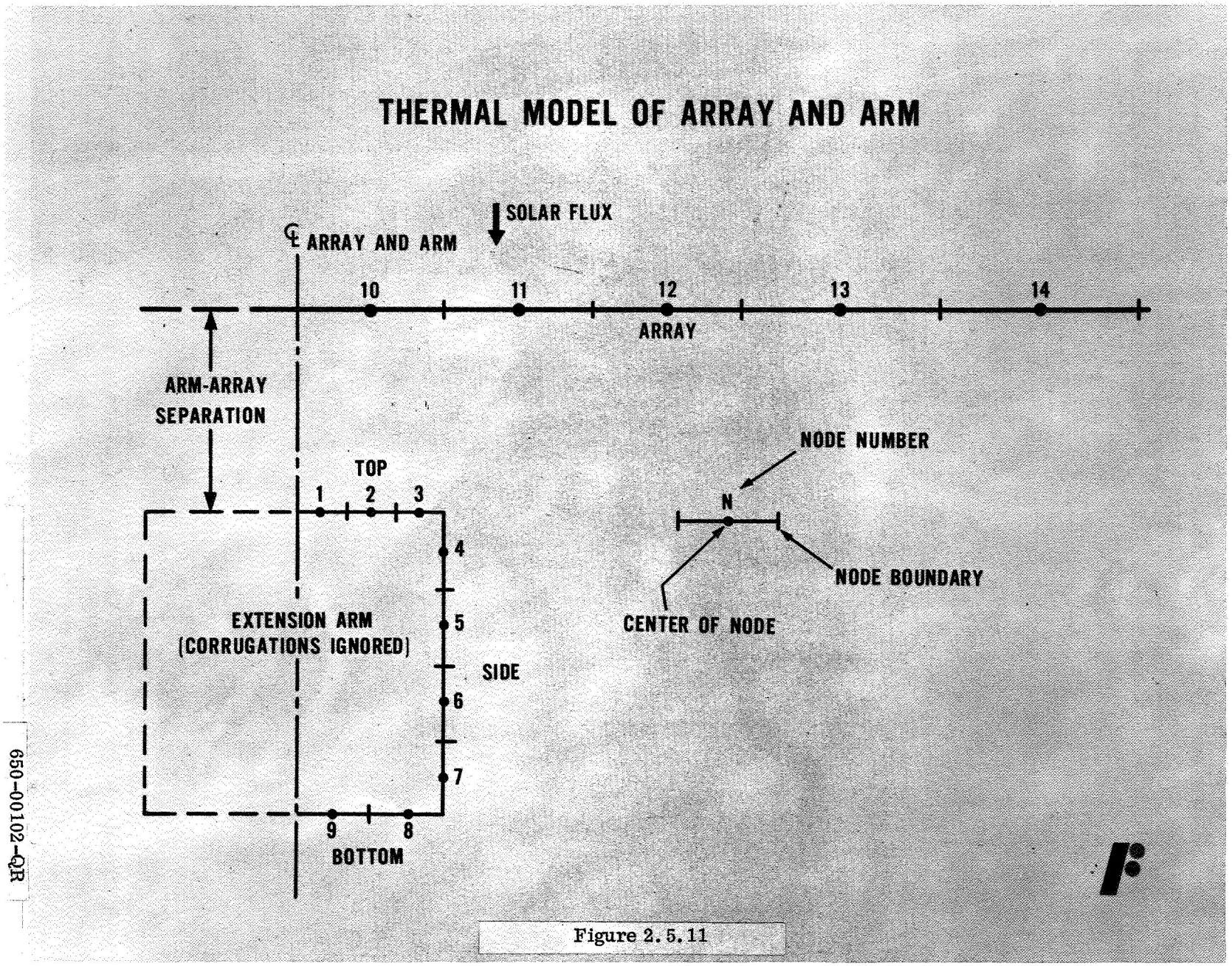

THERMAL MODEL OF ARRAY AND ARM
SOLAR FLUX
℄ ARRAY AND ARM
10
11
12
13
14
ARRAY
ARM-ARRAY SEPARATION
TOP
1
2
3
4
5
6
7
8
9
SIDE
BOTTOM
EXTENSION ARM (CORRUGATIONS IGNORED)
NODE NUMBER
N
NODE BOUNDARY
CENTER OF NODE

Figure 2.5.11

array temperatures with the high conductivity arm. This is due to the extreme difference in the top surface temperature of the arms, as shown in Figure 2.5.14. The high temperature associated with the low conductivity arm implies that its top surface is the more significant contributor of infrared radiation to the array.

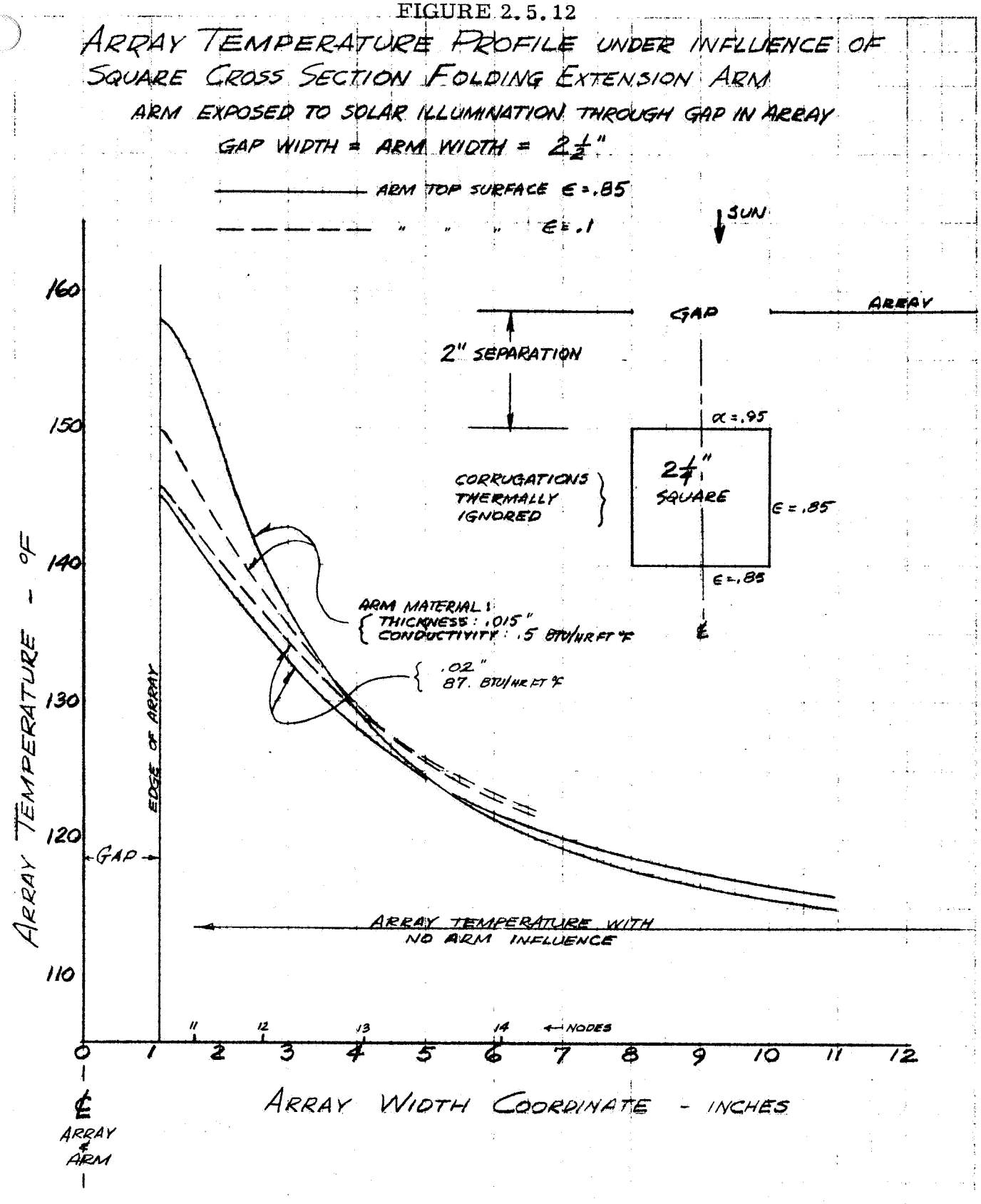
A comparison of Figures 2.5.12 and 2.5.13 demonstrates a significant trend: Narrowing the gap in the array improves the array temperature profile. A further narrowing of this gap, by allowing the arm to run cooler under its lower sun absorption, will reduce array temperatures below those of Figure 2.5.13, even though for the low conductivity arm, the maximum array temperature (at the gap edge) will apparently not be significantly reduced.

Having concluded that a minimum gap width is desirable, the question arises as to whether solar cells should cover the entire array up to the edge of the gap. The array power-to-weight ratio may increase if cells were to be moved away from this "inefficient", high temperature area next to the gap. Moreover, by utilizing a low absorptance, high emittance thermal coating instead of cells in this area, the temperature of the cells further away may be lessened due to the resultant lower arm temperature. To discover the degree of improvement possible with such a technique, the array-arm configuration corresponding to Figure 2.5.13(a 1-1/2" gap width) was modified by reducing the absorptance of the array front surface from .7 to .25 for a distance of 1-3/8" from the gap edge (nodes 10 and 11 of the thermal model). For purposes of comparison, the resultant temperature distribution is plotted (dashed curves) in Figure 2.5.13. The decrease in array temperature outside this reduced α area is not significant.

2.5.2.2 · Continuous Array Above Arm - 2-1/4" Square

With a gap in the array above the arm, Figure 2.5.14 shows the very extreme (most likely intolerable) temperature gradients across the arm of low conductivity (on the order of 200^{o}F), due primarily to the arms sun exposure. The condition of no direct solar flux was thus examined by assuming a continuous array substrate above the arm. Node 10 in the thermal model was extended to "cover" the entire gap of the previous model.

FIGURE 2.5.12



NOTE: TEMPERATURE PROFILE SYMMETRICAL ABOUT ℄

FIGURE 2.5.13

ARRAY TEMPERATURE PROFILE UNDER INFLUENCE OF SQUARE CROSS SECTION FOLDING EXTENSION ARM

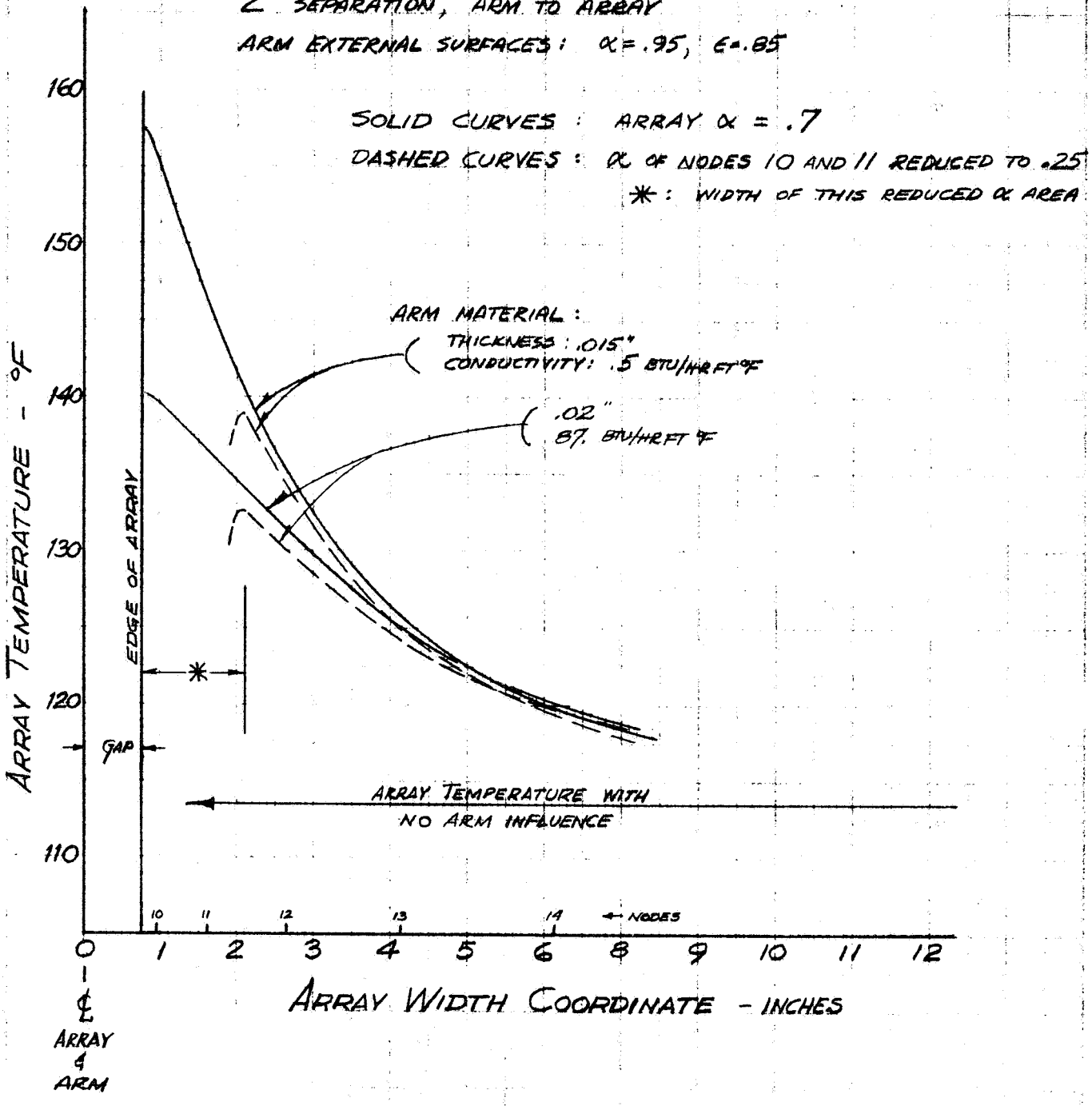
ARM EXPOSED TO SOLAR ILLUMINATION THROUGH GAP IN ARRAY

GAP WIDTH = 1.5"

2½" SQUARE ARM CROSS SECTION

2" SEPARATION, ARM TO ARRAY

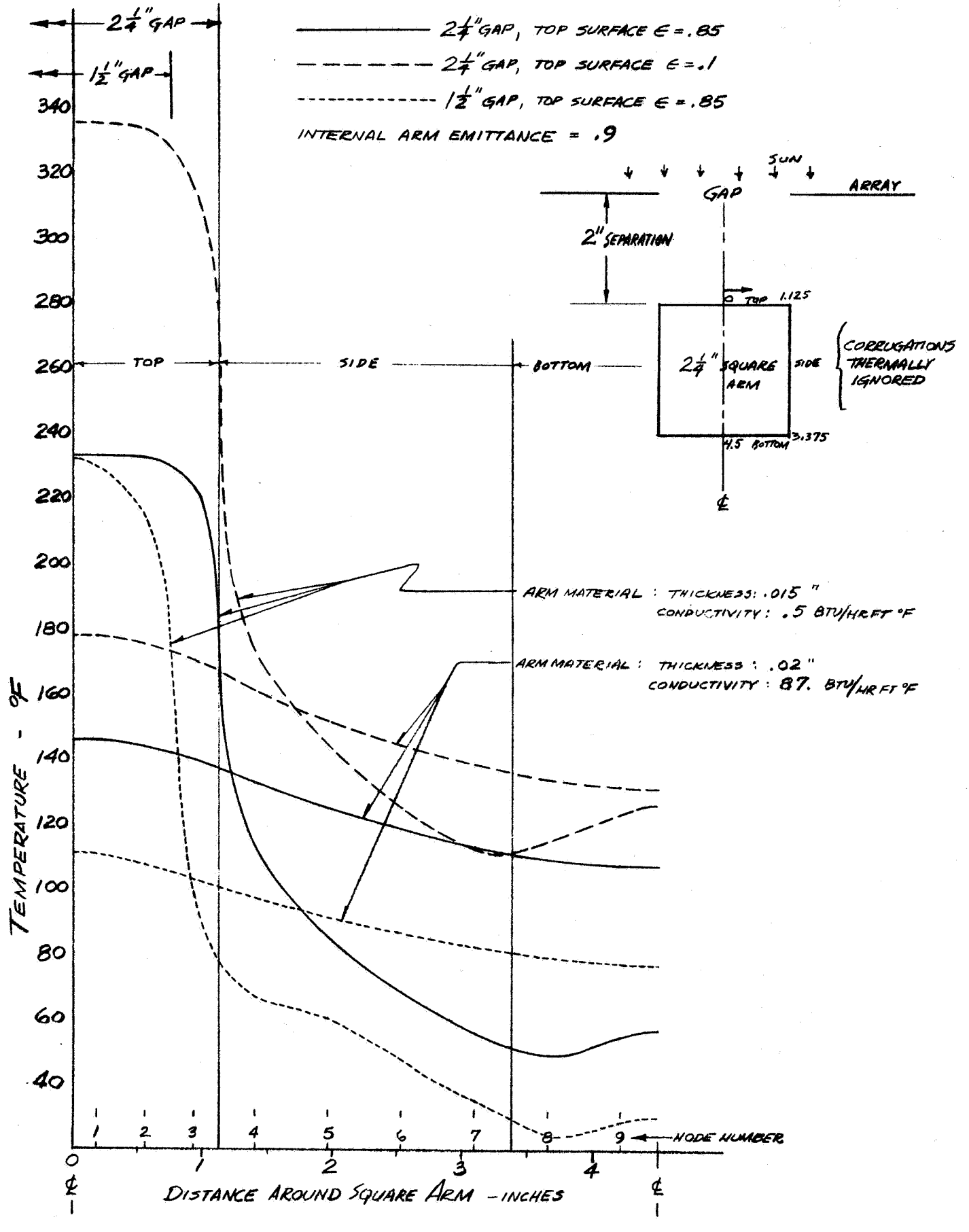
ARM EXTERNAL SURFACES: $\alpha = .95$, $\epsilon = .85$



NOTE: TEMPERATURE PROFILE SYMMETRICAL ABOUT ℄

FIGURE 2.5.14

TEMPERATURE DISTRIBUTION IN $2\frac{1}{4}$" SQUARE ARM EXPOSED TO DIRECT SUN THROUGH GAP IN SOLAR ARRAY



It is obvious that to minimize temperature-induced distortion of the extension arm, external surfaces of the arm should be of minimum emittance so as to minimize the heat ransfer with the external environment. There is, however, the thermal interaction of the arm and array to be considered, and any low emittance surface close to the rear face of the array would have the effect of interferring with the radiative heat transfer from the array (by means of reflecting this infrared radiation), resulting in locally increased array temperature. The question naturally arises, then, as to whether a low ϵ or a high ϵ arm external surface would least affect array temperatures. The flux contribution to the array from a low ϵ surface is primarily in the form of reflected energy from the array itself; a high ϵ arm surface would contribute primarily direct radiation based on its own temperature. If the arm is correlated to a single layer radiation shield, then the low ϵ surface would be a more effective shield; i.e., maintain higher array temperatures. Thus it appears that a high ϵ, say "black", arm would be more desirable with respect to lower array temperatures; it would, however, suffer from more severe circumferential temperature gradients and resultant distortion. There must then be a systems evaluation to determine the "optimum" arm thermal coatings: a high ϵ to minimize array local temperature increase while suffering thermal distortion, or a low ϵ to minimize distortions at the expense of array higher local temperatures.

A "minimum" emittance of .05 was applied to the arm external surfaces in an effort to minimize the temperature gradients across the arm. The rear surface of the array was allowed to "view" itself via reflections from the arm; the corrugated surface permits an assumption of diffuse reflectivity. Both the "low" conductivities of .5 BTU/hr. ft. ^{o}F and 1.0 BTU/hr.ft. ^{o}F were examined; the resultant arm temperature profiles differ negligibly as shown in Figure 2.5.16. What is significant is the dramatic reduction in temperature gradient across the arm (compare Figures 2.5.14 and 2.5.16) brought about by not allowing direct sun impingement.

Array temperatures in the vicinity of the arm do not differ appreciably between the gap and no-gap cases (compare Figures 2.5.13 and 2.5.15).

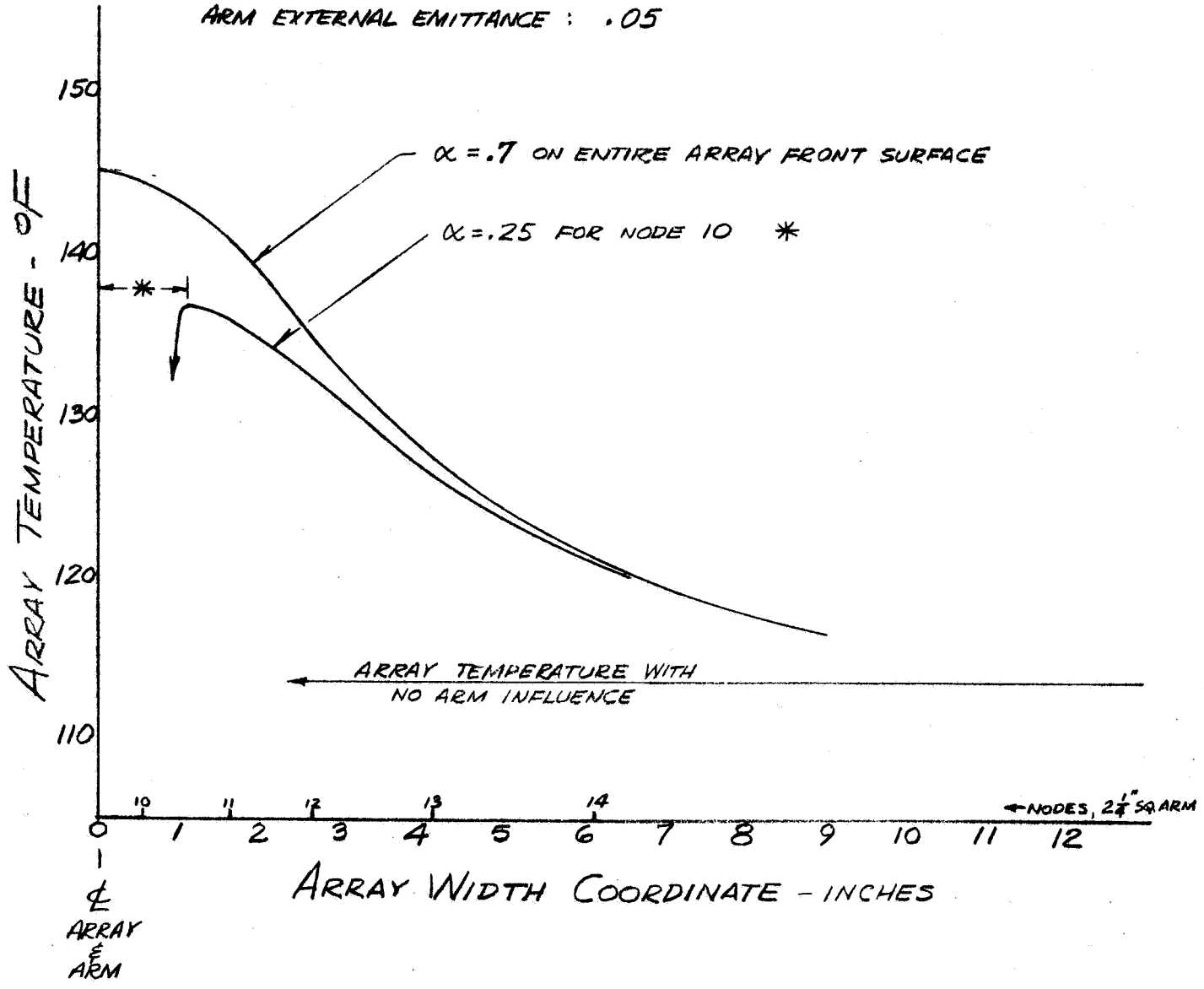
FIGURE 2.5.15

ARRAY TEMPERATURE PROFILE UNDER INFLUENCE OF SQUARE CROSS SECTION FOLDING EXTENSION ARM - CONTINUOUS ARRAY ABOVE ARM - NO DIRECT SOLAR FLUX

2¼" SQUARE ARM, 2" BETWEEN ARM AND ARRAY

ARM MATERIAL : THICKNESS : .015"
CONDUCTIVITY : .5 BTU/HR FT °F } NO NOTICEABLE DIFFERENCE
OR 1.0 BTU/HR FT °F }

ARM EXTERNAL EMITTANCE : .05

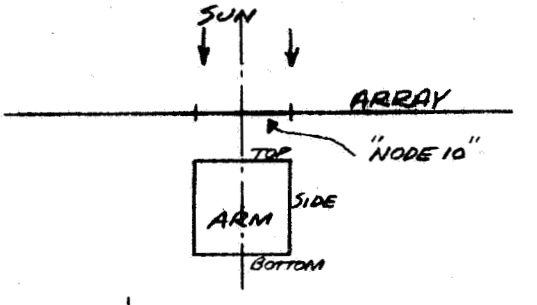


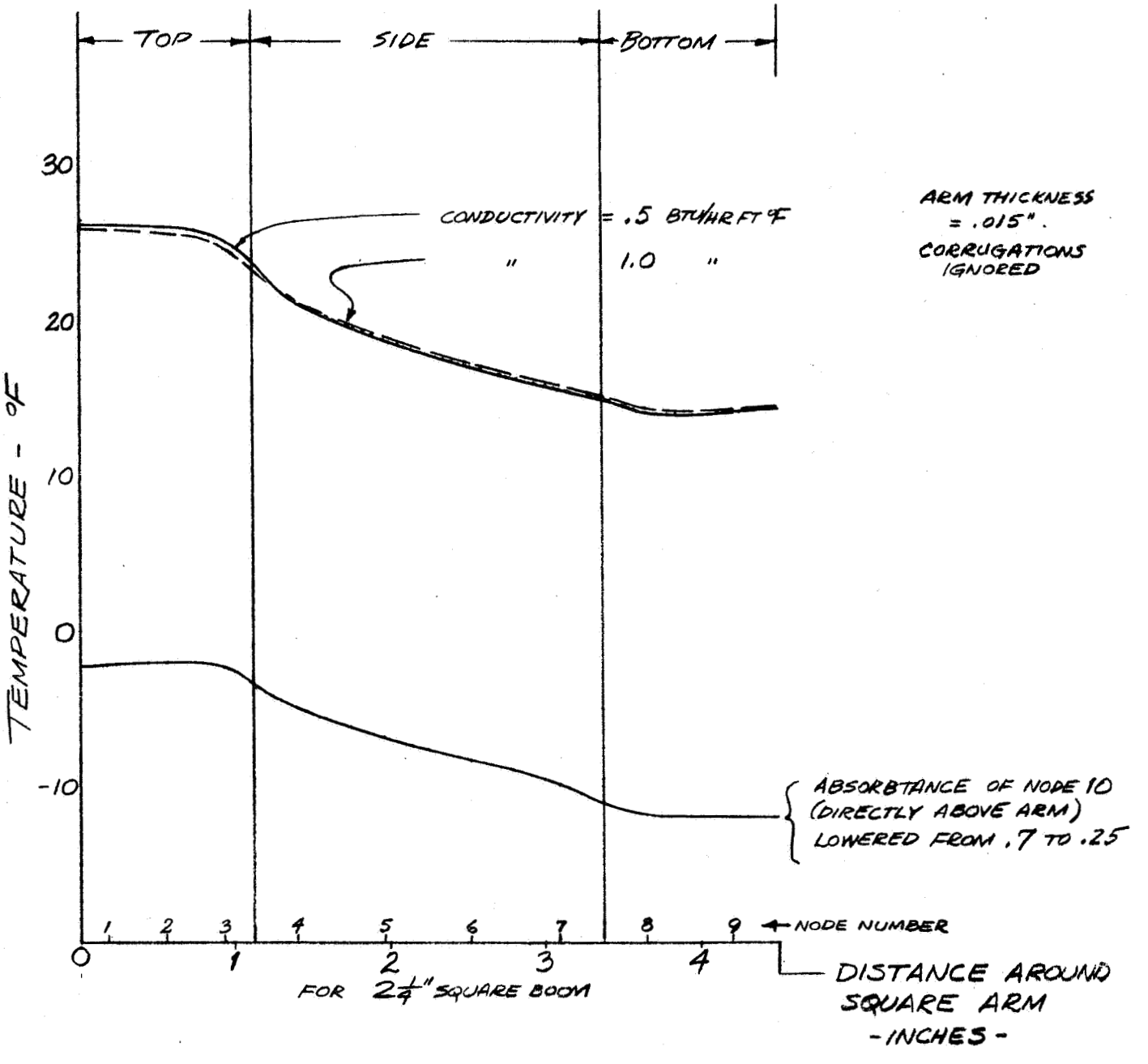
NOTE : TEMPERATURE PROFILE SYMMETRICAL ABOUT ℄

FIGURE 2.5.16
TEMPERATURE DISTRIBUTION IN 2¼" SQUARE ARM WITH RADIATIVE INPUT FROM ARRAY ONLY (NO DIRECT SOLAR FLUX)

EXTERNAL ARM EMITTANCE : .05
INTERNAL " " : .9

ARRAY-ARM SEPARATION : 2"





There is a slight improvement (reduction) in array temperature when the absorptance of node 10 (directly above the arm) is lowered from .7 (solar cells) to .25 (thermal coating - no cells), as illustrated in Figure 2.5.15. The gradient across the arm is also reduced somewhat, from 12°F to 10°F, as is the overall temperature level of the arm (Figure 2.5.16).

2.5.2.3 Three Inch Square Arm

Based on structural analysis subsequent to the 2-1/4" arm thermal study, arm size was revised upward to 3" square; a thermal model similar to the one sketched in Figure 2.5.11 was employed, with arm-array separations of 2" and 6". An arm lateral conductivity of .5 BTU/hr.ft.°F and .015" thickness (or .68 BTU/hr. ft.°F with the .011" thickness) was considered.

Four different arm coating patterns were examined: in addition to all "black" (ϵ = .85) and all "metallized" (ϵ = .05) arms, there were the cases of a black top, metallized sides and bottom, and black top and sides, metallized bottom. The array and arm temperature profiles are illustrated in Figures 2.5.17 and 2.5.18. As expected, as a particular pattern tends to reduce the temperature gradient across the arm, the local temperature elevation of the array increases. Thus, an all black arm results in the minimum increase in array temperature together with a maximum temperature difference between arm top and bottom surfaces; an all metallized arm induces reversed characteristics. The 120°F gradient through the black arm precludes its consideration; the optimum arm thermal coating is at present taken to be the minimum emittance one, most likely a vacuum deposited metal coating such as aluminum.

2.5.3 Maximum Temperatures Of Array And Arm

Primarily for purposes of materials evaluation, the maximum expected temperatures of array and arm were determined; maximum arm temperature is experienced at the sub-solar point of a low altitude Earth orbit, maximum array temperature is taken at a spacecraft distance from the Sun equal to the mean Venus distance. The 3" square extension arm with 2" spacing between arm and array was examined.

CIRCUMFERENTIAL TEMP. DISTRIBUTION 3 INCH SQUARE EXTENSION ARM

2 in. SPACE BETWEEN ARRAY AND ARM

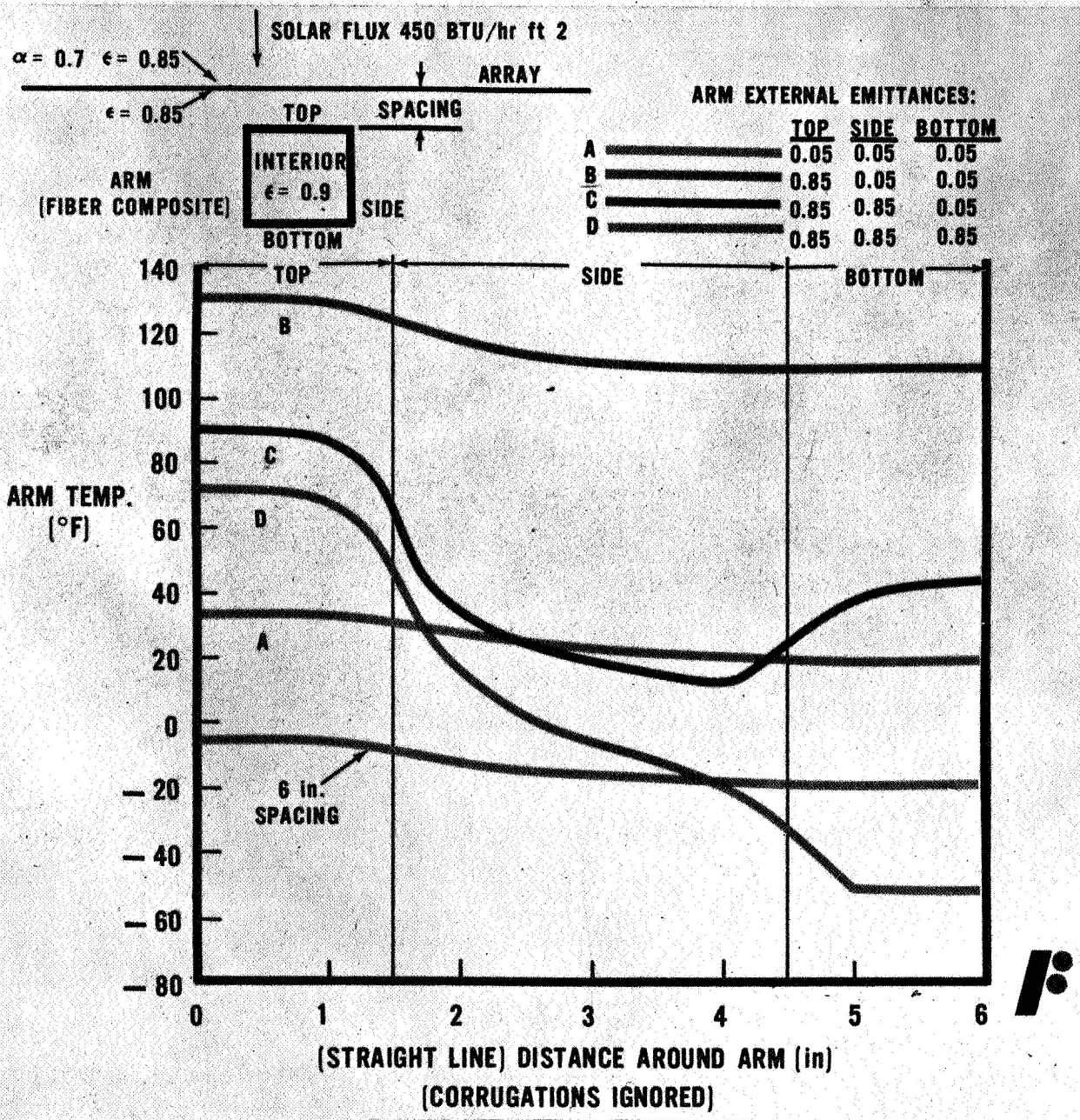


Figure 2.5.17

ARRAY TEMPERATURE PROFILE IN VICINITY OF 3 INCH SQUARE EXTENSION ARM

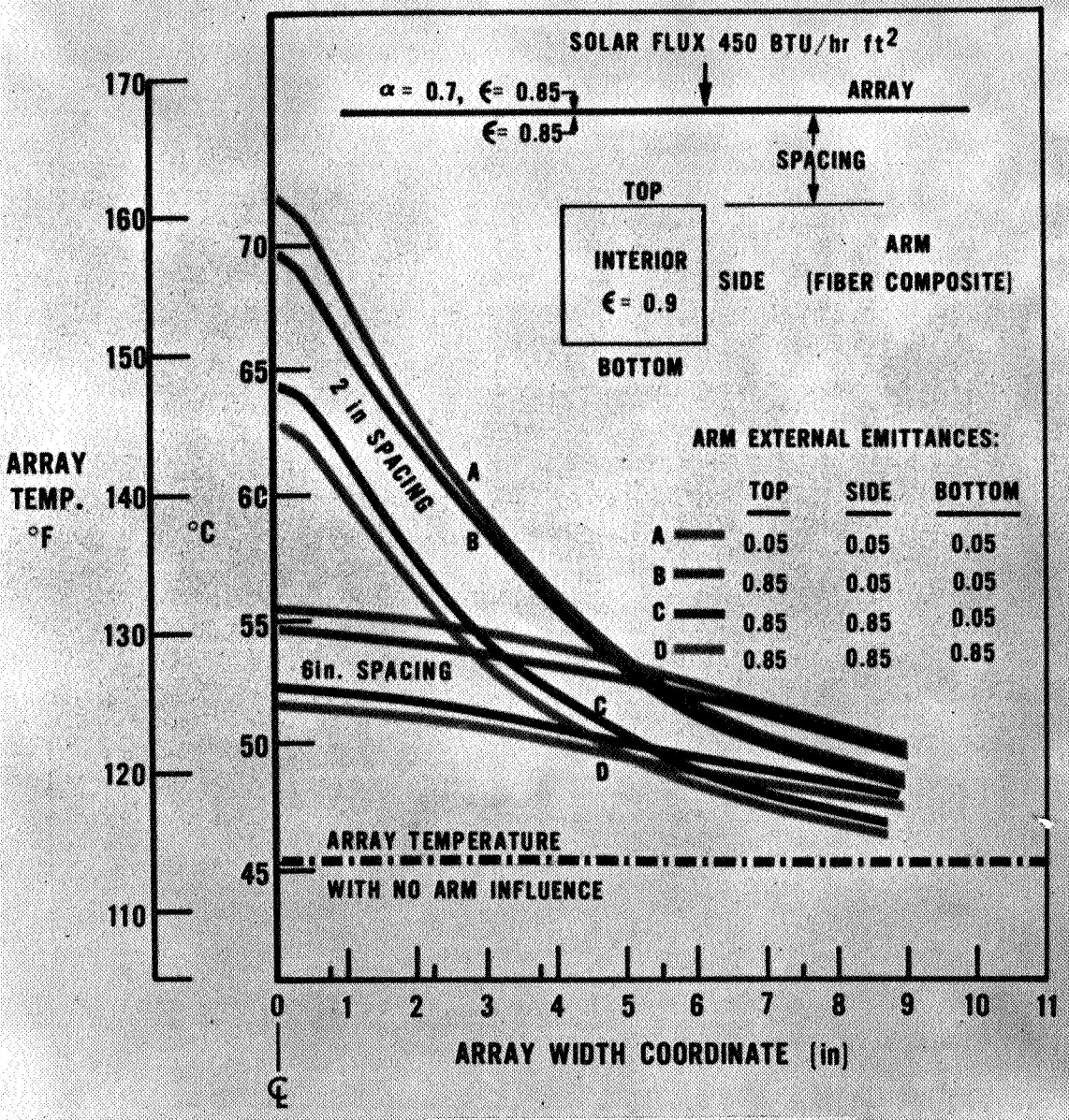


Figure 2.5.18

The Earth inputs (albedo and infrared radiation) were obtained from Reference 2.5.2 for a 100 n.m. altitude, solar array normal to the sun. No Venus albedo or infrared inputs were considered-only the solar flux of 840 BTU/hr.ft.^{2}. Figures 2.5.19 and 2.5.20 depict the temperature profiles of array and arm for these maximum temperature conditions. The maximum array temperature (near Venus) is 265^{o}F at the array centerline; maximum arm temperature (near Earth) is 280^{o}F. There still exists an acceptably small temperature gradient through the arm- 7^{o}F near the Earth and 16^{o}F at the Venus distance.

2.5.4 References

Reference 2.5.1 Fairchild Hiller Report, 652-00101SR, November 67, "Two Computor Programs for Solar Cell Array Thermal Analysis: Transient Temperature Behavior in Planet Penumbra and Reflected Radiation View Factors Due to Specular Circular Boom Adjacent to Array:.

Reference 2.5.2 "Radiation Heat Transfer Analysis for Space Vehicles" by J. A. Stevenson and J. C. Grafton of North American Aviation, Aeronautical Systems Division, Air Force Systems Command, Wright-Patterson AFB, ASD Technical Report 61-119 December 1961.

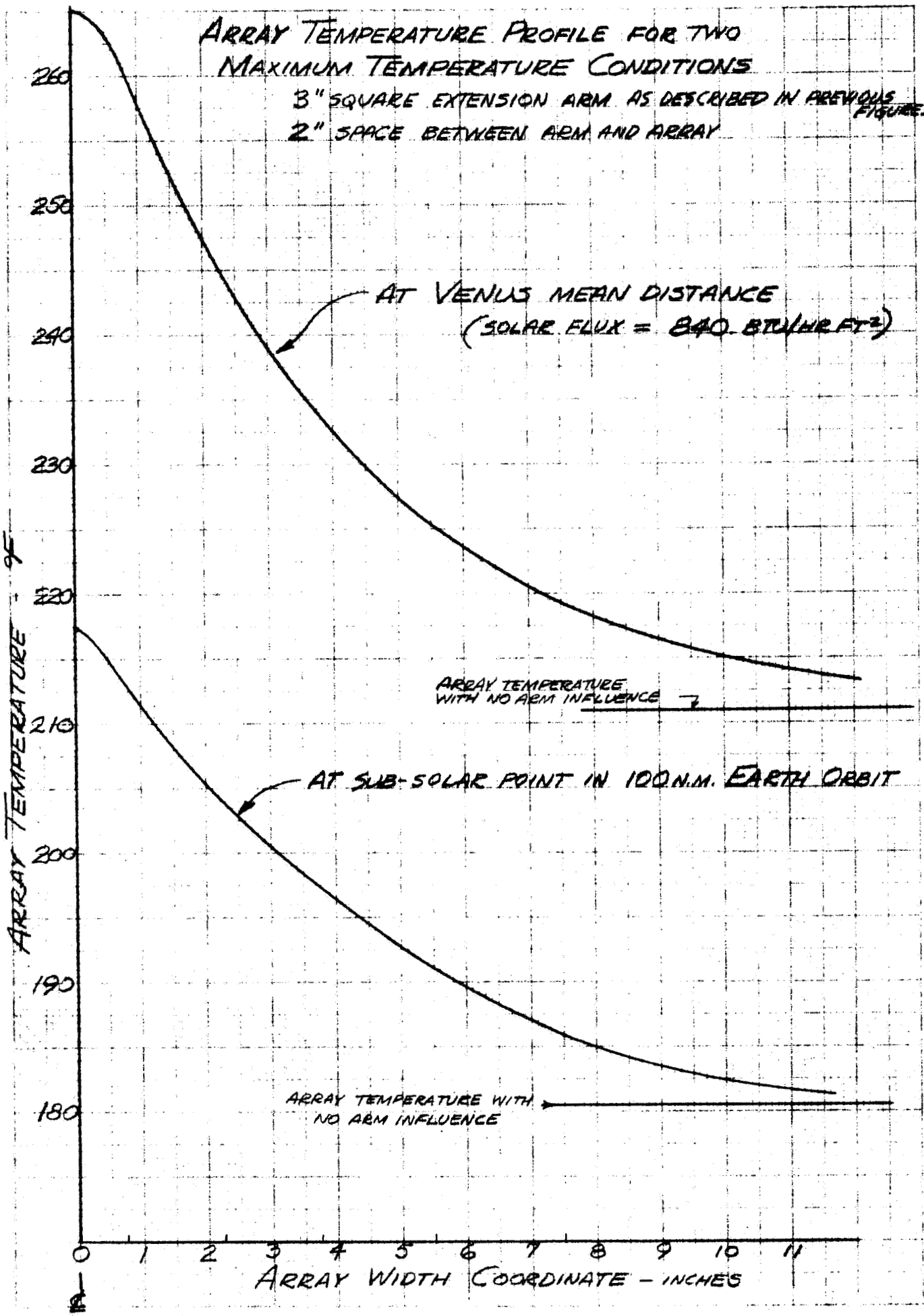

ARRAY TEMPERATURE PROFILE FOR TWO MAXIMUM TEMPERATURE CONDITIONS
3" SQUARE EXTENSION ARM AS DESCRIBED IN PREVIOUS FIGURES
2" SPACE BETWEEN ARM AND ARRAY
AT VENUS MEAN DISTANCE
(SOLAR FLUX = 840 BTU/HR FT²)
ARRAY TEMPERATURE WITH NO ARM INFLUENCE
AT SUB-SOLAR POINT IN 100 N.M. EARTH ORBIT
ARRAY TEMPERATURE WITH NO ARM INFLUENCE
ARRAY TEMPERATURE - °F
260
250
240
230
220
210
200
190
180
0
1
2
3
4
5
6
7
8
9
10
11
ARRAY WIDTH COORDINATE - INCHES

FIGURE 2.5.19

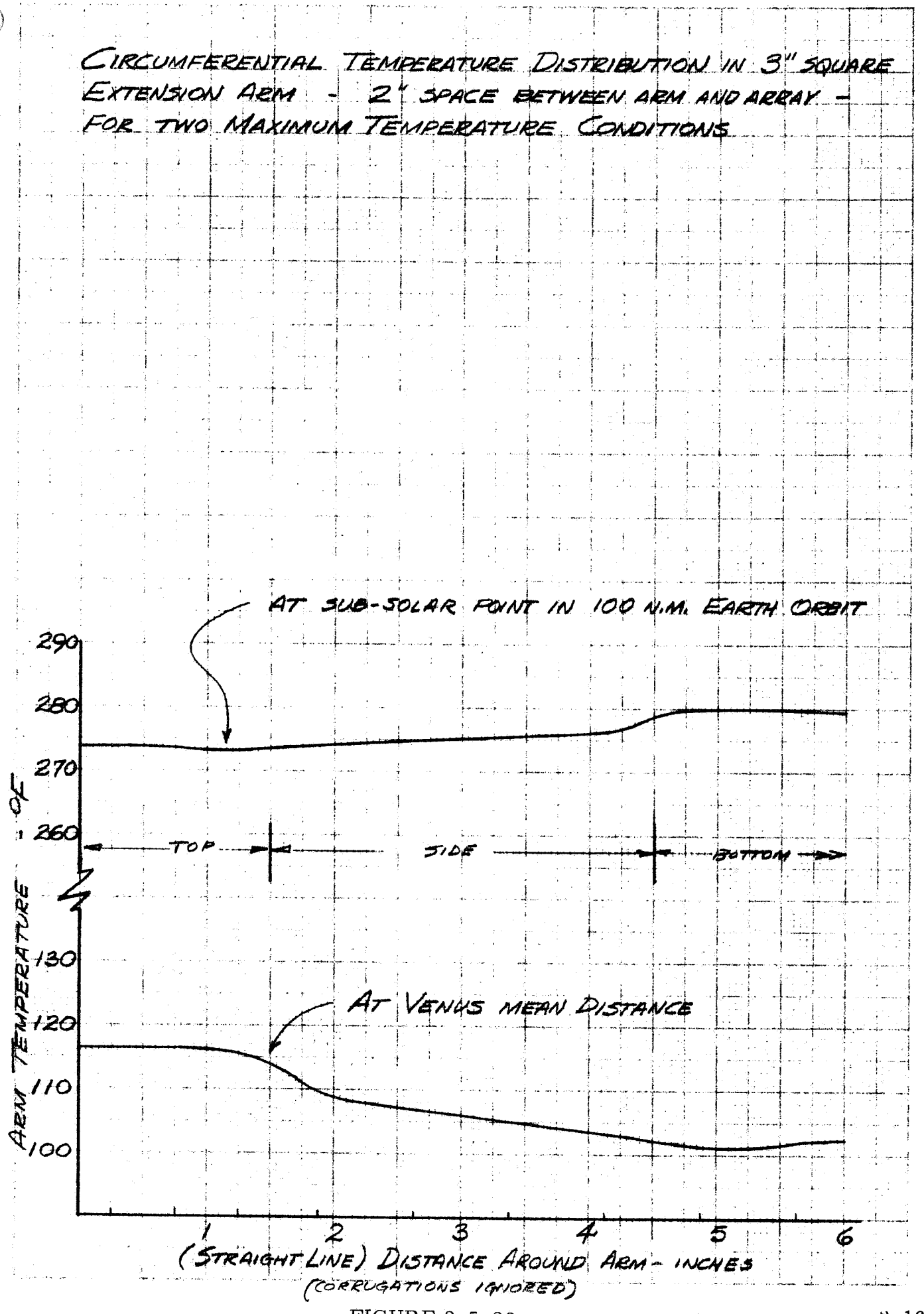

CIRCUMFERENTIAL TEMPERATURE DISTRIBUTION IN 3" SQUARE EXTENSION ARM - 2" SPACE BETWEEN ARM AND ARRAY - FOR TWO MAXIMUM TEMPERATURE CONDITIONS
AT SUB-SOLAR POINT IN 100 N.M. EARTH ORBIT
290
280
270
260
TOP
SIDE
BOTTOM
ARM TEMPERATURE - °F
130
120
110
100
AT VENUS MEAN DISTANCE
1
2
3
4
5
6
(STRAIGHT LINE) DISTANCE AROUND ARM - INCHES
(CORRUGATIONS IGNORED)

FIGURE 2.5.20

2.6 RELIABILITY

Three (3) candidate designs were analyzed for their probability of successful deployment. The design which exhibits the best reliability, the Folding Arm, has been selected as the most feasible approach to a light weight, high power solar array. The two other systems analyzed were the Hingelock and TEE with two configurations of each design considered. For the purpose of the analysis, five assumptions were made:

- Ten deployment cycles during ground test.
- One and a half deployment cycles in space.
- Each cycle takes four minutes to accomplish.
- Manufacturing would be in accordance with the design and any defects caused during fabrication would not go undetected prior to launch.
- The reliability of structural members is unity based upon application of proper safety margins.

2.6.1 Discussion

Mechanical systems suffer three (3) basic types of mortality; infant, chance and wear-out. Figure 2.6.1 graphically depicts the relationship of these types of failure. Notice that at any time (T), the gross mortality for a mechanical system is the summation of the ordinates at that time. Infant failure may be eliminated through proper inspection and test and was not considered in this analysis. By first comparing the random failure rates of the three (3) systems and then superimposing the wear-out failures, a comparison could be made. Based on past experience with Tubular Extendible Elements, it is known that wear-out symptoms appear in the element(s) after only a few deploy/retract cycles in their present state of development. That is, the wear-out curve for a TEE of Hingelock device rises much faster than does the curve for a Folding Arm design. Therefore, if the random failure rate reliability of each of the candidate design were similar (they were), then the early wear-out of TEE and Hingelock would make their total reliabilities less than the Folding Arm's, providing the mission time was greater than the wear-out time. It is felt that 11-1/2 cycles could cause a serious wear-out problem in all except the Folding Arm

design and this would interfere with mission accomplishment.

2.6.2 Candidate Designs

Seven (7) analyses were performed; six (6) were documented in detail, but the seventh (7) case proved too trivial for documentation. The cases evaluated are shown in Figures 2.6.2 through 2.6.4.

Figure 2.6.2, Configuration A represents the design which is proposed as the most feasible approach to a light weight, high power solar array. Although Configuration B has fewer functional blocks, its reliability is somewhat lower than A's due to the (relatively) high failure rate torque motor which more than offsets the effect of the clutches in Configuration A.

Figure 2.6.3 shows the TEE system which was evaluated. The dotted lines connecting the deployment mechanisms indicates that some type of synchronization of the torque motors, either electrical or mechanical in nature, is required. Analysis of the synchronizing loop was not performed because the relative reliabilities of the candidate configurations had already been determined, making further investigation redundant.

Figure 2.1.4 ,the Hingelock Mechanism is identical to Figure 2.6.3 except that one deployment mechanism is required instead of two. Therefore, a Hingelock Mechanism's reliability will differ from the corresponding TEE configuration by slightly greater than the difference of one torque motor. In fact, the torque motor is estimated to account for 96.6% of the total failure rate of a deployment mechanism (as shown in the functional block diagram.)

2.6.3 Failure Mode and Effects

The Failure Mode and Effects study has been started and is still in progress. The purpose of this study is to identify potential modes of failure, their effects on mission success, to pinpoint areas requiring special attention and to remove susceptability to critical failure through redesign or redundancy.

Since a structure such as a solar array is highly vulnerable to space hazards, redundant features were incorporated into the design. The solar cell strings in each module have been arranged in such a manner that a hit by a meteorid, causing loss of a string, would constitute the least degradation of power output. Also, redundancy has been employed extensively in the array. Redundant module electrical connectors, each with redundant pins, connect to redundant bus bars extending along the length of the array so that loss of a single pin, connector or conductor would cause negligible loss of power. A 50% redundancy has been designed into the slip rings; each ring additionally uses two redundant brushes. At this time, it is not known whether a main power connector will be used between the bus bars and the slip rings; but, if employed it will also have redundant pins.

TYPICAL BASIC MORTALITY TYPES

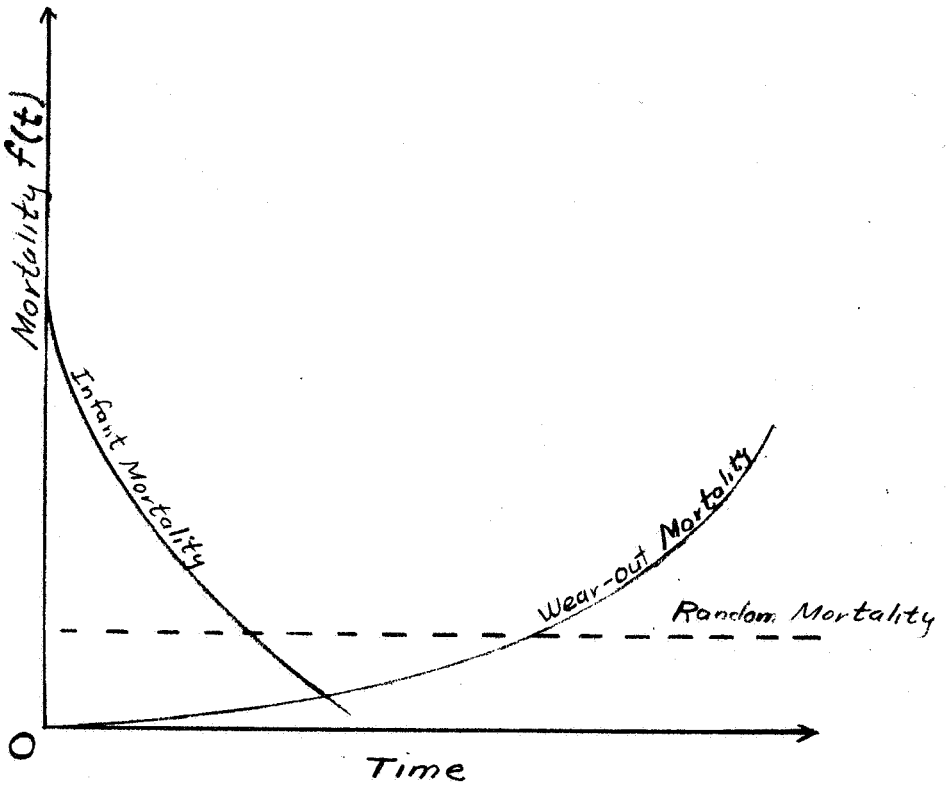
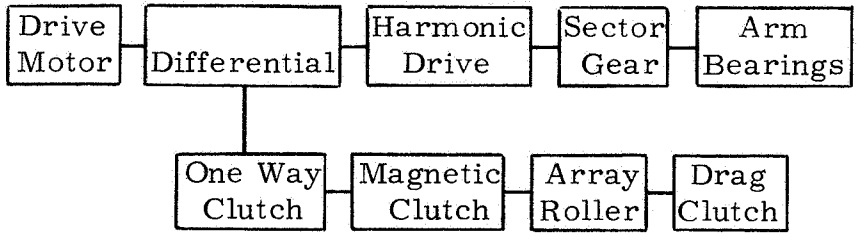
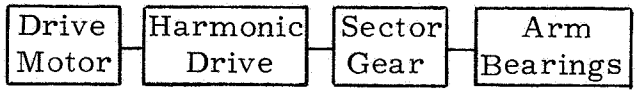


Figure 2.6.1

FOLDING ARM MECHANISM



Configuration A
P_s(random) = 99.98%



Configuration B
P_s(random) = 99.97%

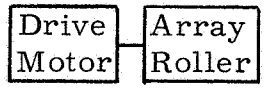


Figure 2.6.2

TEE MECHANISM

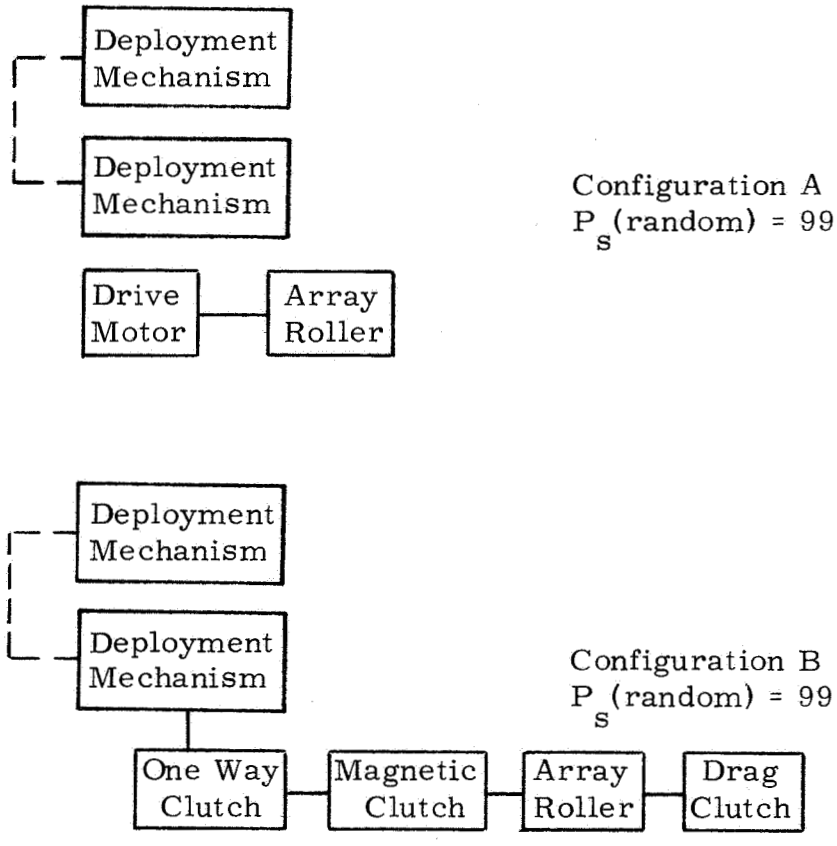


Figure 2.6.3

HINGELOCK MECHANISM

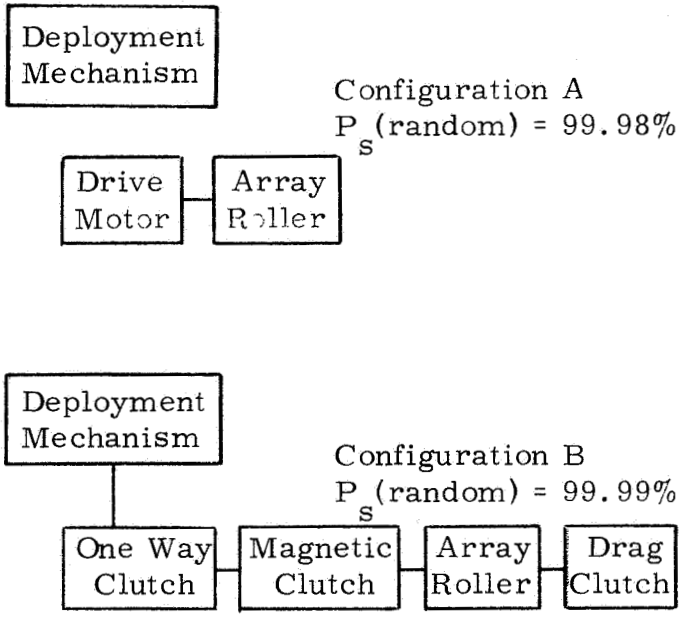


Figure 2.6.4

2.7 DESIGN SELECTION

In the preceeding sections of this report, parametric investigations were conducted on the most significant factors affecting the power/weight ratio of a roll-up solar array. It is interesting to note that, for a 250 to 275 square foot array, and for the mounting surface dimensional restrictions and general requirements of the array specifications, an array aspect ratio between three (3) and six (6) (which corresponds to array width of seven (7) to nine(9) feet) results in the maximum power/weight ratio. This factor was brought out in the studies on packaging volume, electrical harness design, the folding arm support system and the array storage drum with its supporting bracketery. It should be noted, however, that one cannot consider the optimum design for any one element, but rather, must consider them all in toto. The result of combining the various elements and arriving at a structural system weight are graphically presented in the figures of Section 2.3 (Structural Analysis).

The result of the system studies and of the parametric analysis dicate the selection of an array panel which is 8.7 feet wide by 35.5 feet long. This corresponds to an aspect ratio of approximately four (4).

Figure 3.1.1 summarizes the weight of the various elements of the three deployment methods which were considered. Figure 3.1.2 summarizes the power/weight ratios obtainable by each of the three systems. Although the Hinge Lock system provides a power/weight ratio of 36.7 and a folding arm system results in a ratio of 35.1, the folding arm system was selected as the preferred design because of the development work required and the time element available for such a development of the Hingelock. The reliability figures, as reflected in the design summary, apply only to the mechanical aspects of the various systems and do not include the wear-out factor. Fairchild Hiller's experience with the TEE device has indicated that such elements may be fabricated and used with high confidence in their reliable operation for a relatively few deployments; however, the wear out rates appear quite high when compared to that of mechanical linkages as typified in the folding arm design. Therefore, the folding arm configuration has been selected. The Hingelock System is under active development at Fairchild Hiller

WEIGHT SUMMARY

	FOLDING ARM	TEE	HINGE-LOCK TUBE
1 MECHANISM & SUPPORTING STRUCTURE	–	24.03	12.27
2 FOLDING ARMS & CABLING SYSTEM	12.49	–	–
3 EXTENDABLE ELEMENTS	–	9.28	4.54
4 DRIVE MOTORS & SYSTEM ELEMENTS	7.52	2.13	1.46
5 SPREADER BAR	1.40	1.21	1.32
6 STORAGE DRUM	1.90	1.90	1.90
7 STORAGE DRUM BRACKETS	4.71	2.02	3.11
8 ARRAY PANEL & WIRING	50.60	50.60	50.60
	78.62	91.02	75.20

Figure 3.1.1

DESIGN SELECTION SUMMARY

CONFIGURATION	POWER (WATTS)	WT. LBS.	POWER / WT.	RELIABILITY	PRODUCIBILITY
FOLDING ARM	2762	78.62	35.13	99.98	STATE OF THE ART
HINGELOCK	2762	75.20	36.73	99.99	DEVELOPMENT REQUIRED
TEE	2735	91.02	30.05	99.98	STATE OF THE ART



650-00102-QR

Figure 3.1.2

and the problem of bearing stresses in the tab and slot areas appears to be yielding to an intensive development program. Again, however, the requirement to use 1968 state-of-the-arts preclude the selection of the Hingelock System.

Figure 3.1.3 is a design summary of the various factors of the selected design comparing them with the required parameters. It should be noted that in all cases the selected design exceeds the requirements for power output and the primary requirement of power/weight of 30 watts/pound. The design power/weight of 35.13 watts/lb is based upon deliverable, useable power at the spacecraft array interface.

The design area selected (277.4 square feet) is obtained by considering the area on each module enclosed within the boundary of the outer-most rows of cells. This area is 27.4 square feet greater than the nominal area of 250 square feet. It must be recognized that a folding arm design by its very nature requires that the length of an array be in increments equal to the length of the various arm elements. An actual area of 250 square feet may be obtained by deleting some of the arm elements. However, shortening the arm elements will pose a problem in supporting these elements during the launch phase in that supporting bracketery must be extended a greater distance from the base structure of the array and, hence, causes a weight penalty. For the study, it is assumed that the 250 square foot nominal panel area is a minimum and that larger areas may be used as required to obtain the maximum power/weight ratio and hence the most efficient design.

DESIGN SUMMARY

REQUIRED	DESIGN
1. 30 WATTS/POUND min.	35.13 WATTS/POUND
2. 10 WATTS/sq. ft NOMINAL	10.39 WATTS/sq. ft
A) 2 cm x 2 cm CELL .008 in. THICK	2 cm x 2 cm CELL, .008 in. THICK
B) 225 CELLS/sq. ft MAXIMUM	223.2 CELLS/sq. ft
C) 49.5 mw/CELL MAXIMUM AT 140 mw/cm^2 55° C.	49.5 mw/CELL @ 140 mw/cm^2 and 55° C
3. 250 sq. ft NOMINAL PANEL AREA	277.4 sq. ft NOMINAL PANEL AREA
4. 2.5 KW OF ELECTRICAL POWER PER PANEL	2.76 KW ELECTRIC POWER PER PANEL

Figure 3.1.3

3.0 CONCLUSIONS

For the reasons presented in Section 2.7, it is seen that care must be exercised in making generalized statements concerning the power/weight factor which may be obtained with this or any other design. One must consider the geometry of the available packaging area, the mounting to which the array must be attached, and similar factors which can significantly effect the overall design.

Fairchild Hiller believes that through consideration of all factors as presented in the body of this report, the folding arm configuration results in an optimum design. The selected configuration exceeds the 30 watt/lb. requirement, feasibility of fabrication has been proven and high reliability is established with confidence.

4.0 RECOMMENDATIONS

Based upon the studies completed, Fairchild Hiller believes that the feasibility of a 30-watt/pound roll-up solar array is established. A working model of the selected design should be manufactured and tested to prove the design concepts and to identify and aid in solving any basic mechanical and/or fabrication problems. Ultimately, the feasibility of a roll-up solar array must be proven through flight experiments.

5.0 NEW TECHNOLOGY

No reportable items of New Technology have been uncovered during this reporting period.

6.0 REFERENCES

For continuity and clarity, references have been placed at the end of each Technical Discussion Section (Reference Section 2.1 through 2.7, where applicable).